



The University of  
**Nottingham**

UNITED KINGDOM • CHINA • MALAYSIA

Chan, Park Hinn (2017) Design study of composite repair system for offshore riser applications. PhD thesis, University of Nottingham.

**Access from the University of Nottingham repository:**

<http://eprints.nottingham.ac.uk/33455/1/CHAN%20PARK%20HINN%20-%20Design%20Study%20of%20Composite%20Repair%20System%20for%20Offshore%20Riser%20Applications.pdf>

**Copyright and reuse:**

The Nottingham ePrints service makes this work by researchers of the University of Nottingham available open access under the following conditions.

This article is made available under the University of Nottingham End User licence and may be reused according to the conditions of the licence. For more details see: [http://eprints.nottingham.ac.uk/end\\_user\\_agreement.pdf](http://eprints.nottingham.ac.uk/end_user_agreement.pdf)

For more information, please contact [eprints@nottingham.ac.uk](mailto:eprints@nottingham.ac.uk)



The University of  
**Nottingham**

UNITED KINGDOM · CHINA · MALAYSIA

Department of Mechanical, Materials and Manufacturing Engineering

# **Design Study of Composite Repair System for Offshore Riser Applications**

by

**Chan Park Hinn, MEng**

Thesis submitted to The University of Nottingham for the  
degree of Doctor of Philosophy

September 2015

## **ABSTRACT**

Risers in offshore operations are subjected to corrosion during their service life cycle. The use of relatively inexpensive, high strength to weight ratio fibre reinforced polymer composite (FRPC) as a load bearing pipe repair sleeve is an emerging technology that is becoming common for offshore applications. Risers experience complex loading profiles and experimental investigations often incur substantial time, complicated instrumentation and setup costs.

The main aim of this research is to develop a design tool for the repair of offshore riser that suffers from external corrosion damage on its surface using FRPC material. The simplest configuration of a fixed platform riser in the form of a vertical single-wall pipe is being considered. Characterization of the stress-strain behaviour of the FRPC laminate in the composite repair system subjected to various load profiles of a common riser is performed. The means of composite repair takes into account the ease of automated installation. The final repair method considers the use of unidirectional pre-impregnated (prepreg) FRPC that is assumed to be helically wounded around the riser.

Finite element models of the composite repair system were developed via ABAQUS. Global analysis of the entire length of the riser was omitted as external corrosions usually occurs in a localised manner on the surface of the riser. Instead, local analyses were conducted where boundary conditions were applied to mimic an infinitely long cylindrical structure such as the riser. The local analyses FEA models were made to capture the stress-strain behaviour of the FRPC laminate subjected to different load profiles including static loadings such as internal pressure, tensile load and bending load. The design loads were

calculated based on a limit analysis known as Double-Elastic Curve method developed by Alexander (2008). Proper element selection and mesh convergence were carried out to determine the FE model that can minimize the time and CPU memory needed for the simulation without compromising the accuracy of the results.

The second part of this research integrated experimental tests to validate the FE model developed using the ABAQUS general purpose code. Due to constraints on cost and supply of materials and equipment, small-scale tests were conducted. Similitude relations were used to determine the scale properties between the model and the prototype. The final results showed that the FE model can represent the real-life tests of corroded riser repaired with off-axis FRPC laminate with great accuracy of more than 85%. Hence can be a useful tool for design and parametric study of the composite repair system.

Using the validated FE model, an extensive parametric study of the composite repair system with respect to varying corrosion defects was conducted. The thickness and length of the repair laminate were compared to the ASME PCC-2 standard. Optimum thickness and length of the composite laminate were determined based on the maximum allowable strains computed using the Double-Elastic Curve method. In addition, varying fibre angle orientation of the unidirectional prepreg was considered as it is one of the main factors in helical winding.

Based on the results from the parametric study, a simple relation was developed to predict the required thickness of the composite repair system subjected to combined loading. This relation combined with the developed FE model can be

used to provide a quick design and performance validation of a composite repair system for offshore riser, which is the main novelty aspect of this research.

## **Acknowledgement**

First and foremost, I would like to thank God for his guidance, and for giving me the wisdom and courage to complete this research work.

I would like to show my gratitude to my supervisor, Dr. Albert Tshai for his unwavering guidance, advice and help from day one of this research, until the completion of this thesis.

I would also like to extend my gratitude to my supervisors from the UK campus, Dr. Mike Johnson and from the China campus, Dr. Choo Hui Leng for their support during my exchange to the respective campuses.

Special thanks to Professor Li Shuguang for his valuable input and comments throughout this research, especially in terms of the finite element modelling.

I would not have had this opportunity were it not for the sponsorship from the University of Nottingham for the Inter-campus PhD Scholarship Program.

Last but not least, I would like to thank my family, especially my mother, who has endured a lot of hardship in raising me and my siblings, and also giving the support and encouragement to pursue my goals.

## **Declaration**

This thesis is submitted for the degree of Doctor of Philosophy in the Department of Mechanical, Materials & Manufacturing Engineering at the University of Nottingham Malaysia Campus. No part of this thesis has been submitted for any other degree or diploma at any other university and institution. As far as the author is aware, all the work in this thesis is original unless reference is made to other works. Parts of the research work of this thesis have been published or presented in the followings:

## **Chapter in Book:**

1. P.H. CHAN, K.Y. TSHAI, M. JOHNSON and S. LI, 2015. Chapter 9: FEA Modelling of FRP Repair in Offshore Risers. *In: PROFESSOR VISTASP KARBHARI, ed., Rehabilitation of pipelines using fibre reinforced polymer (FRP) composites: 3. Design and Analysis* 1st Edition. Woodhead Publishing Ltd UK. 177-209

## **Journal Papers:**

2. P.H. CHAN, K.Y. TSHAI, M. JOHNSON and S. LI, 2015. The Flexural Properties of Composite Repaired Pipeline: Numerical Simulation and Experimental Validation. *Composite Structures* 133, 312-321
3. P.H. CHAN, K.Y. TSHAI, M. JOHNSON, H.L. CHOO, S. LI and K. ZAKARIA, 2015. Burst Strength of Carbon Fibre Reinforced HDPE Strip Pipeline Repair System - A Numerical and Experimental Approach. *Journal of Composite Materials*.49(6), 749-756

4. P.H. CHAN, K.Y. TSHAI, M. JOHNSON and S. LI, 2014. FEA of Combined Static Loadings on Offshore Pipe Riser Repaired with Fibre Reinforced Composite Laminates. *Journal of Reinforced Plastics and Composites*. 33(6), 514-525
5. P.H. CHAN, K.Y. TSHAI, M. JOHNSON and H.L. CHOO, 2014. Finite Element Modelling of Static and Fatigue Failure of Composite Repair System in Offshore Pipe Risers. *Advanced Materials Research: Material Research and Applications*. 875-877, 1063-1068.
6. P.H. CHAN, K.Y. TSHAI, M. JOHNSON and H.L. CHOO, 2012. Finite Element Modelling of Composite Repair in Offshore Pipe Riser. *Advanced Materials Research: Advanced Materials and Processes II*. 557-559, 2239-2242.

### **Conference Papers/Abstracts:**

1. P.H. CHAN, K.Y. TSHAI, M. JOHNSON, H.L. CHOO and S. LI, 2013. A Finite Element Study of the Influence of Coupled Loadings on Offshore Pipe Riser Repaired with Fibre Reinforced Composite. *In: M. JAAFAR, K.H. LEONG, A.R. AZURA and A.Y. LEONG, eds., 8th Asian-Australasian Conference on Composite Materials 2012 (ACCM-8): Composites: Enabling Tomorrow's Industry Today 2. Asian Australasian Association for Composite Materials (AACM)*. 1580-1585
2. P.H. CHAN, K.Y. TSHAI, M. JOHNSON, H.L. CHOO and S. LI, 2012. Finite Element Modelling of Composite Repair in Offshore Pipe Riser.



In: 2nd International Conference on Chemical Engineering and Advanced Materials (ICCEAM 2012), Guangzhou, China.

3. P.H. CHAN, K.Y. TSHAI, M. JOHNSON and H.L. CHOO, 2012. Finite Element Modelling of Static and Fatigue Failure of Composite Repair System in Offshore Pipe Risers. In: 2012 International Conference on Advanced Material and Manufacturing Science (ICAMMS), Beijing, China.

# Table of Contents

ABSTRACT .....	i
Acknowledgement .....	i
Declaration.....	ii
Table of Contents.....	v
List of Figures.....	xi
List of Tables .....	xxiv
Abbreviations.....	xxvi
Nomenclature.....	xxviii
Chapter 1 Introduction.....	1
Chapter 2 Literature Review.....	5
2.1 Introduction.....	5
2.2 Conventional offshore riser repair methods .....	6
2.3 Composite Repair for Onshore Pipelines .....	7
2.3.1 Types of Composite Repair .....	9
2.3.2 Existing Onshore Composite Repair Products .....	10
2.4 Integration of Composite Repair in Offshore Riser.....	14
2.4.1 Limitations in the Application of Composite in Riser Repair .....	14
2.4.2 Automated Riser Repair Machine .....	17
2.5 Previous Studies on Composite Repair System.....	24
2.5.1 Composite Bonded Repair in Other Applications .....	24

2.5.2 Application of FRPC in Onshore Pipeline Repair .....	27
2.5.3 Application of FRPC in Offshore Riser Repair .....	30
2.5.4 Bonding of Composite to Steel Pipe/Riser .....	33
2.6 Standards & Guidelines .....	37
2.6.1 Standards for Pipeline Design .....	38
2.6.2 Standards for Offshore Riser Design .....	38
2.6.3 Standards for the Evaluation of Corroded Pipeline/Riser Residual Strength .....	39
2.6.4 Standards for Corroded Pipeline/Riser Repair .....	40
2.7 Concluding Remarks .....	41
Chapter 3 Design of Composite Repair System for Offshore Riser .....	44
3.1 Introduction .....	44
3.2 Loading Conditions of a Riser .....	45
3.2.1 Functional Loads .....	45
3.2.2 Environmental Loads .....	46
3.2.3 Installation Loads .....	47
3.2.4 Accidental Loads .....	48
3.2.5 Load Cases .....	48
3.3 Design Requirements .....	48
3.4 Residual Strength of Corroded Risers .....	49
3.5 Minimum Repair Thickness of the Composite Laminate .....	53
3.6 Axial Length of the Laminate Repair .....	57

3.7 Design Conditions .....	58
3.8 Concluding Remarks .....	64
Chapter 4 Finite Element Analysis .....	65
4.1 Introduction.....	65
4.2 Fundamentals of FE Modelling within ABAQUS® .....	66
4.2.1 Non-linear Solution in ABAQUS Standard.....	66
4.2.2 Selection of Element Type.....	67
4.2.3 Mesh Refinement.....	71
4.3 FEA Model of Composite Repair System .....	74
4.3.1 Steel Riser.....	74
4.3.2 Composite Laminate.....	75
4.3.3 Materials .....	84
4.3.4 Boundary Conditions.....	87
4.3.5 Interaction Properties.....	88
4.4 Validation of Numerical Model.....	92
4.4.1 Classical Mechanics.....	92
4.4.2 Case study of Helicoid Epoxy Sleeve (HES) <sup>TM</sup> .....	94
4.5 Individual Static Loading .....	108
4.5.1 Internal Pressure, $P_{int}$ .....	109
4.5.2 Tensile Load, $F_t$ .....	112
4.5.3 Bending Load, $M_b$ .....	115
4.6 Combined Static Loading .....	118

4.6.1 Combined Internal Pressure, $P_{int}$ and Tensile Load, $F_t$ .....	119
4.6.2 Combined Internal Pressure, $P_{int}$ , Tensile Load, $F_t$ and Bending Moment, $M_b$ .....	124
4.7 Response of FRPC Repair Laminate .....	129
4.8 Cyclic Loading.....	135
4.8.1 Design Conditions .....	136
4.8.2 Numerical Modelling.....	137
4.8.3 Results and Discussion .....	138
4.9 Concluding Remarks .....	142
Chapter 5 Experimental Testing .....	145
5.1 Introduction.....	145
5.2 Methodology.....	145
5.3 Materials .....	146
5.4 Experimental Setup.....	149
5.5 Similitude Relations .....	155
5.6 Experimental Validation.....	161
5.6.1 Bare Riser without Corrosion .....	161
5.6.2 Bare Riser with Corrosion .....	162
5.6.3 Repaired Riser .....	166
5.6.4 Comparison between Full Scale Model and Scaled Down Prototype.....	169
5.7 Concluding Remarks .....	171

Chapter 6 Parametric Study of Composite Repair System for Offshore Riser .....	173
6.1 Introduction.....	173
6.2 Types of Reinforcing Fibres .....	174
6.2.1 Individual Static Load.....	177
6.2.2 Combined Static Load .....	182
6.3 Laminate/Fibre Orientation .....	187
6.3.1 Combined Internal Pressure, $P_{int}$ & Tensile Load, $F_t$ .....	190
6.3.2 Combined Internal Pressure, $P_{int}$ , Tensile Load, $F_t$ & Bending Moment, $M_b$ .....	195
6.4 Wrapping Angle.....	199
6.5 Varying Corrosion Defects .....	202
6.5.1 Varying Corrosion Length.....	202
6.5.2 Varying Corrosion Width .....	206
6.6 Concluding Remarks .....	215
Chapter 7 Conclusions.....	217
7.1 Primary Achievements and Contributions to New Knowledge.....	217
7.2 Recommendations for Future Work .....	220
References.....	221
Appendix A Industrial Needs for Composite Repair Machine and Its Preliminary Design .....	231
A.1 Background.....	231

A.2 Statement of Requirements .....	232
A.3 Riser Traversing Module .....	235
A.3.1 Improvements on Design .....	238
A.4 Inspection Module .....	238
A.5 Surface Preparation Module .....	240
A.6 Wrapping Module .....	244
A.6.1 Assumptions .....	245
A.6.2 Calculations of Wrapping Geometry .....	248
A.6.3 Mechanical System Design.....	254
A.6.4 Improvements on Design .....	257
A.6.5 Controlling .....	260
A.7 Summary .....	263
Appendix B Calculations of wrapping geometry .....	264
Appendix C MATLAB Code for Wrap Geometry .....	268

## List of Figures

Figure 1-1, Methodology .....	4
Figure 2-1, Mechanical gouge dent on a pipe.....	8
Figure 2-2, External corrosion on pipe .....	8
Figure 2-3, Internal corrosion on pipe .....	8
Figure 2-4, Types of composite repair: (a) Wet lay-up (b) Pre-cured layered (c) Pre-cured stand-off sleeve (Alexander & Ochoa, 2010) (Alexander, 2006) (Clock Spring, 2012) .....	10
Figure 2-5, Installation of Clock Spring® on a steel pipe (Clock Spring, 2012) .....	11
Figure 2-6, Installation of AquaWrap® on a corroded pipeline (Alexander 2005) .....	12
Figure 2-7, Prototype of the unmanned underwater robotic crawler (Chatzakos, et al., 2010) .....	18
Figure 2-8, Sequence of actions for the translational motion along the length of the riser (Psarros, et al., 2010) .....	18
Figure 2-9, Sequence of actions for the rotational motion around the circumference of the riser (Psarros, et al., 2010).....	19
Figure 2-10, Pipe inspection robot by Yukawa et al. ( (Yukawa, et al., 2006))	20
Figure 2-11, 3D model of the compliant mechanism of SMA-actuated pipe crawler, (a) crawling device with clamping rings, (b) SMA U-shape strips (Balaji, et al., 2008).....	21
Figure 2-12, Full assembly of ACCUWRAP™ (SMC, 2011) .....	22
Figure 2-13, Semi-automatic composite repair machine Previous Studies on Composite Repair System (Boulet d'Auria, et al., 2013).....	23



Figure 2-14, (a) Web buckling of unstrengthened RHS (b) Web yielding and debonding of CFRP strengthened RHS (Zhao, et al., 2006) .....	25
Figure 2-15, Bending test setup and finite element model of I-beam strengthened with CFRP strips (Narmashiri, et al., 2010) .....	26
Figure 2-16, Finite element model of cracked steel tube with FRPC patching (Lam, et al., 2011).....	26
Figure 2-17, 3D finite element model used in Duell et al.'s work (Duell, et al., 2008).....	28
Figure 2-18, Comparison between experimental and FEA results (CC = Circumferential stain in corroded region , CRC = circumferential strain in corroded region of repair pipe) (Meniconi, et al., 2002) .....	29
Figure 2-19, Comparison of buckling shapes between full-scale testing and finite element modelling (Shouman & Taheri, 2011) .....	30
Figure 2-20, FRPC-wrapped specimens cured under saltwater conditions (Seica & Packer, 2007) .....	31
Figure 2-21, Finite element model of repaired pipe and enlarged view of corroded region mesh (Esmaeel, et al., 2012) .....	32
Figure 2-22, Finite element model used in Haghani's work (Haghani, 2010)..	35
Figure 2-23, Finite element model of FRP-to-steel joint (Yang et al, 2013) ...	35
Figure 2-24, Debonding between the CFRP strip and steel beam (Bocciarelli et al, 2008) .....	36
Figure 2-25, Shear stress at steel-composite interface of the finite element model (Alexander, 2007) .....	37
Figure 3-1, Parabolic criteria for classifying corrosion defects according to predicted failure stress (ASME, 1991) .....	50

Figure 3-2, Process of assessing the remaining strength of a corroded pipe (ASME, 1991).....	51
Figure 3-3, Pressure level relations (API, 1999) .....	56
Figure 3-4, Limit state analysis of bare riser subjected to $P_{in}$ .....	62
Figure 3-5, Limit state analysis of bare riser subjected to $F_t$ .....	62
Figure 3-6, Limit state analysis of bare riser subjected to $M_b$ .....	62
Figure 3-7, Limit state analysis of bare riser subjected to $P_{in}$ , $F_t$ & $M_b$ .....	63
Figure 4-1, Continuum 3D brick element with 8 nodes (a) and 20 nodes (b) ..	68
Figure 4-2, Conventional and continuum shell elements .....	69
Figure 4-3, Coarse mesh with S4R element (riser 1672 elements; sleeve 1034 elements).....	70
Figure 4-4, Coarse mesh with C3D8R element (riser 3458 elements; sleeve 1119 element): (a) Corroded riser, (b) Corroded riser with CRS .....	71
Figure 4-5, Intermediate mesh with S4R element (4305 elements) .....	72
Figure 4-6, Fine mesh with S4R element (6536 elements) .....	72
Figure 4-7, Biased mesh with gradual decrease in element size using S4R element (2046 elements).....	72
Figure 4-8, Biased mesh with fine mesh at corroded region using S4R element (2669) elements .....	72
Figure 4-9, Riser model with 2 elements in thickness direction.....	73
Figure 4-10, Riser model with 3 elements in thickness direction.....	73
Figure 4-11, Riser model with 4 elements in thickness direction.....	73
Figure 4-12, Riser model with 6 elements in thickness direction.....	73
Figure 4-13, Hoop stress and hoop strain at varying S4R element mesh density .....	74

Figure 4-14, Coordinate system of FRPC .....	77
Figure 4-15, AS4/3501-6 carbon/epoxy unidirectional lamina strength properties on Autodesk® <i>Simulation Composite Analysis</i> .....	81
Figure 4-16, AS4/3501-6 carbon/epoxy unidirectional lamina and constituent properties on Autodesk® <i>Simulation Composite Analysis</i> .....	82
Figure 4-17, Ramberg-Osgood model .....	85
Figure 4-18, Quarter pipe model with cross sectional view .....	88
Figure 4-19, Full pipe model in four-point bending setup .....	88
Figure 4-20, Sectional cut out detail of the Helicoid Epoxy Sleeve System (HES) <sup>TM</sup> system (Merit Technologies Sdn. Bhd., Malaysia) .....	95
Figure 4-21, API 5L grade X52 steel pipe with Helicoid Epoxy Sleeve <sup>TM</sup> system installed.....	99
Figure 4-22, Meshed parts: (a) API 5L grade X52 pipe with corroded section, (b) corroded pipe with HES <sup>TM</sup> , (c) carbon fibre-reinforced PE strip, and (d) epoxy grout .....	100
Figure 4-23, Normalised modulus of fibre-reinforced composite at varying angle .....	102
Figure 4-24, Contour plot of hoop strain on the corroded X52 steel pipe.....	104
Figure 4-25, Computation of PACL and design pressure of an uncorroded pipe .....	104
Figure 4-26, Computation of PACL and design pressure of corroded pipe ...	105
Figure 4-27, Computation of burst pressure of corroded pipe repaired with HES <sup>TM</sup> system.....	105
Figure 4-28, Pressure against hoop strain curves for uncorroded pipe, corroded pipe and corroded pipe repaired with HES <sup>TM</sup> system.....	106

Figure 4-29, HES <sup>TM</sup> repaired pipe at burst pressure (a) failure within the repaired region and (b) close up of failure region .....	107
Figure 4-30, $\sigma_h$ contour plot of corroded riser at 22MPa .....	110
Figure 4-31, $\varepsilon_h$ contour plot of corroded riser at 22MPa .....	110
Figure 4-32, $\sigma_h$ contour plot of repaired riser at 22MPa.....	111
Figure 4-33, $\varepsilon_h$ contour plot of repaired riser at 22MPa .....	111
Figure 4-34, Limit state analysis of riser subjected to $P_{int}$ .....	112
Figure 4-35, $\sigma_a$ contour plot of corroded riser at 1785kN .....	113
Figure 4-36, $\varepsilon_a$ contour plot of corroded riser at 1785kN.....	113
Figure 4-37, $\sigma_a$ contour plot of repaired riser at 1785kN .....	114
Figure 4-38, $\varepsilon_a$ contour plot of repaired riser at 1785kN.....	114
Figure 4-39, Limit state analysis of riser subjected to $F_t$ .....	115
Figure 4-40, $\sigma_b$ contour plot of corroded riser at 120kNm.....	116
Figure 4-41, $\varepsilon_b$ contour plot of corroded riser at 120kNm .....	116
Figure 4-42, $\sigma_b$ contour plot of repaired riser at 120kNm .....	117
Figure 4-43, $\varepsilon_b$ contour plot of repaired riser at 120kNm.....	117
Figure 4-44, Limit state analysis of riser subjected to $M_b$ .....	118
Figure 4-45, $\sigma_a$ contour plot of corroded riser at combined 22MPa and 1785kN .....	120
Figure 4-46, $\sigma_h$ contour plot of corroded riser at combined 22MPa and 1785kN .....	120
Figure 4-47, $\varepsilon_a$ contour plot of corroded riser at combined 22MPa and 1785kN .....	121
Figure 4-48, $\varepsilon_h$ contour plot of corroded riser at combined 22MPa and 1785kN .....	121

Figure 4-49, $\sigma_a$ contour plot of repaired riser at combined 22MPa and 1785kN	122
Figure 4-50, $\sigma_h$ contour plot of repaired riser at combined 22MPa and 1785kN	122
Figure 4-51, $\varepsilon_a$ contour plot of repaired riser at combined 22MPa and 1785kN	123
Figure 4-52, $\varepsilon_h$ contour plot of repaired riser at combined 22MPa and 1785kN	123
Figure 4-53, Limit state analysis of riser subjected to $P_{int}$ and $F_t$ (Axial Strain)	123
Figure 4-54, Limit state analysis of riser subjected to $P_{int}$ and $F_t$ (Hoop Strain)	124
Figure 4-55, Limit state analysis (axial strain) of riser subjected to $P_{int}$ , $F_t$ and $M_b$	125
Figure 4-56, $\sigma_a$ contour plot of corroded riser at combined 22MPa, 1785kN and 78kNm	126
Figure 4-57, $\sigma_h$ contour plot of corroded riser at combined 22MPa, 1785kN and 78kNm	127
Figure 4-58, $\varepsilon_a$ contour plot of corroded riser at combined 22MPa, 1785kN and 78kNm	127
Figure 4-59, $\varepsilon_h$ contour plot of corroded riser at combined 22MPa, 1785kN and 78kNm	127
Figure 4-60, Limit state analysis (hoop strain) of riser subjected to $P_{int}$ , $F_t$ and $M_b$	128
Figure 4-61, Input of cyclic bending load	137

Figure 4-62, Defect region and locations of node 1 and node 2 on the laminate .....	138
Figure 4-63, Strain energy release rate for AO laminate.....	138
Figure 4-64, $f_{crit}$ for AO and HO laminate at node 1 and node 2 .....	139
Figure 4-65, Contour plot of axial strain .....	140
Figure 4-66, Axial stress vs. number of cycles for AO and HO laminates ....	141
Figure 4-67, Hoop stress vs. number of cycles for AO and HO laminates ....	141
Figure 4-68, Final bonded state of AO laminate on riser .....	142
Figure 4-69, Final bonded state of HO laminate on riser .....	142
Figure 5-1, Dumbbell specimens.....	147
Figure 5-2, True stress vs. true strain curve of the chosen mild steel pipe.....	148
Figure 5-3, Length of pipe relative to bending rig.....	149
Figure 5-4, Machined corroded region and location of the two strain gauges	150
Figure 5-5, Four-point bending setup with the aid of an Instron load frame..	151
Figure 5-6, Insulation film applied on top of strain gauges.....	151
Figure 5-7, Specimens of mild steel pipe wrapped with Panex35/MTM57 ...	153
Figure 5-8, Pipe specimen sealed within a nylon bagging film.....	154
Figure 5-9, Vacuum bagging of the pipe specimen.....	154
Figure 5-10, Curing of the composite prepreg performed with the aid of vacuum bagging .....	155
Figure 5-11, Similitude scaling between model and prototype .....	157
Figure 5-12, Bending moment diagram for four-point bend setup.....	159
Figure 5-13, Experiment and FE results of mild steel pipe .....	162
Figure 5-14, Section thickness of pipe in FE model.....	162
Figure 5-15, Experiment and FE results of corroded mild steel pipe.....	163

Figure 5-16, Raw experimental data & polynomial curve fit data .....	164
Figure 5-17, Percentage difference & RMS error between experimental and simulation results at varying wall thickness in the corroded region...	165
Figure 5-18, Experiment and FE results of corroded mild steel pipe repaired with MTM57 carbon/epoxy prepreg – (a) 0° prepreg, (b) 30° prepreg (c) 60° prepreg (d) 90° prepreg.....	166
Figure 5-19, Percentage difference & RMS error between experimental and simulation results of different specimens .....	167
Figure 5-20, Load-strain curve of bare pipe, corroded pipe and corroded pipes (Mild Steel pipe) repair with varying fibre angle orientation (Panex35/MTM57 Carbon/Epoxy prepreg) – (a) Experimental results (b) FE simulation results .....	168
Figure 5-21, FE results of full scale and scaled models for corroded mild steel pipe repaired with MTM57 carbon/epoxy prepreg – (a) 0° prepreg, (b) 30° prepreg (c) 60° prepreg (d) 90° prepreg.....	170
Figure 5-22, Load-strain curve of bare pipe, corroded pipe and corroded pipes (API 5L X60 pipe) repaired with varying fibre angle orientation (AS4/3501-6 Carbon/Epoxy prepreg) – FE simulation results .....	171
Figure 6-1, Load profiles on composite repair system .....	174
Figure 6-2, Weight gain percentage in glass- and carbon- (a) polyester, (b) Vinyl ester composites (Kootsookos, et al., 2011) .....	175
Figure 6-3, Internal pressure vs. hoop strain of corroded riser repaired with [0°] and [90°] laminates .....	177
Figure 6-4, Hoop strain contour plot of corroded riser repaired with: (a) [0°] carbon/epoxy, (b) [0°] E-glass epoxy at design load of 22MPa.....	178

Figure 6-5, Hoop strain contour plot of corroded riser repaired with: (a) [90°] carbon/epoxy, (b) [90°] E-glass epoxy at design load of 22MPa.....	179
Figure 6-6, Tensile load vs. axial strain of corroded riser repaired with [0°] and [90°] laminate .....	180
Figure 6-7, Bending Moment vs. axial strain of corroded riser repaired with [0°] and [90°] laminate .....	182
Figure 6-8, Load vs. axial strain plot of corroded riser repaired with unidirectional axially orientated [0°] and hoop orientated [90°] laminates.....	183
Figure 6-9, Load vs. hoop strain plot of corroded riser repaired with unidirectional axially orientated and hoop orientated laminates .....	184
Figure 6-10, Load vs. axial strain plot of corroded riser repaired with unidirectional axially orientated [0°] and hoop orientated [90°] laminates.....	186
Figure 6-11, Ply stack plot for 90° unidirectional laminate in hoop direction	188
Figure 6-12, Ply stack plot for 0° unidirectional laminate in axial direction .	189
Figure 6-13, Ply stack plot for quasi-isotropic [90°/±45°/0°]s laminate .....	189
Figure 6-14, Ply stack plot for balanced and symmetric [90°/±30°]s laminate .....	189
Figure 6-15, Ply stack plot for angle ply [±55°]s laminate .....	190
Figure 6-16, Load vs. hoop strain plot of corroded riser repaired with different orientation of carbon/epoxy laminates.....	191
Figure 6-17, Load vs. axial strain plot of corroded riser repaired with different orientation of carbon/epoxy laminates.....	192



Figure 6-18, Stress at different plies of the $[90^\circ/\pm 30^\circ]_s$ laminate subjected to combined $P_{in}$ and $F_t$ : (a) (b) $-30^\circ$ ply, (c) (d) $+30^\circ$ ply, (e) (f) $90^\circ$ ply .....	194
Figure 6-19, Load vs. axial strain plot of corroded riser repaired with different orientation of carbon/epoxy laminates subjected to combined internal pressure, tensile and bending load .....	195
Figure 6-20, Axial and hoop stresses at different plies of the $[90^\circ/\pm 30^\circ]_s$ laminate subjected to combined $P_{in}$ , $F_t$ and $M_b$ : (a) (b) $-30^\circ$ ply, (c) (d) $+30^\circ$ ply, (e) (f) $90^\circ$ ply.....	197
Figure 6-21, Axial and hoop stresses at different plies of the $[90^\circ/\pm 45^\circ/0^\circ]_s$ laminate subjected to combined $P_{in}$ , $F_t$ and $M_b$ : (a) (b) $0^\circ$ ply, (c) (d) $-45^\circ$ ply, (e) (f) $+45^\circ$ (g) (h) $90^\circ$ ply.....	198
Figure 6-22, Load vs. axial strain plot of corroded riser repaired with varying wrapping angle of carbon/epoxy laminates subjected to combined internal pressure, tensile and bending load.....	200
Figure 6-23, Load vs. hoop strain plot of corroded riser repaired with varying wrapping angle of carbon/epoxy laminates subjected to combined internal pressure, tensile and bending load.....	201
Figure 6-24, Varying corrosion length with constant width of 50mm (a) 200mm (b) 400mm (c) 600mm (d) 800mm (e) 1000mm (f) 1200mm .....	203
Figure 6-25, Axial strain vs. length of corrosion with varying thickness of the composite repair.....	204
Figure 6-26, Axial strain vs. thickness of repair at varying length of corrosion .....	205

Figure 6-27, Comparison between ASME PCC-2 and FE simulation results at varying length of corrosion.....	206
Figure 6-28, Varying corrosion width with constant defect length of 600mm (a) 60° (b) 120° (c) 180° (d) 240° (e) 300° (f) 360° .....	207
Figure 6-29, Axial strain vs. width of corrosion at varying percentage wall thickness on the corroded region .....	208
Figure 6-30, Axial strain vs. wall thickness of corroded region at varying width of corrosion.....	209
Figure 6-31, Axial strain vs. thickness of repair at varying depth of corrosion .....	210
Figure 6-32, Comparison between ASME PCC-2 and FE simulation results at varying depth of corrosion.....	211
Figure 6-33, 3D plot of input data (FE simulation) and predicted data (regression analysis) .....	212
Figure 6-34, Comparison of FE simulation and predicted results for $t_{repair}$ of repaired API 5L X52 steel riser: (a) $W_c = 30^\circ$ , (b) $W_c = 60^\circ$ and (c) $W_c = 120^\circ$ .....	214
Figure A-1, Requirements of the CRS.....	232
Figure A-2, Key elements of composite pipeline repair machine .....	234
Figure A-3, Two main methods of moving along pipe .....	235
Figure A-4, Method of moving along pipe: (a) Wheeled motion, (b) Legged motion, (c) Inchworm motion.....	236
Figure A-5, 3D model of pipe crawler prototype developed by Bill Margeison (Margerison & Johnson, 2012).....	237

Figure A-6, Sequence of the pipe crawler navigating over a flange (Margerison & Johnson, 2012).....	238
Figure A-7, MEC-Combi Crawler developed by Innospection Ltd (a) crawler machine (b) subsea inspection (Innospection Ltd, 2013) .....	240
Figure A-8, Diver operating the Cavidyne CaviBlaster™ (CaviDyne, 2014)	241
Figure A-9, MC211 hydraulically powered twin brushes device (UES, 2014) .....	242
Figure A-10, Proserv marine growth removal (MGR) tool (Proserv, 2014) ..	242
Figure A-11, Cleaning module prototype (Carey & Johnson, 2013) .....	243
Figure A-12, Typical completed CRS wrap showing the end effect geometry at both ends of the repair .....	246
Figure A-13, Contour plot of axial strain on the composite repair sleeve with (a) uniform 45°helical wrap, (b) 45° helical wrap with 90° on both ends	247
Figure A-14, Contour plot of <i>SDV2</i> on the composite repair sleeve with (a) uniform 45°helical wrap, (b) 45° helical wrap with 90° wrap at both ends .....	248
Figure A-15, Wrap profile for the CRS at varying angles - (a) 30°, (b) 45°, (c) 60° and (d) 90° (hoop) .....	251
Figure A-16, Force components acting on the prepreg tape and riser.....	252
Figure A-17, Rendered image of the pipe wrapper prototype (Land, et al., 2012). .....	254
Figure A-18, Diagram of pipe wrapper prototype (Land, et al., 2012) .....	255
Figure A-19, Dimensions of the roll.....	256
Figure A-20, Rendered image of improved design of the wrapping module .	258
Figure A-21, Wrapping sequence of the wrapping module.....	259

Figure A-22, Flow chart for the wrapping sequence ..... 262

Figure B-1, Developed envelope of prepreg path..... 264

## List of Tables

Table 2-1, Components on the semi-automatic composite repair machine and their functions (Boulet d'Auria, et al., 2013) .....	23
Table 3-1, Temperature derating factor, $f_t$ (ASME, 2003) .....	57
Table 3-2, Design load and maximum permissible strain for different load cases .....	63
Table 5-1, Material properties for Panex35/MTM57 unidirectional prepreg. 148	
Table 5-2, Curing conditions and alternative cure cycle for autoclave cure of MTM57 .....	155
Table 5-3, Similitude relations (Ramu et al, 2012) .....	157
Table 5-1, Mechanical properties of API 5L X60 steel pipe .....	85
Table 5-2, Material properties of the chosen FRPC laminate .....	86
Table 5-3, Fracture and fatigue properties .....	91
Table 5-4, Comparison between classical mechanics and numerical results ...	94
Table 5-5, Percentage difference & RMS error between experimental and simulation results .....	164
Table 5-6, Mechanical Properties of API 5L X52 Steel .....	101
Table 5-7, Material properties of epoxy grout and carbon fibre-reinforced PE strip .....	102
Table 5-8, Results from design standards, experimental test and FEA simulation .....	108
Table 5-9, Stress and strain comparison between corroded riser and repaired riser .....	118
Table 5-10, Response of FRPC laminate at plastic analysis collapse load ....	130

Table 5-11, Steel-composite interface and composite interlaminar fatigue properties .....	136
Table 6-1, Hoop strain of various riser at 22MPa .....	179
Table 6-2, Axial strain of various riser at 1785kN tensile load.....	181
Table 6-3, Comparison of axial strain values of riser at 120kNm.....	182
Table 6-4, Axial and hoop strains of riser subjected to combined 22MPa internal pressure and 1785kN tensile load .....	185
Table 6-5, Comparison of strain values of riser at 22MPa, 1785kN and 78kNm .....	186
Table 6-6, Axial and hoop strains of riser repaired with different types of laminate orientation subjected to 22MPa ( $P_{in}$ ) and 1785kN ( $F_t$ )..	193
Table 6-7, Axial and hoop strains of riser repaired with different types of laminate orientation at 22MPa ( $P_{in}$ ), 1785kN ( $F_t$ )and 78kNm ( $M_b$ ) .....	193
Table 6-8, Appropriate thickness of repair at varying length of corrosion ....	205
Table 6-9, Thickness of repair at varying depth of corrosion.....	210
Table 6-10, Design load and maximum permissible strain for API 5L X52 steel riser .....	213
Table 7-1, Input parameters for wrapping profile .....	250

## Abbreviations

API	American Petroleum Institute
ASME	American Society of Mechanical Engineers
ASTM	American Standard for Testing and Materials
CFRP	Carbon fibre reinforced polymer
CRS	Composite repair system
DEC	Double elastic curve
DL	Design load
DNV	Det Norske Veritas
DOF	Degree of freedom
FE	Finite element
FEA	Finite element analysis
FRPC	Fibre reinforced polymer composite
ISO	International Organization for Standardization
MAOP	Maximum allowable operating pressure
MCT	Multi-continuum theory
PACL	Plastic analysis collapse load
RC	Corroded riser
RHS	Rectangular hollow section

RVE	Representative volume element
SCR	Steel catenary riser
SIF	Stress intensity factor
SLS	Serviceability limit state
SMA	Shape memory alloy
SMTS	Specified minimum tensile strength
SMYS	Specified minimum yield strength
TLP	Tension leg platform
VIV	Vortex induced vibrations
WWFE	Worldwide failure exercise



## Nomenclature

$d_c$	Depth of the corrosion defect
$D_{p,i}$	Inner diameter of the riser/pipe
$D_{p,o}$	Outer diameter of the riser/pipe
$E_a$	Young's Modulus of the FRPC laminate in the axial direction
$E_c$	Young's Modulus of the FRPC laminate in the circumferential direction
$E_f$	Young's Modulus of the fibre
$E_m$	Young's Modulus of the matrix
$E_p$	Young's Modulus of the riser material
$E_1$	Longitudinal modulus of FRPC laminate
$E_2$	Transverse modulus of FRPC laminate
$EI_{s-c}$	Combined flexural rigidity of steel riser repaired with FRPC laminate
$f_d$	Design factor for internal pressure
$f_e$	Weld joint factor
$f_t$	Temperature de-rating factor specified in ASME B31.8
$F$	Sum of axial loads acting on the riser/pipe

$F_{eff}$	Effective tensile force acting on the steel pipe due to welded end caps
$F_t$	Tensile force
$G_{12}$	In place shear modulus
$G_{equivC}$	Critical equivalent strain energy release rate
$G_I$	Mode I energy release rate
$G_{II}$	Mode II energy release rate
$G_{III}$	Mode III energy release rate
$G_{IC}$	Mode I critical energy release rate
$G_{IIC}$	Mode II critical energy release rate
$G_{IIIC}$	Mode III critical energy release rate
$I_c$	Second moment of area for the FPRC repair sleeve
$I_s$	Second moment of area for the steel riser/pipe
$L_c$	Length of the corrosion defect
$L_{over}$	Overlap length of the FRPC laminate
$L_{taper}$	Taper length of the composite repair
$M$	Folias factor
$M_b$	Bending moment
$n$	Hardening exponent in the Ramberg Osgood model

$P$	Transverse force acting on the riser/pipe
$P_b$	Burst pressure of uncorroded pipe
$P_{b,corr}$	Burst pressure of corroded pipe
$P_{cont}$	Contact pressure
$P_d$	Design pressure
$P_{in}$	Internal pressure
$P_s$	Maximum allowable pressure for the riser/pipe with defect
$P_t$	Hydrostatic test pressure (internal minus external pressure)
$r_p$	Radius of the riser/pipe
$S$	Scale factor
$S_{12}$	In plane shear strength
$t_{min}$	Minimum required thickness of the repair laminate
$t_p$	Wall thickness of the riser pipe
$t_s$	Remaining wall thickness at defect region of the riser/pipe
$\nu_{12}$	Poisson ratio
$\nu_f$	Fibre volum fraction
$X^T_1$	Longitudinal tensile strength
$X^T_2$	Transverse tensile strength
$X^C_1$	Longitudinal compressive strength

$X_2^C$	Transverse compressive strength
$\alpha$	Yield offset Ramberg-Osgood
$\varepsilon_a$	Allowable axial strain on the repair laminate
$\varepsilon_{12u}$	In plane shear failure strain
$\varepsilon_1^T$	Longitudinal tensile failure strain
$\varepsilon_2^T$	Transverse tensile failure strain
$\varepsilon_1^C$	Longitudinal compressive failure strain
$\varepsilon_2^C$	Transverse compressive failure strain
$\sigma_{flow}$	Flow stress of the riser material
$\sigma_h$	Hoop stress
$\sigma_y$	Yield stress of the riser/pipe material
$\tau$	Equivalent frictional stress
$\tau_{eq}$	Equivalent frictional stress
$\tau_{crit}$	Critical frictional stress
$\mu$	Coefficient of friction
$\gamma$	Shear strain

# Chapter 1 Introduction

Offshore pipe risers are deployed under harsh environmental conditions that frequently cause corrosion to both its internal and external surfaces. Throughout the life cycle of the risers, they must remain intact and functional within a predefined safety limit during its operation under a combination of complex loadings. The typical load profiles sustained by offshore risers include hydrostatic pressure (internal and external), tension, bending, torsion, impact and fatigue (ABS, 2008) (DNV, 2010). When localised corrosion occurs on the surface of the riser, a weak spot is created, thus reducing the ability of the riser to sustain these loads. Conventional repair techniques incorporating welded or bolted external steel clamps that are attached to the exterior surface of the riser faced numerous challenges, including mobilisation of the heavy clamp, safety associated with welding on an operating riser and the excessive installation expenses. The use of fibre-reinforced polymer composite (FRPC) as a load bearing sleeve has emerged as a promising means of pipeline rehabilitation due to advantages such as high specific strength, high corrosion resistance, lightweight, do not require welding and are simple to install (Patrick, 2010). Amid the popularity of FRPC repair techniques, it is mostly applied on onshore pipelines and less on offshore risers due the complexity of loading conditions and the difficulty of performing the job on subsea risers.

The current project aims to conduct an in-depth review into the recent advances in various FRPC rehabilitation techniques, hence to identify its most prominent challenges and limitations as the subject of further research investigation to determine the governing parameters crucial for the application FRPC as a load

bearing riser repair sleeve. The performances of the FRPC repair system will be evaluated under loading conditions mimicking those conducted in the local analysis in the design of a riser. In order to address the viability of the composite repair sleeve, innovative design based on integrated computational simulations and experimental validations, as outlined below will be performed.

- Riser interface design and treatment technology for corroded riser (RC).
- Process, properties and structural characteristics of the repair system.
- Local analysis on the complex load bearing capacity of the composite repair system.
- Damage and failure initiation of the composite repair system.
- Ease of installation, economic viability and structural integrity during installation.

### 1.1 Hypothesis and Objectives

Based on the project background discussed above, there are a number of imminent research questions which are required to be appropriately addressed in the current research project:

- How do the different types of loading profiles such as combined loads (i.e. internal pressure, tension and bending), and fatigue load that are typical to offshore risers in real life scenario affect the performance of a FRPC repair applied on a localised corrosion defect on the riser?
- How do the parameters of the FRPC repair such as fibre types, fibre volume fraction, fibre orientation etc. affect the performance of the repaired system?

- How can the design of FRPC repair on a corroded riser be formulated systematically with considerable accuracy representing the load profiles sustained by the riser?

The objectives developed from the proposed hypothesis are outlined as below:

- 1) To analyse the effectiveness of FRPC in repairing external corrosion defect on steel risers
- 2) To determine the effects of various loading profiles on the behaviour of the FRPC repair on corroded steel risers
- 3) To study the effect of different parameters of the composite repair system such as the dimensions of the corrosion defect, types of reinforcing fibre and laminate orientation on its performance
- 4) To formulate a numerical simulation model and a set of procedures that can be used to design the FRPC repair on corroded risers.

The research methodologies involve the development of an accurate finite element analysis model of the riser and the FRPC. Accuracy of the numerical solution will be validated with lab scale experimental data. Numerous key parameters (e.g. load profiles, defect size, material properties, repair thickness, etc.) are varied and the optimised output to the research questions are sought. The validated FEA model serves to provide a useful platform for parametric study of the composite repair system for corroded offshore risers, and to furnish informed decision for the development of an automated wrapping module, which will be developed based on existing design concepts of automated pipe traversing machine. The methodology of this research work is summarised in a flowchart in Figure 1-1.

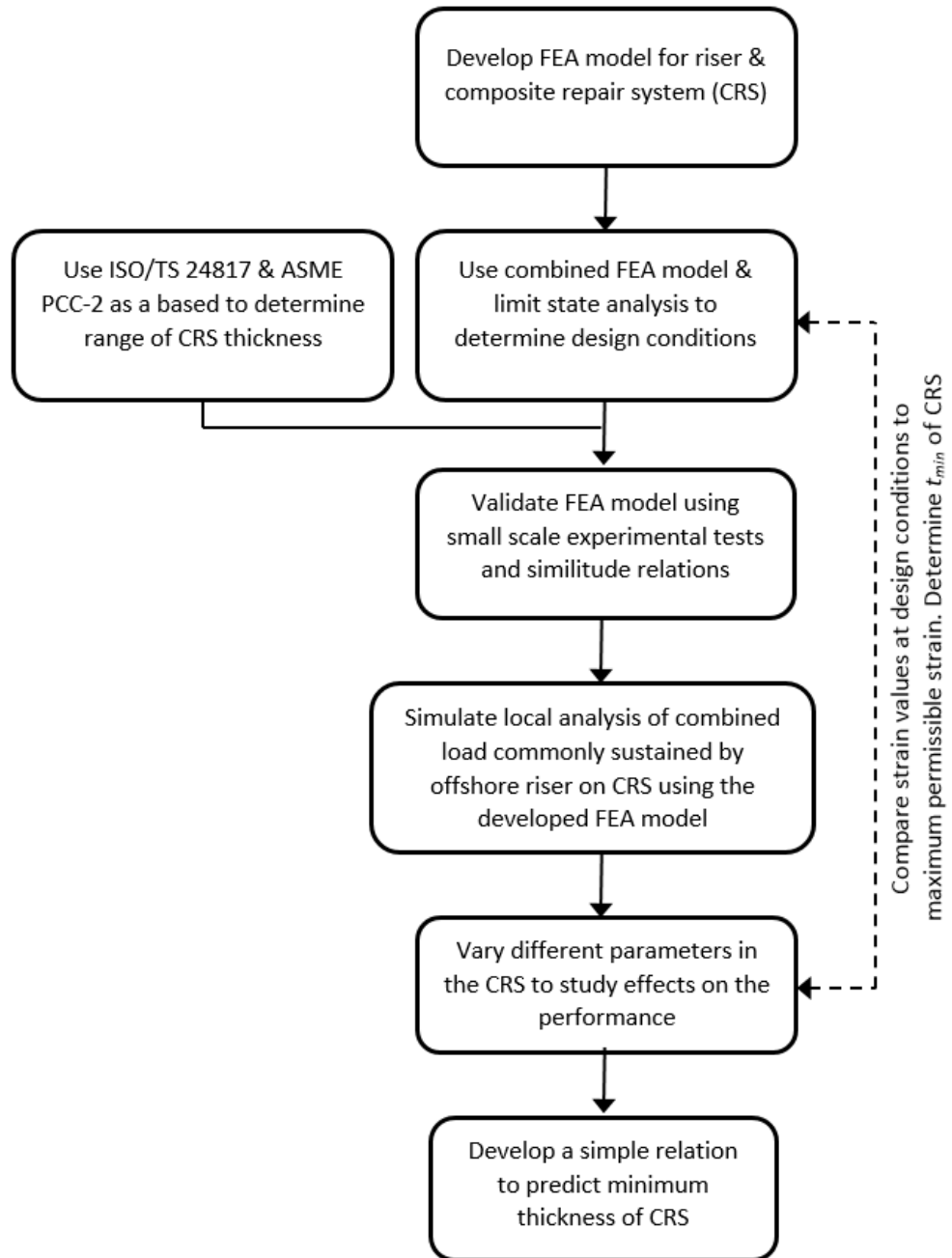


Figure 1-1, Methodology



## **Chapter 2 Literature Review**

### **2.1 Introduction**

Risers in offshore application are subjected to corrosion during their service life cycle. As the field of offshore riser repair constantly seeks improvement over the decades, the use of relatively inexpensive, high strength to weight ratio fibre reinforced polymer composite (FRPC) as a load bearing sleeve for corroded offshore risers has started to emerge as a significant element in the field of research and development. The literature review done in this research covered a wide range of topics. The first part of this review covers the typical offshore riser repairs that were introduced prior to the emergence of composite repair. The suitability and limitations of these repair techniques are discussed, which prompts the need for composite repair to be introduced in the offshore industry. The pros and cons of using composite as a repair material are studied in order to understand the significant research gaps needed to confidently apply this repair technique in offshore risers in the near future. Hence, the existing composite repair products for onshore pipelines are identified. In addition, standards and guidelines that are relevant to riser design, pipeline repair and composite testing and qualifications are being addressed. Research works on composite repair relevant to onshore pipelines and offshore pipes/risers are scrutinized. The adhesive bonding behaviour between steel and polymeric composite materials is studied as it is one of the elements that ensure the quality of the repair. In addition, the different works on existing automated pipe crawlers and pipe wrapping devices are looked into in order to understand and propose a composite repair system that suits the needs for an automated composite repair machine. A

summary of the literature review is given at the end of the chapter whereby the novel research elements are identified.

## **2.2 Conventional offshore riser repair methods**

Riser is one of the most critical components in offshore operation as it is one of the main elements for extraction of crude oil from the seabed. It is the link between the seabed and surface in which the main function can be split into drilling or production. A riser is a long slender vertical cylindrical pipe placed at or near the sea surface and extending to the ocean floor (Chakrabarti & Frampton, 1982). Risers are subjected to various types of loading due to the forces imposed by its operation and environment. For a riser to be fit for operation, the design of risers must comply to the safety limit of various loads in which it must sustained throughout its life cycle. Being submerged under water, a riser is subjected to a corrosive environment that can cause significant material loss on its surface. Apart from that, the erosion on the inner steel surface due to the fluid in the riser often causes internal corrosion and localised corrosion known as pitting. When the extend of such corrosion exceeds an allowable threshold, the performance of a riser can deteriorate so much that it can no longer sustain the different loadings (e.g. internal pressure, tensile force, bending force) at an acceptable limit.

In order to maintain the safe and reliable operation of a riser subjected to excessive corrosion, repair techniques to restore the strength of the riser must be applied. The earliest means of repairing a riser involves retrieving the corroded section of the riser to the surface where conventional onshore repair techniques or replacement of the part can be done (Webb, 1980). This technique is the least

favourable one as production needs to be halted, thus causing major inventory losses. Further development in this area saw the invention of a repair method that employs a cofferdam to be temporarily installed around the defective section of the riser to provide a dry and safe area for experience diver to carry out repair using welded or bolted steel clamp around the weaken area of the riser. However, such method is limited to shallow water depths where the damage on the pipe has to be near to the water surface (Tiratsoo, 2003). In addition, incorporation of an annular gap between the steel clamp and the riser that is then filled with a grout material such as epoxy can serve to transfer the load from weaken riser pipe to the steel sleeve more effectively (Palmer & King, 2008).

The use of steel clamps necessitates the mobilisation of heavy structures from onshore sites to offshore platforms, which incurs high logistics cost. As the main content being transported by risers is hydrocarbon substances, application of hyperbaric welding during installation of these steel clamps involves high risk. In addition, the labour cost for underwater welder can be significant due to the risk involved such as underwater explosion, electric shock and accumulation of nitrogen diffused into bloodstream.

### **2.3 Composite Repair for Onshore Pipelines**

Similar to offshore industry, onshore pipelines can be subjected to corrosion which causes material losses on the surface of the steel pipelines. The main difference between onshore pipelines repair and offshore risers repair is in the process itself. As onshore pipelines are not submersed under water, the factors that affect a repair can be easily controlled and fibre-reinforced polymer composites has been widely introduced over the past decades. Similar to offshore

risers, onshore oil and gas pipelines carry hydrocarbon fluids that are highly flammable. The use of FRPC material as means of repair can eliminate hot work and the shutdown of pipeline operation (Patrick, 2004). A survey conducted by the US Department of Transportation showed that the overall costs can be reduced by 24% by using composite repair instead of welded steel sleeves. When compared to the replacement of the whole defective pipe section, the cost can be further reduced to approximately 73% (RSPA, 2000). To date, various companies in the oil and gas industry have developed composite repair systems that are capable of restoring the strength of onshore pipelines sustaining different types of defects such as mechanical gouge dent (Figure 2-1), external corrosion (Figure 2-2) and internal corrosion (Figure 2-3).



Figure 2-1, Mechanical gouge dent on a pipe



Figure 2-2, External corrosion on pipe



Figure 2-3, Internal corrosion on pipe

### **2.3.1 Types of Composite Repair**

The two main categories of composite repairs applicable to onshore pipelines are flexible wet lay-up systems and pre-cured layered system (Rehberg, et al., 2010) (Patrick, 2010). Wet lay-up system involves the use of flexible fibre reinforced fabric that is wetted with an uncured resin matrix on-site which is manually applied around the pipelines. The wetted fabric will then cure to form a stiff shell around the damaged pipe. An alternative form of wet lay-up system incorporates the use of pre-impregnated flexible fibre reinforced fabric that is prevented from curing before its application. Such systems can be water-activated, UV-activated, or temperature activated. Pre-cured layered system uses a pre-manufactured fibre-reinforced composite that is bonded to the defective pipe and held together between layers using an adhesive. Another form of pre-cured system that is not widely used in existing composite repair products is the pre-cured stand-off sleeve. Stand-off sleeve provide higher structural integrity than both wet lay-up system and pre-cured layered system as it can be pre-manufactured to the required dimensions under optimum curing conditions. However, such systems are sized to specific diameters (Shamsuddoha, et al., 2013). Figure 2-4 shows the different types of composite repair systems.

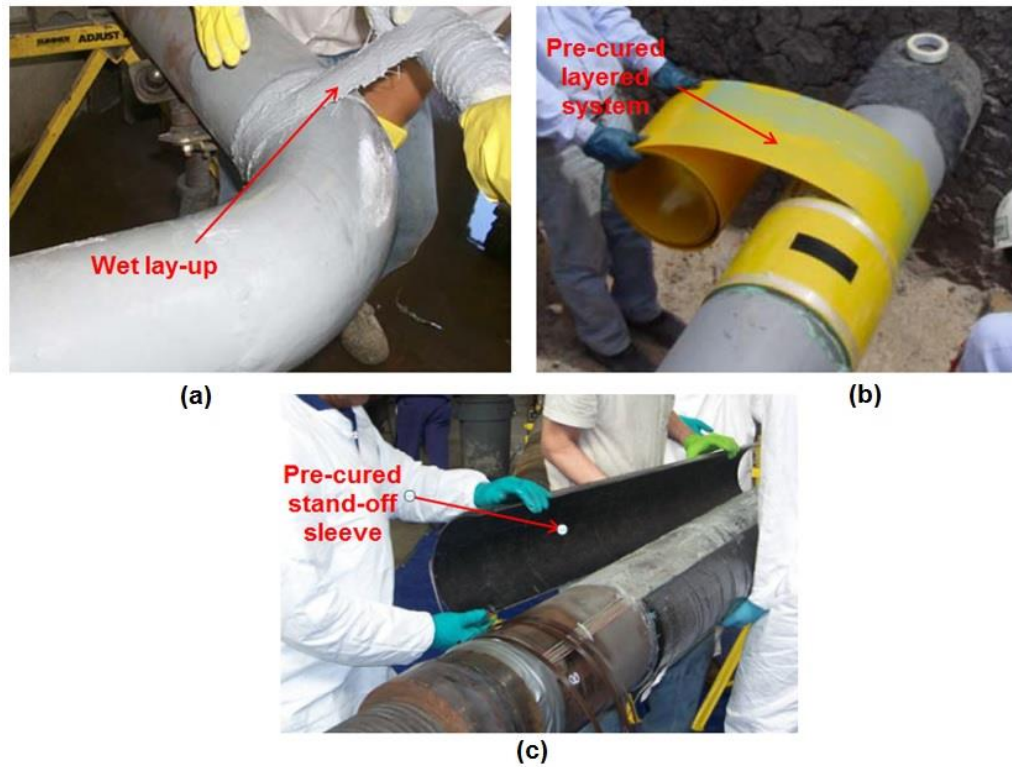


Figure 2-4, Types of composite repair: (a) Wet lay-up (b) Pre-cured layered (c) Pre-cured stand-off sleeve (Alexander & Ochoa, 2010) (Alexander, 2006) (Clock Spring, 2012)

### 2.3.2 Existing Onshore Composite Repair Products

The first composite repair system for onshore pipelines that was widely used is designed and developed by Clock Spring, Inc. The product named Clock Spring® is a pre-cured layered system that utilises E-glass/Polyester material with a methacrylate adhesive that bonds the pre-cured composite layers. Figure 2-5 illustrates the manual installation operation of Clock Spring® on a steel pipe. In 1991, the Gas Research Institute conducted a research over a period of approximately five years to assess the performance of Clock Spring®. This report covered the basic history and development of Clock Spring® and documents the efforts such as material testing, short and long term stress rupture testing, adhesive testing, burst test considering various types of defects and the

field assessment of Clock Spring®. In addition, it also provides a general procedure for the safe application of Clock Spring® (Alexander, 2006).



Figure 2-5, Installation of Clock Spring® on a steel pipe (Clock Spring, 2012)

The drawbacks of the Clock Spring® pre-cured system is its limitation to designated pipe sizes and straight pipe sections. Over the years, the pipeline industry started exploring the use of flexible wet lay-up systems due to its ability to conform to any pipe diameters and geometries. In 2005, Stress Engineering Services, Inc. performed a series of test to evaluate the AquaWrap® composite repair system developed by Air Logistics, Inc. for mechanically-damaged pipelines. The AquaWrap® is an example of a flexible wet lay-up system that consists of a water-activated pre-impregnated (i.e prepreg) composite that is installed over the damage area. A typical installation of AquaWrap® on a damaged pipeline is shown in Figure 2-6. The repaired specimens were pressure cycled at 100% maximum allowable operating pressure (MAOP), which is equivalent to 72% specified minimum yield stress (SMYS) of the pipe. The results of the tests have proven that the AquaWrap® can increase the fatigue life from 103,712 pressure cycles for an unrepaired pipe to 928,736 cycles for a repaired pipe (Alexander, 2005).



Figure 2-6, Installation of AquaWrap® on a corroded pipeline (Alexander 2005)

Similar tests were also conducted by Worth (Worth, 2005). In his analysis of AquaWrap® for repairing damaged pipelines, Worth performed a series of individual test on the product to identify its flexural strength, compressive strength, interlaminar shear, glass-transition temperature, flammability, burst strength, adhesion to steel, chemical resistance, cure time, impact resistance and long term performance. The results of the analysis revealed that AquaWrap® can increase the strength and durability of the damaged virgin pipes cause by external corrosion and a minimum of four layers is recommended on any repair installation. In 2006, another evaluation of the AquaWrap® repair system was conveyed. Along with this evaluation, both the previous test reports of AquaWrap® conducted by Alexander and Worth were reviewed and the results of this evaluation complimented the previous findings. It is confirmed that the design of AquaWrap® conforms to the ASME PCC-2, Repair Standard, Article 4.1 (Francini & Kiefner, 2006).

Recognizing the potential for developing a composite repair for pipelines, Armor Plate, Inc. initiated an extensive testing program in year 1997 to ensure that the Armor Plate® pipe wrap system would adequately meet the repair needs of the



pipeline industry. The Armor Plate® pipe wrap is a 3-part wet-layup system that consists of the resin, putty and Armor Fiber™. Stress Engineering Services, Inc. was again selected as the engineering firm to conduct the evaluation. The results of the evaluation demonstrated that Armor Plate® is a valid method for repairing corroded and mechanically-damaged pipes. The strength of the repair is governed by the thickness of the Armor Plate® wrap and the tensile stress at each layer of the wrap, where effective stress transfer initiates once plastic flow occurs in the steel pipe beneath the repair (Alexander & Wilson, 2000). In year 2000, Armor Plate, Inc. successfully expanded their business as numerous world-wide installations of the Armor Plate® pipe wrap system were made in regions such as Alaska, Saudi Arabia, China and South Africa (Nace International, 2011).

In 2000, WrapMaster, Inc. developed a repair system, PermaWrap™ which is similar to Clock Spring® in a sense that pre-cured composites was employed as the reinforcement of the repair system. The pre-cured composite used in this system are hard shell with adhesive installed between layers. One of the main advantages of PermaWrap™ is that the repairs are magnetic pig detectable and available in a range of widths (Alexander, 2006).

At present, there are various products of composite repair for onshore pipelines available in the market. Diomandwrap® is a carbon wrap system developed by Citadel Technologies, Inc. The wrap used in this repair system is a bi-directional woven carbon-fiber material which can provide reinforcement in the hoop and axial directions. Because of the higher elastic modulus of carbon fibres compared to glass fibres, Diomandwrap® is applicable to higher pressure pipelines (Citadel Technologies, 2011). Another example of composite repair

used to industrial pipelines is the A+ Wrap<sup>TM</sup> developed by Pipe Wrap, LCC. This system utilises a factory pre-impregnated (prepreg) glass fiber with moisture cured polyurethane resins (Pipe Wrap, 2011).

## **2.4 Integration of Composite Repair in Offshore Riser**

The intense interest in the research and development of alternative rehabilitation system for repairing offshore risers has seen a shift from off-site rehabilitation to in-situ repair using steel clamp and grouting. An ideal means of repair should involve a reliable and safe method which requires no shutdown of operation in order to minimise the time and production loss. In the recent years, there are increasing discoveries of oil reserves being found at great depth into the ocean seabed. A report made by the US Minerals Management Service (federal agency responsible for offshore leases and oil activities) stated that twelve deepwater discoveries were made in Gulf of Mexico alone in 2003, three of which were at depth greater than 2500m (Ochoa & Salama, 2005). At such depth, it is apparent that there is a need for more economical and facile maintenance of the offshore facilities including riser repair. Thus, repair of risers using fibre-reinforced polymer composite materials have emerged as an attractive option to be implemented in this field. The FRPC offers great advantages such as high specific strength, high corrosion resistance, good thermal insulation, do not require welding and are simple to install (Ochoa & Salama, 2005).

### **2.4.1 Limitations in the Application of Composite in Riser Repair**

The impediment of composite repair in offshore risers is mainly due to the uncertainties related to the application of the composite material itself. In general,

the barriers to greater acceptance of composites into the offshore industry can be divided into four main key issues which are (Martine, 2007),

- 1) Technical – Industry competence and familiarity with metallic;
- 2) Financial – costing methods, excluding life cycle costing;
- 3) Commercial – difficulty of entry into established supply chains;
- 4) Awareness – perceptions and lack of knowledge of industry engineer

The major focuses in research of composite repair system are technical and awareness.

The transition of composite repair from onshore pipelines to offshore riser are hindered by the lack of databases for the long-term damage mechanisms for life prediction and no proper in-service integrity monitoring (Ochoa & Salama, 2005). Due to the nature of the composite material itself, where diversity in reinforcement and matrix combination along with different manufacturing parameters such as winding angle, fibre volume fraction, curing temperature are feasible, it gives rise to many uncertainties in the ultimate performance and lifespan of the composite. Various failure criteria of fibre-reinforced composites are developed by researches to predict the failure behaviour of composites under static load, long term loading and fatigue loading. However, among all these criteria, no benchmark exists to validate the accuracy of the results (Hinton, et al., 2004).

In addition to the behaviour of the composite material itself, the robustness of the metal-composite interface is crucial in composite repair system. Although composite materials have already been widely used in aerospace and automotive industry, the joining of composite material to steel components is still a non-

trivial task, which is highly dependent of several factors such as type of adhesive, modes of loading and geometry of the adhesive joint (Anyfantis & Tsouvalis, 2013). The availability of well-defined data for the determination of the strength and durability of the metal-composite bond in tubular wrap is still scarce.

The stress-strain behaviour of composite materials can be non-linear and their properties are dependent on time and environmental conditions. There is a significant lack of relevant performance information related to the application of composite material in hostile offshore environments. Standards that describes the design of offshore risers relative to the different types of loadings are readily available but are all based on the use of steel materials. There is no recognised database for the design properties of composite materials in offshore application (Ochoa & Salama, 2005), which is essential for the design of composite repair system for offshore risers.

On top of that, there is no proper health monitoring system applicable to composite repair system for offshore risers. Various research works, verification and certification on composite repair system for steel pipelines have utilised strain gauges as a means of monitoring the performance of the system. Murad (Murad, 2011) (Murad, et al., 2013) developed an integrated structural health monitoring approach for composite-based pipeline repair. However, the cumbersome process of installing electrical strain gauges on the steel pipe prior to the application of the composite repair greatly limits its adoption in offshore subsea application.

## **2.4.2 Automated Riser Repair Machine**

Current practice of composite repair systems highly rely on manual deployment of the FRPC material onto the defective area of the steel pipe, e.g. underwater composite repair near the splash zone and at shallow depths are viable through human divers. Deepwater repairs at depth of 100 metres and more are not feasible via manual human divers due to the oxygen toxicity effects. In addition, quality of repairs can be compromised due to minimal visibility and harsh conditions of the current forces and cold temperatures which can affect the human diver. In order to maximise the potential of composite repair for offshore risers, the feasibility of developing more advanced systems, i.e. unmanned automated repair machines has attracted great interest amongst major players in the oil and gas sector.

### **2.4.2a Pipe Traversing/Crawling Machine**

For automated repair to be achievable underwater, automated pipe crawling systems must be design to carry the repair machine to the corroded site of the riser. Several researches on pipe traversing machine have been reported. Chatzakos et al. developed prototype of an unmanned underwater robotic crawler for subsea flexible risers. The testing of the prototype is shown in Figure 2-7. This robotic crawler uses an inchworm translational motion to navigate along the length of the riser. The inchworm crawling is achieved by alternating activation of grippers and linkage mechanism between two main bodies. The linkage mechanism joins the two bodies and provides translational and rotational degrees of freedom. Figure 2-8 shows the sequence of action for the linear translational motion along the length riser, while Figure 2-9 shows the sequence

of rotational motion around the circumference of the riser. However, the module attached to this prototype only consists of a non-destructive testing (NDT) equipment used for inspection (Chatzakos, et al., 2010). For semi-automated or fully automated repair to be conducted, repair modules need to be designed and built on the pipe crawlers.



Figure 2-7, Prototype of the unmanned underwater robotic crawler (Chatzakos, et al., 2010)

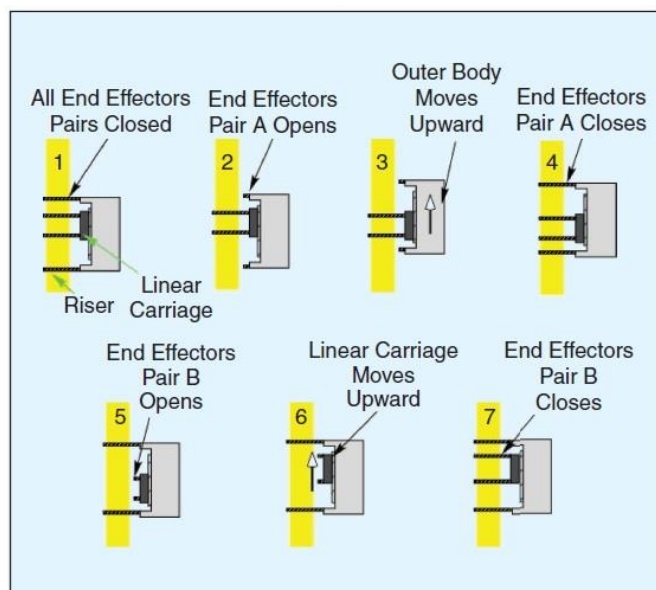


Figure 2-8, Sequence of actions for the translational motion along the length of the riser (Psarros, et al., 2010)

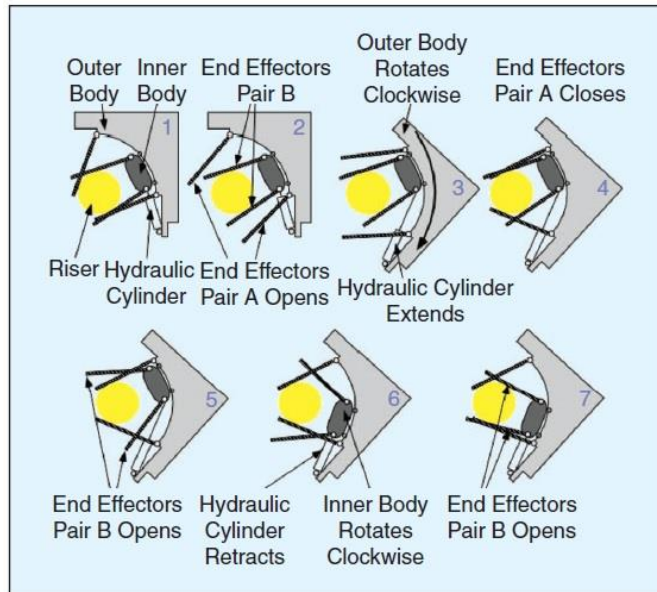


Figure 2-9, Sequence of actions for the rotational motion around the circumference of the riser (Psarros, et al., 2010)

Yukawa et al. (Yukawa, et al., 2006) developed an onshore oil plant pipe inspection robot that can traverse along vertical piping, where attachment on the pipe is achieved using the power generated by wheel-type magnets. This robot consists of three connected units, with each unit having a “drive part” and a “lift part”. The robot is capable of traversing flanges by moving these three parts independently as shown in Figure 2-10. This mechanism is achieved by the combination of driving and lifting motion provided by the “drive part” and “lift part”. The “drive part” contains a motor that drives the magnetic wheels to enable the robot to move along the pipe. Once the sensor detects the presence of a flange, the motor on the “drive part” stops. At the same time, the motor on the “lift part” of the first unit overcomes the magnetic force to lift the unit so that it can avoid the flange. The drive motor on the other two units then moves the robot along the pipe. The combination of driving and lifting of the three separate units enables the robot to traverse flanges. The advantage of this system is that

the use of magnetic wheels makes it possible for different diameters of pipe to be accommodated. However, the use of magnetic force for attachment on to the pipe might be insufficient due to the larger weight of the overall automated repair machine which will consist of additional modules.

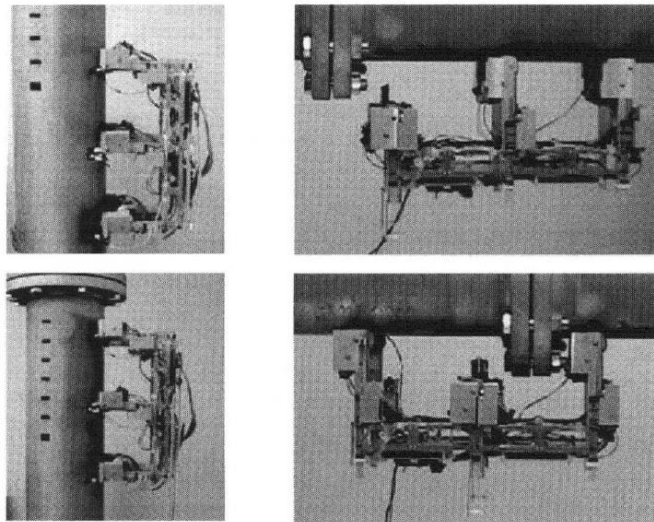


Figure 2-10, Pipe inspection robot by Yukawa et al. ( (Yukawa, et al., 2006))

Another type of pipe crawler that utilises no mechanical actuation is developed by Balaji et al. (Balaji, et al., 2008) This external pipe crawler uses a compliant mechanism that is actuated using shape memory alloy (SMA) wire and strip. Figure 2-11 shows the 3D model of the pipe crawler with the enlarged view of the SMA U-shaped strip. This design provides a compact machine that can navigate through tight spaces beneath the offshore platforms. However, it is only applicable to a specific pipe diameter. In addition, the time taken for heating and cooling of the SMA wire and strips causes the crawling speed to be very low (approximately 1mm/min).



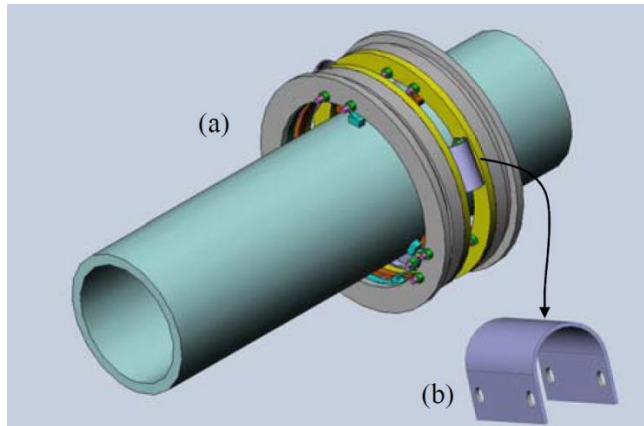


Figure 2-11, 3D model of the compliant mechanism of SMA-actuated pipe crawler, (a) crawling device with clamping rings, (b) SMA U-shape strips  
(Balaji, et al., 2008)

#### **2.4.2b Composite Wrapping Machine**

Various manual wrapping machines have been developed to aid the process of wrapping a tape around the circumference of a pipe. A few examples are the ACCUWRAP™ (SMC, 2011), DEKOMAT® KGR-Junior (DEKOTECT GmbH, 2014) and Tapecoat Hand Wrapster (Farwest Corrosion Control, 2014). These machines all have similar functions and are based on the same working principles. Figure 2-12 shows the complete assembly of the ACCUWRAP™.

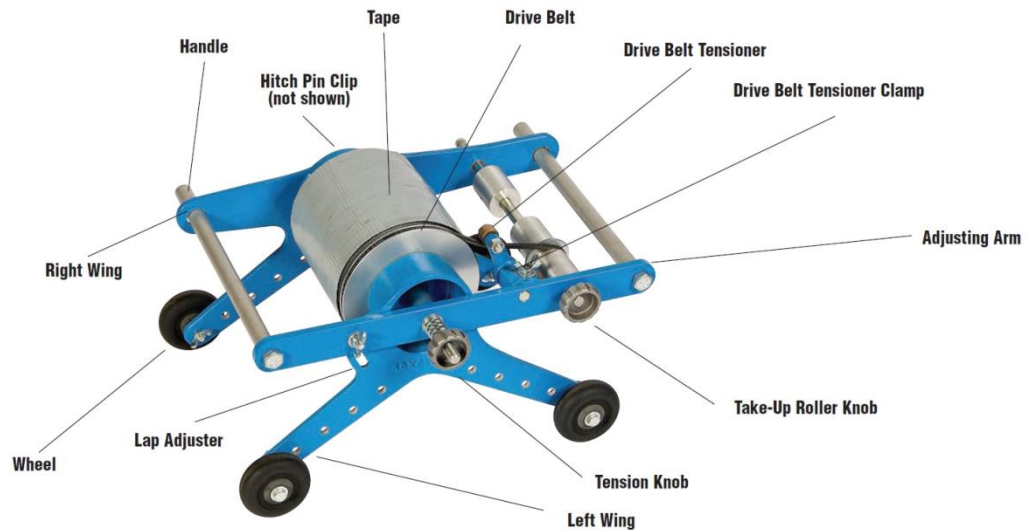


Figure 2-12, Full assembly of ACCUWRAP™ (SMC, 2011)

One of the main features of these machines is that they enable constant tape tension to be applied during the wrapping process via the means of a tension spring. They are also capable of providing constant overlap in the wrap. The wheels provide controlled motion over the pipe surface and are adjustable to accommodate a range of pipe diameters. These features can be incorporated into the design of composite repair machine where automation can be encompassed by the addition of motors and actuators (SMC, 2011).

A notable research on the application of composite repair in subsea environment was conducted by Boulet d'Auria et al. (Boulet d'Auria, et al., 2013) where a semi-automatic repair machine showed in Figure 2-13 was developed and tested underwater with the aid of divers. The function of each of the numbered components in Figure 2-13 is shown in Table 2-1. The burst test results on the repaired specimen using this machine demonstrated that the machine provides good quality of repair (burst occurred outside of repaired region) with optimised repeatability.

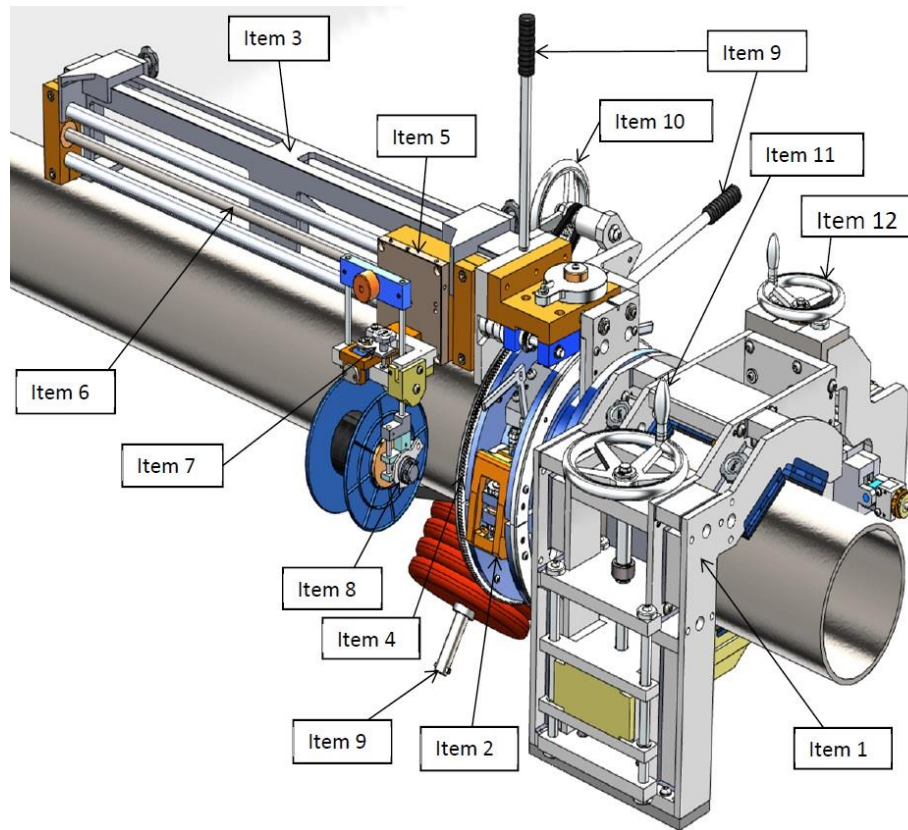


Figure 2-13, Semi-automatic composite repair machine Previous Studies on Composite Repair System (Boulet d'Auria, et al., 2013)

Table 2-1, Components on the semi-automatic composite repair machine and their functions (Boulet d'Auria, et al., 2013)

Item	Component	Function
1	Aluminium frame	Body of the machine that holds the other components
2	Clamping system	To clamp the machine on different diameters of pipe
3	One-metre arm	Holds the long screw, can revolve around the pipe
4	Pipe	The pipe to be repaired
5	Impregnated frame	Holds the resin where the composite tape will be impregnated
6	Long screw	Allows the impregnated frame to travel back and forth on the one-metre arm
7	Gear box	Allows the reversing inclination of the impregnated composite tape
8	Tensioner	Controls the tension applied on the composite tape
9	Three handling bars	Allows the handling of the machine through divers assistance
10-12	Rotating handlers	Rotated to drive the moving parts of the machine (to be replaced by motors in the future)

## **2.5 Previous Studies on Composite Repair System**

### **2.5.1 Composite Bonded Repair in Other Applications**

Prior to the introduction of FRPC material for steel pipelines rehabilitation, FRPC has been widely used in other repair applications such as aircraft structure, concrete piles and steel beams. These studies can be categorised into two major parts which is experimental study and finite element analysis. Although different in terms of geometry, materials, boundary conditions and loading conditions, these studies provide an understanding to the different behaviours of composite material in strengthening structurally weakened structures. This serves as a foundation to the research of composite repair system for pipelines.

Experimental investigation of carbon fibre reinforced polymer (CFRP) strengthened steel rectangular hollow section (RHS) subjected to transverse end bearing load was done by Zhao et al (Zhao, et al., 2006). The ultimate load capacity of the RHS was found increased by 50% with the application of CFRP strengthening. The failure mode of the RHS changed from web buckling to web yielding as shown in Figure 2-14. Nevertheless, debonding of the CFRP plate from the RHS is observed.

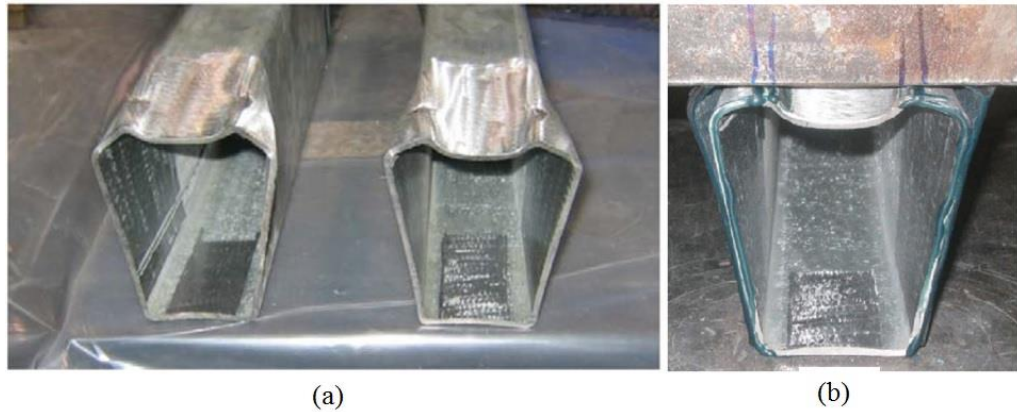


Figure 2-14, (a) Web buckling of unstrengthened RHS (b) Web yielding and debonding of CFRP strengthened RHS (Zhao, et al., 2006)

A study on strengthening of steel I-beams using CFRP strips was conducted by Narmashiri et al. where both full-scale experimental tests and finite element modelling were used (Narmashiri, et al., 2010). The four point bending setup and modelling of the CFRP strips on the sides of the I-beam are shown in Figure 2-15. The steel beam, adhesive and CFRP strips were modelled using three-dimensional ten-node triangle elements and nonlinear trial and error static analysis was carried out. This is done by increasing the load applied to the structure step by step. The maximum bending load is determined when the plastic strain in the first element reaches the ultimate tensile strain. The experimental and numerical results show good agreement, where application of CFRP strips was found able to increase the load capacity of the beam and decrease deformations.

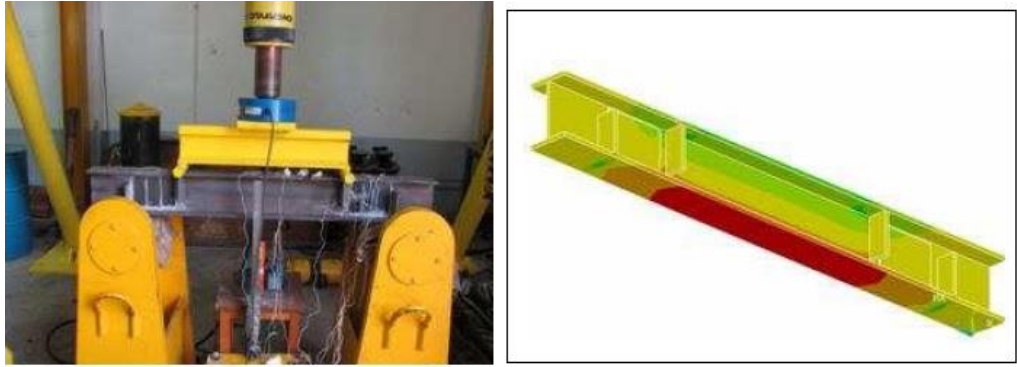


Figure 2-15, Bending test setup and finite element model of I-beam strengthened with CFRP strips (Narmashiri, et al., 2010)

A finite element study of cracked steel circular tube repaired by FRPC patching is executed by (Lam, et al., 2011). The cracked steel tube was modelled using three-dimensional twenty node quadratic solid elements while the adhesive and FRPC patching were modelled using eight node reduced integration shell elements as shown in Figure 2-16. The mode I stress intensity factor ( $\sigma_I$ ) of cracked steel members was found to be reduced with the application of FRPC patching. Using the  $\sigma_I$  and Paris equation, the fatigue life of the cracked steel member was increased by 22 times with the application of FRP patching.

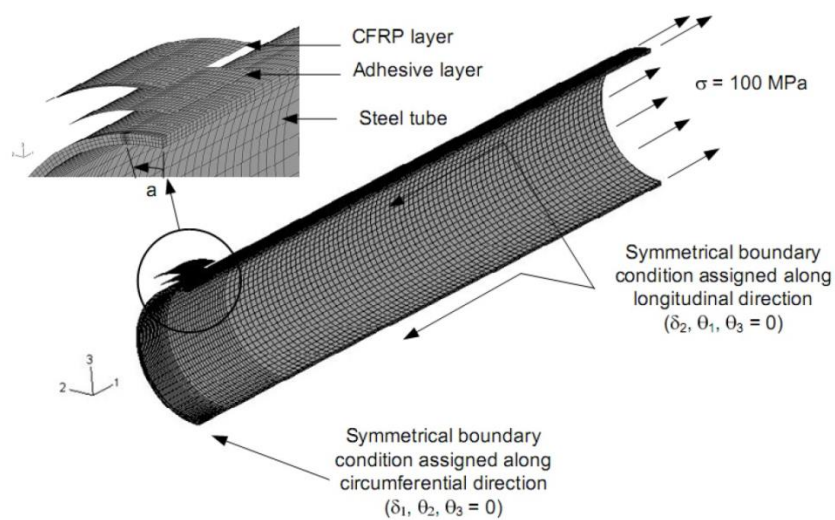


Figure 2-16, Finite element model of cracked steel tube with FRPC patching (Lam, et al., 2011)

The various works conducted have showed that application of FRPC to reinforce structural element is a viable option. Experimental testing can be used as a means of determining the effectiveness of the repair or reinforcement. The use of numerical modelling can be a more cost effective solution where accurate results have been shown to be attainable through numerous previous studies.

### **2.5.2 Application of FRPC in Onshore Pipeline Repair**

Research on composite repairs for onshore pipelines has been widely explored over the years. Duell et al. studied the effects of varying corrosion length of the structural performance of a corroded steel pipe repaired with carbon/epoxy fabric subjected to pure internal pressure (Duell, et al., 2008). Their work involved both full-scale experimental testing and finite element modelling. The steel substrate, filler putty and CFRP were all meshed using ten node tetrahedral solid elements as shown in Figure 2-17. The finite element model was able to predict accurately the burst pressure of the repaired specimen. For an axisymmetric defect of 6 inches length in the longitudinal direction, both the FEA predicted and tested burst pressures were 43.8MPa. For a slot defect of 6 x 6 inches, the FEA predicted result was approximately 3.7% higher than the tested result.

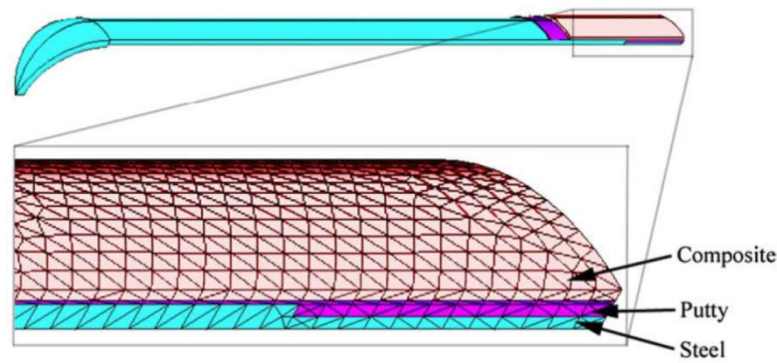


Figure 2-17, 3D finite element model used in Duell et al.'s work (Duell, et al., 2008)

Stress analysis was conducted by Meniconi et al. (Meniconi, et al., 2002) to examine the stress transfer in a pressurised corroded steel pipe repaired with different types of composite repair system – wet-layup of dry fibre glass fabric with liquid resin, pre-cured glass fibre composite and pre-impregnated composite fabric wrapped with water. Finite element analysis that uses 20-node, reduced integration solid elements was also built to produce a model that can well represent the composite repair system. The experimental and FEA results (Figure 2-18) show good agreement in the elastic region with slight deviation after yielding. The abbreviation “CC” and “CRC” in Figure 2-18 denotes the circumferential strain on the unrepaired pipe and repaired pipe respectively, while the 150% denotes the increase of the repair laminate’s modulus by 50%. This is based on the hypothesis that continuously wrapped fibres develop more circumferential stiffness than flat tensile specimens, as properties for composite laminates are usually tested via flat tensile specimens.



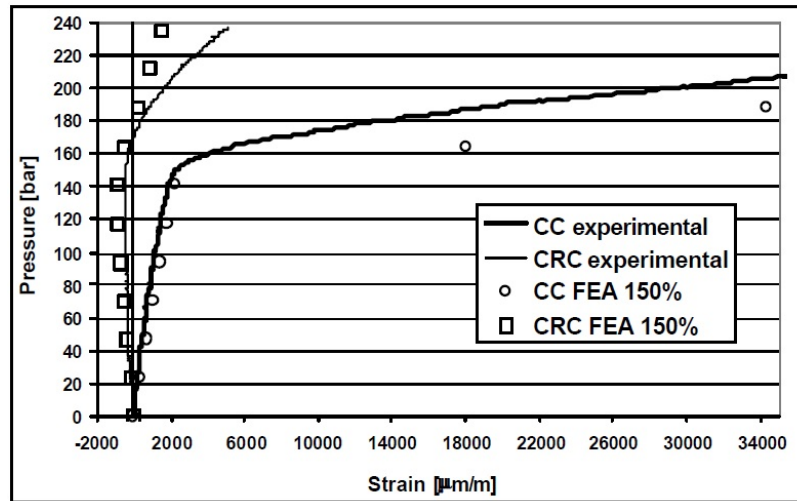


Figure 2-18, Comparison between experimental and FEA results (CC = Circumferential stain in corroded region , CRC = circumferential strain in corroded region of repair pipe) (Meniconi, et al., 2002)

Experimental and numerical investigation of externally reinforced damaged pipelines with carbon fibre polymer matrix composite is conducted by Lukacs et al (Lukacs, et al., 2010). The test focus on unreinforced and reinforced pipelines subjected to cyclic loading of internal pressure followed by burst test. The repaired specimens were able to sustain  $10^5$  pressure cycles without failing but no effort was done to study the stress-strain behaviour of the repaired pipes under such loading. Cyclic pressure (100 psi to 72% SMYS) tests were also conducted by Stress Engineering, Inc. in the evaluation of the Aquawrap® system in repairing mechanically damaged pipes (Alexander, 2005). The use of the Aquawrap® composite sleeves was found capable to increase the fatigue life of a damaged pipe from 100 cycles to 100,000 cycles.

The compressive strain limits of composite repaired pipelines were investigated by Shouman and Taheri (Shouman & Taheri, 2011). In their work, buckling behaviour of the composite repaired system was investigated using both full-

scale testing and finite element modelling. The finite element model was meshed with a total of 16,320 three dimensional reduced integration, eight node linear solid elements. The finite element model was able to capture the buckling behaviour of the repaired pipe, with local buckling occurring in the unrepaired (undamaged) section of the pipe as shown in Figure 2-19.

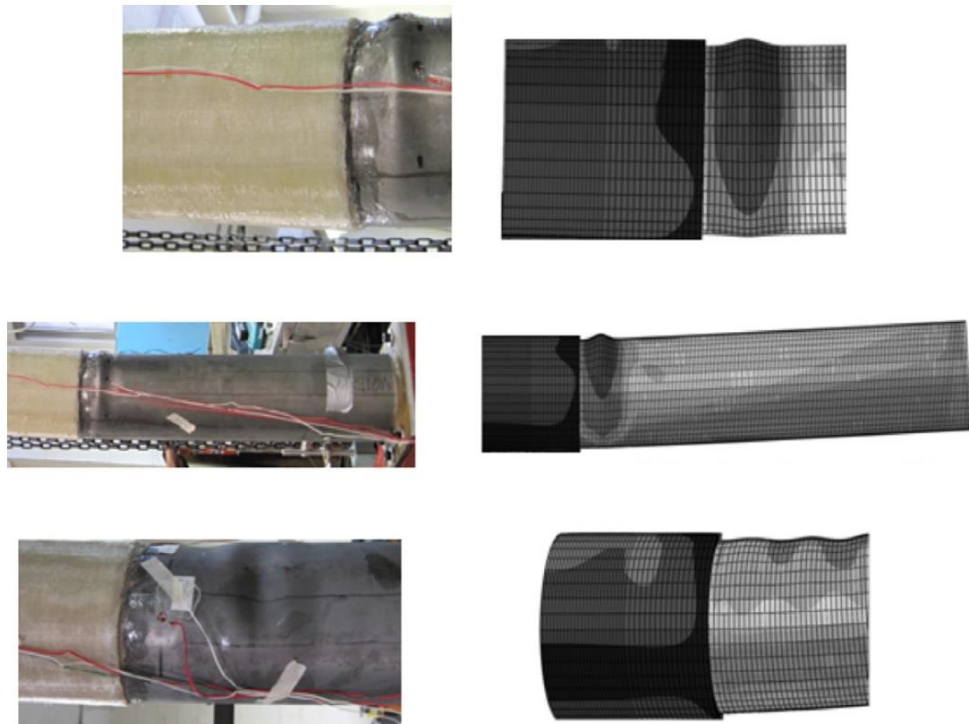


Figure 2-19, Comparison of buckling shapes between full-scale testing and finite element modelling (Shouman & Taheri, 2011)

### 2.5.3 Application of FRPC in Offshore Riser Repair

In recent efforts to administer the use of composite repair in offshore pipelines and risers, the need for more extensive research on different factors that affect the performance of the repair has been prompted. Based on the various literatures on composite repair system for offshore industry, it is concluded that the works done thus far were focused on two major aspects, (i) the performance of composite repair system subjected to different conditionings (i.e. saltwater

exposure, temperature variation, moisture absorption) and (ii) the performance of the composite repair system subjected to additional loads sustained by offshore risers compared to onshore pipelines.

The rehabilitation of underwater tubular steel structures with FRPC material was carried out by Seica and Packer (Seica & Packer, 2007). The flexural strength of in-air versus underwater cured of the structurally reinforced steel tubes with FRPC were investigated using full-scale experimental tests. The curing of FRPC wrap on the steel pipes is shown in Figure 2-20. Increase in ultimate bending strength and flexural stiffness were attained by both in-air and underwater specimens, with in-air specimens showing superiority over underwater ones.



Figure 2-20, FRPC-wrapped specimens cured under saltwater conditions (Seica & Packer, 2007)

In the work conducted by Esmael et al., steel pipes reinforced with FRPC were immersed in saltwater for 225 days and subjected to thermo-cycling with a temperature range of +5°C to +55°C. It was found that the moisture and hot-cycle conditioning degraded the modulus of elasticity of the composite material.

Finite element model using three-dimensional eight node reduced integration linear solid continuum elements (Figure 2-21) was used to back-calculate the degraded modulus value. Reasonable correlation between experimental and numerical results was obtained by using a 76.5% degradation in the modulus of the composite (Esmaeel, et al., 2012).

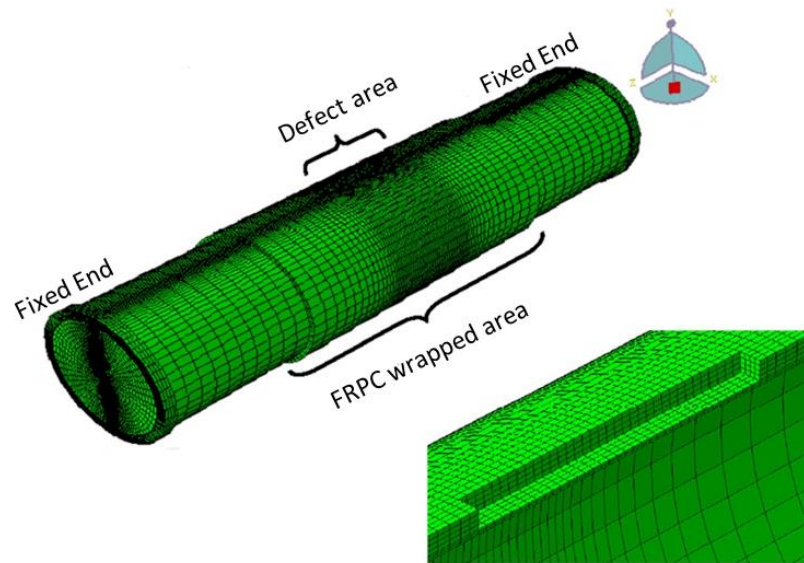


Figure 2-21, Finite element model of repaired pipe and enlarged view of corroded region mesh (Esmaeel, et al., 2012)

In addition, a program to evaluate different composite repair products in subsea environment run by Stress Engineering, Inc. is currently underway. Test samples were placed in seawater test facility for 10,000 hours and will be removed for pressure, tension and bending tests (Alexander & Bedoya, 2011). The result of this program is yet to be documented as it is still on-going. A study to extend onshore pipeline repair to offshore steel risers with carbon-fibre reinforced composites by understanding the complex combined load profiles of a riser was done by Alexander and Ochoa (Alexander & Ochoa, 2010). Finite element modelling and full-scale tests were used to address the viability of reinstating the capacity of corroded risers in sustaining combined internal pressure, tensile and

bending load through rehabilitation using carbon fibre composites. Distinctive from other numerical assessment of composite repair, Alexander and Ochoa utilised four-node reduced integration shell elements instead of solid continuum elements. The prototype tests demonstrated the capability of the unique limit analysis and strain based design methods to assess the performance of steel pipe repaired with composite reinforcement. A wide variety of research works have been conducted by Alexander and his team over the years. Integrated analysis and testing programmes such as pressure cycle testing of composite reinforced steel pipes for long-term design, wrinkle bend tension testing of repair systems were conducted (Alexander, 2012).

#### **2.5.4 Bonding of Composite to Steel Pipe/Riser**

The bonding of the reinforcing FRPC material to the steel riser is essential for the repair to be functional. Over the years, numerous studies related to the steel-composite bond strength have been reported where FRPC has been widely used to reinforce structural steel members such as columns and beams. The accuracy of the prediction using the finite element model highly depends on the input parameters used to define the bond between the inner surface of the composite and the outer surface of the steel riser. A full finite element analysis should include effects of bending, adherent shear, end effects and the non-linear behaviour of the adhesive and adherents. The most widely used approaches in characterizing the bond strength of adhesive joints using finite element analysis can be divided into two main categories which are the continuum mechanics approach (stress based), and the fracture mechanics approach (Banea & da Silva, 2009) (Andre, et al., 2012). The continuum mechanics approach is basically a strength-based approach where maximum stress or strain criterion is used to

determine the strength of the bond. The fracture mechanics approach is based on the fracture properties of the joint components, where the failure criterion is expressed as either the energy release rate or the stress intensity factor.

Haghani (Haghani, 2010) conducted both numerical and experimental study on the adhesive joints between FRPC laminates and steel members. Within the finite element model, the FRPC laminate, adhesive and steel member were modelled using three dimensional 8-node reduced integration elements as shown in Figure 2-22. Continuum approach of maximum stress/strain linear elastic analysis was used to predict the adhesive bond behaviour. Good agreement is observed between the experimental work and finite element analysis in terms of strain distribution at the mid-thickness of the adhesive in Haghani's work. However, the experimental test showed that failure is more prone to occur at the steel-adhesive interface. A similar approach was used by Yang et al. where different FRP-to-steel joint configurations and a beam bonded with FRPC are studied (Yang, et al., 2013). Two-dimensional plain stress four-node quadrilateral elements were used in the finite element model as shown in Figure 2-23. It was determined that the interfacial stresses varied with different FRP-to-steel joint configurations. Future study must be conducted to relate joint models to specific FRP-strengthened steel structures.

The drawback of continuum mechanics approach is that it assumes a perfect bond between the adhesives and adherends, hence omitting the adhesion properties of the interface. This gives rise to singular strain distribution due to the bi-material wedge at the idealised joint. The strain distribution at the edge of the bond is hence dependent on the degree of mesh refinement (Bogy, 1968)

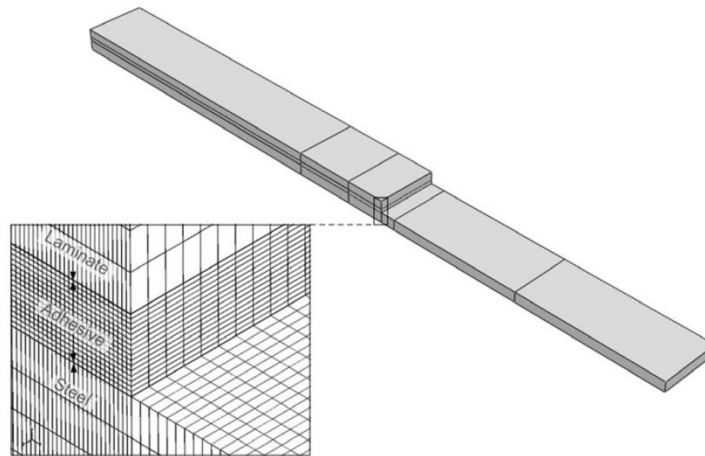


Figure 2-22, Finite element model used in Haghani's work (Haghani, 2010)

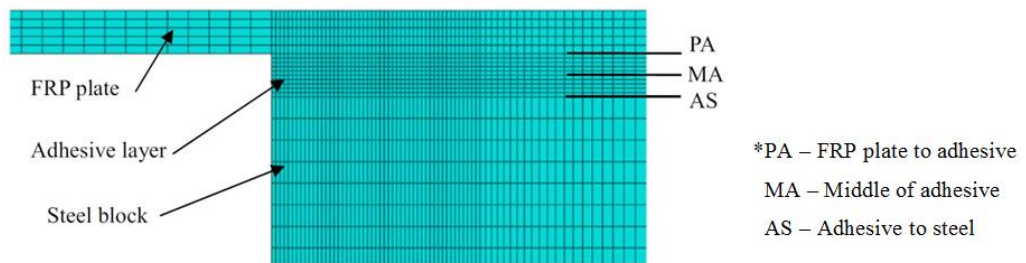


Figure 2-23, Finite element model of FRP-to-steel joint (Yang et al, 2013)

The fracture mechanics approach can be modelled using finite element analysis by including a zone of discontinuity modelled by cohesive elements. Bocciarelli et al. studied the debonding of CFRP on a steel beam reinforced with CFRP strips subjected to three point bending using cohesive interface elements (Bocciarelli, et al., 2008). The finite element model was able to capture the debonding behaviour (Figure 2-24) both quantitatively and qualitatively, with numerical results showing reasonable agreement to experimental measurements.

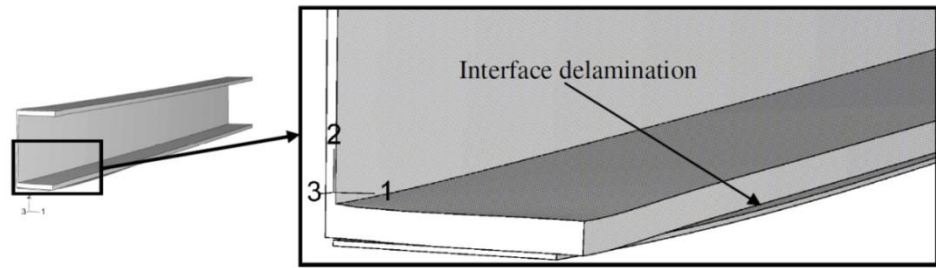


Figure 2-24, Debonding between the CFRP strip and steel beam (Bocciarelli et al, 2008)

The study of bonding strength of composite material onto steel adhered in composite repair for pipelines (i.e. encircling composite sleeve) is still scarce. In most of the literature on composite repair of steel pipes, the finite element models consider a continuum mechanics approach. For example, in Alexander's work of developing a composite repair system for reinforcing offshore risers, the author utilised this standard requirement to assess the bond strength of the composite repair by examining the maximum shear stress at the steel-composite interface of the finite element model (Alexander, 2007). According to Section II-3 of the Article 4.1 in the ASME PCC-2 standard, a minimum bond strength of 4MPa is required for metal substrate to composite adherent lap shear test. Disbond regions were assigned to the models to study the effects they had on the shear stress distribution of at steel-composite interface. It was determined that the highest shear stress at design load occurred in repair with outer disbond regions as shown in Figure 2-25 but the minimum bond strength value (4MPa) was not exceeded.



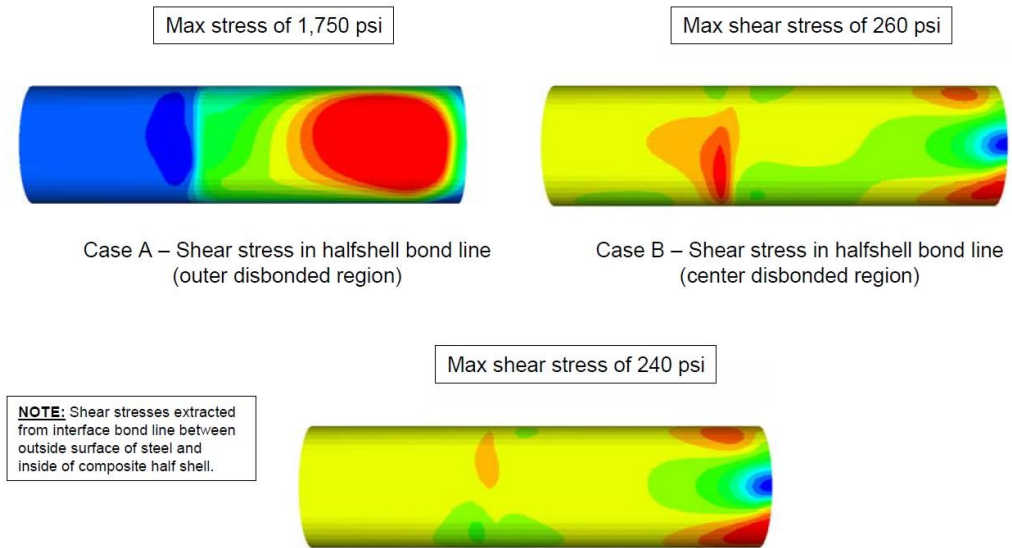


Figure 2-25, Shear stress at steel-composite interface of the finite element model (Alexander, 2007)

## 2.6 Standards & Guidelines

For the thorough study on the composite repair system for risers, there must be an in-depth understanding on the existing of relevant industrial standards and guidelines for certain practices. These standards are set by governing bodies such as the *American Society of Mechanical Engineers (ASME)*, *American Petroleum Institute (API)*, *International Organization for Standardization (ISO)* and *Det Norske Veritas (DNV)*, and are developed to a series of well-planned tests to validate different governing parameters that can be transformed into a standard practicable set of instructions. In order to provide an overall picture of the current code of practices, the different industrial standards and guidelines can be broken down to three major categories . The three major categories are:

- 1) Standards for pipeline design
- 2) Standards for riser design

### 3) Standards for pipeline and riser repair

#### **2.6.1 Standards for Pipeline Design**

ASME B31.4, (2006) Pipeline Transportation for Hydrocarbon Liquid and Other Liquids (ASME, 2006), and ASME B31.8 (2003) Gas Transmission and Distribution Piping System (ASME, 2003) are standards related to the design of pipelines which provide information on the stress and strain limits of industrial oil and gas pipelines. The ASME B31.4 prescribes requirements for the design, material, construction, assembly, inspection, and testing of liquid piping system. This standard gives a reference to the allowable stress values of piping system manufactured using different steel materials. In addition, it also explains the viable repair and maintenance methods for the pipelines suffering from different defects. The ASME B31.8 covers the similar scope as the ASME B31.4 but is applicable to gas piping system. Although not specifically intended for offshore risers, these standards provide a good foundation for pipeline design that in turn defines the requirements on the repair using FRPC materials. The API RP 1111 (1999) Design, Construction, Operation and Maintenance of Offshore Hydrocarbon Pipelines (Limit State Design) (API, 1999) provides the design cycles of offshore steel pipelines/risers based on limit states imposed by different design conditions such as the burst due to internal pressure and the combined bending and tension during operation.

#### **2.6.2 Standards for Offshore Riser Design**

Offshore risers are more complicated than onshore pipelines due to additional stresses, fatigue and harsh environment. The API RP 2RD (1998) *Design of Risers for Floating Production Systems (FPSs) and Tension-Leg Platforms*

(*TLPs*) (API, 1998) and, DNV-OS F201 (2010) *Dynamic Risers* (DNV, 2010), *ABS (2008) Guide for Building and Classing Subsea Riser Systems* (ABS, 2008) are similar standards that provide a better insight into the design of risers. For example, the DNV-OS F201 covers the design, materials, fabrication, testing, operation, maintenance and re-assessment of single pipes steel riser systems. It provides the design philosophy, safety requirements and classification of loads for riser system. The framework for global analysis, combined loading analysis, load effect assessment and fatigue analysis are elaborated.

It is hence prudent to utilise these standards to evaluate the design loads computed in the current study against the range of design loads that is set within the safety limits by these standards. The understanding of the different types of loads sustained by a live riser can be used to determine the load cases in of the composite repair system. The different types of static and dynamic analysis run on a riser system can be translated to the analysis of the composite repair system applied on corroded risers. The global analysis is not taken into consideration as the corrosion on the riser occurs in a localised manner. The composite repair is thus designed based on the requirement to suppress the stresses suffered by the corroded riser in the form of local analyses.

### **2.6.3 Standards for the Evaluation of Corroded Pipeline/Riser Residual Strength**

The composite repair system serves as a remedy for deteriorated pipeline/riser that is manifested in the form of an external corrosion. Before concluding that a means of repair is required on a corroded pipeline/riser, its residual strength must be determined. The ASME B31G (1991) *Method for Determining the Remaining*

*Strength of Corroded Pipelines* (ASME, 1991) and DNV-RP-F101 (2010) *Corroded Pipelines* (DNV, 2010) are standards that provide guidelines to assess the condition of corroded pipelines. It is worthy to note that these standards are meant for the application of corroded pipelines where the residual strength is determined mainly based on the internal pressure. The effects of combined internal pressure and axial loads such as bending and tensile loads are outside the scopes of these standards. In addition, it is not applicable to pipelines suffering from mechanical damage (i.e. gouge and dents) or sharp defects (i.e. cracks). In terms of evaluating the residual strength of corroded risers, there is no specific standard that can address this problem. The existing standards applicable to pipelines are therefore used as a guide to obtain an approximate value to be implemented into the design equations of the composite repair system. Ultimately, the finite element analysis is used as a tool to optimise the composite repair system based on the residual strength of the risers when different sizes of corrosion defects are modelled.

#### **2.6.4 Standards for Corroded Pipeline/Riser Repair**

Once the corroded pipeline/riser is proven to be non-functional or approaching failure, a repair method can be applied on the corroded region in order to restore the strength of the pipeline/riser. The current research is solely focused on the application FRPC as a repair technique. The ASME PCC-2 (2008) Repair of Pressure Equipment and Piping, Article 4.1, Non-Metallic Composite Repair Systems for Pipelines and Pipework: High Risk Application (ASME, 2008) and the ISO/TS 24817 (2006) Petroleum, Petrochemical and Natural Gas Industries – Composite Repairs for Pipework – Qualification and Design, Installation, Testing and Inspection (ISO, 2006) are employed to determine the required

properties and parameters of the composite repair. Both of these standards employ the same equations in the computation of the required thickness of the composite repair. The equations are based on parameters from both the repair material and the substrate. The parameters include the modulus of elasticity for the FRPC and the pipe material, the yield strength of pipe material, the dimensions of the pipe as well as the maximum allowable pressure of the corroded pipe. However, the shortcoming of these standards is that the maximum allowable working pressure (MAWP) is computed based on the ASME B31G which has the limitation of being only applicable to individual internal pressure load case. The required thickness computed using the ASME PCC-2 is hence compared to those obtained via a limit analysis using finite element simulation to account for the case of combined loadings.

## **2.7 Concluding Remarks**

Based on the literature review discussed, it can be observed that composite repair for offshore riser is a potential means of reinforcement for offshore steel risers. Composite repair for onshore pipelines has been widely used in the industry where numerous research and technical reports have been conducted to validate their functionality. In an effort to integrate the use of composite repair for offshore structures, different studies have been conducted to characterize the performance of such repair. Several research gaps were identified and are further discussed in the paragraphs below.

Most of the studies on composite repair system for steel pipes were done on the basis of static loading with majority of them related to the capacity of the repaired system in sustaining the hoop load as this is the main concern in onshore

pipeline failures (Duell, et al., 2008) (Meniconi, et al., 2002). Investigations of composite repair system for offshore pipeline/riser applications were mostly focused on the environmental conditioning of the composite material rather than on the different loading conditions sustained by subsea risers. Studies on combined loading such as internal pressure, tension and bending were limited. In addition, the design of the composite repair system in this study were done based on the industrial standard ASME PCC-2 and ISO/TS 24817. No effort was conducted to formulate an accurate and repeatable design tool for composite repair system in offshore riser applications.

The research on the failure mechanisms within the composite material itself and the steel-composite interface is scarce. One of the major aspects in reinforcing steel structures with FRPC is to study the bond behaviour between the two. Although various literatures on the bonding strength and behaviour of the steel-composite interface is extensive, majority of the studies were conducted on coupon test specimens (Haghani, 2010) (Bocciarelli, et al., 2008) (Yang, et al., 2013). Characterization of the actual behaviour of the steel-composite bond were also manifested in full-scale test and finite element modelling but limited to patch repair (Zhao, et al., 2006) (Narmashiri, et al., 2010) instead of full encircled wraps. Local analysis of bond integrity at the steel-composite interface under cyclic loading mimicking wave/current forces is an important aspect that is not addressed.

In this study, the understanding of the industrial design standards and guidelines were used as a basis to ensure that the study of the CRS for offshore risers are aligned with the riser design requirements. Understanding the effects of different loading conditions on the composite repair system is one of the essential steps to

extending its application to offshore riser. With a design and analysis tool that can accurately predict the behaviour of the composite repair system, confidence level in its application on offshore risers can be increased and can be made repetitive according to a set of standard procedures. However, to the best of the author's knowledge, there is no comprehensive research work which addresses this issue. The lack of such information can hinder the application of composite repair system at inaccessible depths via automated machine. Thus, this research gap has prompted the research work documented in this thesis.

# **Chapter 3 Design of Composite Repair System for Offshore Riser**

## **3.1 Introduction**

The literature review conducted in Chapter 2 reveals that the existing standards and regulations do not have any specific guidelines on the design of oil and gas offshore riser rehabilitation using FRPC. Nevertheless, there are several standards available for the repair of onshore pipelines using FRPC (ASME, 2008). These standards provide a basis for the design of composite repair system for offshore riser. Based on the standards developed for composite repair of onshore pipelines, modifications and enhancements were carried out to include additional constraints and loading conditions commonly experienced by offshore riser. Review into the types of constraints and loadings sustained by typical offshore riser, along with the procedure for evaluation of residual strength of a corroded riser were outlined in the current chapter. Based on the calculated residual strength of the corroded riser, the basic requirements (thickness and length) of the composite repair can be determined through the established formulations as described in ASME PCC-2 (ASME, 2008). The computed dimensions of the composite repair systems provide a starting point for optimisation of the composite rehabilitation performance based on various factors such as loading conditions, fibre type, fibre orientation angle and severity of corrosion defect on the riser surface.



## **3.2 Loading Conditions of a Riser**

The design of a composite repair system for an offshore riser can vary significantly from that of an onshore pipeline. This is due to the fact that risers are vertically suspended below oil rig floating platform and largely submerged underwater whereas typical onshore pipelines are horizontally supported. The position of the riser along with its subsea environment poses more complicated loading conditions which are required to be taken into account when designing the composite repair system. These additional loading conditions can be categorised into functional loads, environmental loads, installation loads and accidental loads.

### **3.2.1 Functional Loads**

Functional loads are the in-service loads that the riser has to sustain during its operation. As the main function of a riser is to carry the oil from the wellhead to the surface, the major functional load is undoubtedly the internal pressure arising from the fluid pressure acting on the internal walls of the riser. Similar to the design of onshore pipelines, two conditions of internal pressure, the burst pressure,  $P_b$ , and the design pressure,  $P_d$ , can be considered in a riser design. The burst pressure,  $P_b$ , also known as the test pressure, is the acting pressure when total failure of the pipe occurs and the internal fluid is no longer contained. The design pressure,  $P_d$ , also known as the maximum allowable operating pressure (MAOP), is the maximum pressure at which a riser may be operated in accordance with the provisions of the design code. Based on a list of steel catenary risers (SCR) available at different tension leg platforms (TLP), namely Auger 1994, Mars 1997, Ram-Powell 1997 and Marlim Semi 1995, the operating

pressure of SCR ranges from 14 to 43 MPa (Howells, 1995). The variation in operating pressure of the riser depends on its nominal pipe size and the wall thickness. It is also determined by function (fluids) of the riser, such as drilling riser, oil or gas transmission riser and water injection riser. In addition to the internal pressure, tension is a common functional load that is applied to a riser. This is usually a constant tensile force imposed on the riser to avoid buckling and excessive bending stresses due to platform motion, wave and current forces and vortex induced vibration (VIV) (Stanton, 2006). The magnitude of the applied tension depends on the weight of the riser, buoyancy of the riser and the lateral forces. The first SCR installed from a moored floating platform in water depth of 910m utilised a design top tension of 1780 kN. This SCR was installed as part of a program conducted by Petrobras to evaluate the use of SCR connected to moored platforms. The monitoring program supplies data from real scale measurements to validate computer models used in the design of floating production platforms, deep water mooring systems and catenary riser. (Machado Filho, et al., 2001).

### **3.2.2 Environmental Loads**

Environmental loads are caused by wind, waves and current forces, and vortex induced vibrations (VIV) (Stanton, 2006). These forces can generate platform motions which displace the risers relative to its mean position. Environmental loads vary significantly with weather conditions and hence are highly climate and location dependent. In most cases, the magnitude of the environmental loads is insufficient to cause static failure of the riser and hence the composite repair system. However, wave and current forces are cyclic in nature. The main sources of fatigue loading on riser can be categorised as:

- (1) First order wave frequency and second order low frequency vessel motions due to waves and wind
- (2) Vortex induced vibration (VIV) of the riser due to currents
- (3) Vortex induced vibration of the riser due to vessel heave (HVIV)
- (4) Vortex induced motion (VIM) of the vessel due to currents

In riser design, fatigue stress analyses are usually conducted through global analyses where the movement of the entire length of the riser from the platform to the seabed is simulated (DNV, 2010). In this research, global analysis was not considered as the composite repair system is considered to be applied on a localised region containing corrosion defect. Hence, two types of local analyses were conducted to study the environmental load, (i) static analysis and (2) simplified low cycle fatigue analysis. In the static analysis, a constant bending load was defined as the only environmental load in order to study the capability of the CRS in withstanding the deformation. In the fatigue analysis, constant loading amplitude and frequency defined based on a specific wave data obtained from literature was applied to study the failure of the CRS through Interlaminar delamination and disbonding between the FRPC and steel riser.

### **3.2.3 Installation Loads**

Installation loads are those that arise during the deployment of the riser. Installation loads are dependent on the installation procedures and the technique in which the riser is tied in to the main production unit on the offshore platform. As defects such as external corrosion that imposes the need for a repair system only takes shape after the riser is in service, installation loads are not a major concern when designing the composite repair system.

### **3.2.4 Accidental Loads**

Accidental loads are those that occur inadvertently due to abnormal operating conditions, technical failure and human error. Accidental loads are those that are unpredictable and situational dependent with examples such as soil-sliding, earthquakes and impacts from foreign objects. It is normally not necessary to combine these loads with other functional and environmental loads unless site-specific conditions indicate such requirement. Therefore, this type of loads is not considered in the current research project.

### **3.2.5 Load Cases**

Based on the loading conditions of a riser as discussed in section 3.2 , a set of typical load cases are derived and used in the study of the CRS with aid of FEA. The effects due to functional and environmental loads are considered and are represented in terms of internal pressure, effective tension and effective bending moment. This is aligned with the load acceptance criteria obtained from section 4, analysis methodology of the DNV-OS-F201 (DNV, 2010) where the main loading effects considered are the differential pressure, bending moment and effective tension. These load cases were being simulated through local static analyses where maximum stresses sustained by the riser were considered. Local analyses of low cycle fatigue load was conducted to examine the integrity of the FRPC interlaminar bond and FRPC to steel riser bond.

## **3.3 Design Requirements**

The design requirements of the CRS can be split into two major considerations:

- 1) The composite material wrapped around the riser must be able to sustain the stresses induced by different loadings to which a riser is susceptible to. These stresses must not exceed the designed limits while the strain must be kept below a threshold value above which it will affect the load carrying capacity of the repaired riser.
- 2) The interfacial bond between the riser and the composite materials must be well established such that the composite will not delaminate from the steel surface. If the steel-composite interface bond is not sufficiently strong, adequate stress transfer from the steel riser to the composite material will not take place.

### **3.4 Residual Strength of Corroded Risers**

An essential part in the design of a composite repair system is to determine the residual strength in the corroded risers. Depending on the severity of the corrosion defect, the level of reinforcement needed to restore the strength of the corroded risers can be determined through a series of design calculations. The residual strength of the corroded riser can be evaluated using the equations provided in the ASME B31G, Methods for Determining the Remaining Strength of Corroded Pipelines (ASME, 1991). It is essential to point out here that employing evaluation based on ASME B31G possessed an inherent limitation whereby the criteria for corroded pipe to remain in-service as presented in this Manual are based upon the ability of the pipe to maintain structural integrity under internal pressure only. It should not be the sole criterion when the pipe is subjected to a significant secondary stresses (e.g., bending, tension), particularly

if the corrosion has a significant transverse component”. Hence, it can only be used as an approximate benchmark and not as an absolute guideline.

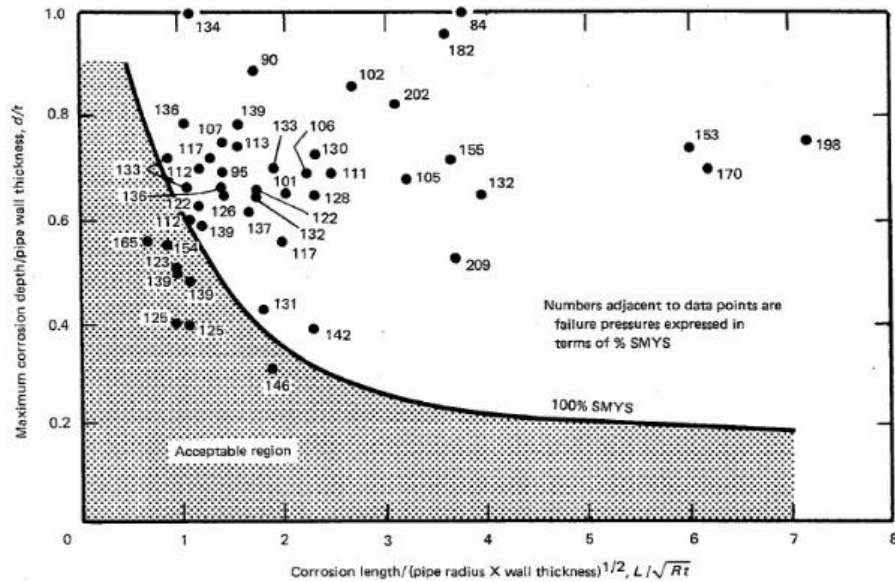


Figure 3-1, Parabolic criteria for classifying corrosion defects according to predicted failure stress (ASME, 1991)

The factors that determine the failure of a corrosion flaw are the corrosion size relative to the size of the pipe and the flow or yield stress of the material. Figure 3-1 shows the relationship between the full-size test failures and the criterion for acceptance of corrosion pits in line pipe. This criterion states that the pipes shall withstand a pressure equal to a stress level of 100% of the specified minimum yield stress (SMYS). The solid line shown in the figure is the line that identifies failure pressures of less than 100% SMYS. The use of 100% SMYS as a reference to acceptable limits indicates that the criterion is very conservative. The acceptable region in the plot is the shaded region and to the left of the solid line. Corrosion pits that have depths and lengths that fall above the curve are not acceptable, and in accordance to the criteria presented, the operating pressure either has to be reduced, or the corrosion pit repaired.

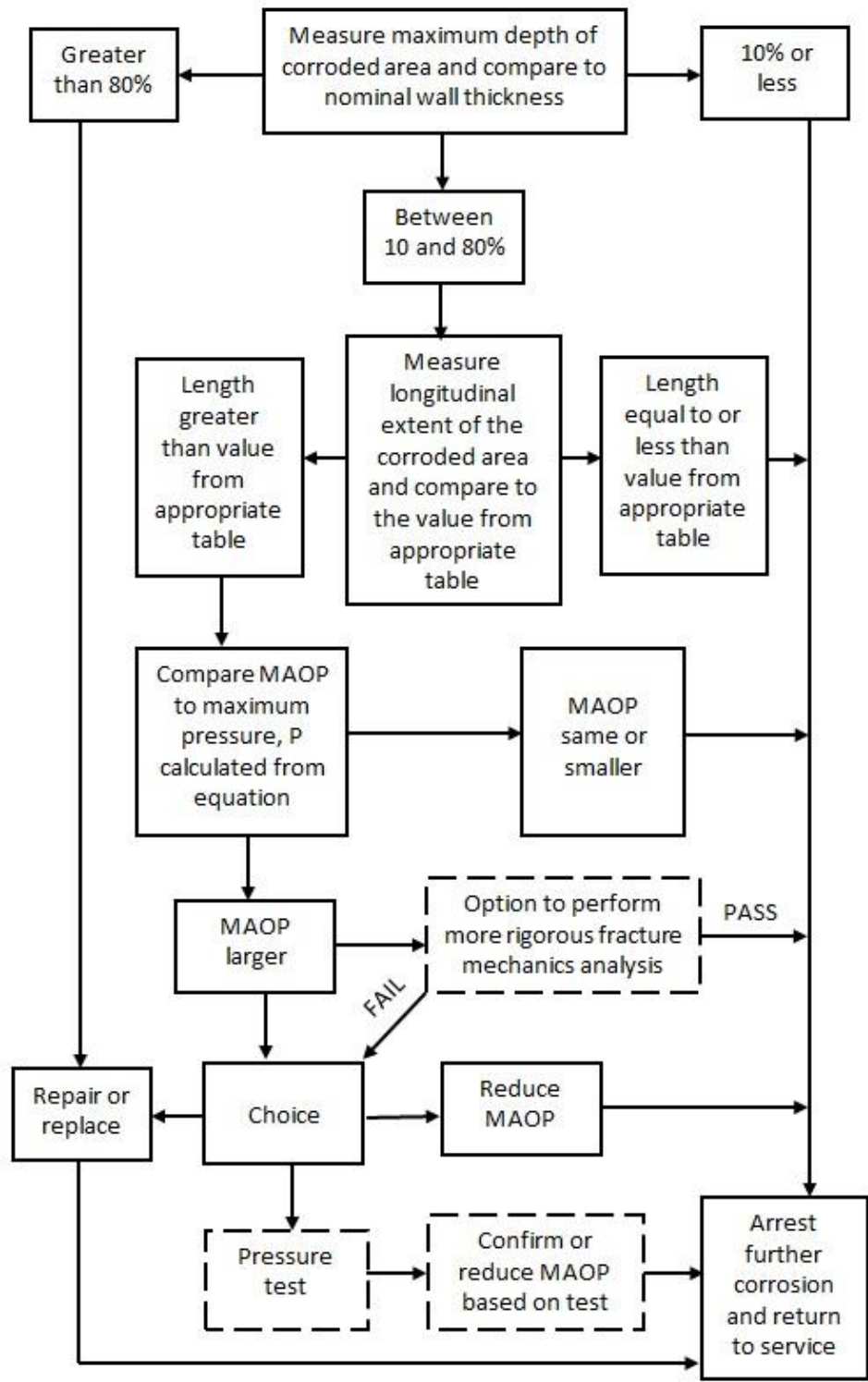


Figure 3-2, Process of assessing the remaining strength of a corroded pipe (ASME, 1991)

The process of assessing the remaining strength of a corroded pipe as suggested in ASME B31G is shown in Figure 3-2. Once the corrosion depth is determined

to be 10% to 80% of the nominal wall thickness of the pipe, the extend of the corrosion area along the longitudinal axis of the pipe is measured. This length must not be greater than the value calculated using Eq. 3-1,

$$L = 1.12B\sqrt{D_o t_p} \quad 3-1$$

Where  $L$  is the maximum allowable longitudinal extent of the corroded area,  $D$  is the nominal outside diameter of the pipe,  $t_p$  is the nominal wall thickness of the pipe, and  $B$  can be computed using Eq. 3-2,

$$B = \sqrt{\left(\frac{d_c/t_p}{1.1d_c/t_p - 0.15}\right)^2 - 1} \quad 3-2$$

where  $d_c$  is the depth of the corrosion. If the corrosion length is greater than the value calculated using Eq. 3-1, then the burst pressure of the corroded pipe must be compared to the maximum allowable operating pressure (MAOP) of an uncorroded pipe to check whether it is fit for operation. The burst pressure of the corroded pipe can be calculated using Eq. 3-3 to Eq. 3-7 provided in the ASME B31G standard (ASME, 1991).

(1) Burst Failure Pressure:

$$P_{b,corr} = \frac{\sigma_{flow} \cdot 2t_p}{D_o} \left[ \frac{1 - \frac{2}{3} \cdot \frac{d_c}{t_p}}{1 - \frac{2}{3} \cdot \frac{d_c}{t_p} \cdot \frac{1}{M}} \right], \quad \sqrt{0.8 \left(\frac{L_c}{D}\right)^2 \left(\frac{D_o}{t_p}\right)} \leq 4.0 \quad 3-3$$

$$P_{b,corr} = \frac{\sigma_{flow} \cdot 2t_p}{D_o} \left[ \frac{1 - \frac{d_c}{t_p}}{1 - \frac{d_c}{t_p} \cdot \frac{1}{M}} \right], \quad \sqrt{0.8 \left(\frac{L_c}{D_o}\right)^2 \left(\frac{D_o}{t_p}\right)} \geq 4.0 \quad 3-4$$

(2) Flow Stress:



$$\sigma_{flow} = SMYS + 68.95MPa \quad 3-5$$

(3) Folias Factor:

$$M = 0.032 \frac{L_c^2}{D_o t_p} + 3.3, \quad L_c^2 / D_o t_p \geq 50 \quad 3-6$$

$$M = \sqrt{1 + \frac{2.51 \left( \frac{L_c}{2} \right)^2}{D_o t_p} - \frac{0.054 \left( \frac{L_c}{2} \right)^4}{(D_o t_p)^2}}, \quad L_c^2 / D_o t \leq 50 \quad 3-7$$

Where  $P_{b,corr}$  is the burst pressure of the corroded pipe,  $\sigma_{flow}$  is the flow stress of the pipe material, and  $M$  is an empirical constant called the Folias Factor. It should be noted that these equations are those used for onshore pipelines where residual strength is computed based on the burst pressure of corroded pipelines. Risers are subjected to much complex loadings compared to onshore pipeline, hence utilization of Eq. 3–3 to Eq. 3–7 for computation of residual strength in corroded riser provide only an approximate value to be used as a reference point for further design calculations. To enhance the accuracy of the design of CRS for riser, numerical simulation was employed in the current research whereby further details will be discussed in Chapter 4 .

### 3.5 Minimum Repair Thickness of the Composite Laminate

The composite repair laminate must be thick enough to sustain the load transferred from defective pipelines. The minimum required laminate thickness can be determined through ASME PCC-2, Repair of Pressure Equipment and Piping (ASME, 2008) or a similar standard ISO/TS 24817, Petroleum, Petrochemical and Natural Gas Industries – Composite Repairs for Pipework – Qualification and Design, Installation, Testing and Inspection (ISO, 2006). With

this minimum thickness of the repair laminate, the burst strength of the corroded pipe will be at least equal to that of a pipe without corrosion. It should be noted that the calculated minimum repair thickness can be used as an approximate reference value for the initial stages of the design such that an input value can be assigned to the numerical models. This is due to the fact that certain calculations in the ASME PCC-2 are based on the ASME B31G which has its limitations when applied for risers which are subjected to combined loadings. A range of thickness values will be modelled to investigate further the required thickness of the repair laminate. The minimum required laminate thickness,  $t_{min}$  of a repaired pipe subjected to internal pressure,  $P_{in}$  is determined by:

$$t_{min} = \frac{D_o}{2SMYS} \cdot \left( \frac{E_p}{E_c} \right) \cdot (P_d - P_s) \quad 3-8$$

where  $E_p$  is the tensile modulus of the pipe material,  $E_c$  is the tensile modulus of the composite laminate in the circumferential direction of the pipe,  $P_d$  is the design internal pressure of the pipe and  $P_s$  is the maximum allowable pressure for the pipe with defect as determined from ASME B31G (ASME, 1991). Based on the design criteria stated in API RP 1111, Design, Construction, Operation and Maintenance of Offshore Hydrocarbon Pipelines (API, 1999), the values of  $P_s$  for pipeline and riser are equivalent to  $P_{b,corr}$  multiply by a safety factor of 0.9 and 0.75 respectively.

When the pipe is subjected to combined  $P_{in}$ ,  $F_t$  and  $M_b$ , the minimum required laminate thickness can be calculated via Eq. 3–9

$$t_{\min} = \frac{D_o}{SMYS} \cdot \left( \frac{E_p}{E_a} \right) \cdot \left( \frac{2F}{\pi D_o^2} - P_s \right) \quad 3-9$$

where  $E_a$  is the tensile modulus of the composite in the axial direction of the pipe and  $F$  is the equivalent axial load due to  $P_{in}$ ,  $F_t$  and  $M_b$  calculated using Eq. 3–10, in units of Newtons.

$$F = \frac{\pi}{4} p D_o^2 + \sqrt{F_{ax}^2 + 4F_{sh}^2} + \frac{4}{D_o} \sqrt{M_{ax}^2 + M_{to}^2} \quad 3-10$$

Where  $F_{ax}$  is the applied axial load,  $F_{sh}$  is the apply shear load,  $M_{to}$  is the applied torsional moment and  $M_{ax}$  is the applied axial moment. For the combined  $P_{in}$ ,  $F_t$  and  $M_b$  loading, the values of  $F_{ax}$  is equivalent to  $F_t$  while the value of  $M_{ax}$  is equivalent to the tensile force due to  $M_b$ .  $F_{sh}$  and  $M_{to}$  are assumed to be zero due to the nature of the loading.

The design internal pressure,  $P_d$  of the pipe can be determined from API RP 1111, Design, Construction, Operation and Maintenance of Offshore Hydrocarbon Pipelines (API, 1999). This process follows a flow where the burst pressure is slowly segmented into lower pressure values based on suitable design (safety) factors. This is illustrated in Figure 3-3.

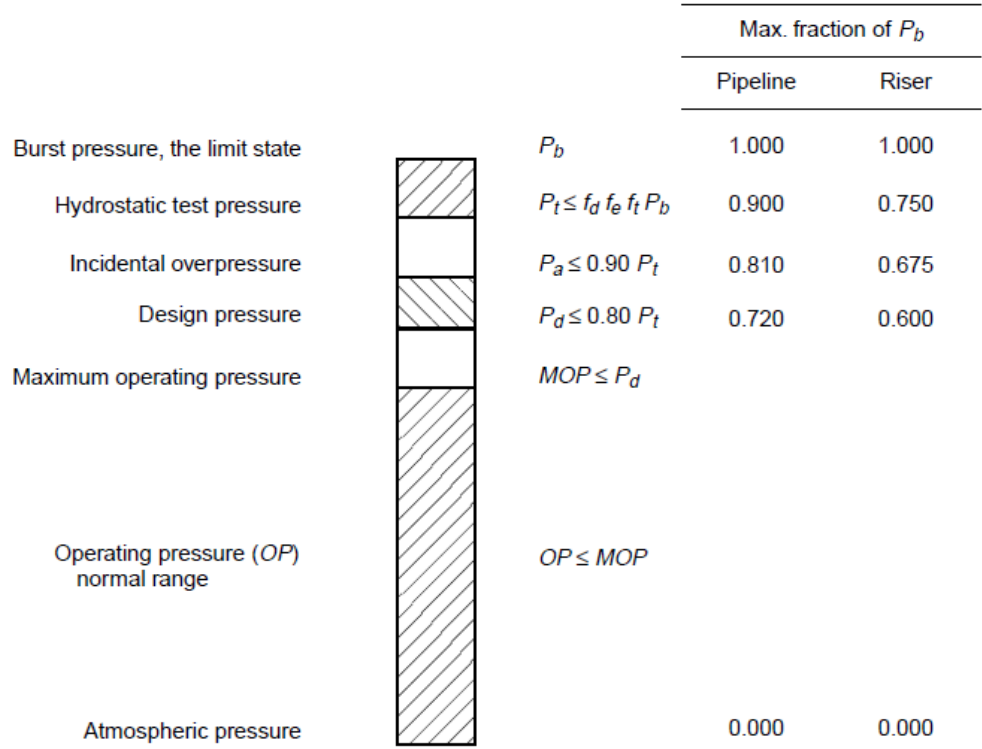


Figure 3-3, Pressure level relations (API, 1999)

The burst pressure,  $P_b$  is usually determined by the diameter and thickness of pipe and the type of material used to construct the pipe. It can be calculated using Eq. 3-11a or Eq. 3-11b. The hydrostatic pressure,  $P_t$  is the value of internal pressure minus the external pressure, with different design factors taken in account, as shown in Eq. 3-13.

$$P_b = 0.9(SMYS + U) \frac{t_p}{D_o - t_p}, \quad D_o/t_p < 15 \quad 3-11a$$

$$P_b = 0.45(SMYS + U) \ln \frac{D_o}{D_i}, \quad D_o/t_p \geq 15 \quad 3-12b$$

$$P_t \leq f_d f_e f_t P_b \quad 3-13$$

$$P_d \leq 0.80 P_t$$

3-14

Where,

$f_d = P_{in}$  design factor (0.75 for risers)

$f_e$  = Weld joint factor (only materials with factor 1.0 are acceptable). The values of  $f_e$  can be found in ASME B31.4, Pipeline Transportation Systems for Liquid Hydrocarbons and Other Liquids (ASME, 2006). Seamless, electric resistance welded, electric flash welded and submerged arc welded pipes all have  $f_e$  value of 1.0.

$f_t$  = Temperature de-rating factor as specified in ASME B31.8, Gas Transmission and Distribution Piping System (ASME, 2003) to account for the thermal stress that arises for high temperature services. The different values for  $f_t$  are shown in Table 3-1.

$U$  = Specified minimum ultimate tensile strength

$D_i$  = Internal pipe diameter.

Table 3-1, Temperature derating factor,  $f_t$  (ASME, 2003)

Temperature (°C)	Temperature derating factor, $f_t$
121 or less	1.000
149	0.967
177	0.933
204	0.900
232	0.867

### 3.6 Axial Length of the Laminate Repair

In order to prevent delamination of the composite material from repaired pipe and to ensure sufficient axial load transfer from the pipe to the composite, the adhesion surface area between reinforcement material and the pipe must be large enough.

The length to which the laminate repair should extend over each side of the corroded region can be determined through Eq. 3–15,

$$L_{over} = 2.5\sqrt{D_o t_p / 2} \quad 3-15$$

where  $L_{over}$  is the overlap length of the composite laminate. The value of  $L_{over}$  is also dependent on the lap shear strength between the composite laminate and the steel pipe,  $\tau$ . Hence, the calculated value of  $L_{over}$  can be checked via Eq. 3–16,

$$L_{over} > \frac{E_a \varepsilon_a t_{min}}{\tau} \quad 3-16$$

Where  $\varepsilon_a$  is the allowable axial strain on the composite laminate. Subsequently the total axial length of the repair can be calculated through Eq. 3–17,

$$L = 2L_{over} + L_{defect} + 2L_{taper} \quad 3-17$$

where  $L_{defect}$  is the axial length of the defect and  $L_{taper}$  is the taper length. The length of the repair is verified through FE models described in Chapter 4 . According to section II-3 of ASME PCC-2 Article 4.1, a minimum lap shear strength of 4MPa between the composite and steel substrate is required (ASME, 2008). Hence, the shear stresses on the inner surface of the composite laminate and outer surface of the steel pipe are monitored to ensure that they do not exceed that value.

### 3.7 Design Conditions

To aid with the design of the composite repair system, a study on the repaired riser pipe subjected to complex loadings is required. Due to the variation of CRS design cases considered in the current research, it is more time efficient to apply the stress-strain analysis to determine the performance of the riser without defect,

riser with corrosion defect and riser repaired with CRS. The stress-strain analysis is conducted via finite element analysis (FEA) which is discussed in Chapter 4 .

Based on ASME Boiler & Pressure Vessel Code Section VIII Division 2, there are three available analysis methods for evaluating the plastic collapse load of pressure vessels. These methods include: (i) Elastic stress analysis method, (ii) Limit load method and (iii) Elastic-plastic stress analysis method (ASME, 2007). In the elastic stress analysis method, a limiting value is used to evaluate the elastic stress of a structure subjected to predefined load. It does not take into account the plastic deformation that occurs when the load increases. The limit load method determine a lower bound to the limit load of a structure and applies design factors to the limit load such that the onset of plastic collapse will not occur (Biel & Alexander, 2005). Limit load method is more suitable for the design of composite repair system as plastic deformation is taken into account in the analysis. This allows the behaviour of the composite to be evaluated when the load is transferred from the steel riser to the composite after a certain amount of plastic deformation. Elastic-plastic stress analysis considers the ultimate stress and perfect plasticity behaviour. In other words, it considers the non-linear deformation of the structure until collapse. Both limit load method and the elastic-plastic analysis method can be analysed numerically.

In the current research, the second method (limit load method) described was used because only the elastic material properties of FRPC are used as the input. Based on section 5, Design Criteria for Riser Pipes of DNV-OS-F201 (DNV, 2010), the serviceability limit state (SLS) requires that the riser must be able to remain in service and operate properly, corresponding to criteria governing the normal operation of the riser. The technique used here is known as the double-

elastic slope method and is founded on a single unified design basis developed by (Alexander, 2007). This design technique was derived from several oil and gas industry design codes and standards and is similar to the criterion of collapse load defined in section 6-153 of ASME Boiler and Pressure Vessel Code (1998), Section VIII, Division 2 (ASME, 2007). The double-elastic slope method allows computation of the plastic analysis collapse load (PACL), i.e. the load at which the material reaches failure after a certain amount of plastic deformation occurs. It is important to consider some level of plasticity as it is needed for load transfer from the steel riser to the composite.

The first step of this method is to simulate a FE model of a non-corroded pipe. The load is then plotted as the ordinate while the strain is plotted as the abscissa in a linear graph. Subsequently, a double elastic curve (DEC) that has a gradient half of the linear elastic region of the load-strain curve is plotted through the origin. The PACL corresponds to the intersection of the DEC and load-strain curves. Finally, the design load (DL) can be determined by dividing the PACL with a margin value which in this case is 2. This value is chosen based on the design procedures for risers as stated in API RP 111 (API, 1999). The fraction of burst pressure (PACL) at design condition is 0.6 as shown in Figure 3-3. By taking into account temperature derating factor for maximum service temperature (Table 3-1) of the riser, the fraction of burst pressure will be equivalent to,

$$P_d = 0.6P_b \times f_T$$

$$P_d = 0.6P_b \times 0.867$$

$$P_d = 0.52P_b$$



$$P_d \approx \text{PA} \cdot \text{CL} / 2$$

The maximum permissible strain limit is defined as the strain value at the intersection of the DEC and DL curves.

The load-strain response of a riser is simulated using FEA, in order to compute the design loads via the DEC method. The riser is an API 5L grade X60 carbon steel pipe commonly used in the oil and gas industry. The simulated riser has an outer diameter of 219mm with a wall thickness of 10.3mm. The length of the riser model for the case of individual internal pressure and tensile load is 2440mm, while the length of the riser model for the case of individual bending and combined loading is 4570mm. Further details of the material input, boundary conditions, loading conditions, meshing and element of the riser FE model are described in Chapter 5.

The computations of design load for individual loading of internal pressure, tensile load and bending moment using the DEC method are shown in Figure 3-4, Figure 3-5 and Figure 3-6. The computation for the design load for combined loading of constant internal pressure at 22MPa (DL), constant tensile load at 1785kN (DL) and varying bending moment is shown in Figure 3-7.

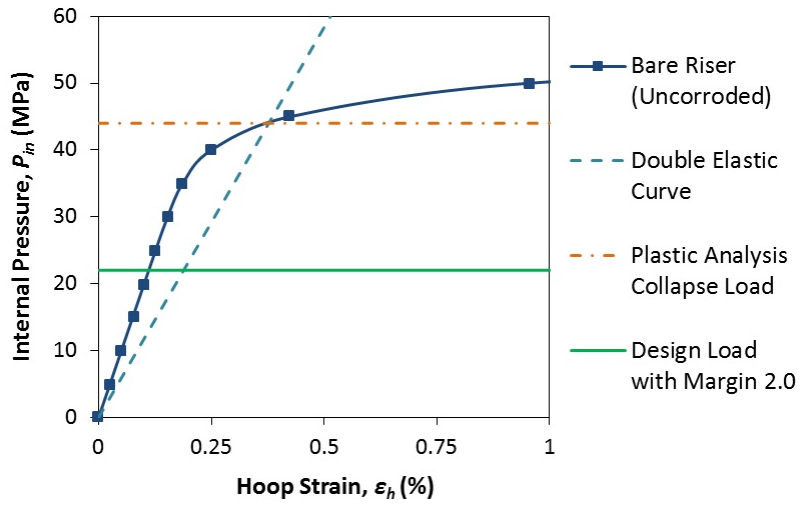


Figure 3-4, Limit state analysis of bare riser subjected to  $P_{in}$

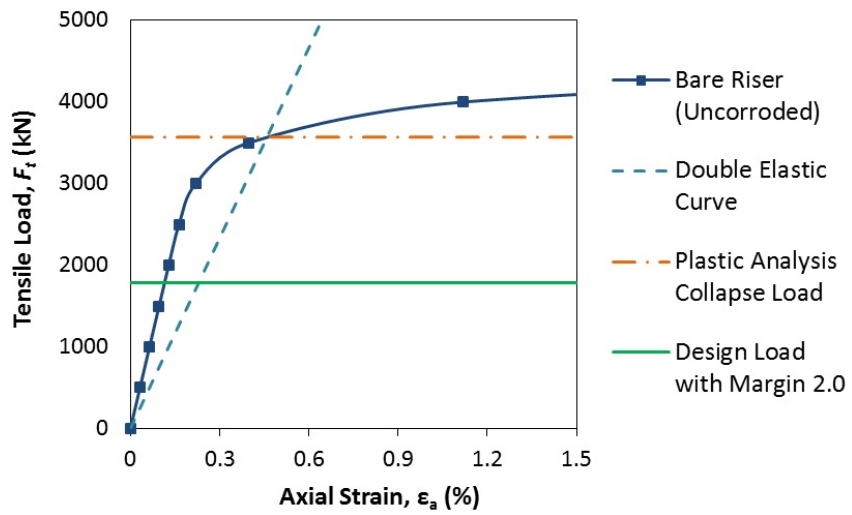


Figure 3-5, Limit state analysis of bare riser subjected to  $F_t$

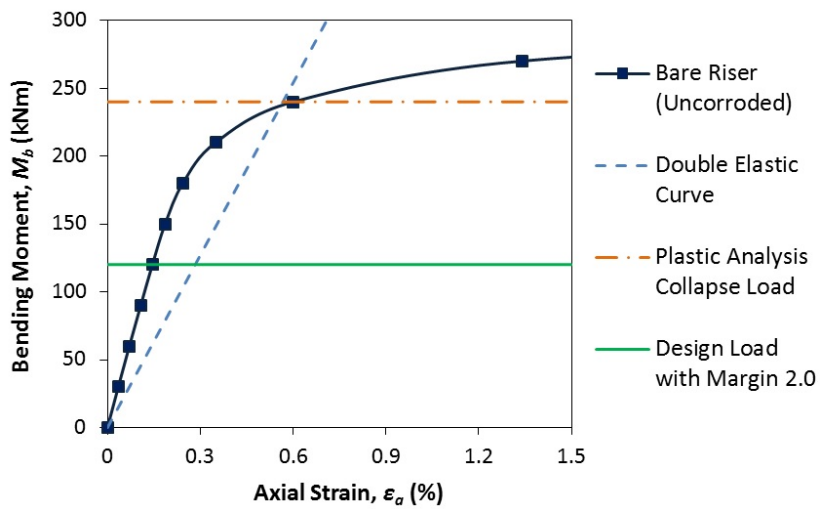


Figure 3-6, Limit state analysis of bare riser subjected to  $M_b$

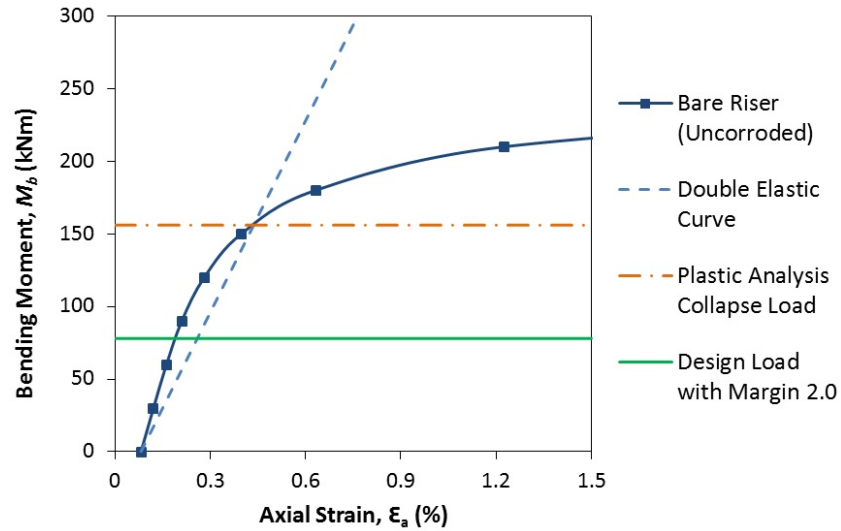


Figure 3-7, Limit state analysis of bare riser subjected to  $P_{in}$ ,  $F_t$  &  $M_b$

The output of the design loads and maximum permissible strains are recorded in Table 3-2. These values are compared to those calculated using the theoretical equations provided in the different design standards and the differences in the results are less than 12%.

Table 3-2, Design load and maximum permissible strain for different load cases

Loading Case	Design Standards		DEC Method
	Design Load	Design Load	Maximum Permissible Strain
Internal Pressure, $P_{in}$	24.9MPa	22MPa	0.1875%
Tensile Load, $F_t$	1697kN	1785kN	0.225%
Bending Moment, $M_b$	113kNm	120kNm	0.255%
Combined Load ( $P_{in} = 22\text{MPa}$ , $F_t = 1785\text{kN}$ )	-	78kNm	0.255%

### **3.8 Concluding Remarks**

The load cases included in the current project were discussed. The equations discussed in this chapter provide benchmark values to be used as a reference in the design and optimization of the CRS, which will be reported in Chapter 4 , Chapter 5 and Chapter 6 . The limit analysis known as double elastic method developed by Alexander (Alexander, 2007) was used as the main technique of evaluation for the CRS. The computed design loads and limit strain values will be used for evaluation of the output results that were obtained from finite element analysis of the CRS. The computed design conditions via the combined use of FEA and DEC method provided close approximation to the design standards. In addition, the load-strain curve provides a clearer representation on the level of stress and strain sustained by the riser and the CRS, as individual load-strain curves can be plotted out. The ease of varying the different inputs (i.e. types of composite material, sizes of corrosion defect, thickness of repair laminate) in the FE model, combined with the straightforward computation of the DEC method, provides an optimization tool for the CRS.

## Chapter 4 Finite Element Analysis

### 4.1 Introduction

Considering the substantial size of typical risers with diameter in the range of 6 to 10 inches, the construction of a full-scale test facility for CRS of risers would require significant investment. Numerical approaches such as FEA, on the other hand provides an efficient and cost effective way to predict the deformation behaviour such as stress and strain response of structural components subjected to various forms of loadings. This chapter provides a detailed description of the application of FE modelling for analysing the CRS of an offshore riser via a general-purpose FE package ABAQUS<sup>®</sup> Standard. Appropriate element selection and localized mesh refinement were applied to reduce computational time and ensure a fast convergence. Validation of the FE models was conducted against both classical mechanics solutions and scaled-down experimental tests (Chapter 5 ). In addition, a case study of the Helicoid Epoxy Sleeve (HES)<sup>™</sup> involving full-scale testing was conducted in collaboration with Merit Technologies Sdn Bhd. The results provide an auxiliary validation method and augment the reliability of the FE approach in optimisation of the CRS for offshore riser.

Local analyses covering the effects of individual static loads (internal pressure, tension, bending load) and combined loads (combined internal pressure and tension, combined internal pressure, tension and bending load) which are common in offshore environment were conducted. Modelling of the relevant parts is accomplished via ABAQUS/CAE which provides an interface for creating parts, materials, assembling a model, assigning section properties and

meshing. Modification of the generated input files enables ease of parametric analysis. Three scenarios were considered in the current FEA of the riser:

- 1) Bare riser without corrosion damage.
- 2) Bare riser with corroded region manifested as material loss in thickness.
- 3) Corroded riser repaired with CRS.

Several cases of the FEA were conducted to capture the stress-strain behaviour of bare riser, corroded riser and riser with CRS subjected to a series of static loadings (i.e. individual loads and combined loads) with consideration being drawn on the minimization of simulation time, memory usage and computer resource were taken in consideration. Further FEA correspond to the establishment of optimum parameters for the CRS with respect to different corrosion size and types of loading will be discussed in Chapter 6 .

## **4.2 Fundamentals of FE Modelling within ABAQUS®**

FEA technique utilized in ABAQUS general purpose codes are discussed in the current section to provide a fundamental guidance for establishing an optimized FE model without compromising the accuracy of the results.

### **4.2.1 Non-linear Solution in ABAQUS Standard**

In CRS, the load shall be effectively transferred from the steel riser to the FRPC material when the riser is subjected to external loadings. Geometrical non-uniformity occurs when the riser is subjected to high magnitudes of loading, specifically in the case of bending. Other sources of nonlinearity such as nonlinear material behaviour and contact must be appropriately captured with the FE model. The material data of the steel riser and CRS were defined through

an elastic-plastic properties and elastic lamina properties, respectively with the FEA. In addition, solution to non-linear problem is highly dependent on element size, element types, boundary conditions, increment size, tolerance value, and solution algorithm which must be chosen with care.

ABAQUS utilises an incremental iteration scheme to establish computation convergence, whereby an equilibrium condition is determined in each increment by finding the deformation gradient tensor. The basic statement for an equilibrium condition is that the internal forces,  $I_{int}$ , and the external forces,  $P_{ext}$ , must be equal.

$$P_{ext} - I_{int} = 0 \quad 4-1$$

Generally, Newton's method is used as the numerical technique to solve non-linear equilibrium equations within each increment. In most cases, it takes more than one iteration in a single increment to determine an acceptable solution. At the end of each iteration, convergence check is performed by comparing the difference between  $P_{ext}$  and  $I_{int}$  to a specified tolerance value, which is set at 0.5% by default. In order to solve non-linear problems efficiently, a reasonable initial and maximum allowable increment size must be assigned. Large increment size might cause convergence issues while increment size that is too small will result in wastage of CPU time and memory.

#### **4.2.2 Selection of Element Type**

Selection of a suitable element type is essential in building an accurate FE model for the CRS. One of the most important factors to consider is the degrees of freedom (DOF) associated with the element, which include (but not limited to) displacement, rotations, temperature and electric potential. Second order

quadratic elements offer a greater nonlinearity capability compared to the first order linear elements, however, in the expense of CPU time and memory requirements. In addition, the boundary conditions, loading conditions and material properties have to be taken into consideration in element selection. In the case of individual internal pressure or individual tensile loading, first order linear continuum elements such as C3D8 (continuum 3D 8 nodes) are capable of providing accurate stress-strain behaviour as there is limited or no bending in these deformation modes, Figure 1(a). However, when considering a riser subjected to transverse bending, second order quadratic continuum elements such as C3D20 (continuum 3D 20 nodes) capable of providing a more accurate representation of the system, Figure 4-1.

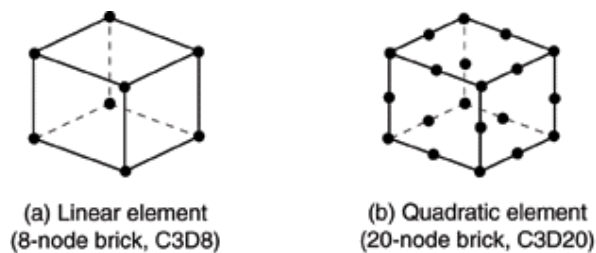


Figure 4-1, Continuum 3D brick element with 8 nodes (a) and 20 nodes (b) Use of first order linear elements may lead to shear locking which is undesirable. The use of C3D8 elements might only be feasible if at least four elements is used in the thickness direction of the riser, which sums up to longer simulation time and higher memory.

Another possibility to reduce the complexity and total number of elements needed is to use structural elements as a substitute for continuum elements. In this research, the geometry of the CRS applied onto a defective riser is essentially cylindrical shell of thin wall thickness. The ratio of the riser wall thickness to radius is equal to or less than 0.1, hence it is thus prudent to consider



shell elements such as SC8 (continuum shell 8 nodes), SC8R (continuum shell 8 nodes reduced integration) and S4R (shell 4 nodes reduced integration). Conventional shell elements such as S4R allow the shell thickness to be defined through section properties (Figure 4-2) and the number of through thickness integration point can be specified, i.e. odd number between 3 and 15 for Simpson integration and even number between 2 and 15 for Gauss integration scheme. On the other hand, the thickness of continuum shell elements must be defined through their nodal coordinates as shown in Figure 4-2. These shell elements are suitable for large strain analysis involving inelastic deformation of materials with a nonzero effective Poisson's ratio. Transverse shear deformation is also taken in account.

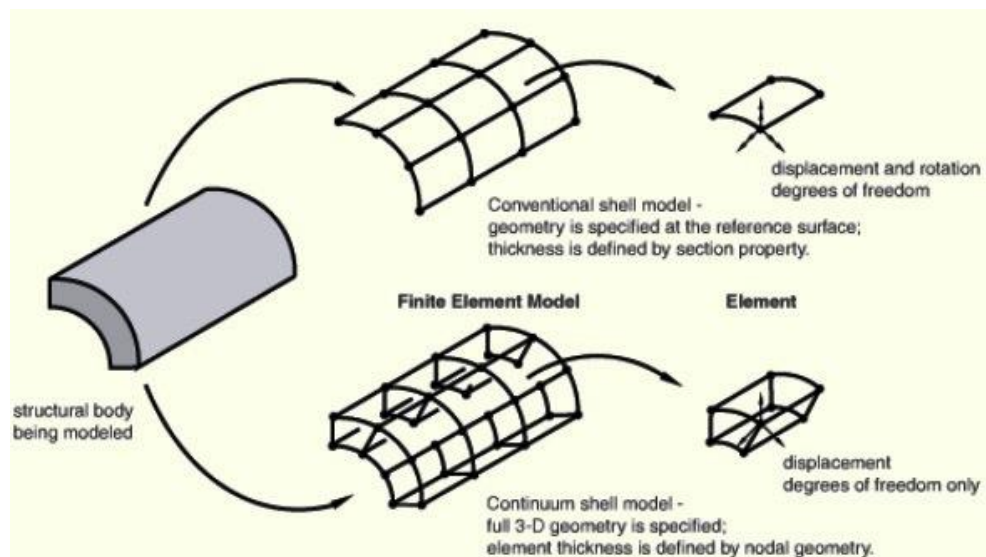


Figure 4-2, Conventional and continuum shell elements

In the work of Kim and Son (2004), the authors found that reduced integration elements could alleviate problem associated with incompressibility. Fully integrated elements tend to over-estimate the element stiffness and potentially cause volumetric 'locking' where the element has higher numbers of constraints than DOFs. In the current work, two types of reduced integration elements,

C3D8R and S4R were considered. The results from the two were compared in terms of the number of elements, CPU time, memory and accuracy of stress-strain result. Figure 4-3 and Figure 4-4 show the meshed models employing S4R elements and C3D8R elements, respectively.

For a corroded riser, the simulated hoop stress within and outside the corroded region is 462.6MPa and 213.7MPa respectively when meshed with S4R elements, while the model meshed with C3D8R elements predicted 434.8MPa and 212.4MPa. The maximum percentage difference between these two models is only 6.4%. However, the use of the C3D8R elements incurs 53% more CPU memory and 73.3% more CPU time compared to S4R elements in this quarter symmetry model. Hence S4R elements were selected to conserve simulation resources.

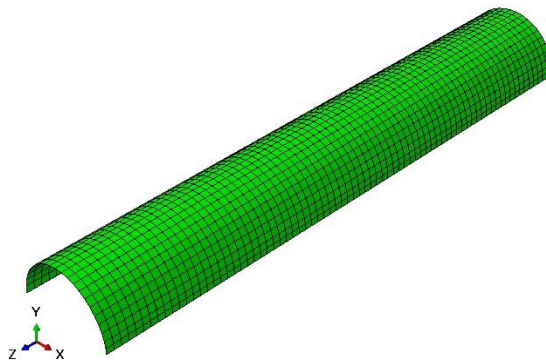


Figure 4-3, Coarse mesh with S4R element (riser 1672 elements; sleeve 1034 elements)

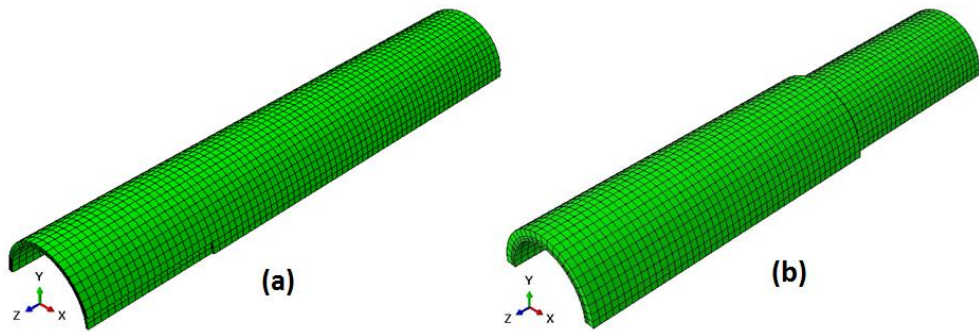


Figure 4-4, Coarse mesh with C3D8R element (riser 3458 elements; sleeve 1119 element): (a) Corroded riser, (b) Corroded riser with CRS

### 4.2.3 Mesh Refinement

The quality of the FE mesh remains one of the key factors affecting the accuracy and efficiency of a structural model. The accuracy of stress and strain on a structure highly depends on the shape and size of the meshed elements. Computer resources required to complete a simulation increase with the level of mesh refinement. Coarse meshing tends to yield inaccurate results, in particular in the area of high stress concentration. Hence, non-uniformly refined meshing technique, with high density mesh defined in region of higher stress concentration has been widely used. Localised mesh density of the CRS of pipeline was defined through partition of the geometric structure into smaller regions and bias edge seeding prior to meshing.

Mesh convergence study was conducted to investigate the appropriate level of mesh refinement. Different meshing were considered, with three level of uniform meshes (coarse, intermediate and fine mesh densities) and two biased mesh with refined density in selected areas as shown in Figure 4-3, Figure 4-5, Figure 4-6 and Figure 4-7.

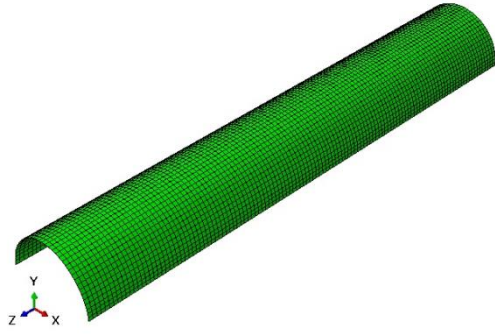


Figure 4-5, Intermediate mesh with S4R element (4305 elements)

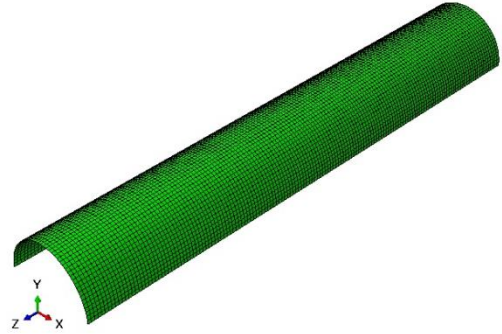


Figure 4-6, Fine mesh with S4R element (6536 elements)

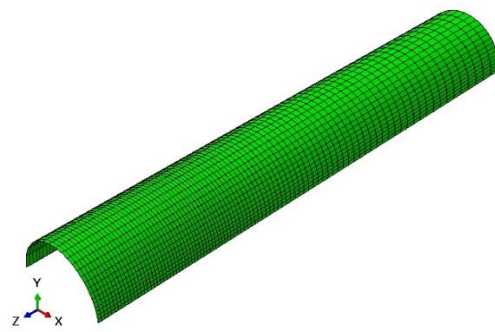


Figure 4-7, Biased mesh with gradual decrease in element size using S4R element (2046 elements)

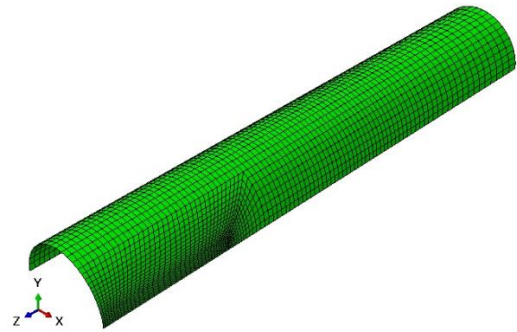


Figure 4-8, Biased mesh with fine mesh at corroded region using S4R element (2669 elements)

For the case of biased meshing, the corroded area of the riser was assigned a much finer mesh density as the region experienced the highest deformation (hence stresses) under application of external loadings. A moderate mesh density was assigned to the region of the riser being wrapped with the FRPC while coarse meshing was used in the region outside of the corroded/repaired region as it resembled the original strength of the pipeline and therefore has comparatively much lower deformation.

In the case of model meshed with C3D8R elements, mesh refinement through thickness, in the radial direction needs to be considered. It can be demonstrated

that a minimum of four C3D8R elements are required to accommodate for an acceptable accuracy in the simulation, as shown in Figure 4-9 to Figure 4-12. Higher number of elements defined through the thickness produced a better approximation in stress variation but increases the memory and computation time. The maximum and minimum hoop stresses was computed at approximately 220MPa and 204MPa at the internal and external riser surface, respectively. When the model was meshed with thin shell elements, S4R, the computed hoop stress was 212MPa, equivalent to the average of that predicted by model meshed with C3D8R elements,

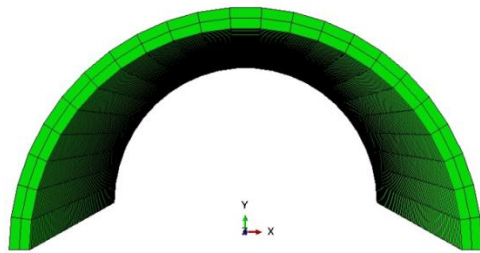


Figure 4-9, Riser model with 2 elements in thickness direction

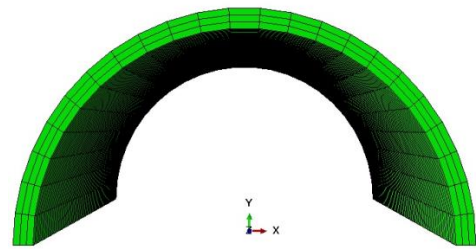


Figure 4-10, Riser model with 3 elements in thickness direction

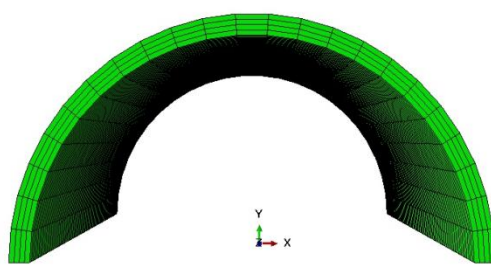


Figure 4-11, Riser model with 4 elements in thickness direction

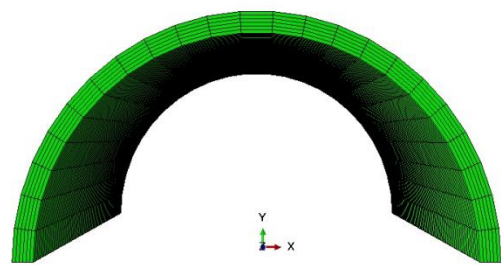


Figure 4-12, Riser model with 6 elements in thickness direction

Figure 4-13 showed the hoop stress and strain computed from models meshed with different density of S4R elements. The results demonstrated that similar level of hoop stress and strain were obtained from models meshed with coarse

meshing ( $\approx 1800$  S4R elements) and fine meshing ( $\approx 6500$  S4R elements), e.g. less than 0.1% difference in magnitude. For the FE models setup in the current work, an intermediate mesh with element characteristic length of approximately 4.6% of the riser diameter was selected.

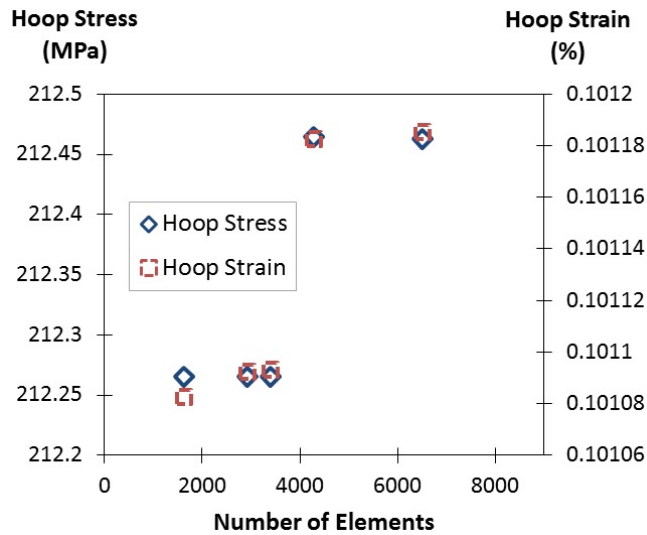


Figure 4-13, Hoop stress and hoop strain at varying S4R element mesh density

### 4.3 FEA Model of Composite Repair System

#### 4.3.1 Steel Riser

A riser system consists of multiple segments of finite length pipe members joined together to form a long slender pipe that extends from the platform above water to the seabed. In the current project, the riser is assumed to be an infinitely long pipe with only a segment of the pipe being modelled within the FEA. Hence, a local instead of global analysis was used as the main approach in this study. The values of different loadings were assumed to be independent along the length of the riser and only the most critical scenarios were considered. It should be noted that the actual presence and effects of joints were not accounted for in the present study as the current research focuses on composite repair applied on

the segment of riser without the presence of odd geometrical components. Instead, a set of artificial boundary conditions were assigned at both ends of the riser to constrain certain DOFs of the riser and this is discussed in section 4.3.4

### **4.3.2 Composite Laminate**

In the field of offshore riser repair where FRPC is used as the main strengthening material to mitigate the effect of further deterioration, the mechanical properties and behaviour of the FRPC must be accurately defined. These properties may include the young's modulus, tensile strength, compressive strength, shear strength, and Poisson's ratio for both the fibre and the matrix respectively. In addition, properties such as the interlaminar strength between adjacent laminas as well as the bond strength between the FRPC and the riser surface are also significant in determining the overall performance of the repair.

#### **4.3.2a Homogenisation of the Composite Properties**

FRPCs are made out of two main components, the reinforcing fibre and the polymer matrix. The types and compositions of the fibres and matrix affect the overall mechanical properties and bulk behaviour of the FRPC. Dedicated orientations of the fibre are often designed to produce a customised reinforcement along a certain axes of the structure. It is hence an anisotropic material and the failure mechanisms can vary vastly depending on the chosen constituent materials and design.

For unidirectional fibre reinforced polymer, the elastic moduli along the direction parallel,  $E_1$ , and transverse,  $E_2$ , to the fibre orientation can be defined through the rule of mixtures, as given in Eq. 4-2 and Eq. 4-3 respectively.

$$E_1 = E_f v_f + E_m (1 - v_f) \quad 4-2$$

$$E_2 = \frac{E_f E_m}{E_m v_f + E_f (1 - v_f)} \quad 4-3$$

where  $E_f$  and  $E_m$  are the elastic moduli of the fibre and matrix respectively and  $v_f$  is the fibre volume fraction. There are different failure criteria specifically developed and applicable for FRPCs. One of the earliest was developed by (Hashin, 1980), where three dimensional failure of unidirectional fibre composites was modelled. The Hashin failure criterion takes into account four distinctive failure modes, namely the tensile and compressive failure modes of the fibre and the matrix, is the only FRPC failure criterion that was adopted into ABAQUS general purpose finite element code. In recent years, an effort was started by (Soden PD, 1998) to assess the different failure criteria for FRPC. The exercise, referred as the “World Wide Failure Exercise (WWFE)” involved leading academics and developers of software and numerical codes specialised in predicting failure in FPRC.

In general, FRPC materials demonstrate orthotropic behaviour, where their mechanical properties vary along three mutually orthogonal axes of the structure. The 3-dimensional constitutive equation relating the stress-strain relationship of a FRPC can be simplified into the form showed in Eq. 4-4,



$$\begin{Bmatrix} \varepsilon_{11} \\ \varepsilon_{22} \\ \varepsilon_{33} \\ \gamma_{12} \\ \gamma_{13} \\ \gamma_{23} \end{Bmatrix} = \begin{bmatrix} 1/E_1 & -v_{21}/E_2 & -v_{31}/E_3 & 0 & 0 & 0 \\ -v_{12}/E_1 & 1/E_2 & -v_{32}/E_3 & 0 & 0 & 0 \\ -v_{13}/E_1 & -v_{23}/E_2 & 1/E_3 & 0 & 0 & 0 \\ 0 & 0 & 0 & 1/G_{12} & 0 & 0 \\ 0 & 0 & 0 & 0 & 1/G_{13} & 0 \\ 0 & 0 & 0 & 0 & 0 & 1/G_{23} \end{bmatrix} \cdot \begin{Bmatrix} \sigma_{11} \\ \sigma_{22} \\ \sigma_{33} \\ \sigma_{12} \\ \sigma_{13} \\ \sigma_{23} \end{Bmatrix} \quad 4-4$$

where the subscript denotes the direction of the properties as shown in Figure 4-14. Axis-1 denotes the direction parallel to the fibres while axis-2 is transverse to the fibres. Axis-3 denotes the out of plane axis.

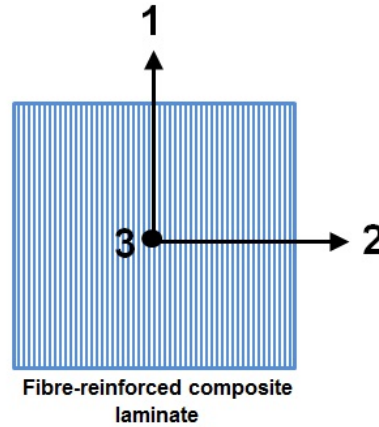


Figure 4-14, Coordinate system of FRPC

$v_{ij}$  has the interpretation of Poisson's Ratio that characterizes the transverse strain in the  $j$ -direction when the material is stressed in the  $i$ -direction.  $v_{ij}$  and  $v_{ji}$  can be related through  $v_{ij}/E_i = v_{ji}/E_j$ . As FRPC is assumed to have unidirectional fibres aligned in one direction, quasi-homogenisation of the FRPC was assumed, where the material was assumed to be transversely isotropic with the plane of isotropy being the 2-3 plane. Hence, the relationships defined in Eq. 4-5 applied.

$$E_2 = E_3 ; v_{12} = v_{13} ; G_{12} = G_{13} \quad 4-5$$

This reduces the number of elastic constants required in the constitutive equation, which can be written in the form showed in Eq. 4-6.

$$\begin{Bmatrix} \varepsilon_{11} \\ \varepsilon_{22} \\ \varepsilon_{33} \\ \gamma_{12} \\ \gamma_{13} \\ \gamma_{23} \end{Bmatrix} = \begin{bmatrix} 1/E_1 & -\nu_{12}/E_1 & -\nu_{12}/E_1 & 0 & 0 & 0 \\ -\nu_{12}/E_1 & 1/E_2 & -\nu_{23}/E_2 & 0 & 0 & 0 \\ -\nu_{12}/E_1 & -\nu_{23}/E_2 & 1/E_2 & 0 & 0 & 0 \\ 0 & 0 & 0 & 1/G_{12} & 0 & 0 \\ 0 & 0 & 0 & 0 & 1/G_{12} & 0 \\ 0 & 0 & 0 & 0 & 0 & 1/G_{23} \end{bmatrix} \cdot \begin{Bmatrix} \sigma_{11} \\ \sigma_{22} \\ \sigma_{33} \\ \sigma_{12} \\ \sigma_{13} \\ \sigma_{23} \end{Bmatrix} \quad 4-6$$

As the thickness of the composite laminate is significantly smaller than the other dimensions, i.e. length and diameter, of the composite repair and the riser, assumption of a plane stress ( $\sigma_{13} = \sigma_{23} = \sigma_{33} = 0$ ) condition was applied within the simulation model. Under this condition, Eq. 4-6 can be further simplified to the form showed in Eq. 4-7.

$$\begin{Bmatrix} \varepsilon_{11} \\ \varepsilon_{22} \\ \gamma_{12} \end{Bmatrix} = \begin{bmatrix} 1/E_1 & -\nu_{12}/E_1 & 0 \\ -\nu_{12}/E_1 & 1/E_2 & 0 \\ 0 & 0 & 1/G_{12} \end{bmatrix} \cdot \begin{Bmatrix} \sigma_{11} \\ \sigma_{22} \\ \sigma_{12} \end{Bmatrix} \quad 4-7$$

which may be reduced to a more concise form as,

$$\{\varepsilon_l\} = [S]\{\sigma_l\} \quad 4-8$$

Here [S] is known as the compliance matrix that relates the stress and strain components in the principal directions of the material. The subscript  $l$  represents the laminate coordinates. Multiplying Eq. 4-8 with  $[S]^{-1}$  yield,

$$\{\sigma_l\} = [Q]\{\varepsilon_l\} \quad 4-9$$

where  $[Q]$  is the stiffness matrix and the terms within the matrix can be defined as,

$$[Q] = \begin{bmatrix} Q_{11} & Q_{12} & 0 \\ Q_{12} & Q_{22} & 0 \\ 0 & 0 & Q_{66} \end{bmatrix} ; \quad 4-10$$

$$\text{where } Q_{11} = \frac{E_1}{1 - \nu_{12}^2 \frac{E_2}{E_1}} ; Q_{12} = \frac{\nu_{12} E_2}{1 - \nu_{12}^2 \frac{E_2}{E_1}} ; Q_{22} = \frac{E_2}{1 - \nu_{12}^2 \frac{E_2}{E_1}} ; Q_{66} = G_{12}$$

As the properties of the material benchmarked in the WWFE were measured in accordance to the failure criterion applicable to FRPC, the material parameters of the CRS as defined in the current work were extracted from those specified in WWFE.

In this study, the main objective was to assess the overall performance of the CRS in offshore applications. Thus, behaviour at a macro-level was considered. Previous studies on composite repaired pipelines subjected to internal pressure revealed that failure in the repaired region is unlikely to happen (Alexander, 2007) (Bedoya, et al., 2010). Macro-behaviour such as the bonding between the FRPC and the riser surface is one that poses more concern and should be considered in the design of composite repair. Withal, progressive failures within the FRPC itself such as matrix cracking, fibre breakage or fibre pull-out are not the significant modes of failure of the CRS.

#### 4.3.2b Multi-continuum Theory (MCT) Failure Criteria

A user defined material, characterized using the multi-continuum theory (MCT) was used in the FE model to assess the condition of the FRPC under the assigned loads. This micromechanics-based theory obeys the fundamental of continuum

mechanics whereby any physical quantity of interest can be evaluated at a material point by averaging the quantity over a representative volume that surrounds the point of interest. For unidirectional FRPC, it is assumed that a representative volume element (RVE) is large enough to contain numerous fibres and an accurate representation can be averaged over the RVE. In short, two constituents (fibre and matrix) co-exist in an RVE.

The first material model for the FRPC which utilizes input parameters of the composite's lamina mechanical properties does not take into account the response beyond the elastic region. Hence, failure of the FRPC could not be taken into account. In order to determine the degree of stress transferred from the corroded riser to the FRPC, the MCT failure criterion of the FRPC were implemented through a user-defined material in a separate material model within the FEA. The advantage of using a MCT failure criterion over traditional FE approach to FRPC is that various modes of failure can be determined. The MCT separates the matrix and fibre properties, handling each composite constituent differently and allows failure to progress through a multi-step damage mechanism. Within the FE model, the MCT code decomposes the stress-strain fields of the laminate down to fibre and matrix constituent level stress-strain fields. The fibre and matrix constituents can then be evaluated based on these constituent stress-strain fields using individual failure criteria for the fibre and matrix constituents respectively.

In this study, the MCT failure criterion was implemented into the ABAQUS model through Autodesk® *Simulation Composite Analysis* plug-in. Figure 4-15 and Figure 4-16 showed the material manager along with the defined materials constants.

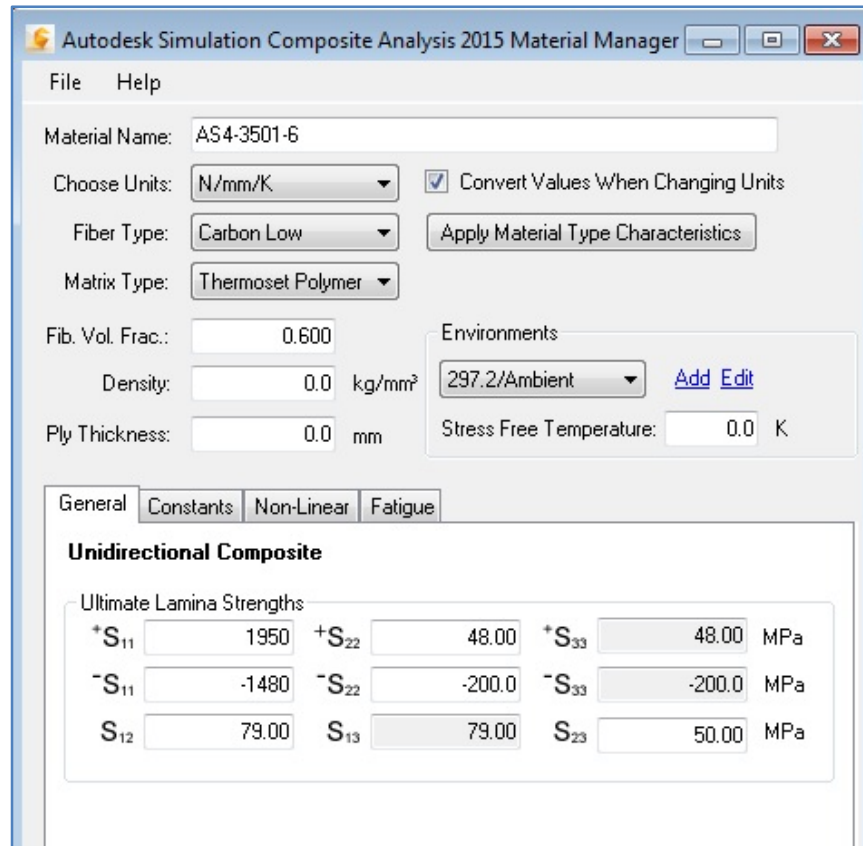


Figure 4-15, AS4/3501-6 carbon/epoxy unidirectional lamina strength properties on Autodesk® *Simulation Composite Analysis*

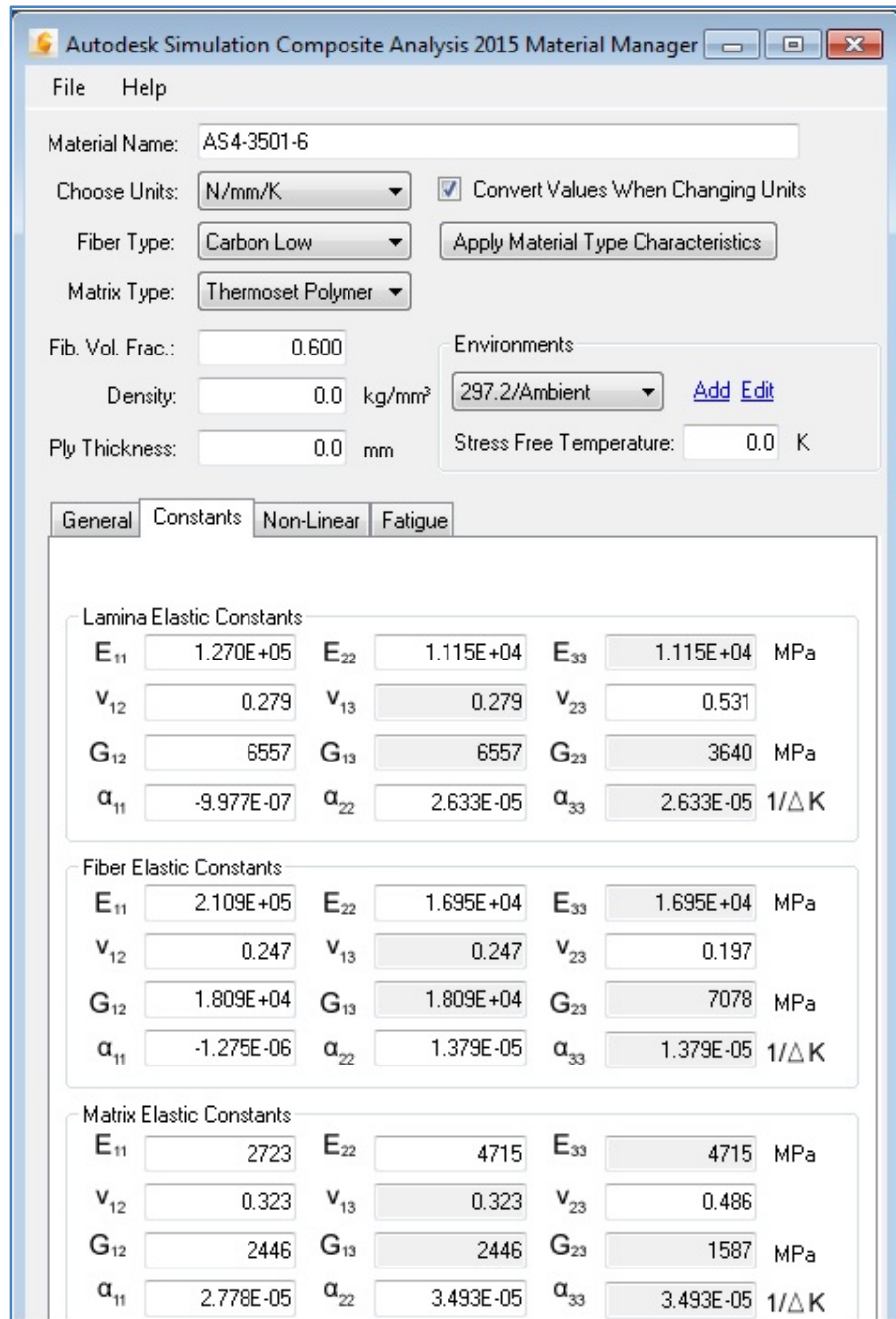


Figure 4-16, AS4/3501-6 carbon/epoxy unidirectional lamina and constituent properties on Autodesk® *Simulation Composite Analysis*

### 4.3.2c Bonding between Composite and Steel Riser Surface

The effectiveness of the CRS is highly dependent on the adhesion between the composite and the steel riser. In real life, variation in material types, curing conditions, installation procedures and techniques tend to result in varying

degrees of localised defects such as micro-voids between the riser and the FPRC where less than perfect bonding is observed. If large disbands appear at the bonding interface, anomaly in the stress distribution would appear and the stress transfer from the steel riser to the composite decreases. To provide a good adhesion between the two materials, surface preparation prior to the installation of the composite material must be observed. The removal of contaminants and surface cleaning can be done by hand or power tools. Australian standard series AS1626 titled “Metal Finishing-Preparation and Pretreatment of Surfaces” provide ten possible methods for surface preparation (MT/9, 1997). One of the surface preparation techniques that utilises high power tool is grit blasting. This technique uses high speed of abrasion particles under compressed air stream to remove unwanted contaminants such as rust from the steel surface. Water jetting is more advantageous as the use of water in replacement of abrasive particles produce less dust. The ideal surface preparation is a NACE No.2/SSPC-SP10, near white metal, blast cleaning, where a surface profile of 63-101 microns is desired (NACE/SSPC, 2006). Taking into account the importance of surface bonding, sensitivity and highly flammable environment, water jet is the most suitable method for surface preparation for rehabilitation of offshore risers. As qualitative and quantitative characterisation of the surface finishing is not included in the current research project, a perfect bonding was assumed within the FEA model. In a separate model, the bonding between the two surfaces was characterised by fracture mechanics in order to study the integrity of the bond at the interface.

### 4.3.3 Materials

#### 4.3.3a Riser Materials

In the oil and gas industry, pipeline are typically selected from a range of welded or seamless carbon steel materials that are standardised by the American Petroleum Institute pipe specification, API 5L. In a Petrobras project involving the design and installation of a SCR in the Marlim Field floating production system, API 5L X60 grade steel pipe was used (Serta, et al., 1996). When there is no significant yield point in the stress-strain behaviour of the material, the stress-strain relationship can be defined using the Ramberg-Osgood model (Eq. 4-11). In the work of (Walker & Williams, 1995) , the model shown in Figure 4-17 was found capable of representing the relationship accurately.

$$E_p \varepsilon = \sigma + \alpha \left( \frac{|\sigma|}{\sigma^0} \right)^{n-1} \quad 4-11$$

where  $E_p$  is the Young's modulus of the steel pipe,  $\varepsilon$  and  $\sigma$  are the nominal strain and stress respectively,  $\alpha$  is the Ramberg-Osgood's model yield offset constant,  $n$  is the hardening exponent and  $\sigma^0$  is the yield stress. The parameters showed in Table 4-1 were extracted from tests run by Ruggieri and Dotta in their work where numerical modelling of crack growth in high pressure pipeline steels was studied (Ruggieri & Fernando, 2011).



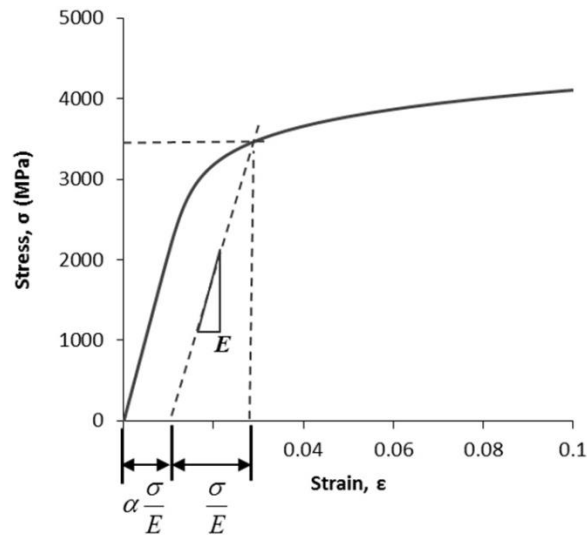


Figure 4-17, Ramberg-Osgood model

Table 4-1, Mechanical properties of API 5L X60 steel pipe

Parameter	Value
Young's Modulus, $E$ [GPa]	210
Poisson's Ratio, $\nu_{12}$	0.3
Yield Stress, $\sigma^o$ [MPa]	483
Ramberg-Osgood's Model Yield Offset, $\alpha$	1
Hardening Exponent in Ramberg-Osgood's Model, $n$	12

#### 4.3.3b FRPC Materials

Carbon and E-glass fibres epoxy composites are the most common FRPC materials used in structural applications. The specific materials chosen for the current study are AS4 (3501-6) carbon/epoxy prepreg and 21xK43 Gevetex (LY556/ HT917/ DY063) E-glass/epoxy composites. The material properties of these composite systems were taken from those used as a benchmark in the WWFE (Soden, et al., 1998). The WWFE has been jointly produced among researches from different institutes and organisations with the aim of closing the

knowledge gap between theoreticians and design practitioners in the field of predicting failure response of FRPC laminates, and thus providing a robust reference for failure criterion of FRPC (Hinton, et al., 2004). The mechanical properties of the selected materials were determined from extensive experiments, where different specimens were fabricated and tested (Soden, et al., 1998). The main properties required as input data for definition of the FRPC laminate repair within the FE model are summarised in Table 4-2.

Table 4-2, Material properties of the chosen FRPC laminate

	<b>AS4</b>	<b>E-glass 21xK43</b>
<b>Fibre type</b>	<b>Carbon</b>	<b>Gevetex</b>
<b>Matrix</b>	3501-6 epoxy	LY556/HT907/DY063 epoxy
<b>Manufacturer</b>	Hercules	DLR
<b>Fibre volume fraction, <math>V_f</math></b>	0.6	0.62
<b>Longitudinal modulus, <math>E_1</math> (GPa)</b>	126	53.48
<b>Transverse modulus, <math>E_2</math> (GPa)</b>	11	17.7
<b>In-plane shear modulus, <math>G_{12}</math> (GPa)</b>	6.6	5.83
<b>Major Poisson's ratio, <math>\nu_{12}</math></b>	0.28	0.278
<b>Through thickness Poisson's ratio, <math>\nu_{23}</math></b>	0.4	0.4
<b>Longitudinal tensile strength, <math>X^T_1</math> (MPa)</b>	1950	1140
<b>Longitudinal compressive strength, <math>X^C_1</math> (MPa)</b>	1480	570
<b>Transverse tensile strength, <math>X^T_2</math> (MPa)</b>	48	35
<b>Transverse compressive strength, <math>X^C_2</math> (MPa)</b>	200	114
<b>In-plane shear strength, <math>S_{12}</math> (MPa)</b>	79	72
<b>Longitudinal tensile failure strain, <math>\mathcal{E}^T_1</math> (%)</b>	1.38	2.132
<b>Longitudinal compressive failure strain, <math>\mathcal{E}^C_1</math> (%)</b>	1.175	1.065
<b>Transverse tensile failure strain, <math>\mathcal{E}^T_2</math> (%)</b>	0.436	0.197
<b>Transverse compressive failure strain, <math>\mathcal{E}^C_2</math> (%)</b>	2	0.644
<b>In-plane shear failure strain, <math>\mathcal{E}_{12u}</math> (%)</b>	2	3.8

#### 4.3.4 Boundary Conditions

Proper boundary conditions must be assigned to the FE model to prevent fictitious stress concentration and to ensure that the behaviour of the riser and composite repair can be accurately captured. Owing to the symmetrical geometry of the corroded riser pipe and boundary/loading conditions, the model can be effectively simplified as a quarter symmetry structure, as shown in Figure 4-18. If on-axis (i.e. axial or hoop orientated) composite laminates are used, both the corroded riser and composite wrap can be modelled as a quarter cylinder (i.e. half in length and half in circumference) with reflective symmetry boundary conditions. When off-axis composite laminates are included, the reflective symmetry conditions are not applicable and a full cylinder must be modelled. The current approach is similar to that used in (Li & Reid, 1992) study on the symmetry condition of laminated fibre reinforced composite structures. The free end of the riser model is allowed to expand in the radial direction and axial direction so that uniform hoop and tensile stress can be observed.

For the transverse bending, a four point bending setup was utilised such that the entire extent of the repaired region is exposed to the maximum bending moment. As the bent riser will be subjected to tension at the top surface and compression at the bottom surface, a full cylinder was modelled to ensure that such behaviour can be accurately captured (Figure 4-19). The ends of the riser model are constrained such that the translational movement in the X and Y directions are not allowed. Rotation about the Z-axis is also constrained.

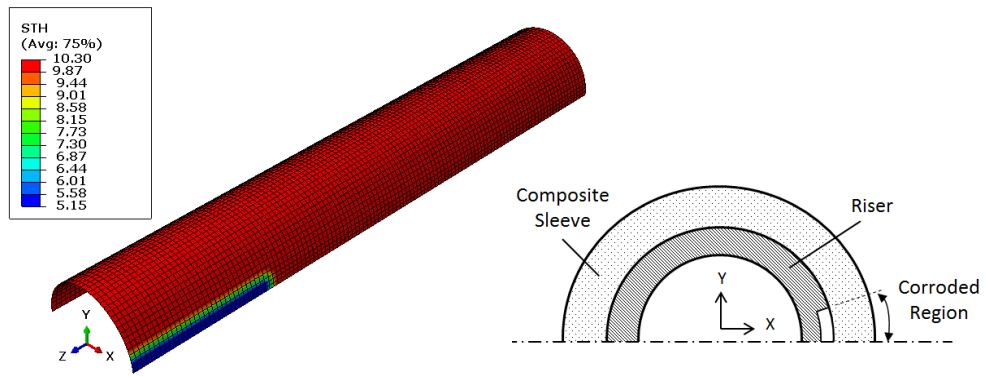


Figure 4-18, Quarter pipe model with cross sectional view

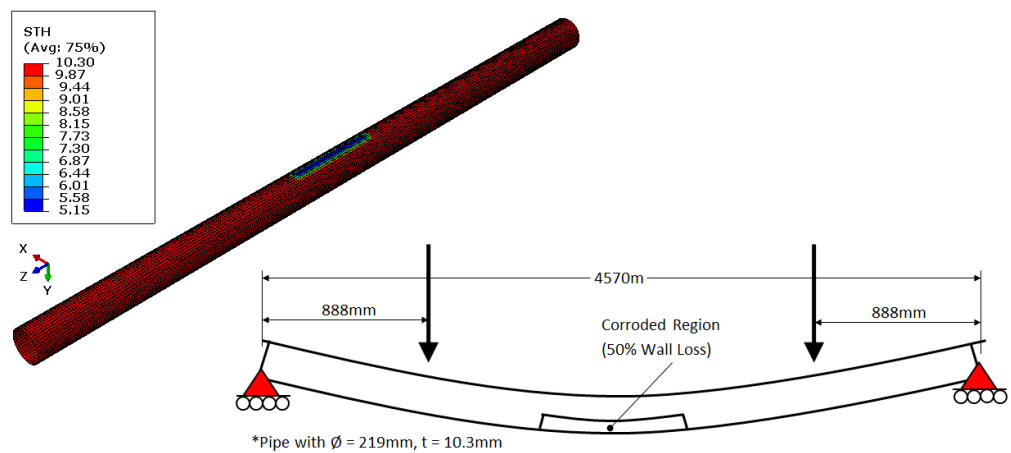


Figure 4-19, Full pipe model in four-point bending setup

### 4.3.5 Interaction Properties

#### 4.3.5a Riser-CRS Surface-to-Surface Interaction Properties

In ABAQUS standard, the contact behaviour between two instances in an assembly can be defined by specifying an appropriate interaction property (normal and tangential) between the surface-to-surface contacts. The default normal interaction property is a “hard” overpressure closure which minimizes the penetration of the slave surface into the master surface. The master surface is usually the stiffer one while the slave surface is the softer one, which in this case are respectively the steel pipe and composite laminate. In the case of the

tangential interaction, the contact is governed by a standard coulomb friction model. The model assumes that there is no relative motion between two contacting surfaces when the equivalent frictional stress,  $\tau_{eq}$  is less than or equal to the critical stress,  $\tau_{crit}$ , Eq. 4–12.

$$\tau_{eq} \leq \tau_{crit} \quad 4-12$$

where  $\tau_{crit}$  is proportional to the contact pressure, as in Eq. 4–13.

$$\tau_{crit} = \mu P_{cont} \quad 4-13$$

while  $\mu$  is the friction coefficient and  $P_{cont}$  represents the contact pressure. For the purpose of the current study, the riser and composite laminate was assumed to establish a perfect bonding and the steel-composite interface was characterised through a ‘rough’ tangential friction formulation within the FE model, which is the ideal condition for stress transfer. However, variation in material types, installation techniques and parameters tend to result in localised micro-voids between surface interfaces of the repair (i.e. between the riser-FRPC and between FRPC laminates) where less than perfect bonding is often observed. With the characterised ‘rough’ tangential contact, the friction coefficient,  $\mu$ , in Eq. 4–13 has a value of infinity which resulted in zero sliding motion between the two surfaces once they come into contact.

Alternatively, a tie constraint can be used to define the bond between the steel riser and the FRPC laminate. Tie constraint is a surface-based constraint that limits the motion of the node on the slave surface to the node on the master surface to which it is closest. The outer surface of the steel riser could be assigned as the master surface while the inner surface of the FRPC could be assigned as

the slave surface. The tie constraint makes the translational and rotational motion as well as other active DOF equal for the pair of surfaces.

#### 4.3.5b Interaction Properties using Fracture Mechanics

In order to study the integrity of the bond between adjacent plies as well as those at the steel-composite interface, fracture mechanics was employed in the characterization of these bonds. The fracture between the adjacent FRPC plies is known as delamination while the fracture between the FRPC and steel riser is known as disbonding. The interlaminar and steel-composite bond strengths can be characterized by their relative energy release rates, which is the energy require to extend the “crack” per unit length.

Since corroded riser with a CRS often subjected to combined loadings in the hoop, longitudinal and transverse directions, mixed mode behaviour is assumed. The Benzeggagh and Kenane (BK) fracture criterion is used to determine the *critical equivalent strain energy release rate*,  $G_{equivC}$ . The relationship between the mode I (tensile), II (in-plane shear) and III (out-of-plane shear) energy release rate and  $G_{equivC}$  is given in Eq. 4–14.

$$G_{equivC} = G_{IC} + (G_{IIC} - G_{IC}) \left( \frac{G_{II} + G_{III}}{G_I + G_{II} + G_{III}} \right)^\eta \quad 4-14$$

When the system is subjected to the combined loadings, the  $G_{IC}$ ,  $G_{IIC}$ ,  $G_{IIC}$  and  $G_I$ ,  $G_{II}$ ,  $G_{III}$  represent the critical energy release rate and energy release rate in mode I, II and III respectively. The values of  $G_{IC}$ ,  $G_{IIC}$  and  $G_{IIC}$  for interlaminar level of composite material were taken from (Liao & Sun, 1996) where these values were determined experimentally through the implementation of a new analytical series solution for AS4 (3501-6 C/E). In the case of steel-composite

interface, the values were obtained from (Andre & Linghoff, 2009), in which the  $G_{IC}$ ,  $G_{IIC}$  and  $G_{IIIC}$  were determined experimentally via double-cantilever beam (DCB) and end-notch flexure (ENF) tests. The corresponding values are listed in Table 4-3.

Table 4-3, Fracture and fatigue properties

		Steel-Composite Interface	Composite Laminate Inter-layer
Fracture Toughness, $G_c$ (N/m)	Mode I	1070	94.44
	Mode II	3644	661.11
	Mode III	3644	850
Fatigue Constants	C1	0.5	0.21164
	C2	-0.1	-6.25
	C3	$7.03226 \times 10^{-12}$	0.33
	C4	4.6	5.55

The virtual crack closure technique (VCCT) criterion is selected as it is suitable for modelling disbonding at the steel-composite interface and delamination in the laminated composite where failure criteria is highly dependent on the mixed-mode ratio. This criterion was used in the static loading case for combined loadings of  $P_{in}$ ,  $F_t$  and  $M_b$  in order to determine the limiting bending load that causes catastrophic failure of the corroded riser repaired with FRPC. The crack-tip node debonds when the fracture criterion,  $f_{criterion}$ , reaches a value of 1.0.

$$f_{criterion} = \frac{G_{equiv}}{G_{equivC}} \quad 4-15$$

where  $G_{equiv}$  is the equivalent strain energy release rate and  $G_{equivC}$  can be determined from Eq. 4-14.

## **4.4 Validation of Numerical Model**

It is important to show that the developed numerical model is accurate enough to be used in the optimisation of the CRS for offshore risers. In general, there are two methods that can be used to validate the results obtained from FE model. The first method uses classical mechanics solutions to obtain the stress and strain values at identical loading conditions and compare the values with those obtained in the FE model. However, these analytical solutions are often built on several assumptions where factors that would affect the results in a real-life scenario are omitted.

The second method employs experimental validation is a much favourable method as a lot of assumptions were made in the derivation of classical mechanics equations. The drawback of experimental validation is the resources and cost involved in preparing and running the tests.

The robustness of the developed FE model was further validated through a case study conducted to evaluate the burst resistant of an industrial carbon fibre reinforced polyethylene strip pipeline repair system. The composite repair system, known as the Helicoid Epoxy Sleeve (HES)<sup>TM</sup> is a commercially available solution designed and developed by Merit Technologies Sdn Bhd. The results obtained through the numerical model and limit analysis were compared to those obtained from a full-scale burst test.

### **4.4.1 Classical Mechanics**

The most fundamental numerical model is one where a bare steel riser is subjected to a single individual loading, i.e. internal pressure. The API 5L X60 steel riser model has a radius,  $r$ , and wall thickness,  $t$ , of 109.5mm and 10.3mm



respectively, giving a  $r/t$  ratio of more than 10. Hence, thin wall assumption was used and the hoop stress can be defined as,

$$\sigma_h = \frac{P_{int} r_p}{t_p}$$

4-16

When the composite repair is applied onto a corroded riser, the strength of the repaired riser in resisting the hoop load can be taken as the sum of the strength in the FRPC laminate and the remaining strength of the corroded riser, as in Eq. 4-17. This relation assumes perfect load transfer from the corroded steel riser to the FRPC laminate.

$$P_{int} = \left[ \frac{\sigma_{h,steel} \cdot t_{corroded}}{r_{steel}} \right] + \left[ \frac{\sigma_{h,comp} \cdot t_{comp}}{r_{comp}} \right] \quad 4-17$$

where  $P_{int}$  is the applied internal pressure,  $\sigma_h$  is the hoop stress,  $t$  is the wall thickness and  $r$  is the radius. The subscripts ‘*corroded*’, ‘*steel*’ and ‘*comp*’ symbolises the corroded section of the pipe, the steel riser and the composite repair respectively. The estimate of hoop stress on the FRPC can be calculated through Eq. 4-18,

$$\sigma_{h,comp} = \frac{P \cdot D}{2t_{comp} \left( 1 + \frac{E_{steel} \cdot t_{corroded}}{E_{comp} \cdot t_{comp}} \right)} \quad 4-18$$

Through Eq. 4-17 and Eq. 4-18, the hoop stress and strain can be calculated and compared to those extracted from the FE model. The output is tabulated in Table 4-4. It can be noted that the discrepancies are minimal. The hoop stresses of the corroded steel riser beneath the composite repair computed through the numerical model and classical mechanics method show reduction by 63.3% and

60.6% respectively compared to the corroded riser without any repair. The results demonstrated that the developed numerical model can sufficiently predict the stress-strain behaviour of the CRS.

Table 4-4, Comparison between classical mechanics and numerical results

		<b>Numerical Model</b>	<b>Classical Mechanics</b>	<b>Percentage Difference (%)</b>
<b>Bare Riser without Corrosion</b>	$\sigma_{h,steel}$ (MPa)	212.462	212.621	0.075
<b>Bare Riser with Corrosion</b>	$\sigma_{h,steel}$ (MPa)	426.606	425.243	0.319
<b>Corroded Riser with CRS</b>	$\sigma_{h,steel}$ (MPa)	156.656	167.846	7.143
	$\sigma_{h,comp}$ (MPa)	92.1965	91.387	0.878

#### 4.4.2 Case study of Helicoid Epoxy Sleeve (HES)<sup>TM</sup>

An experimental burst strength analysis was conducted on the simulated corroded steel pipe repaired with CRS constitutes of carbon fibre strip and epoxy grout, known as the HES<sup>TM</sup> system, to validate the viability of the repair under a predefined level of hydrostatic loading (internal pressure), Figure 4-20.

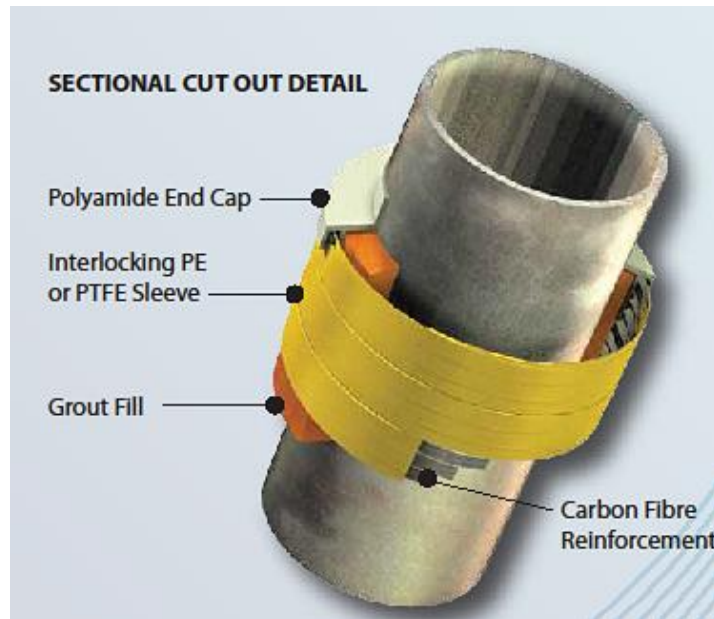


Figure 4-20, Sectional cut out detail of the Helicoid Epoxy Sleeve System (HES)<sup>TM</sup> system (Merit Technologies Sdn. Bhd., Malaysia)

API 5L X52 grade steel pipe with dimensions of 219mm outer diameter × 12.7mm wall thickness × 3000mm length was machined with a 50% material loss in its wall thickness to simulate external corrosion defect that the pipe suffers when exposed to excessive detrimental environmental conditions. A corresponding FE model was developed for evaluation of the HES<sup>TM</sup> pipeline rehabilitation system. Experiment conducted on an industrial based CRS served to provides a reliable measurement and reference for evaluating the accuracy of the developed FEA code against industrial design standards.

#### 4.4.2a Calculations of the Hydrostatic & Burst Pressure Based on Industrial Design Standards

As the application of the HES<sup>TM</sup> system focuses on integration into offshore risers, the burst pressure,  $P_b$ , of the API 5L grade X52 steel pipe can be calculated through Eq. 4-19, which is found in the ‘Stress criteria for metallic risers,

chapter 2, section 3' of the American Bureau of Shipping (ABS) standard, Guide for Building and Classing Subsea Riser System (ABS, 2006).

$$P_b = 0.90(SMYS + SMTS) \left( \frac{t_p}{D_o - t_p} \right) \quad 4-19$$

where  $P_b$  = burst pressure,  $SMYS$  = specified minimum yield strength,  $SMTS$  = specified minimum tensile strength,  $t_p$  = nominal wall thickness and  $D_o$  = outer diameter of the pipe. According to API RP 1111 (API, 1999), the hydrostatic pressure,  $P_t$ , can be calculated by multiplying the burst pressure with a few design and derating factors, as shown in Eq. 4–20.

$$P_t = f_d f_t P_b \quad 4-20$$

The design factor,  $f_d$  is 0.75 for risers while the temperature derating factor,  $f_t$  is taken as 1.0 in the condition when the temperature is less than 121°C. The same equations, Eq. 4–19 and Eq. 4–20 can be used to calculate the corresponding pressure values for the corroded X52 steel pipe by reducing the wall thickness accordingly.

#### 4.4.2b Recommended size of the CRS

The minimum required composite laminate thickness,  $t_{repair}$ , can be determined based on the Appendix III Short-Term Pipe Spool Survival Test of the ASME PCC-2 – Repair of Pressure Equipment and Piping, Article 4.1, Non-Metallic Composite Repair Systems for Pipelines and Pipework: High Risk Application (ASME, 2008), as in Eq. 4–21.

$$t_{repair} = \frac{1}{S_c} \cdot \left( \frac{P_d D_o}{2} - SMYS \cdot t_s \right) \quad 4-21$$

where  $D_o$  = external pipe diameter,  $SMYS$  = specified minimum yield strength of the pipe,  $S_c$  = tensile strength of carbon fibre strip and  $t_s$  = remaining wall thickness at defect region of the pipe. According to the segmentation of different pressure values given in the API RP 1111 (API, 1999), the design pressure,  $P_d$ , can be taken as 0.8 times of the hydrostatic test pressure and the  $t_{repair}$  is determined to be 1.08 mm, i.e. a minimum of 2 layers of the carbon fibre reinforced PE strip, each of which having a thickness of 0.8 mm will be required.

A sufficient composite-pipe adhesion surface is required for adequate load transfer from the pipe to the CRS to prevent delamination at the surface interface. The total axial length of the repair required to ensure an effective pipe rehabilitation can be computed from Eq. 4-22.

$$L_{total} = 2 \times L_{grout} + L_d \quad 4-22$$

where  $L_{grout}$  is the grout length of the epoxy grout extending at each ends of the defect and  $L_d$  is the axial length of the defect. The  $L_{grout}$  can be computed using Eq. 4-23 and is based on the lap shear strength of the epoxy grout to steel,  $\tau_{grout}$ , which can be measured based on ASTM D3165 (ASTM, 2008).

$$L_{grout} = \frac{2F_{eff}}{\pi\tau_{grout}D_o} \times SF \quad 4-23$$

where  $F_{eff}$  is the effective tensile force acting on the steel pipe due to the welded end caps. A safety factor,  $SF$ , of 3 was employed in the calculation of the  $L_{grout}$  to account for the long term degradation of the adhesive strength.

#### 4.4.2c Experimental Setup

API 5L grade X52 steel pipe with dimensions of 219 mm OD, 12.7 mm WT and 3000 mm L was supplied by Sumimoto Metal Industries Ltd., Japan. Both ends of the pipe were welded with adequate strength plates and non-destructive testing was carried out to ensure the quality of the weld. A metal loss equivalent to 50% original wall thickness was machined onto the external surface of the pipe to simulate the corrosion defect. The total axial length of the defect is 622 mm and over the full circumference of the pipe. Prior to installation of the HES™ system, surface preparation was conducted by abrasive blasting to a minimum standard of SA 2.5 and a minimum surface profile of 70 microns. The abrasive blasting was extended to 25 mm over the length of the repair zone at both ends. During installation of the HES™ system, the carbon fibre reinforced PE strip was wound around the pipe, forming an annulus of 25 mm between the strip and the pipe. Polyamide end caps were placed at both ends of the sleeve to prevent leakage prior to the injection of the epoxy grout. The full setup of the HES™ system on the pipe is shown in Figure 4-21. The HC68 epoxy grout with filler is allowed to cure for 21 days. The internal pressure was applied at a rate of 0.05 MPa/s and hold for 10 minutes at both design pressure and hydrostatic pressure respectively before increasing the pressure to a level where bursting of the repaired pipe occurred.



Figure 4-21, API 5L grade X52 steel pipe with Helicoid Epoxy Sleeve™ system installed

#### 4.4.2d Numerical Modelling

FE model of the pipe and the HES™ system were developed within ABAQUS® v6.11-3. The pipe was meshed with a total of 3900 S4R elements. The HES™ system was separated into two parts within the model, (i) the epoxy grout contacting the external surface of the corroded portion of the pipe and (ii) the carbon fibre reinforced PE strip enclosed the epoxy grout. This is an idealization of the HES™ system where perfect bonding is assumed between the epoxy grout-steel pipe and the epoxy grout-carbon fibre strip surface interfaces. This assumption omits defects such as micro-voids at the interfaces of the repair which can arise due to variation in material types, installation techniques and curing process. In this study curing of the epoxy grout was conducted under a controlled environment to ensure uniform bonding between the parts. The epoxy grout was modeled using solid elements as the wall thickness to radius ratio,  $t/r$ , is over 0.1. It was meshed with a total of 3900 reduced integration, eight nodes linear brick elements, C3D8R while the carbon fibre reinforced PE strip was meshed with a total of 1596 S4R elements. The individual meshed parts of the

pipe, epoxy grout and carbon fibre reinforced PE strip, along with the assembled model are shown in Figure 4-22.

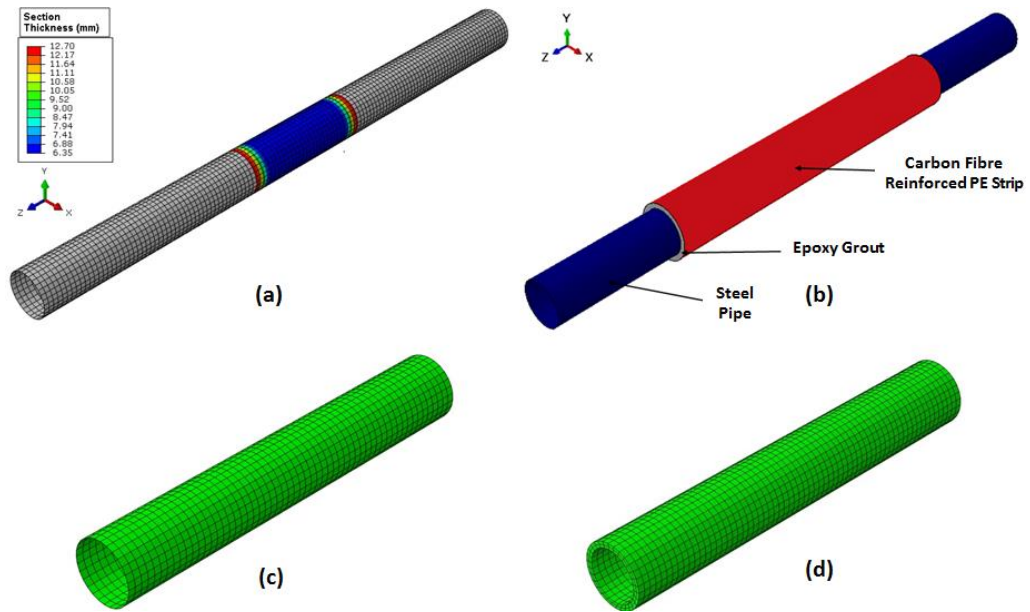


Figure 4-22, Meshed parts: (a) API 5L grade X52 pipe with corroded section, (b) corroded pipe with HES™, (c) carbon fibre-reinforced PE strip, and (d) epoxy grout

The stress-strain relationship of the API 5L grade X52 steel pipe was defined using Ramberg-Osgood material model, Eq. 4-24, as this model was found capable of representing the relationship accurately.

$$E\varepsilon = \sigma + \alpha \left( \frac{|\sigma|}{\sigma_y} \right)^{n-1} \quad 4-24$$

where  $E$  = Young's modulus,  $\varepsilon$  = strain,  $\sigma$  = stress,  $\alpha$  = yield offset factor,  $n$  = hardening exponent and  $\sigma_y$  = yield stress of the steel pipe. The model parameters, shown in Table 4-5, were extracted from (Ruggieri & Fernando, 2011) where crack growth in high pressure pipeline was numerically modelled.



Table 4-5, Mechanical Properties of API 5L X52 Steel

Parameter	Value
Young's Modulus, $E$ [GPa]	210
Poisson's Ratio, $\nu$	0.3
Yield Stress, $\sigma_y$ [MPa]	358.5
Ramberg-Osgood's Model Yield Offset, $\alpha$	1
Hardening Exponent in Ramberg-Osgood's Model, $n$	12

The epoxy grout was modelled as an isotropic material with its Young's modulus taken from measured data. Lamina properties were assigned to the carbon fibre reinforced PE strip. The stress-strain relation of the lamina can be defined through Eq. 4-25,

$$\begin{Bmatrix} \varepsilon_1 \\ \varepsilon_2 \\ \gamma_{12} \end{Bmatrix} = \begin{bmatrix} 1/E_1 & -\nu_{12}/E_1 & 0 \\ -\nu_{12}/E_1 & 1/E_2 & 0 \\ 0 & 0 & 1/G_{12} \end{bmatrix} \cdot \begin{Bmatrix} \sigma_{11} \\ \sigma_{22} \\ \sigma_{33} \end{Bmatrix} \quad 4-25$$

The longitudinal modulus was taken from those measured experimentally while the transverse modulus was assumed to be one-tenth of the longitudinal modulus. Based on the rule of mixture for unidirectional fibre-reinforced composite laminate, the transverse modulus is always lower than the longitudinal modulus. Mallick demonstrated that the normalised modulus of a fibre-reinforced composite at  $90^\circ$  is approximately 10 times lower in magnitude than the normalised modulus at  $0^\circ$ , as shown in Figure 4-23 (Mallick, 2007).

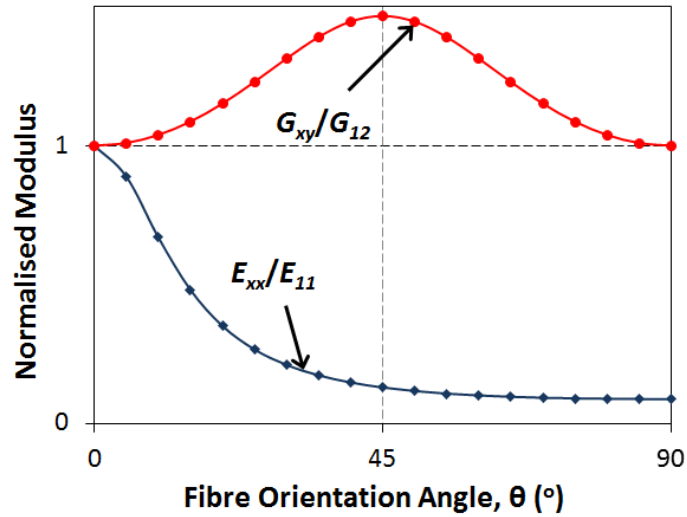


Figure 4-23, Normalised modulus of fibre-reinforced composite at varying angle

As showed in Figure 4-20, the carbon fibre reinforced PE strip was wound around the pipe at a helical angle that is approximately  $90^\circ$  to its longitudinal axis such that the rehabilitation provides maximum hoop reinforcement against internal pressure. Within the FE model, the composite strip was modelled in such a way that the fibres are aligned in the hoop direction. This can be achieved using a transformation matrix,  $T$ , shown in Eq. 4-26 to rotate the material orientation into the hoop direction. Material properties for the epoxy grout and composite strip are shown in

Table 4-6.

$$[T] = \begin{bmatrix} \cos^2 \theta & \sin^2 \theta & 2 \sin \theta \cos \theta \\ \sin^2 \theta & \cos^2 \theta & -2 \sin \theta \cos \theta \\ -\sin \theta \cos \theta & \sin \theta \cos \theta & \cos^2 \theta - \sin^2 \theta \end{bmatrix} \quad 4-26$$

Table 4-6, Material properties of epoxy grout and carbon fibre-reinforced PE strip

Parameter	Value
<i>Carbon Fibre Reinforced Polyethylene Strip</i>	
Longitudinal Modulus, $E_1$ [GPa]	141
Transverse Modulus, $E_2$ [GPa]	14.1
In-Plane Shear Modulus, $G_{12}$ [MPa]	75.46
Major Poisson's Ratio, $\nu_{12}$	0.34
Longitudinal Tensile Strength, $X_T$ [MPa]	1880
<i>Epoxy Grout</i>	
Young's Modulus, $E$ [GPa]	8.951
Poisson's Ratio, $\nu_{12}$	0.24

#### 4.4.2e Results and discussion

##### *Numerical Analysis*

The main output of the FEA required for the computation of burst pressure and design pressure through Double Elastic Slope method is the hoop strain. Figure 4-24 depicts the hoop strain of the corroded X52 steel pipe. The computations of the plastic analysis collapse load, PACL (burst pressure) and design pressure for all three cases, (1) Uncorroded pipe; (2) Corroded pipe and (3) Corroded pipe repaired with HES<sup>TM</sup> system are shown in Figure 4-25, Figure 4-26 and Figure 4-27 respectively. The computed design pressure for an uncorroded bare pipe is 25.2 MPa. At this design pressure, the maximum allowable hoop strain,  $\epsilon_{h,max}$  is 0.211%, as shown by the vertical dotted line in Figure 4-25. From Figure 4-26, it is apparent that the corroded riser can no longer function under normal operating conditions as the design pressure is only 12.6 MPa which is half of an uncorroded pipe. At 25.2 MPa, the hoop strain on the corroded pipe has exceeded the maximum allowable hoop strain.

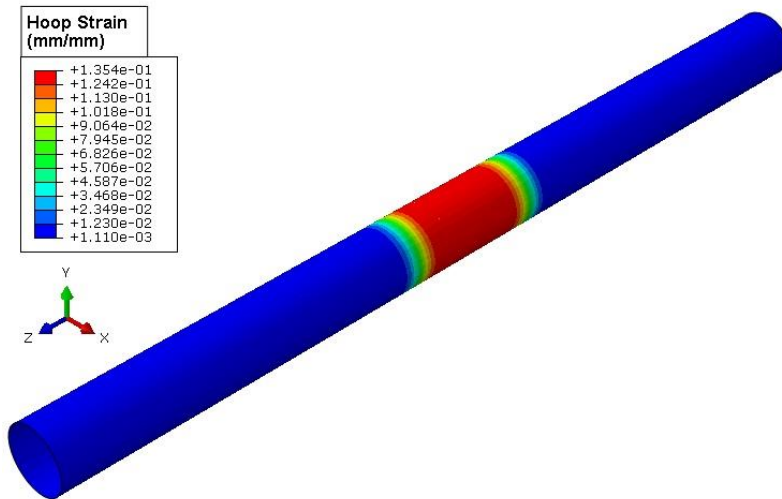


Figure 4-24, Contour plot of hoop strain on the corroded X52 steel pipe

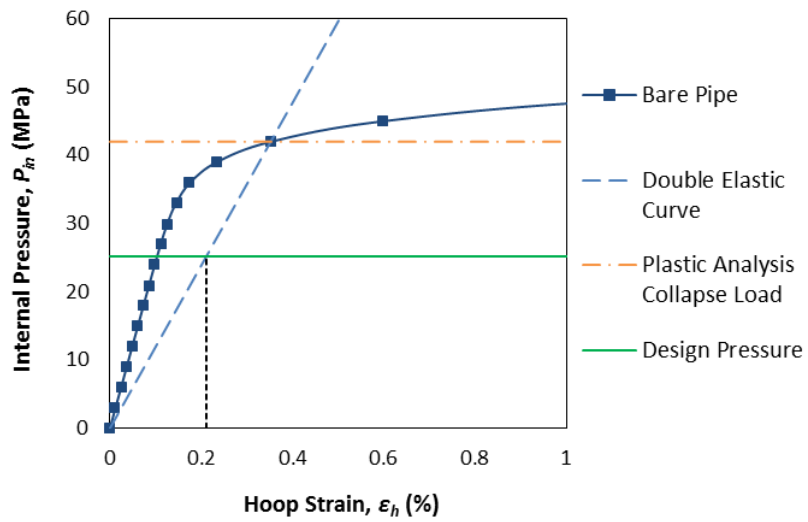


Figure 4-25, Computation of PACL and design pressure of an uncorroded pipe

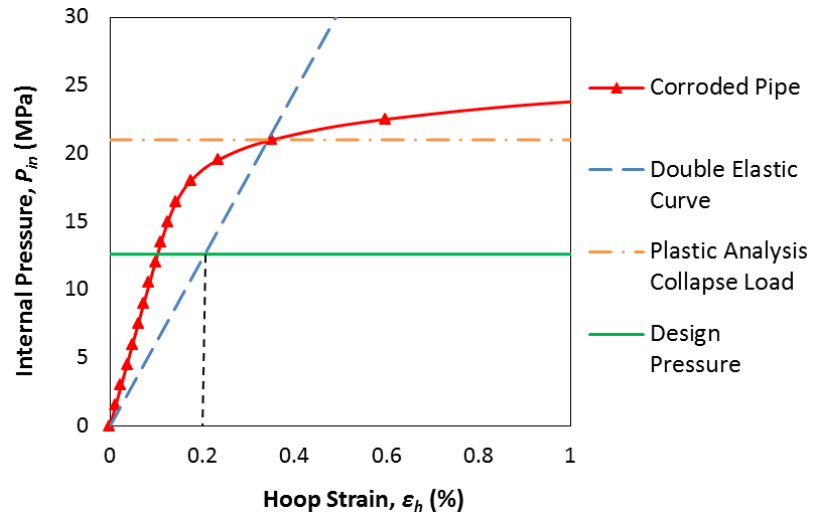


Figure 4-26, Computation of PACL and design pressure of corroded pipe

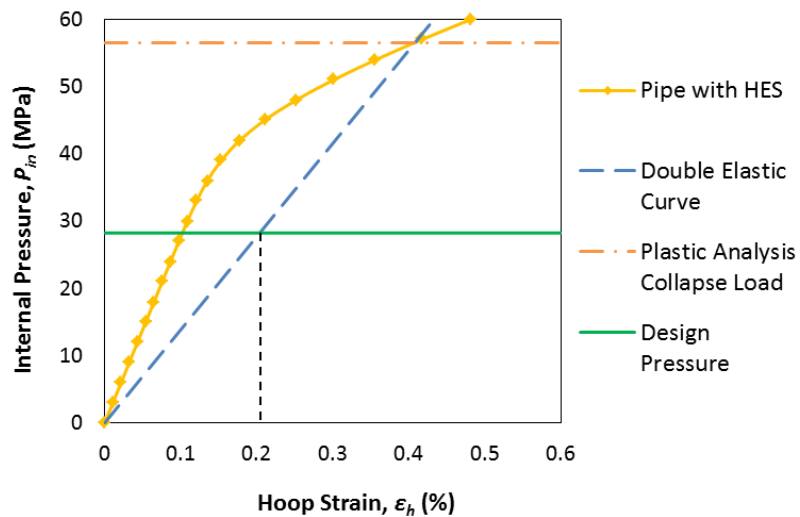


Figure 4-27, Computation of burst pressure of corroded pipe repaired with HES™ system

The pressure against hoop strain curves for all three cases are plotted in Figure 4-28. It can be observed that the HES™ system is capable to restore the strength of a corroded pipe. In fact, the simulated performance of a repaired pipe was found better than that of the uncorroded bare pipe by 12%. Considering the maximum allowable hoop strain of 0.211%, the corroded pipe repaired with HES™ system is capable of withstanding design pressure up to 28.25 MPa, as

shown in Figure 4-27. The FEA results demonstrated that the HES™ system can increase the strength of the corroded pipe by 124%.

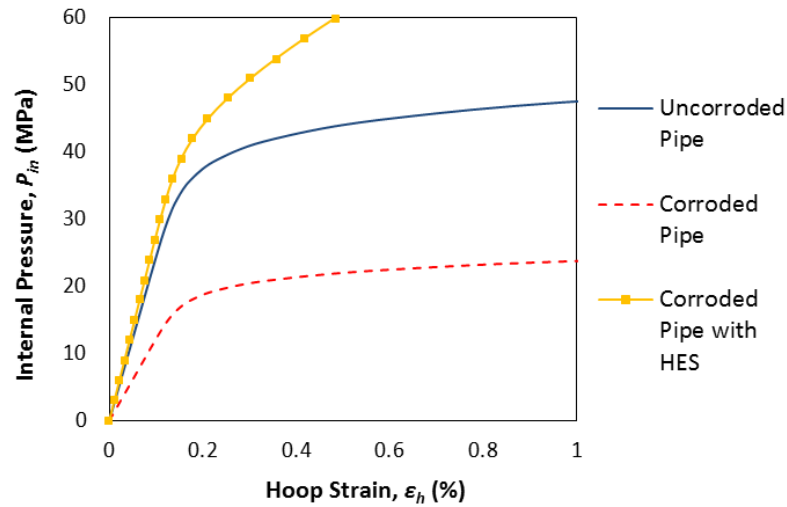


Figure 4-28, Pressure against hoop strain curves for uncorroded pipe, corroded pipe and corroded pipe repaired with HES™ system

### *Experimental Results*

Field test conducted on the corroded API 5L grade X52 steel pipe repaired with the HES™ system shows that the repair system capable of restoring the structural strength of the corroded pipe. The burst pressure was recorded as 53.5 MPa, which is higher than the burst pressure of an uncorroded X52 steel pipe as calculated through Eq. 4–19. At the burst pressure, ultimate failure occurred within the repaired region, where bursting of the pipe and the HES™ system was observed. Pieces of broken epoxy grout can be seen, as shown in Figure 4-29, signifying that the epoxy grout failed in a brittle manner.

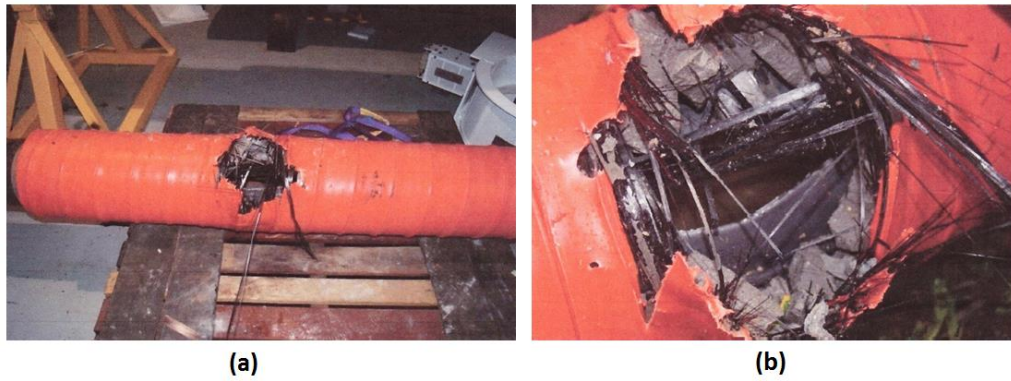


Figure 4-29, HES<sup>™</sup> repaired pipe at burst pressure (a) failure within the repaired region and (b) close up of failure region

### *Comparison of Industrial Standards, Numerical Analysis and Experimental Test*

The results obtained via FEA are compared to those obtained using the industrial standards and field testing. For the case of uncorroded pipe and corroded pipe, burst pressure and design pressure calculated using and Eq. 4–20 can be compared to those computed using Double Elastic Slope method through outputs obtained from FEA. For the case of corroded pipe repaired with HES<sup>™</sup> system, comparison of the burst pressure between field test and those obtained from Double Elastic Slope method are tabulated in Table 4-7. The FEA results showed good correlation with the ASME standards with deviation of less than 10%. In addition, the percentage difference between the field test and FEA results for the corroded pipe repaired with HES<sup>™</sup> is only 5.61%. This signifies that FEA along with limit analysis can be used as a tool for the evaluation of a corroded pipe. The equations used to calculate the burst and design pressures of the corroded pipe are only applicable to cases where internal pressure is the sole loading. When dealing with risers subjected to a series of combined loadings, a slightly different approach in the FEA needs to be taken into consideration.

Table 4-7, Results from design standards, experimental test and FEA simulation

	Uncorroded Pipe		Corroded Pipe		Corroded Pipe Repaired HES™	
	Standards	FEA	Standards	FEA	Test	FEA
Design Pressure (MPa)	27.24	25.2	14	12.6	-	-
Hydrostatic Test Pressure (MPa)	34.05	31.5	17.6	15.75	-	-
Burst Pressure (MPa)	45.4	42	23.4	21	53.5	56.5
Percentage Difference (%)	7.48		10.00		5.61	

The field test measurement demonstrated that the combination of the epoxy grout and carbon fibre reinforced PE strip is capable of restoring the strength performance of a corroded steel pipe subjected to pure internal pressure. The performance of the HES™ system was found to conform to various industrial design standards. The use of FEA was able to capture the behaviour of the HES™ system with deviation less than 10%. With the current input parameters, studies on the sensitivity of different variables that govern the behaviour of the repair can be conducted within the FEA in the future.

#### 4.5 Individual Static Loading

Three main types of static loads acting on a functioning riser, include the internal pressure,  $P_{int}$ , tensile load,  $F_t$  and bending moment,  $M_b$  were separately analysed to study the performance of the corroded riser and those repaired with FRPC. A simulated external corrosion defect having a rectangular shape with predefined length and width was machined onto a localised section of the pipeline



#### **4.5.1 Internal Pressure, $P_{int}$**

FE model was developed to investigate the performance of bare riser, corroded riser and repaired riser subjected to static internal pressure.

##### **4.5.1a Bare Riser without & with Corroded Region**

Using the double-elastic slope method (discussed in Chapter 4), the design pressure,  $P_d$  was determined to be 22MPa while the maximum permissible hoop strain,  $\epsilon_{h-max}$  was 0.1875%. The hoop stress and hoop strain of the bare riser were found uniform over the riser surface, at 233.64MPa and 0.111% respectively.

A corroded region was modelled at the mid-section of the riser where it is manifested as a 50% loss in the wall thickness. This was achieved by reducing the section thickness of designated shell elements. The corroded region has an axial length of 600mm and circumferential length of 50mm with a wall thickness of 5.15mm as illustrated in Figure 4-18. The hoop stress and hoop strain of the corroded riser are shown in Figure 4-30 and Figure 4-31, respectively. The maximum hoop strain was computed at 0.264%. This value is well exceeds the maximum permissible hoop strain  $\epsilon_{h-max}$ , which signify that the corroded riser is no longer fit for operation. The corresponding hoop stress was 466.59MPa, which is 96.6% of the riser's yield stress (483MPa). The load-strain curve in Figure 4-34 clearly shows that the load carrying capacity of the riser has deteriorated drastically.

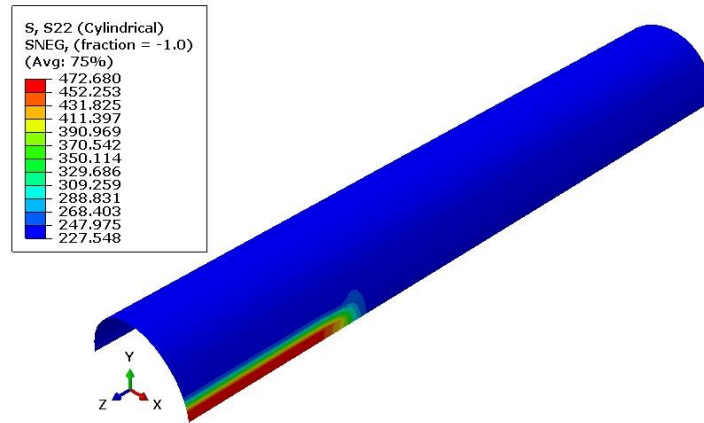


Figure 4-30,  $\sigma_h$  contour plot of corroded riser at 22MPa

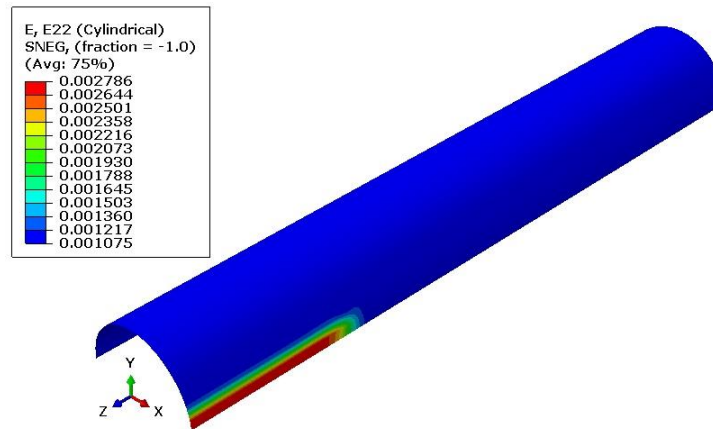


Figure 4-31,  $\epsilon_h$  contour plot of corroded riser at 22MPa

#### 4.5.1b Corroded Riser Repaired with Composite Laminate

The repair sleeve was modelled over a designated length of the riser. The material properties of the laminate were defined using lamina properties, where transversely isotropic material properties are assumed. The repair laminate was modelled in such a manner that the fibres are aligned in the hoop direction of the riser. This type of orientated repair is similar to most of the commercially available products where unidirectional laminate is wrapped around the riser with the fibres aligned perpendicular to the axis of the pipe. The hoop stress and hoop strain of the corroded riser beneath the repair are shown in Figure 4-32 and

Figure 4-33, respectively. As depicted, the hoop strain at design load (22MPa) has reduced by an approximately 69.57% with the CFRP rehabilitation. The curve in Figure 4-34 shows the hoop strain of the repaired riser under increasing internal pressure where there is an approximately linear relationship. This suggests that the hoop stress can be successfully transferred to the FRPC laminate, signifying that the amount of stress sustained by steel riser is reduced to within its elastic limit. The higher stress and strain values outside of the repaired region, as depicted in Figure 4-32 and Figure 4-33 signifies that further increase in internal pressure will most likely results in bursting outside the repaired region.

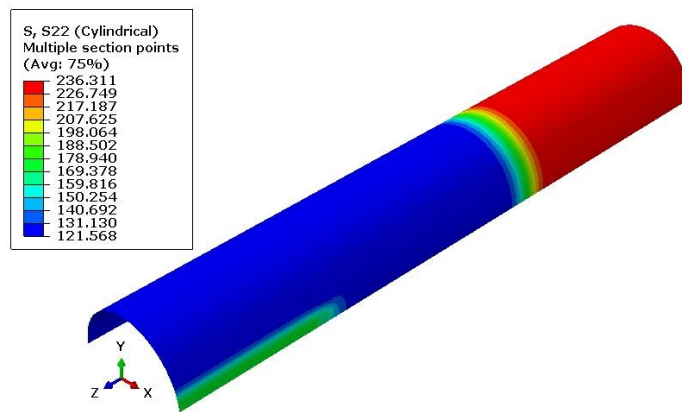


Figure 4-32,  $\sigma_h$  contour plot of repaired riser at 22MPa

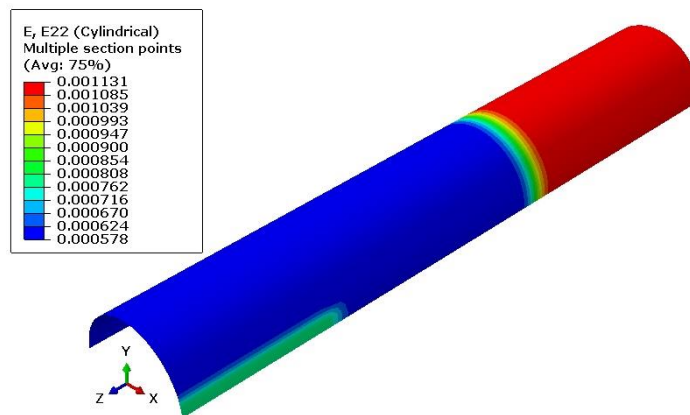


Figure 4-33,  $\epsilon_h$  contour plot of repaired riser at 22MPa

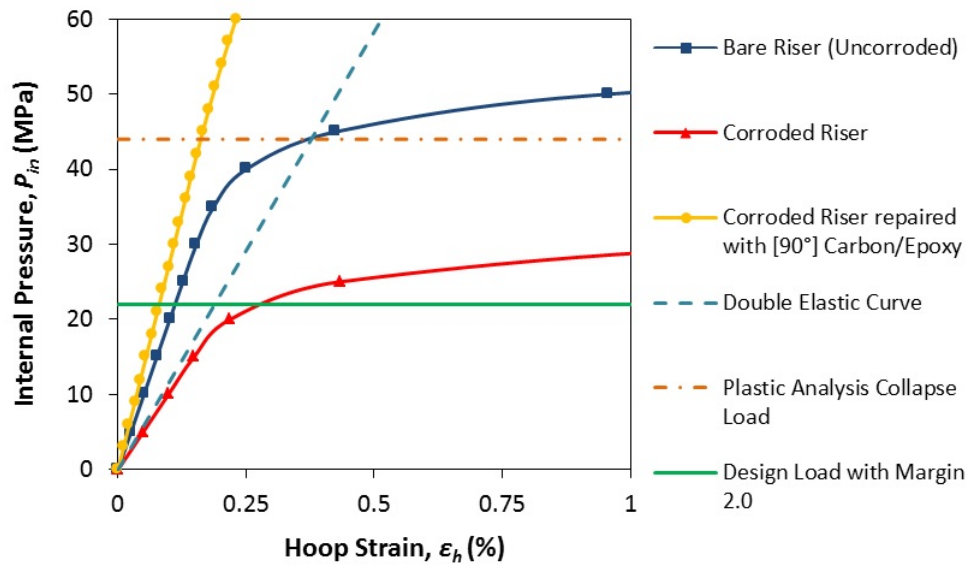


Figure 4-34, Limit state analysis of riser subjected to  $P_{int}$

#### 4.5.2 Tensile Load, $F_t$

##### 4.5.2a Bare Riser with & without Corrosion Defect

The second load case where static tensile load was applied on risers to minimize lateral movement. As discussed in Chapter 3, the design load as computed from using double-elastic curve method was tensile load,  $F_t = 1785\text{kN}$  and the maximum permissible tensile/axial strain,  $\epsilon_{a-max} = 0.225\%$ . The tensile stress experienced by the riser without corrosion is still 50% below the yield stress, at 242.33 MPa while the tensile strain approached approximately half of the maximum permissible tensile strain, at 0.115%. The riser without corrosion defects was found fit for function under individually applied static tensile load of 1785kN.

As illustrated in the Figure 4-35, the maximum axial stress on the corroded riser was computed at 337.6MPa, which is well below the yield stress of the riser. The maximum axial strain, shown in Figure 4-36, was 0.165%, which is below the maximum permissible axial strain,  $\epsilon_{a-max}$ . It can be observed that the individual

effect of tensile load on a corroded riser is not as detrimental as the impact of internal pressure alone. However, stress concentration exists at the edge of the corrosion where there is a sudden change in the thickness of the riser. This high stress concentration region can be site of a fatigue damage initiation. Hence, attention is needed to mitigate this condition to prevent further deterioration of the riser.

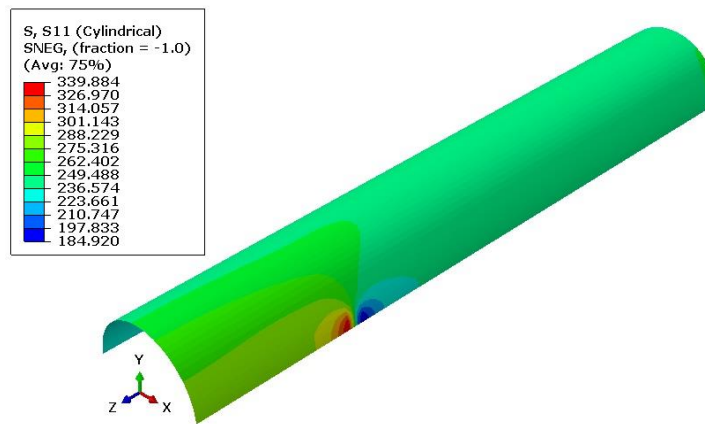


Figure 4-35,  $\sigma_a$  contour plot of corroded riser at 1785kN

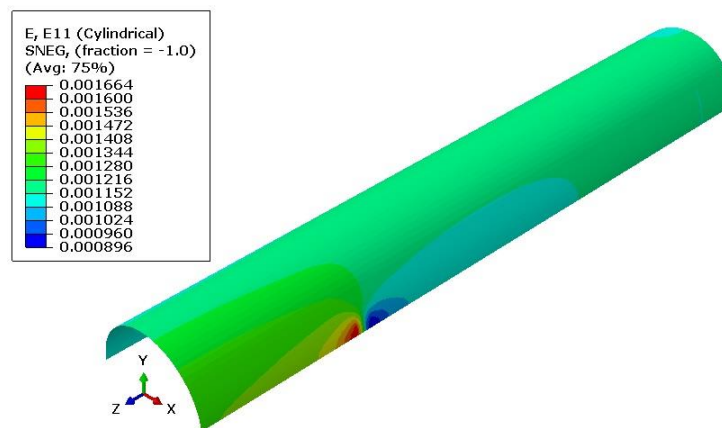


Figure 4-36,  $\varepsilon_a$  contour plot of corroded riser at 1785kN

#### 4.5.2a Corroded Riser Repaired with Composite Laminate

Figure 4-37 and Figure 4-38 show the axial strain of the corroded region beneath the composite laminate. The stress at the edge of the corrosion defect was found reduced by 9.18%, which is a relatively small amount compared to the case of

pure internal pressure where a reduction of 43.57% was obtained. Figure 4-39 shows the load-strain curve of the repaired riser subjected to tensile load. Although still within the limits of the maximum permissible axial strain,  $\epsilon_{a,max}$ , the results suggested that reinforcement solely in the hoop direction of the riser is not ideal.

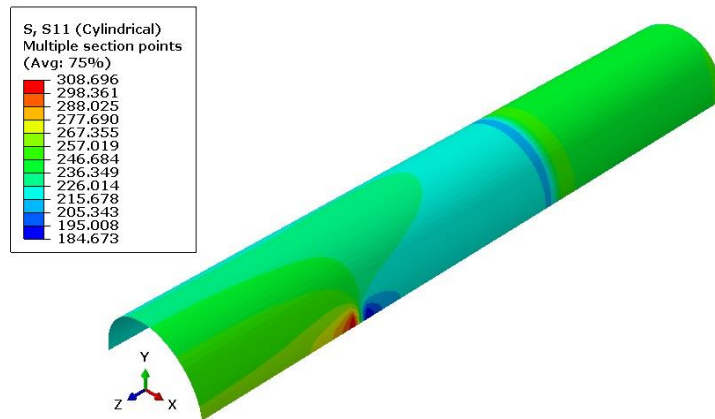


Figure 4-37,  $\sigma_a$  contour plot of repaired riser at 1785kN

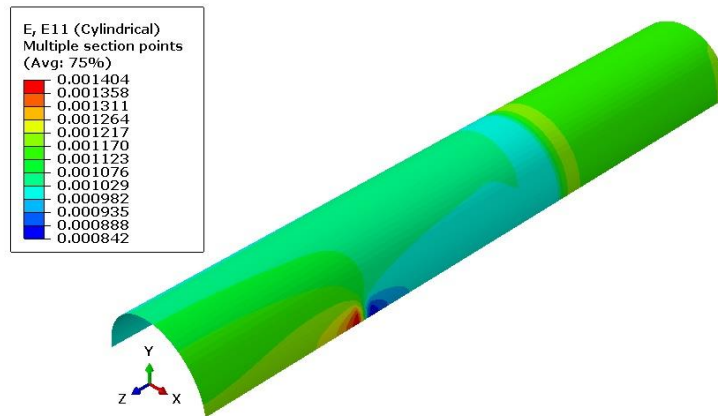


Figure 4-38,  $\epsilon_a$  contour plot of repaired riser at 1785kN

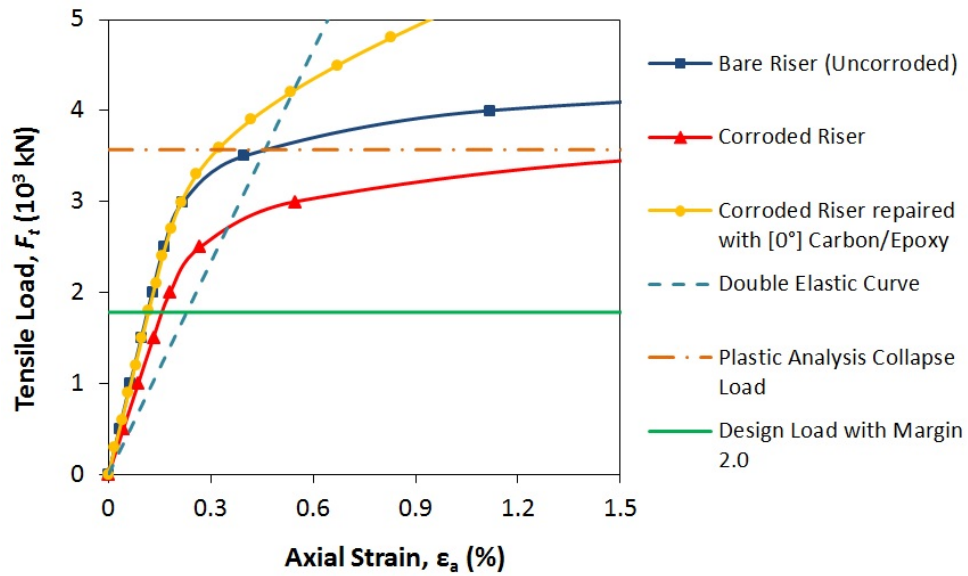


Figure 4-39, Limit state analysis of riser subjected to  $F_t$

### 4.5.3 Bending Load, $M_b$

#### 4.5.3a Bare Riser without & with Corroded Region

The effects of bending load on the riser were studied through a local analysis where the bending stress and strain at the corroded region of the riser was examined. Global analysis of the entire length of the riser from the platform to the seabed connections is not considered. A four-point bending setup was used in the current study, as shown in Figure 4-19. This setup provides a constant bending moment between the load span compared to three-point bending where the moment gradually increases to a maximum at the midpoint of the pipe. The output as obtained from double elastic curve method suggested a design load for bending moment of 120kNm and a maximum permissible bending/axial strain,  $\epsilon_{b-max}$  of 0.255%. The highest axial stress and strain was found occurred at the mid-section of the riser, which is in tension due to the bending moment. The stress and strain reduces gradually away from the mid-section as flexural modulus of the steel riser is uniform throughout the entire length of the riser.

The maximum bending stress, 427.5MPa (Figure 4-40) occurred at the corroded region is equivalent to 88.5% of the yield stress. The maximum bending strain at the corroded region is approximately 0.236%, which is close to the maximum permissible bending strain,  $\epsilon_{b-max}$ , as shown in Figure 4-41. The  $\epsilon_{b-max}$  appears at the edges of the corroded region due to the sudden drop in flexural rigidity of the riser as the wall thickness reduces.

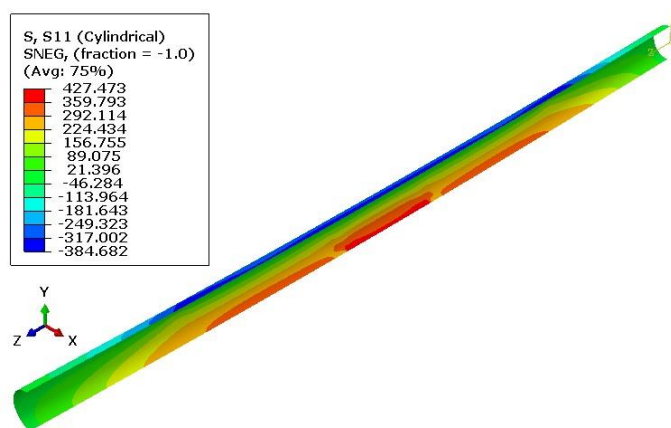


Figure 4-40,  $\sigma_b$  contour plot of corroded riser at 120kNm

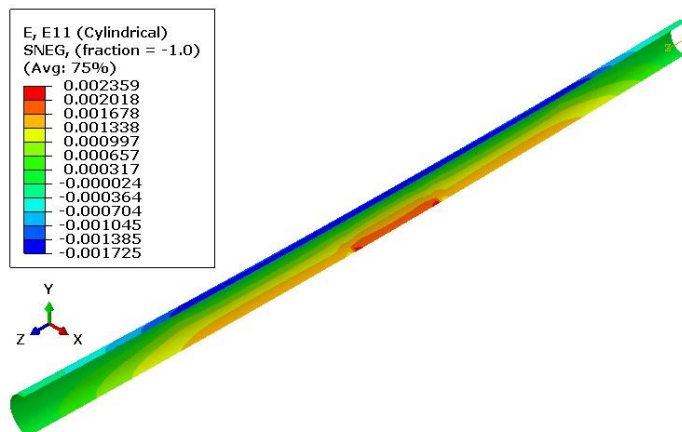


Figure 4-41,  $\epsilon_b$  contour plot of corroded riser at 120kNm

#### 4.5.3a Corroded Riser Repaired with Composite Laminate

Figure 4-44 also shows the stress-strain response at the corroded region beneath the repair. Similar to the case of tensile loading, no significant increases in the



flexural strength of the repaired riser was observed. The reductions in axial stress and strain of the repaired riser were about 6.8% and 20.5% respectively. The reinforcement provided by the FRPC is directionally dependent. The fibres aligned in the hoop direction of the riser provide minimal strengthening to the corroded riser under external bending load. Comparison of the corroded riser and corroded-repaired riser are summarised in Table 4-8.

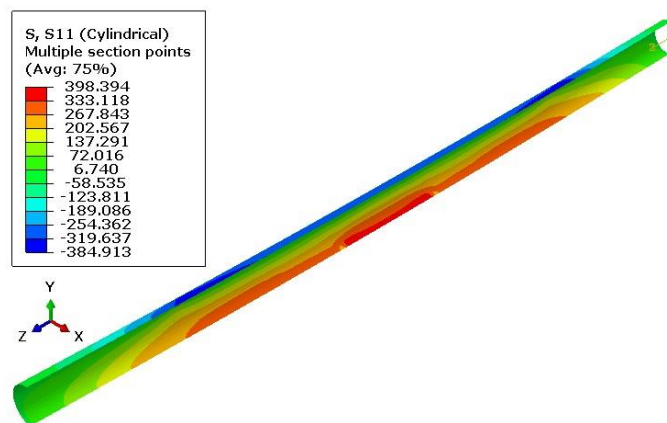


Figure 4-42,  $\sigma_b$  contour plot of repaired riser at 120kNm

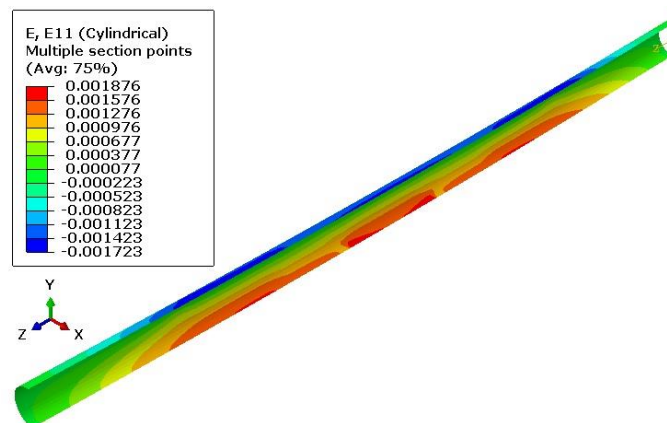


Figure 4-43,  $\varepsilon_b$  contour plot of repaired riser at 120kNm

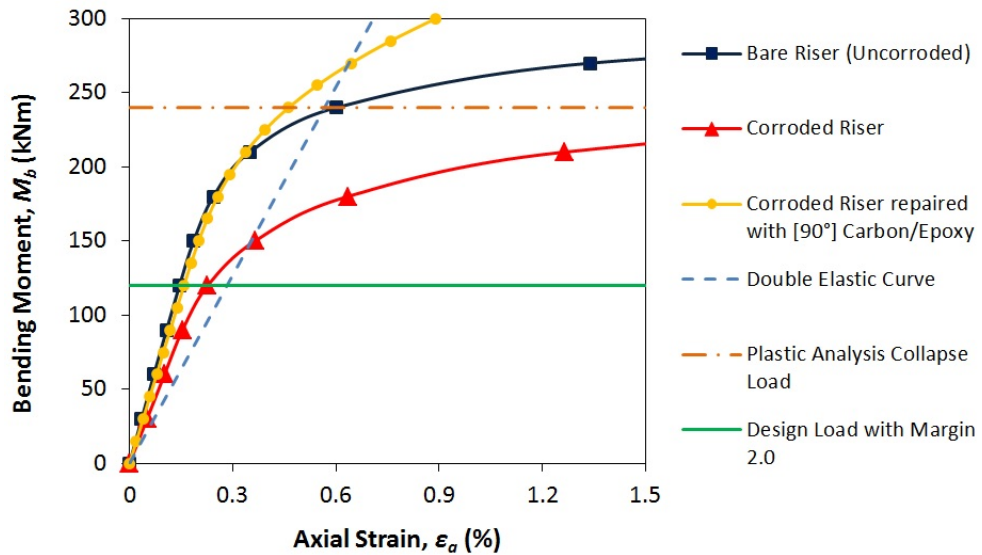


Figure 4-44, Limit state analysis of riser subjected to  $M_b$

Table 4-8, Stress and strain comparison between corroded riser and repaired riser

Individual Static Load	Corroded Riser		Repaired Riser		Percentage Reduction (%)	
	Stress, $\sigma$ (MPa)	Strain, $\epsilon$ (%)	Stress, $\sigma$ (MPa)	Strain, $\epsilon$ (%)	Stress	Strain
Internal Pressure, $P_{int}$	476.280	0.2786	236.311	0.1131	50.38	59.40
Tensile Load, $F_t$	339.884	0.1664	308.696	0.1404	9.18	15.63
Bending Moment, $M_b$	427.473	0.2359	398.394	0.1876	6.80	20.47

#### 4.6 Combined Static Loading

The study of combined static loading can better emulate the real-life working conditions of a riser where multiple loadings act on the riser simultaneously. The addition of various loads acting on the riser can significantly vary the stress-

strain behaviour of the riser, hence affecting the design requirement of the CRS. The anisotropic nature of the FRPC material properties could be designed to alter the ultimate performance of the repair. In the current project, investigation on combined loadings can be separated into two categories – (1) combined internal pressure and tensile load, and (2) combined internal pressure, tensile load and bending moment.

#### **4.6.1 Combined Internal Pressure, $P_{int}$ and Tensile Load, $F_t$**

##### **4.6.1a Bare Riser with & without Corrosion Defect**

Combined internal pressure and tensile load were applied to the riser and their effects on the riser were studied. The internal pressure and tensile force at design loads as calculated using the limit analysis, were 22MPa and 1785kN respectively. Under uncorroded condition, the hoop and tensile strains were far below the maximum permissible hoop and axial strains.

Figure 4-45 and Figure 4-46 show that both the axial and hoop stresses on the corroded region of the riser were higher than the uncorroded case, with hoop stress close to the yield stress of the riser. The hoop strain (Figure 4-48) on the corroded region of the riser was approximately 0.194%. It should be noted that this value is lower than the hoop strain recorded on the corroded riser subjected to pure internal pressure, which is above 0.25%. This could be attributed to the Poisson Ratio effect due to the tensile load which yields negative hoop strain. The hoop stress is found to be the dominant factor affecting the design of the CRS.

Within the FEA, both the internal pressure and tensile load were ramp with a predefined fixed increment in order to obtain a plot of load versus strain at fixed

interval. The load-strain curves for hoop and axial strains (Figure 4-45 to Figure 4-48) indicated that the localised corrosion defect has a higher detrimental effect in the hoop direction. Maximum permissible hoop strain was exceeded while the maximum permissible axial strain was not reached.

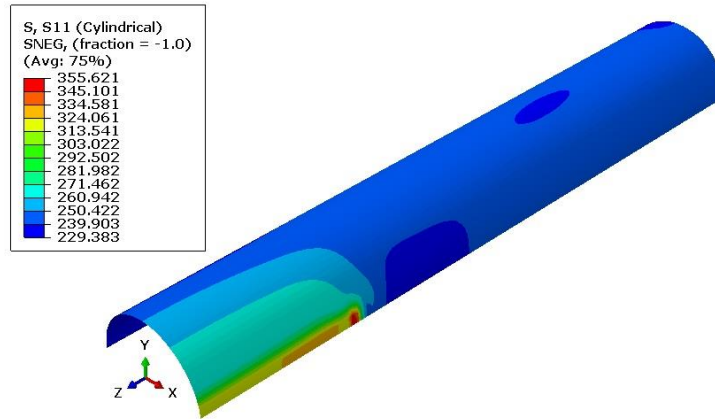


Figure 4-45,  $\sigma_a$  contour plot of corroded riser at combined 22MPa and 1785kN

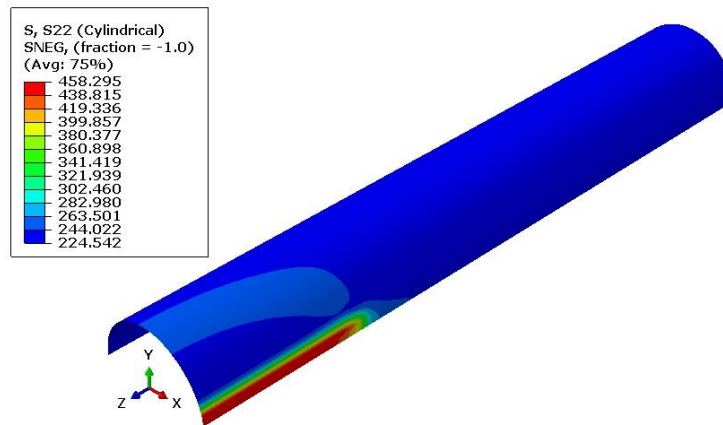


Figure 4-46,  $\sigma_r$  contour plot of corroded riser at combined 22MPa and 1785kN

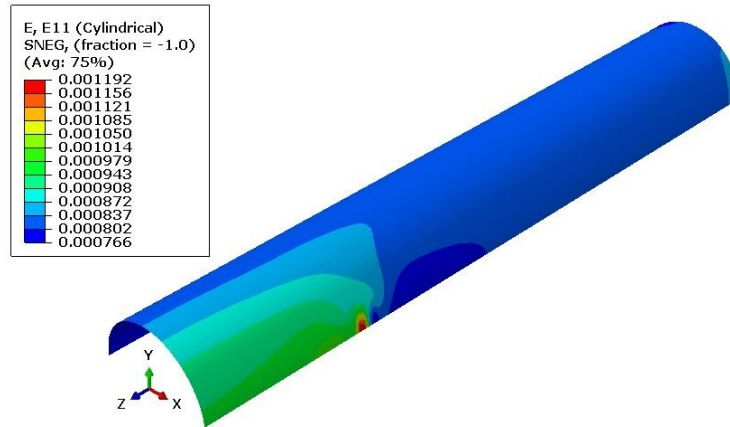


Figure 4-47,  $\varepsilon_a$  contour plot of corroded riser at combined 22MPa and 1785kN

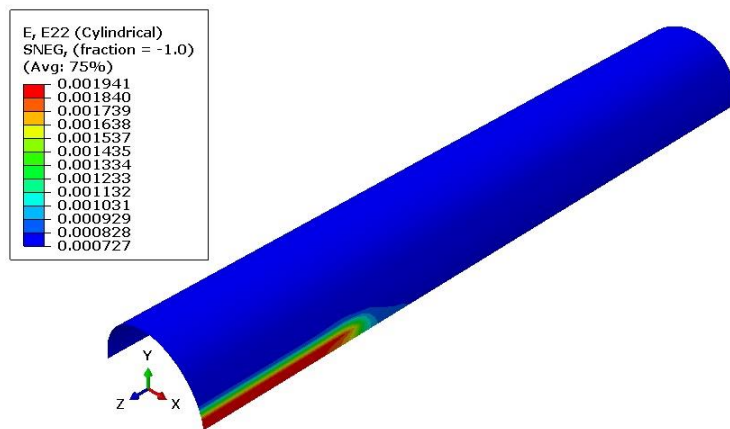


Figure 4-48,  $\varepsilon_h$  contour plot of corroded riser at combined 22MPa and 1785kN

#### 4.6.1b Corroded Riser Repaired with Composite Laminate

Figure 4-49 to Figure 4-52 display the axial and hoop stresses and strains on the steel riser beneath the composite repair. In terms of strengthening the riser in the axial direction, the composite repair provided a poorer performance as the maximum stress and strain is still observed within the repaired region (shown in Figure 4-49 and Figure 4-51). In contrary, the hoop stress and strain levels were reduced significantly with composite repair as the fibres are aligned in the hoop direction. The load-strain plots in Figure 4-53 and Figure 4-54 show a clearer comparison between the corroded riser and the repaired riser. The use of the hoop orientated composite repair was able to restore the strength of the corroded

riser in the hoop direction to the original uncorroded state. However, the hoop orientated repair was not able to strengthen the riser in the axial direction. As shown in Figure 4-53, the axial strain of the repaired riser at the plastic analysis collapse load (PACL) is approximately 0.4%, which exceeds the acceptable limits of 0.225%.

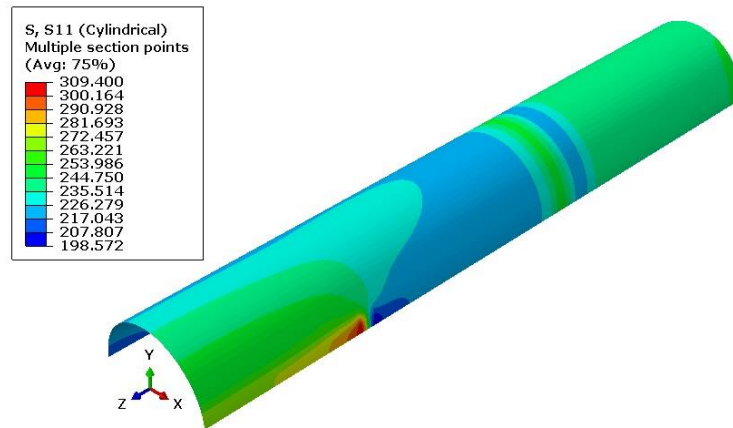


Figure 4-49,  $\sigma_a$  contour plot of repaired riser at combined 22MPa and 1785kN

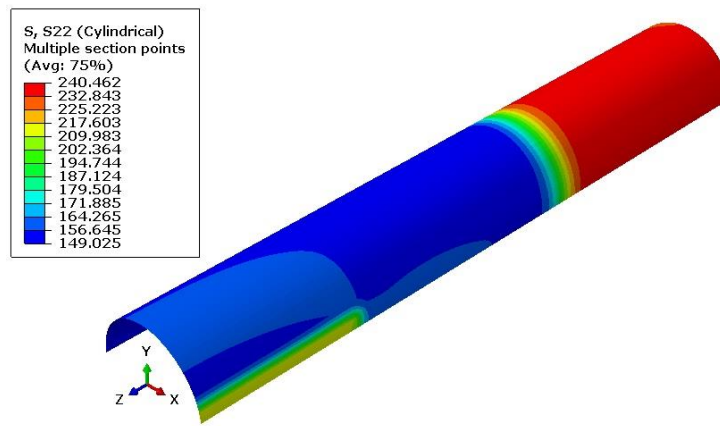


Figure 4-50,  $\sigma_h$  contour plot of repaired riser at combined 22MPa and 1785kN

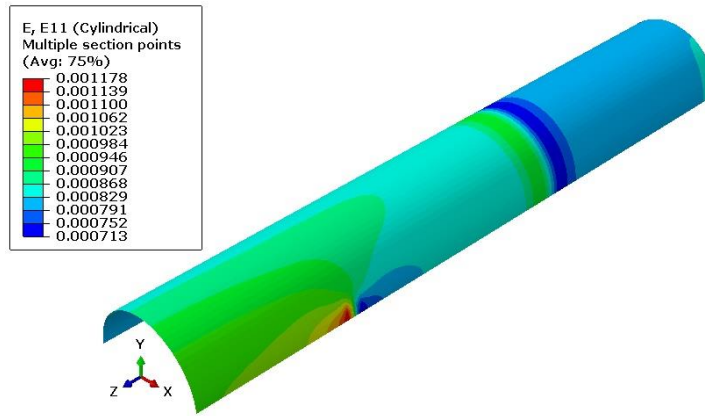


Figure 4-51,  $\epsilon_a$  contour plot of repaired riser at combined 22MPa and 1785kN

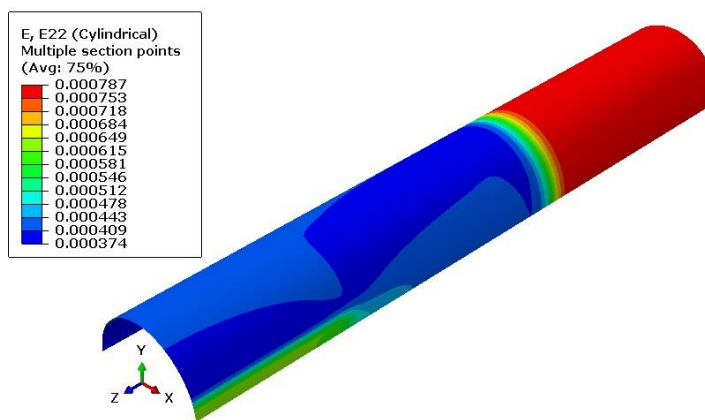


Figure 4-52,  $\epsilon_h$  contour plot of repaired riser at combined 22MPa and 1785kN

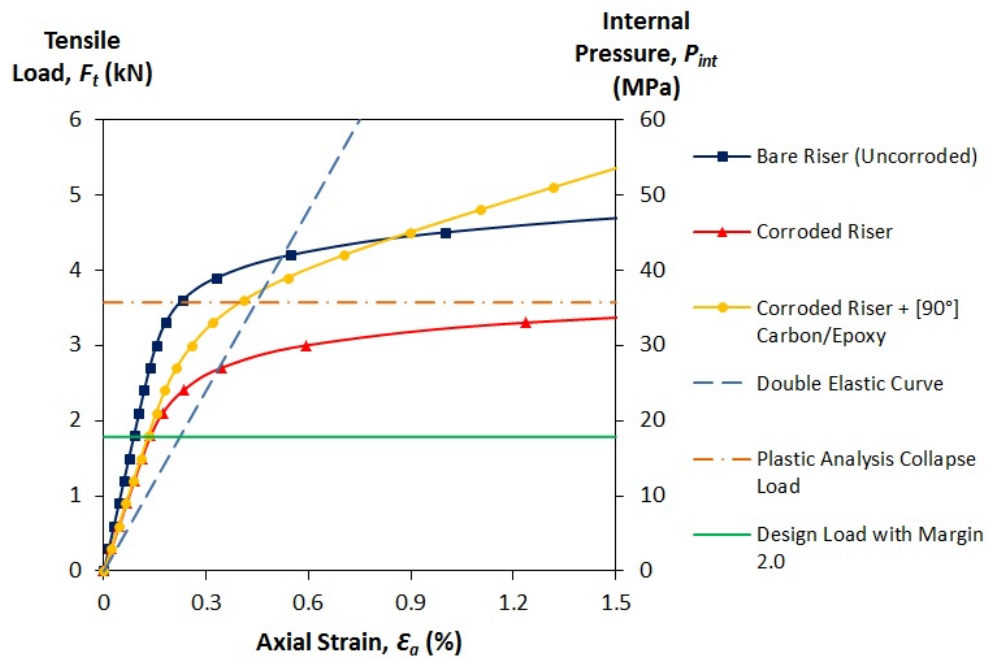


Figure 4-53, Limit state analysis of riser subjected to  $P_{int}$  and  $F_t$  (Axial Strain)

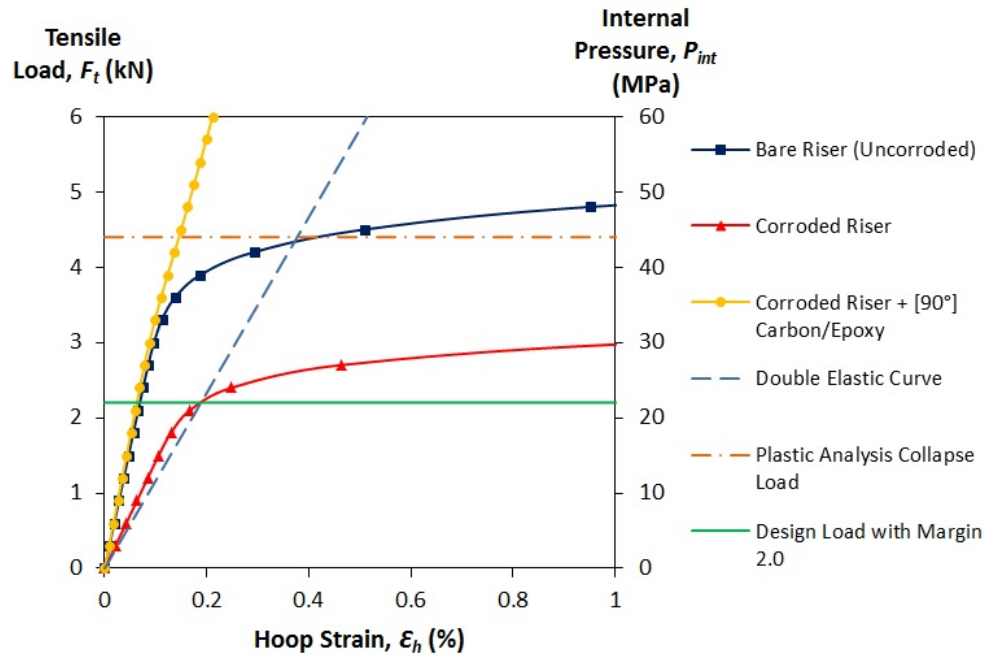


Figure 4-54, Limit state analysis of riser subjected to  $P_{int}$  and  $F_t$  (Hoop Strain)

#### 4.6.2 Combined Internal Pressure, $P_{int}$ , Tensile Load, $F_t$ and Bending

##### Moment, $M_b$

##### 4.6.2a Bare Riser with & without Corrosion Defect

Combined internal pressure, tensile load and bending moment were applied to simulate the real life working conditions of a riser. The values of the internal pressure and tensile load were kept at design conditions, at 22MPa and 1785kN respectively; while a range of bending moment was applied onto the riser. The setup used a four-point bend similar to that described in Figure 4-19. The bending moment corresponds to the transverse motion of the riser which arises due to subsea wave/current forces. The limit analysis of the riser subjected to such combined loadings is shown in Figure 4-55. When loaded simultaneously, the axial stress and strain of the riser increases, causing the riser to fail at lower bending loads. The magnitude of the PACL was computed as 156kNm, which is



35% lower than PACL of 240kNm when the bending load was applied individually.

The hoop stress and strain were significantly lower than those in the axial direction. This can be attributed to the high net positive axial force (tension) acting on the riser as a result of combined tensile and bending load. The stress and strain in the compressive region of the bent riser were found less significant as it is counteracted by the tensile force applied on the riser.

The corrosion defect causes the performance of the riser to experience significant deterioration. At the design load of 78kNm, the axial stress of the corroded region went well beyond the yield stress of the riser material (Figure 4-56). The maximum axial strain on the corroded region, recorded at approximately 0.4% has exceeded the maximum permissible bending/axial strain (0.255%) by more than 50%, indicating the failure has occurred on the riser.

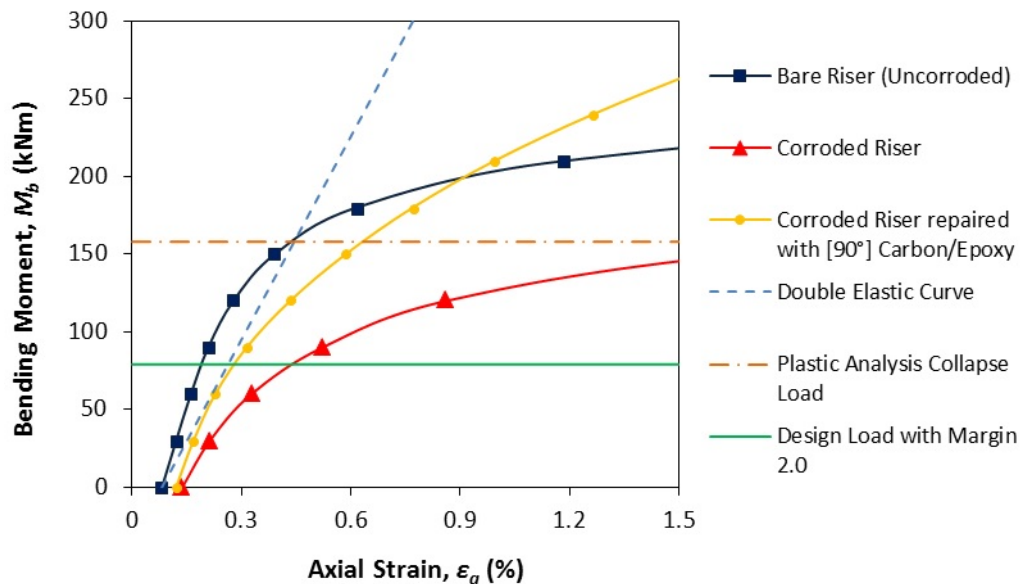


Figure 4-55, Limit state analysis (axial strain) of riser subjected to  $P_{int}$ ,  $F_t$  and

$$M_b$$

The corrosion defect also causes high hoop strain of 0.283% in the corroded region, which exceeds the maximum permissible hoop strain (0.1875%) by 50%. Figure 4-60 shows the limit state analysis of the hoop strain within the corroded region. Without any corrosion defect, the increase in bending load yields negative hoop strains on the corroded region. The sum of the axial tensile forces as a result of the combined effects of tension and bending moment was greater compared to the hoop load imposed by the internal pressure. However, the corrosion defect causes a drastic increase in hoop stress. The thinning of pipe wall on the corroded region cause by the axial forces facilitates the increase in hoop stress.

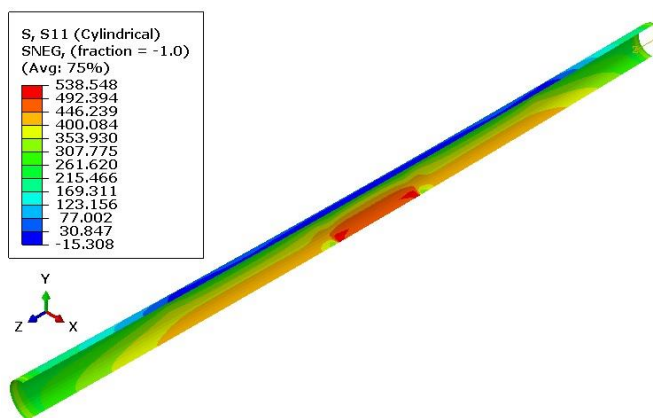


Figure 4-56,  $\sigma_a$  contour plot of corroded riser at combined 22MPa, 1785kN and 78kNm

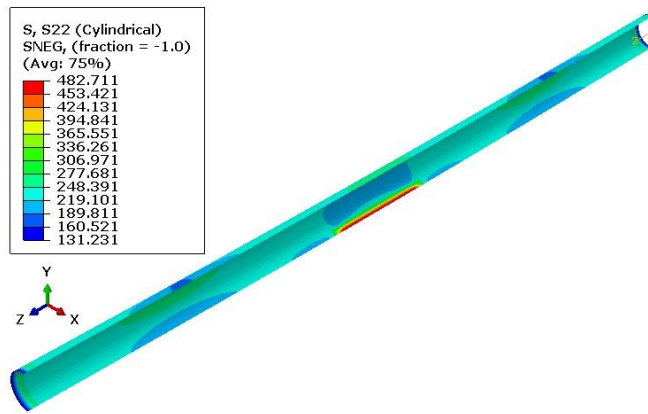


Figure 4-57,  $\sigma_h$  contour plot of corroded riser at combined 22MPa, 1785kN and 78kNm

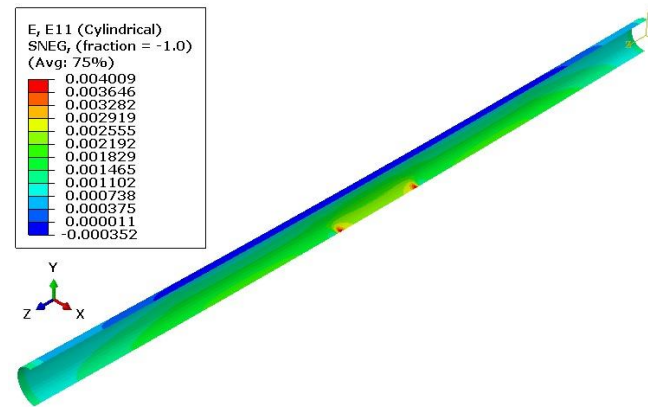


Figure 4-58,  $\epsilon_a$  contour plot of corroded riser at combined 22MPa, 1785kN and 78kNm

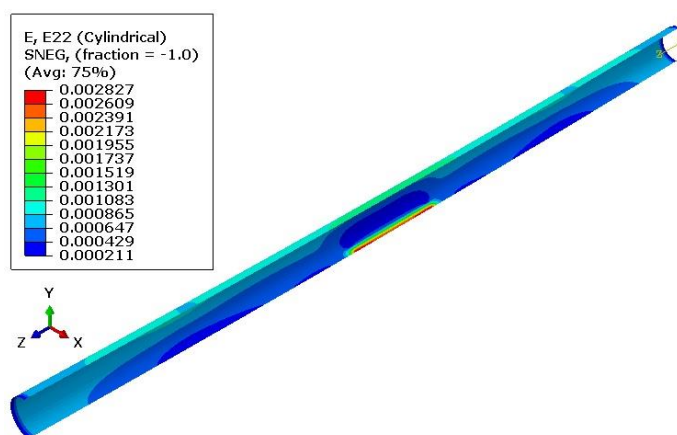


Figure 4-59,  $\epsilon_h$  contour plot of corroded riser at combined 22MPa, 1785kN and 78kNm

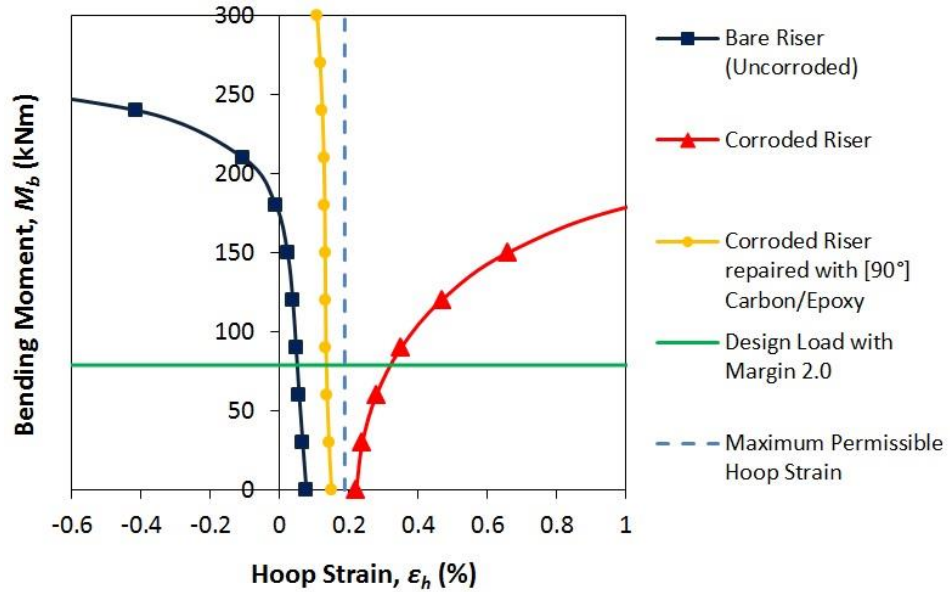


Figure 4-60, Limit state analysis (hoop strain) of riser subjected to  $P_{int}$ ,  $F_t$  and

$M_b$

#### 4.6.2b Corroded Riser Repaired with Composite Laminate

The conventional composite repair with fibres aligned in the hoop direction was investigated. The load-strain curve of the repaired riser is shown in Figure 4-55. As depicted, the CRS is incapable of reinforcing the corroded riser as the maximum permissible bending/axial strain has exceeded at design load. This suggests the need for a thicker composite repair which can further increase the axial strength and flexural rigidity of the repaired riser. However, thicker composite repair equates to more material that incurs higher cost. An alternative method to enhance the strengthening effects of the CRS is to vary the fibre angle orientation with respect to the riser's axis.

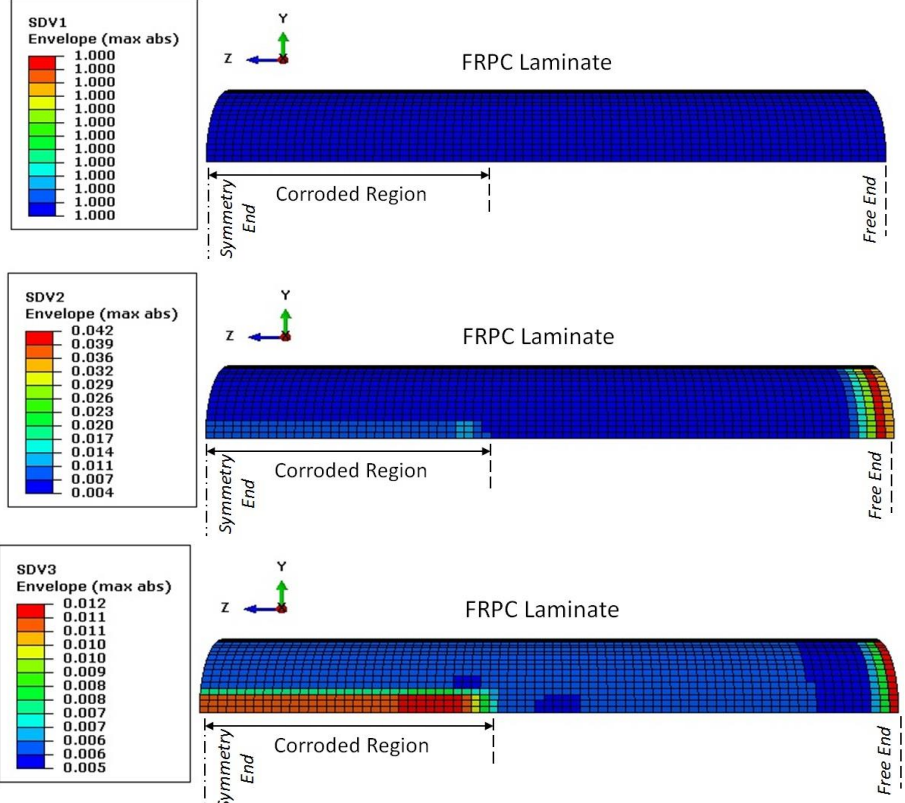
As depicted in Figure 4-60, the use of the hoop orientated CRS reduces the hoop strain significantly such that the strain values fall within the acceptable limit. The application of the CRS capable of increasing the flexural strength of the corroded riser as well as the hoop strength due to the effective stress transfer.

#### 4.7 Response of FRPC Repair Laminate

As discussed in section 4.3.2b , the MCT failure criterion was used to characterise the behaviour of FRPC repair laminate. There are three main state dependent variables (SDVs) that describe the response of the FRPC. The output variable SDV1 has values 1, 2 and 3, where 1 = no damage, 2 = matrix failure and 3 = fibre failure. SDV2 is a variable that ranges from 0.0 to 1.0 and is used to indicate the fraction of the matrix failure criterion that has been satisfied. SDV2 = 0 implies that the matrix stress state is zero, while SDV2 = 1 implies that the matrix stress state has reached failure level. SDV3 is a similar variable to SDV2 but it describes the state of the fibre. The use of the unidirectional AS4/3501-6 carbon/epoxy wrapped in the hoop direction (i.e. 90°) to repair the corroded riser under different load cases is studied. A discussion of the results for each of the loading cases is shown below.

At design loads, no failure occurs within the AS4-3501-6 carbon/epoxy laminate, indicated by SDV1 = 1. All these cases simulate ideal stress transfer from the corroded riser to the FRPC laminate as a perfect bond was assumed. Hence, even by sustaining the maximum stress transferred from the corroded riser, the AS4 carbon/epoxy laminate will not fail at design conditions under all the static loading cases. The response of the FRPC laminate at PACL was also examined to determine whether failure occurs on the FRPC laminate.

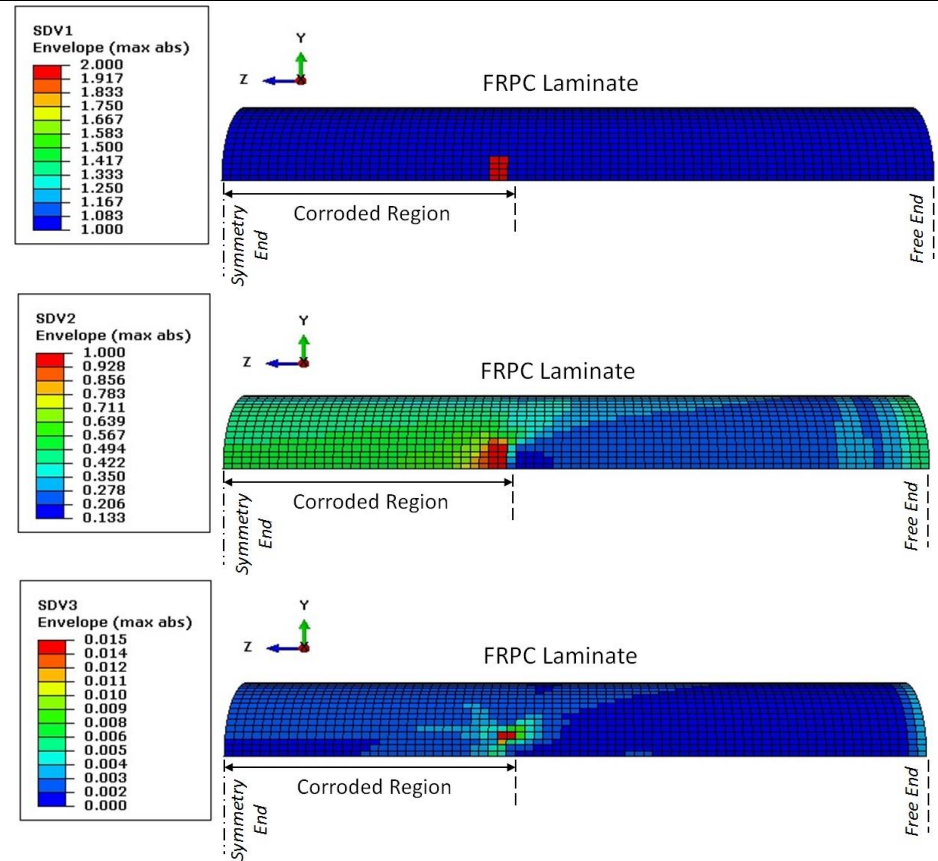
Table 4-9, Response of FRPC laminate at plastic analysis collapse load

Loading Case	Loading Condition: Plastic Analysis Collapse Load (PACL)	
	Observations	FEA Results
<p><b>Individual Static Load:</b> 1) Internal Pressure</p>	<ul style="list-style-type: none"> <li>- Even at 44MPa, the FRPC laminate did not fail as the variable SDV1 still has a value of 1.</li> <li>- SDV2 has low values indicating that the matrix is still far from failing.</li> <li>- Fibres are able to sustain the hoop stress induced by the internal pressure. Higher stress states were observed at the corroded region.</li> </ul>	 <p>The FEA results section contains three vertically stacked plots, each representing a different stress variable (SDV1, SDV2, and SDV3) in an FRPC laminate. Each plot shows a cylindrical model with a 'Corroded Region' indicated by a dashed line. The left end is labeled 'Symmetry End' and the right end is 'Free End'. A coordinate system with Y (vertical), Z (horizontal), and X (out of page) axes is shown at the top of each plot. To the left of each plot is a color-coded legend for the 'Envelope (max abs)' values.</p> <ul style="list-style-type: none"> <li><b>SDV1 Envelope (max abs):</b> Legend values range from 1.000 (red) to 1.000 (blue). The plot shows a uniform blue color across the entire length of the laminate, indicating a constant value of 1.000.</li> <li><b>SDV2 Envelope (max abs):</b> Legend values range from 0.042 (red) to 0.004 (blue). The plot shows low stress values (mostly blue and cyan) across the length, with a slight increase in stress (yellow and orange) at the 'Corroded Region'.</li> <li><b>SDV3 Envelope (max abs):</b> Legend values range from 0.012 (red) to 0.005 (blue). The plot shows low stress values (mostly blue and cyan) across the length, with a significant increase in stress (yellow, orange, and red) at the 'Corroded Region'.</li> </ul>

**Individual Static Load:**

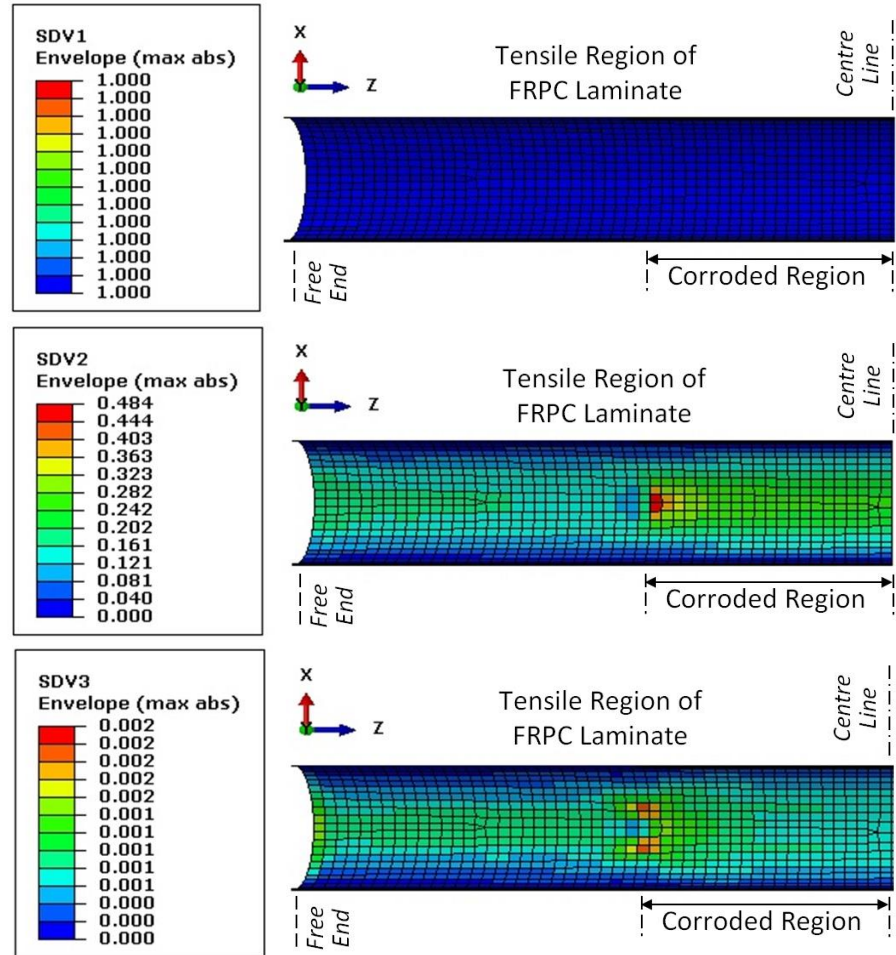
2) Tensile Load

- At 3570kN, matrix failure occurs near the corner of the corroded region due to high stress concentration. However, application of such a high value of tension on the risers is unlikely.
- SDV2 shows that the stress on the matrix is much higher within the corroded region.
- Although still far from failing, SDV3 indicates that the fibres sustain higher stresses at the corner of the corroded region. This can be induced by the redistribution of stress as the matrix fails.



**Individual Static Load:**  
3) Bending Moment

- At a high bending moment of 156kNm, no failure occurs within the FRPC laminate.
- SDV2 indicates that the corner of the corroded region is the critical area where stress state of the matrix is higher.
- SDV3 has low values, e.g. less than 0.002. Fibres are not sustaining maximum axial stress caused by bending as they are perpendicular to the axis of the riser.
- Failure in the CRS will most likely take the form of disbonding of the FRPC from the steel riser.

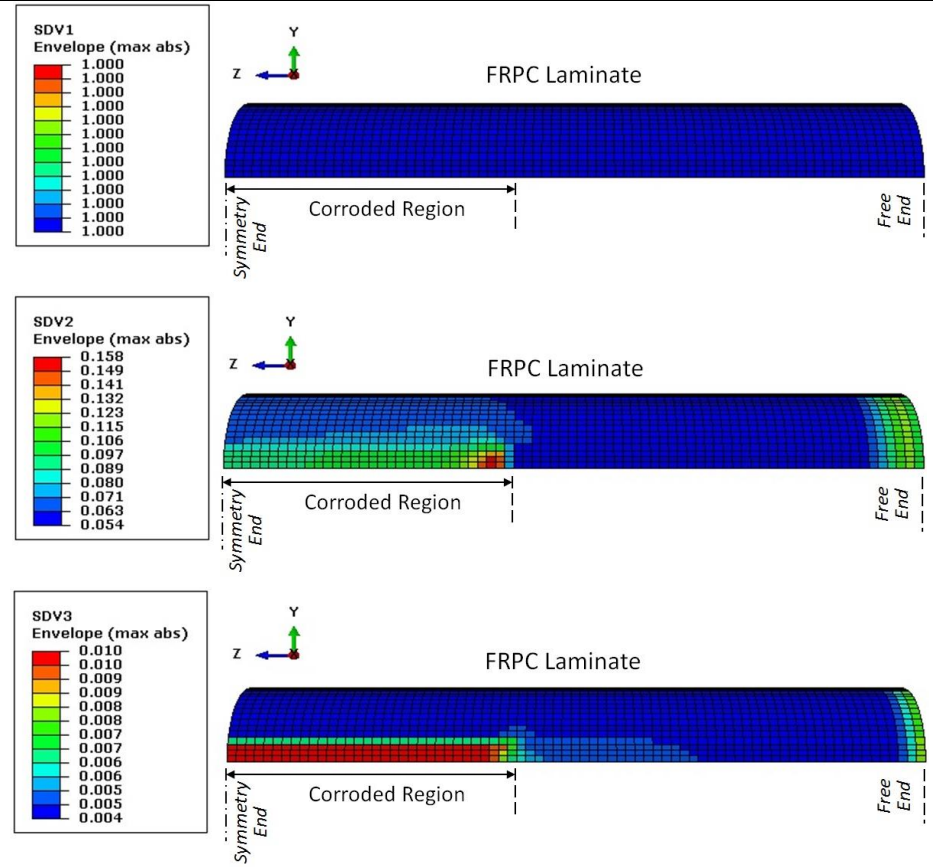




**Combined Static Load:**

1) Internal Pressure + Tensile Load

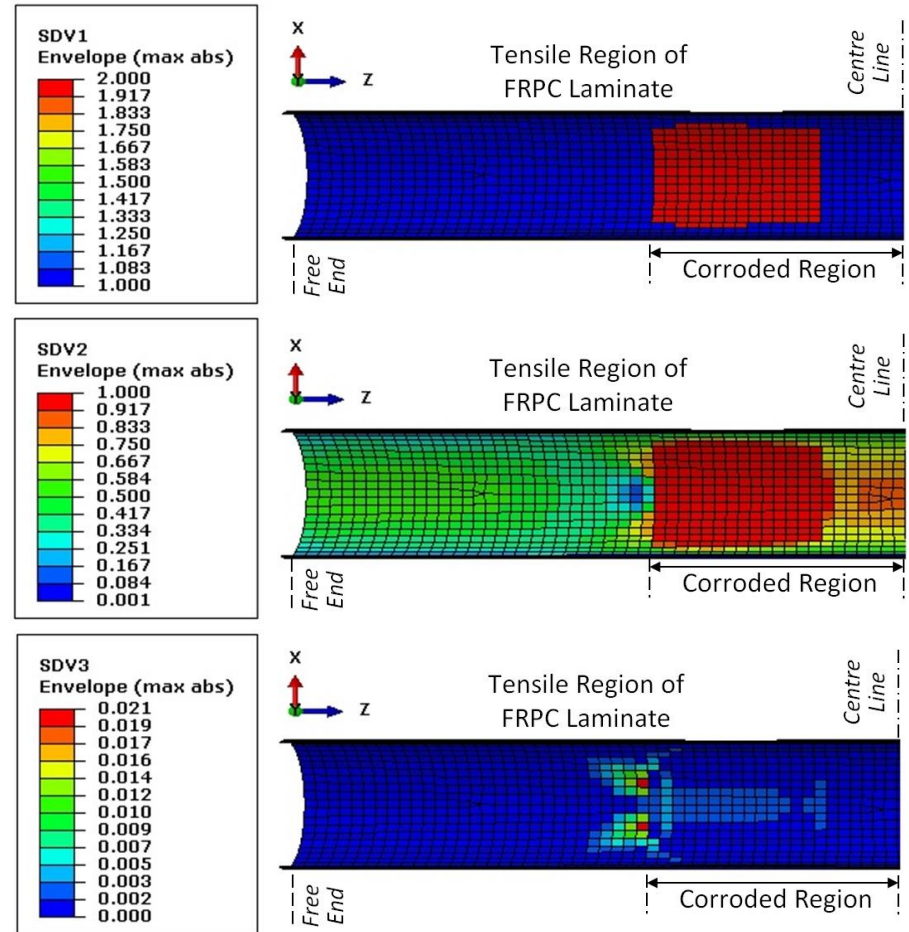
- At 44MPa and 1785kN, no failure is predicted on the FRPC laminate.
- The addition of tensile force increases the stress within the matrix. SDV2 has a higher maximum value of 0.158 compared to the pure internal pressure case where maximum value of SDV2 is only 0.042.
- Fibres are still able to sustain the hoop stress. However, off-axis fibre alignment may be able to reduce to stress carried by the matrix.



**Combined Static Load:**

2) Internal Pressure + Tensile Load + Bending Moment

- Matrix failure occurs within the FRPC laminate. However, the axial stress on the riser has exceeded the yield strength of the riser and failure will occur outside the repaired region before the complete failure of the FRPC.
- SDV2 shows that matrix cracking propagates from the corners of the corroded region.
- SDV3 indicates that the fibres are not providing maximum reinforcement as they are not aligned in the axial direction. Consequently, the matrix is carrying higher load which leads to crack initiation.



## 4.8 Cyclic Loading

The cyclic behaviour of offshore pipe riser repaired with FRPC was studied. FE model that takes into account failure mechanisms of the composite interlaminar delamination, disbonding at the composite-steel riser interface, and the maximum permissible strain of the repaired riser was developed. The effects of combined static loads on composite interlaminar and steel riser-composite interface bond were captured through a fracture mechanics approach called Virtual Crack Closure Technique (VCCT). The effects of cyclic bending due to dynamic subsea wave forces were evaluated through a direct low cycle fatigue analysis, where the onset of fatigue delamination and disbonding growth are characterized based on the Paris Law. The fatigue crack growth initiation criterion,  $f$ , and crack evolution are represented through Eq. 4-27 and Eq. 4-28 respectively.

$$f = \frac{N}{c_1 (G_{\max} - G_{\min})^{c_2}} \geq 1.0 \quad 4-27$$

$$\frac{da}{dN} = c_3 (G_{\max} - G_{\min})^{c_4} \quad 4-28$$

where  $N$  is the number of cycles,  $G_{\max}$  and  $G_{\min}$  are strain energy release rates when the model is loaded up to maximum and minimum load respectively, while  $c_1$ ,  $c_2$ ,  $c_3$  and  $c_4$  are material constants. The materials constants were adapted from NASA's reports on fatigue characterisation of graphite epoxy composite and development of benchmark examples for fatigue growth predictions prepared by (O'Brien, et al., 2010) and (Krueger, 2011). Madelpech et al (Madelpech, et al., 2009) studied the fatigue behaviour of disbond mechanism in metallic structures repaired with bonded composite patch provided the material

constants of fatigue crack growth at the steel-composite interface. The fatigue criterion constants are recorded in Table 4-10. Due to limitation of available data and resources, it is important to note that values for the energy release rate and fatigue constants used in this study are not taken from measurements of the exact material used in the FE modelling.

Table 4-10, Steel-composite interface and composite interlaminar fatigue properties

		<b>Steel-Composite Interface</b>	<b>Composite Laminate Inter-layer</b>
	<b>c<sub>1</sub></b>	0.5	0.21164
<b>Fatigue Constants</b>	<b>c<sub>2</sub></b>	-0.1	-6.25
	<b>c<sub>3</sub></b>	$7.03226 \times 10^{-12}$	0.33
	<b>c<sub>4</sub></b>	4.6	5.55

#### 4.8.1 Design Conditions

Data on the cyclic bending load was based on nonlinear dynamic analysis of marine risers under random loads in Indian Offshore (Khan, et al., 2011). In Khan et al.'s study, it was found that the maximum bending stress (along the length of the riser) due to random wave and current forces is 263.73MPa. This value was interpreted as the maximum amplitude of the cyclic bending while the computed average of the random wave, having a period of 14.4 seconds were taken as input data in the FE model. Linear periodic loading as shown in Figure 4-61 was used.

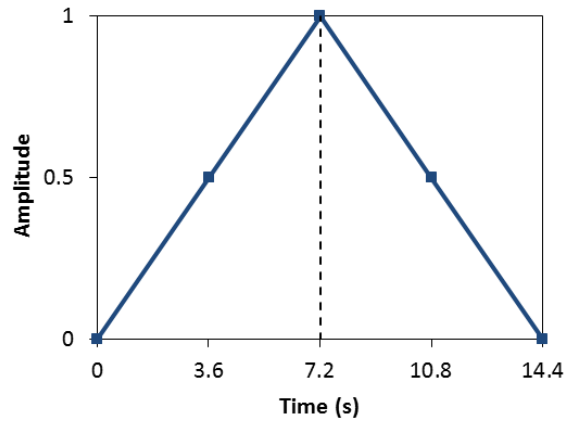


Figure 4-61, Input of cyclic bending load

#### 4.8.2 Numerical Modelling

ABAQUS® v6.11-3 was used to model the corroded riser and CRS. Both the steel riser and composite sleeve were meshed with four-node reduced integration shell elements, S4R. The bending configuration, boundary conditions, and dimensions of the riser and corroded region are identical to those described in Figure 4-19. Stress amplitude for bending was set to vary between zero and maximum values while the amplitude for internal pressure and tensile load were kept constant at DL throughout the time step. An initial disbond defect was modelled at the edge of steel-composite interface and interlayer of the composite laminate. The dimensions of the defect was  $2\text{mm} \times 2\text{mm}$  along the axial and arc length respectively, as shown in Figure 4-62. The size of the initial defect is similar to those quoted in the study of inherent defect size in composite materials (Considine, 2010). Two types of laminate orientation were considered in this work. Two types of fibre orientation were considered, (i) unidirectional axially orientated (AO) repair where the fibres are aligned along the axis of the riser and (ii) hoop orientated (HO) repair where the fibres are aligned in the circumferential direction of the riser.

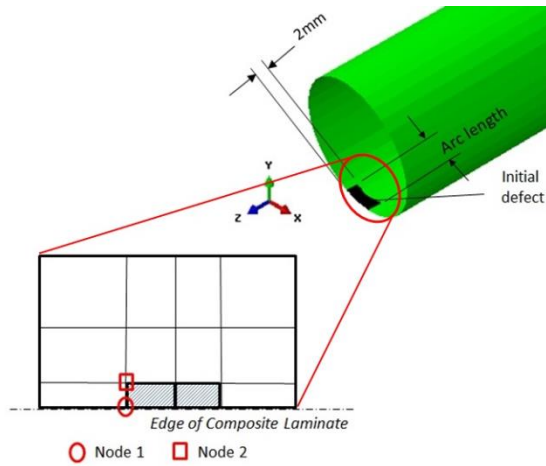


Figure 4-62, Defect region and locations of node 1 and node 2 on the laminate

### 4.8.3 Results and Discussion

#### 4.8.3a Effects of Static Loading

When subjected to a combination of mixed mode static loadings, it can be observed that mode I separation has negligible effects, as shown in Figure 4-63. The dominant separation is in Mode II with slight contribution from Mode III, indicating that disbonding at the steel-composite interface and delamination with the composite under combined  $P_{in}$ ,  $F_t$  and  $M_b$  are largely due to in-plane and out-of-plane shear stresses.

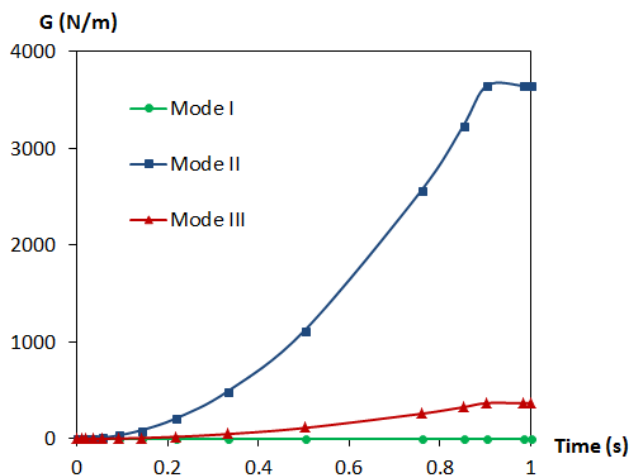


Figure 4-63, Strain energy release rate for AO laminate

Nevertheless, these two failure mechanisms are unlikely to occur at design conditions, which is equivalent to bending moment of 78kNm. As depicted in Figure 4-64, only slight disbonding ( $f_{criterion} > 1$ ) occurred at the node near the edge of the laminate (node 1 in Figure 4-62) for the corroded riser repaired with AO laminate while no disbonding was observed for the HO laminate.

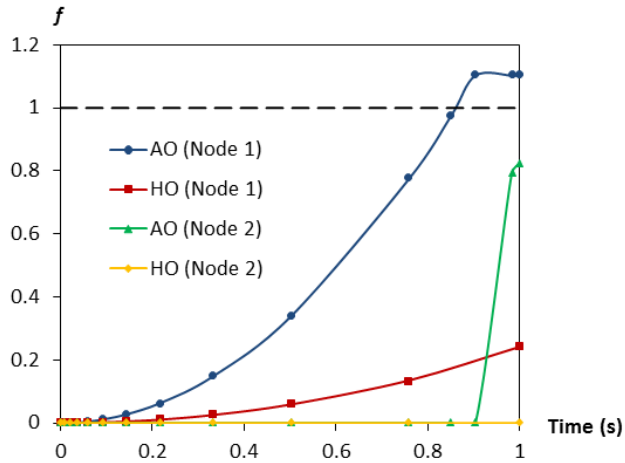


Figure 4-64,  $f_{criterion}$  for AO and HO laminate at node 1 and node 2

The high value of  $f_{criterion}$  at node 1 arises due to the defect modelled at the edge of the laminate. The disbonding did not propagate to the inner node (node 2 in Figure 4-62) as the  $G_{equiv}$  did not reach the  $G_{equivC}$ . As the bending moment increased further, extensive yielding outside the repaired region takes place, indicating that failure has occurred. Figure 4-65 shows the contour plot where an obvious transition of strain was observed from the repaired region to the bare, unrepaired pipe region.

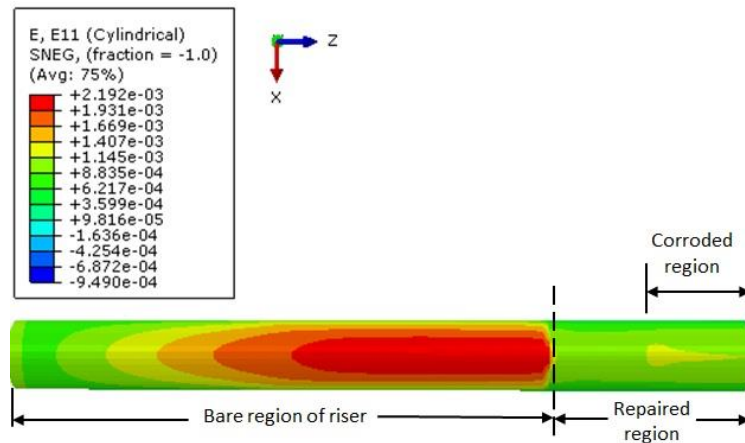


Figure 4-65, Contour plot of axial strain

### 4.8.3b Effects of Cyclic Loading

The low cyclic fatigue analysis revealed that the CRS is more susceptible to failure at the steel-composite interface. With the presence of an initial bonding defect between the FRPC and the steel riser, low cycle fatigue bending load can cause the disbonding to propagate. The disbonding was observed to propagate rapidly, as shown by the axial ( $\sigma_a$ ) and hoop ( $\sigma_h$ ) stresses experienced in the AO and HO composite laminates with increasing number of fatigue cycles, depicted in Figure 4-66 and Figure 4-67, respectively. The result demonstrated that the AO laminate was able to sustain higher stress in the axial direction before disbonding takes place (Figure 4-66) and vice versa for the HO laminate (Figure 4-67). Once disbonding occurs, the stress levels on the laminate drops to much lower values, indicating that load transfer from the corroded riser to the CRS is no longer effective. The high rate of disbonding propagation may be attributed to the coarse meshing. A finer mesh can provide better propagation rate but must be compromised by longer simulation time. However, it is observed that no disbonding occurs when there is no initial disbond defect being modelled between the FRPC laminate and the steel riser.



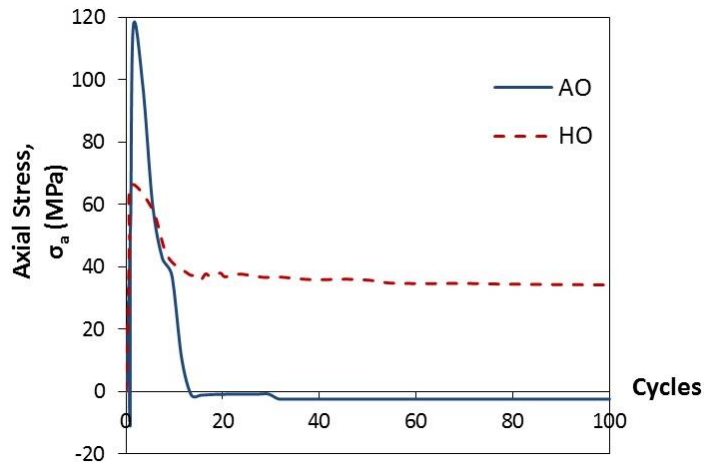


Figure 4-66, Axial stress vs. number of cycles for AO and HO laminates

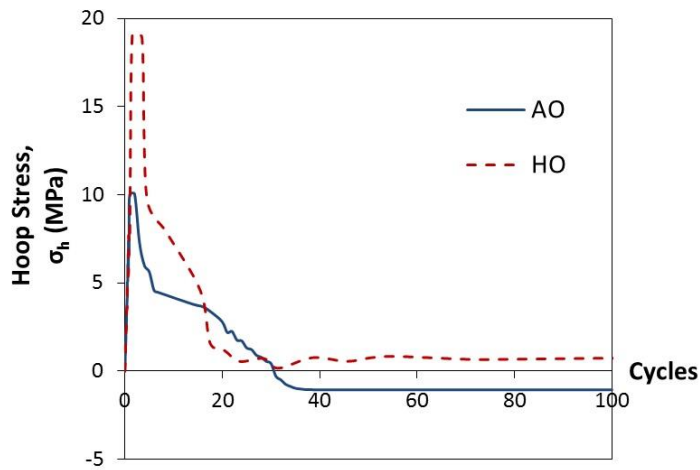


Figure 4-67, Hoop stress vs. number of cycles for AO and HO laminates

### 4.8.3c Effects of Laminate Orientation

Different laminate orientations affected the degree of debonding between the composite and steel riser surface. Figure 4-68 and Figure 4-69 show the final bonded state of the corroded risers repaired with AO and HO laminates respectively. The value of 1 signifies complete bonding while 0 indicates complete disbonding. The HO laminate provided better bonding between the steel-composite interfaces where a large proportion of the corroded region is still bonded by the CRS. For corroded riser repaired with unidirectional AO laminate,

failure of the system can be observed as the remaining bonded area is too small for any significant load transfer. This is also observed in Figure 4-66 and Figure 4-67 where the HO laminate was still able to carry higher amount of stress compared to the AO laminate after certain degree of disbonding in both axial and hoop directions.

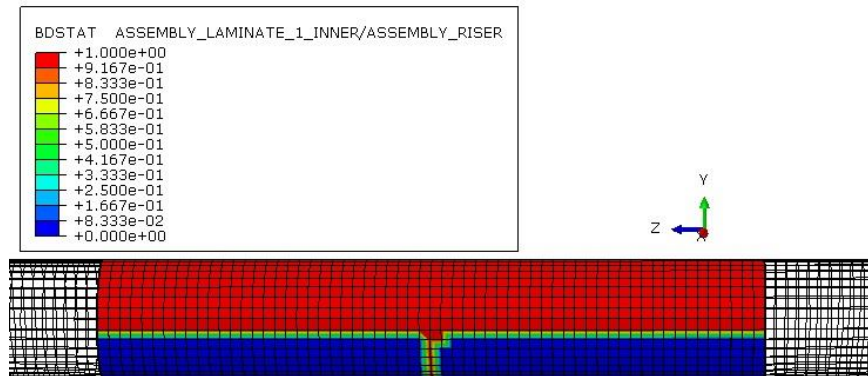


Figure 4-68, Final bonded state of AO laminate on riser

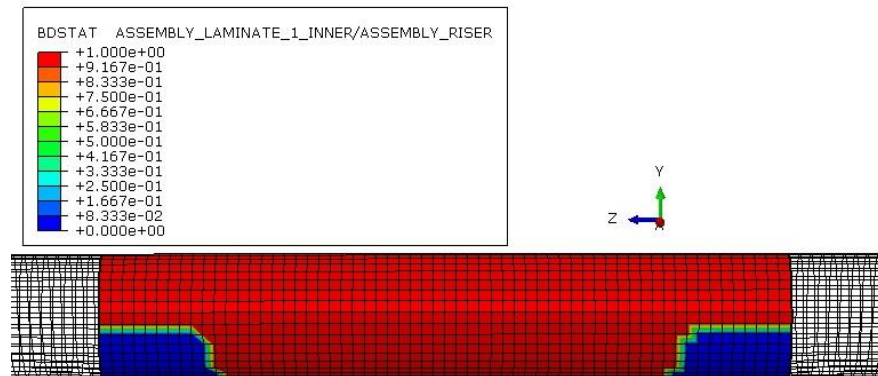


Figure 4-69, Final bonded state of HO laminate on riser

#### 4.9 Concluding Remarks

The use of FEA has proved to be an effective tool to study the CRS for offshore riser repair. The convergence study of the FE model was important in order to produce a model that is sufficiently accurate in capturing the behaviour of the

CRS. The use of S4R shell elements instead of three dimensional continuum elements reduces the simulation resources in terms of time and memory space. A finite element model with optimal mesh density was produced. The validation of this numerical model was conducted via classical mechanics equations and also through a case study of an industrial pipe rehabilitation product (HES<sup>TM</sup>). Further validation through a set of scaled-down experimental tests is demonstrated in Chapter 5 .

The study of the CRS was conducted at a macro level where the rules of mixture are applied. The properties of the FRPC were directly obtained from values quoted in other literatures. Along with the assumptions of perfect bonding between the steel riser and the composite material, the FE model was validated to be sufficiently accurate in predicting the CRS under different types of loadings. Validation of the FEA model using classical mechanics equations show great accuracy with percentage difference of less than 8%. The use of MCT failure criteria to characterise the FRPC demonstrated that no micro-failures such as matrix cracking or fibre breakage occur in the repair laminate under normal operating conditions.

Within the FEA, the hoop and axial stresses and strains were used to evaluate the performance of the CRS. It was shown that combined loadings cause higher level of stress and strain in both the hoop and axial direction of the riser. The localised corrosion defect has a more prominent deterioration effect on the riser in terms of hoop and flexural strength. The use of conventional composite repair where the reinforcing fibres are aligned in the hoop direction is incapable of reinforcing a corroded riser such that it can function within the safety limits.

Study on cyclic loading demonstrated that disbonding at the composite-steel riser interface dominated the failure mechanism of the CRS compared to the interlaminar delamination. When subjected to static loadings, neither of the failure mechanisms were observed and further increment in bending load causes failure of the steel riser outside the repaired region. In contrast, with the presence of an initial disband defect, low cycle fatigue loading weakens the bond between the composite and steel riser which subsequently causes initiation and propagation of disbonding between the two. By minimising the defect size at the steel-composite interface, the occurrence of such failure under low-cycle fatigue conditions can be prevented. Hence, careful surface preparation, adequate use of adhesive and wrapping technique are important to ensure sufficient level of integrity in adhesion between the two surfaces with minimised defects.

Local analyses have shown that the major design study that needs to be accounted for is the static analysis of combined load. Low cycle fatigue analysis has demonstrated that no failure via steel-composite disbonding will occur if no initial defect is present at the edge of the steel-composite interface. The factors affecting the performance of the composite repair are types of reinforcing fibre, angle orientation of composite laminate, dimensions of the composite repair (i.e. thickness and length) and the dimensions of the localised corrosion defect (i.e. width and length). These factors can be further studied by modifying the FE model within the CAE interface or directly amend the parameters in the input file.

## **Chapter 5 Experimental Testing**

### **5.1 Introduction**

Analysis of the design and deformation stress-strain responses of a series of CRS subjected to varying functional and environmental loadings were conducted in Chapter 3 and Chapter 4. In order to further prove the accuracy of the FEA model, validation was carried out against scaled experimental four-point bending analysis. Within the scaled experimental setup, readily available materials were used in a four-point bending test scaled to a significantly smaller size. Full scale testing was not chosen in the current research mainly due to the limited material availability and cost, long lead times in materials preparation, experimental setup and resources. This chapter outlined the materials, equipment and setup of the four-point bending experimental. Throughout the chapter, the simulation setup was referred as the model while the experimental setup was referred as the prototype. Detailed discussion of a similitude approach used to relate the full scale model to the scaled down prototype was explained. As in the case of the FEA, three conditions of the pipe were setup for the four-point bending tests, as described below:

- 4) Bare pipe without corrosion damage.
- 5) Bare pipe with corroded region manifested as material loss in thickness.
- 6) Corroded pipe repaired with composite laminates.

### **5.2 Methodology**

The FEA model developed in this work was validated by determining the accuracy of the simulated strain output with that of the experimentally measured

deformation strain in the case of four-point bending. A single element linear electrical resistance strain gauge with a gauge length of 6 mm was used to measure the strain in the axial direction of the bent pipe. The strain in the transverse direction was not measure as it has been shown in the FEA models that the axial strain is the more dominant factor when the pipe is subjected to bending. In order to determine the level of accuracy of the FEA model, the comparison of the FEA and experimental results are carried out in 3 consecutive cases,

- 1) Both model and prototype are identical in terms of materials and size
- 2) Both model and prototype are identical in terms of materials, the model was defined in full scale (e.g. actual pipe dimension) while the prototype was scaled to a smaller size
- 3) Model and prototype are different in terms of materials, the model was defined in full scale (e.g. actual pipe dimension) while the prototype was scaled to a smaller size

### **5.3 Materials**

The materials used in this study differ between the simulation and experiment. However, step by step comparison between the simulation and experimental results are conducted following the 3 consecutive cases described in section 5.2 . It should be noted that the simulation described in Chapter 4 were setup based on material properties that are used widely in the industry for applications of oil and gas pipeline. On the other hand, the experimental analyses were developed by utilising materials that can be obtained at lower cost and are readily available, i.e. mild steel pipe. These mild steel pipes were chosen from the same batch to

avoid inconsistency in material properties. Dumbbell specimens were machined from the mild steel pipes, Figure 5-1, for characterisation of the mechanical properties in tension. The specimens were prepared in accordance to ES EN ISO 377, Steel and Steel Products – Location and Preparation of Samples and Test Pieces for Mechanical Testing (CEN, 1997)



Figure 5-1, Dumbbell specimens

A total of four specimens were tested in accordance to ES EN 10002-1, Metallic Materials – Tensile Testing – Part 1: Method of Test at Ambient Temperature (CEN, 2001). The specimens were loaded at a rate of 1 mm/min at ambient temperature, 25°C. The average of the stress-strain data were obtained and converted into true stress versus true strain curve, which were used as the input data for the FE model of mild steel pipe for case 1 and 2 as defined in section 5.2 . The tensile true stress-true strain curve as obtained from the chosen mild steel pipe material is shown in Figure 5-2.

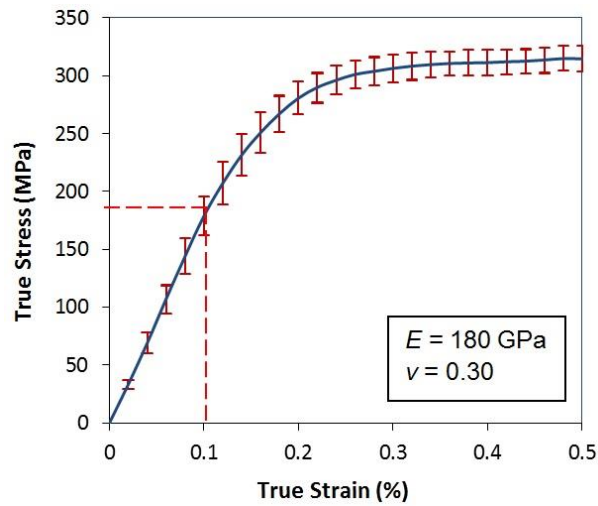


Figure 5-2, True stress vs. true strain curve of the chosen mild steel pipe

For the composite material, purchase of any specific prepreg has to be done in bulk which increases the cost of this research. Hence, a Panex35/MTM57 unidirectional carbon/epoxy prepreg system manufactured by Cytec® which is readily available in the University’s composite stock was chosen as the repair material. The material properties are obtained from open literature as defined by Coutts-Smith et al. (Coutts-Smith, et al., 2013) in their work of exploring the bend-twist coupling and structural response of thin laminated beams manufactured using Panex35/MTM57 carbon/epoxy. The preparation and testing conducted by Coutts-Smith et al. were in accordance to ASTM Standard D3039 (ASTM, 2000) for tensile properties and ASTM Standard D5379 (ASTM, 2012) for in-plane shear properties. The material properties of Panex35/MTM57 are shown in Table 5-1.

Table 5-1, Material properties for Panex35/MTM57 unidirectional prepreg

Property	Value
Longitudinal Modulus, $E_1$ (GPa)	129
Transverse Modulus, $E_2$ (GPa)	7.51
Longitudinal Tensile Strength, $X^T_1$ (MPa)	1630



Transverse Tensile Strength, $X_{T_2}^T$ (MPa)	34.5
Longitudinal Tensile Failure Strain, $\varepsilon_{T_1}^T$ (%)	1.25
Transverse Tensile Failure Strain, $\varepsilon_{T_2}^T$ (%)	0.421
Poisson Ration, $\nu_{12}$	0.264
In-plane Shear Modulus, $G_{12}$ (GPa)	3.68

#### 5.4 Experimental Setup

Based on the readily available apparatus and materials, the pipe dimension for the four-point bending test (prototype) was scaled down by a ratio of 6.488:1. Pipe specimens of 1000 mm in length, 1.59 mm in thickness and 34.93 mm in outer diameter were setup with both of it ends extended well beyond the supports of the four-point bending rig, as shown in Figure 5-3.

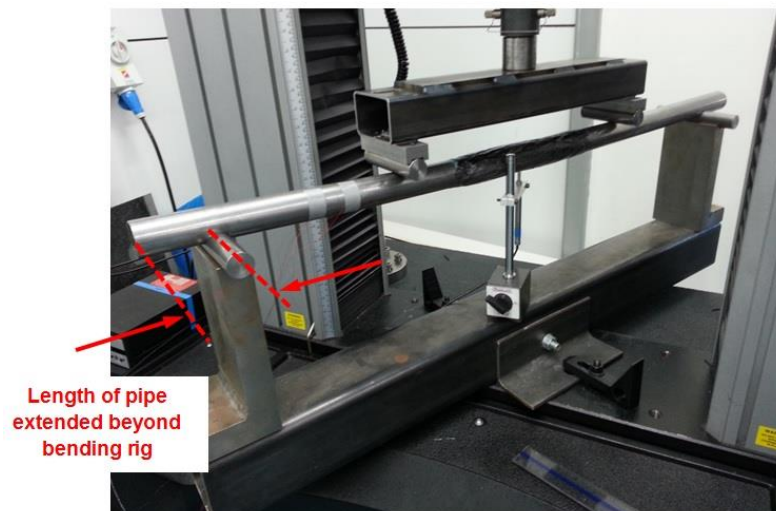


Figure 5-3, Length of pipe relative to bending rig

An equivalent external corrosion of 50% loss in wall thickness, measuring 93 mm in axial length and 8 mm in width (projected arc), was machined in the middle section of the pipe. Two uniaxial, single element linear strain gauges were used to measure the strain on the pipe surface within the region wrapped by the carbon/epoxy prepreg, one is bonded to pipe surface within the corroded

section while the other is bonded to pipe surface outside of the corroded region, as shown in Figure 5-4.

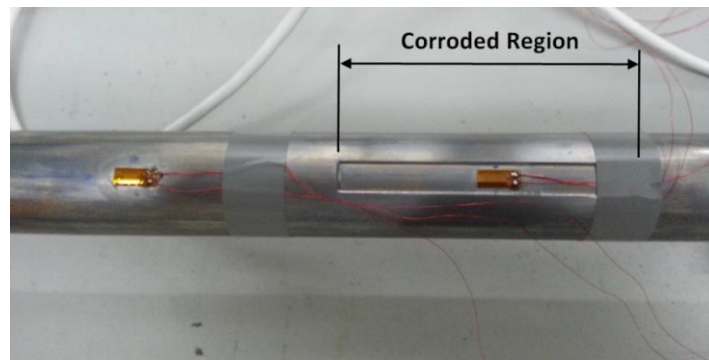


Figure 5-4, Machined corroded region and location of the two strain gauges

A four-point bending rig with total span of 860 mm between the two supports and a span of 400 mm between two loading points was used. The four-point bending test was conducted with the aid of an Instron series 5581 floor model load frame equipped with a 50 kN load cell. The supports of the four-point bend setup were machined from two rollers in such a way that the pipe's lateral movements were fully constrained. The complete setup of the pipe and bending rig on the load frame is shown in Figure 5-5. Bending load of 4 kN was applied onto the pipe at a rate of 2 mm/min.



Figure 5-5, Four-point bending setup with the aid of an Instron load frame

The mild steel pipes were wrapped with the Panex35/MTM57 carbon/epoxy prepreg, with the fibre direction being varied at different angles, where the fibres of the prepreg were aligned along the axis of the pipe ( $0^\circ$ ), followed by  $30^\circ$ ,  $45^\circ$ ,  $60^\circ$  and lastly  $90^\circ$  where the fibres are in the hoop direction. It must be clarified that the prepreg wrapped with fibre orientation parallel, i.e.  $0^\circ$ , to the longitudinal axis of pipe was made possible due to the large size of the prepreg sheet and the small diameter of the pipe. Prior to the wrapping of carbon/epoxy prepreg, the strain gauges were covered with a layer of insulation film (as shown in Figure 5-6) due to the conductive nature of the carbon fibre within the prepreg.

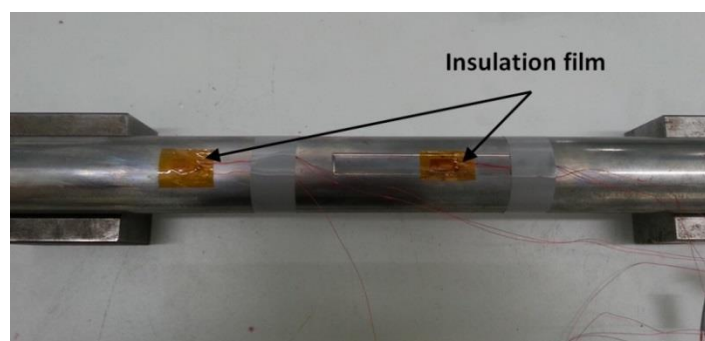


Figure 5-6, Insulation film applied on top of strain gauges

Most conventional composite repair method for pipeline consists of a flexible layup of on-site wetted or pre-impregnated composite laminate where final curing takes place at the site of repair, or installation of pre-cured shells that are pre-manufactured for specific pipe diameter. Considering the repair method of winding a prepreg tape around the riser, the axial orientated repair laminate is not practically achievable as the wrap must progress around the length of the pipe in a circumferential wind, making it more of a helical winding. In the industry, an axially orientated repair laminate can be achieved with pre-cured half cylinder shells that are bonded to the pipe. Although on-axis on-site wrapping of prepreg composite laminate is technically not viable, the modelling of pure on-axis and off-axis plies as well as the combination of both were conducted with the aim to provide further insight into the effects of fibre orientation on rehabilitation performance of the CRS. Figure 5-7 shows the wrap done at varying angles. It can be observed that the ends of the wrap were not properly aligned around the circumference of the pipe due to the helical wrap angle of the prepreg sheet at a particular fibre orientation. However, the wraps are sufficiently long such that they extend way beyond the corroded section and the end effects in this case can be assumed to be negligible.

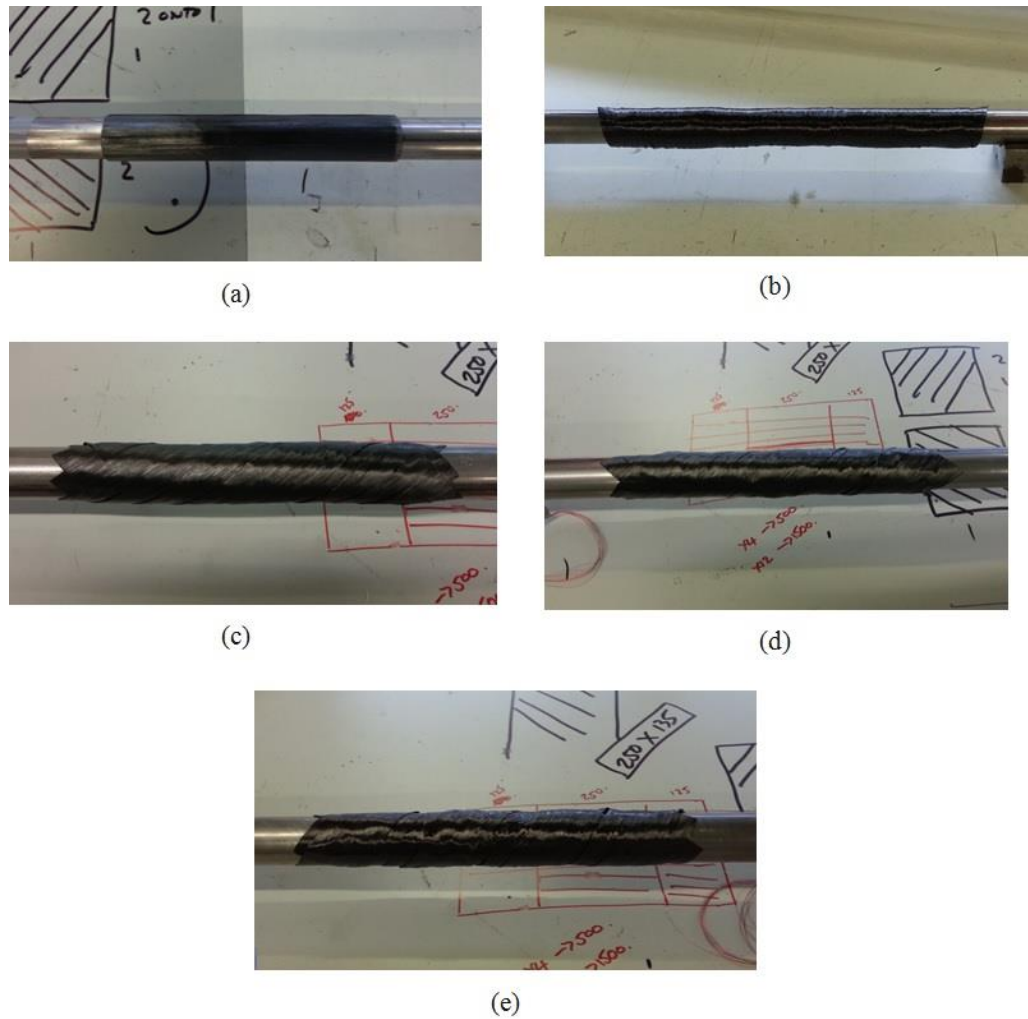


Figure 5-7, Specimens of mild steel pipe wrapped with Panex35/MTM57 carbon/epoxy prepreg (a) 0° wrap (fibres aligned along axial direction of the pipe), (b) 90° wrap (fibres in hoop direction), (c) 30° wrap, (d) 45° wrap, and (e) 60° wrap

After wrapping the corroded pipes with the carbon/epoxy prepreg, a release film was wrapped on top of the prepreg to absorb excessive resin flow during the curing process. A breather felt was then used to wrap the whole specimen to ensure that the pressure is uniformly distributed during the curing process. The whole specimen was sealed inside a nylon bagging film for vacuum bagging. Figure 5-8 shows the specimen being sealed air-tight inside a nylon bagging film. Figure 5-9 shows a compressor connected to the valve of the nylon bagging

apparatus while Figure 5-10 shows an image captured at the end of the vacuum bagging process.

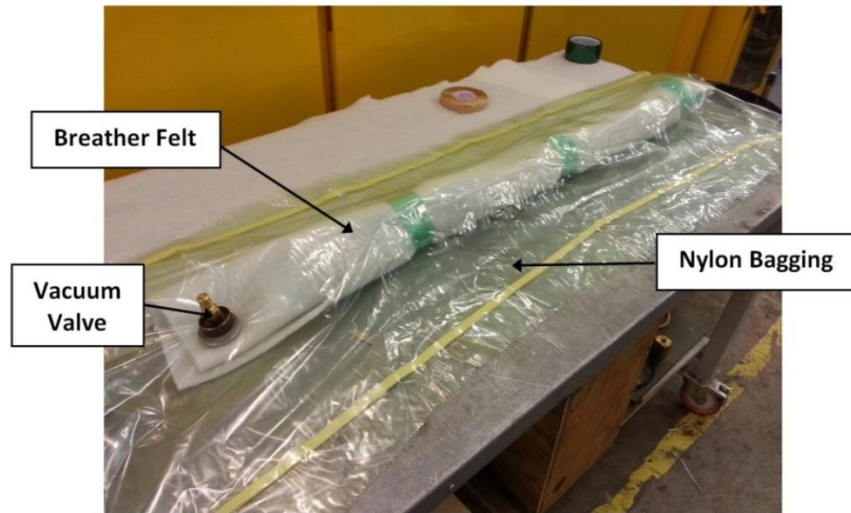


Figure 5-8, Pipe specimen sealed within a nylon bagging film

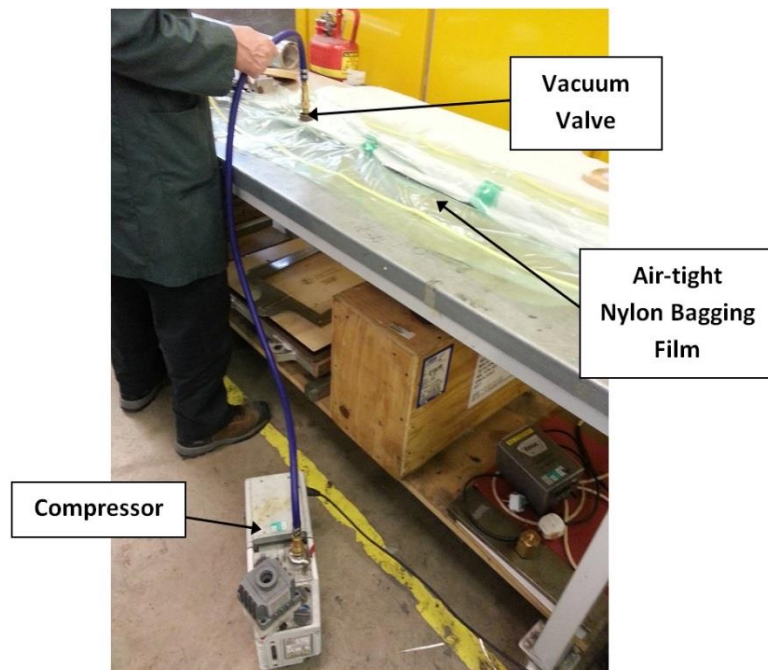


Figure 5-9, Vacuum bagging of the pipe specimen



Figure 5-10, Curing of the composite prepreg performed with the aid of vacuum bagging

The composite prepreg was allowed to cure within an autoclave at 0.62MPa, under a controlled cycle of 100°C for 3 hours as recommended in the MTM57 MSDS sheet (UMECO, 2012). The different curing time needed for alternate curing cycles at different temperatures is shown in Table 5-2. The usual 120°C for 1 curing cycle was not used to prevent the damaging of strain gauges under high temperature.

Table 5-2, Curing conditions and alternative cure cycle for autoclave cure of MTM57

Autoclave cure	
Vacuum bag pressure	Minimum of 980mbar (29"Hg)*
Autoclave pressure	6.2 bar (90 psi)**
Ramp rate	1 to 3°C (1.8 to 5.4°F)/minute
Recommended cure cycle	1 hour at 120°C, +5/-0°C (248°F, +9/-0°F)
Cool down	Maximum of 3°C (5.4°F)/minute to 60°C (140°F)
Alternative cure cycles	
Temperature	Duration
80°C (176°F)	12 hours
100°C (212°F)	3 hours

## 5.5 Similitude Relations

In order to minimise cost in terms of raw materials, experimental equipment and setup time, small scale testing was utilised in the present work. Scaling laws

fulfilling similitude requirements were applied between the simulation (model) and the scaled experimental setups (prototype). Similitude relations can be derived based on material properties and loading cases of the model and the prototype, and hence are varied from case to case basis. It should be noted that when scaling is done between model and prototype of the same material (i.e. bare pipe) subjected to an individual loading type alone, the relations can be straight forward. Based on the size ratio between the two and the types of the applied load (i.e. point load, uniformly distributed load, pressure, moment), the value of the applied load can be increased, decreased or maintained to produce identical stress-strain curves. For example, when an internal pressure is applied to a thin shell tube ( $r/t \geq 10$ ), the equation relating the stress to the applied pressure can be computed using equation using Eq. 5-1.

$$\sigma_{hoop} = \frac{P_{int} r}{t} \quad 5-1$$

If the dimensions of the pipe are scaled using a consistent size ratio,  $S$ , both the pipe radius,  $r$  and thickness,  $t$  shall be reduced by the same order of magnitude. Hence, applying the same magnitude of internal pressure,  $P_{int}$  will result in the same stress value, as shows in Figure 5-11. The subscript “ $o$ ”, “ $m$ ” and “ $p$ ” denote the outer radius, model and prototype respectively. The similitude relations which consider loading within the elastic region of a material can be relatively straightforward. Table 5-3 shows a set of similitude relations as a function of geometrical parameters, material properties and loadings (Ramu, et al., 2012). In the present work, a scaled four-point bending test was conducted to validate the accuracy of the FE model. In determining the scaling ratio between the model and the prototype that consist of a single material, the applied bending load can be scaled based on the relation shown in Table 5-3.



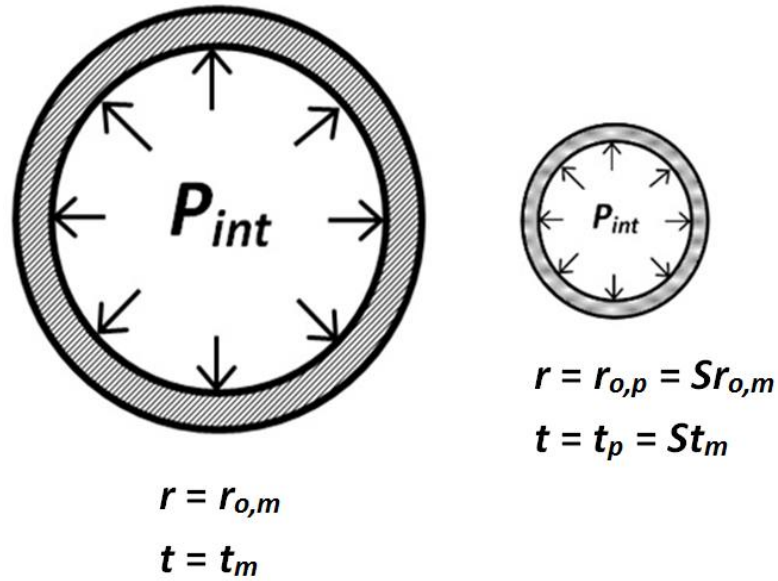


Figure 5-11, Similitude scaling between model and prototype

Table 5-3, Similitude relations (Ramu et al, 2012)

Parameters	Scale factor
Dimension ( $h_p$ = Height or $t_p$ = Thickness)	$S$
Area $A_p$	$S^2$
Volume $V_p$	$S^3$
Linear Displacement $U_p$	$S$
Moment of inertia $I_p$	$S^4$
Frequency $f$	$S^{-1/2}$
Density $\rho_p$	$S_E/S$
Point Load $F_p$	$S_E \cdot S^2$
Line Load $F_L$	$S_E \cdot S$
Uniformly Distributed surface Load $P_p$	$S_E$
Shear force $V_p$	$S_E \cdot S^2$
Moment, M or Torque $T$	$S_E \cdot S^2$
Stress $\sigma_p$	$S_E$

$S$ -Geometric scale factor,  $S_E$ -Ratio of Young's Modulus of model and prototype

In the case of an additional material, i.e. the prepreg FRPC, the interaction between the two dissimilar materials must be taken into account. In the current study, it was assumed that the steel and the composite are perfectly bonded such that an ideal deformation stress transfer from the steel pipe/riser to the composite is achieved. In order to accurately compute the scaling ratio between a model

and a prototype that each contains two dissimilar materials subjected to bending load, the flexural stiffness must be calculated. Derisi et al. carried out a similitude study on the bending stiffness of composite tubes whereby an ‘equivalent’ aluminium tube that matched the flexural stiffness of the laminated composite tube was created in order to match the stress-strain behaviour between the two. (Derisi, et al., 2012). In the present work, a limitation exists in identifying a prototype that is capable of matching the flexural stiffness of the model. Hence, a similitude relation was built by comparing the flexural stiffness of the CRS model and prototype respectively, and scaling was performed on the value of the bending load accordingly. Within the elastic limits, the combined flexural stiffness of the pipe repaired with prepreg FRPC is taken as the sum of the individual flexural stiffness of the pipe and the prepreg, as shown in Eq. 5–2.

$$EI_{s-c} = E_s I_s + E_c I_c \quad 5-2$$

Where  $E$  is the modulus of elasticity and  $I$  is the second moment of area for a cylindrical structure. The subscript “s” and “c” denotes the steel pipe and prepreg composite, while the subscript “s-c” represents the pipe repaired with prepreg. The combined flexural stiffness of the repaired pipe for the model and the prototype can then be written as,

$$(EI_{s-c})_M = (E_s I_s)_M + (E_c I_c)_M \quad 5-3a$$

$$(EI_{s-c})_P = (E_s I_s)_P + (E_c I_c)_P \quad 5-3b$$

where subscripts  $M$  and  $P$  denotes the model and prototype respectively. For a beam subjected to bending, the bending stress and bending strain can be related to the applied bending moment via the following equations,

$$\sigma_b = \frac{My}{I} \quad 5-4a$$

$$\varepsilon = \frac{\sigma_b}{E} \quad 5-4b$$

where  $y$  is the distance from the point where stress is computed to the neutral axis of the structure. The resulting bending strain (as a function of the flexural stiffness of the repaired pipe) can be derived by combining equations Eq. 5-3a, 5-3b, 5-4a and 5-4b, as shown in Eq. 5-5a and Eq. 5-5b.

$$\varepsilon_M = \left[ \frac{M_M y_M}{(EI_{s-c})_M} \right] \quad 5-5a$$

$$\varepsilon_P = \left[ \frac{M_P y_P}{(EI_{s-c})_P} \right] \quad 5-5b$$

Figure 5-12 demonstrates a schematic of the experimental setup as well as the distribution of the bending moment along the length of the pipe subjected to four point bending.

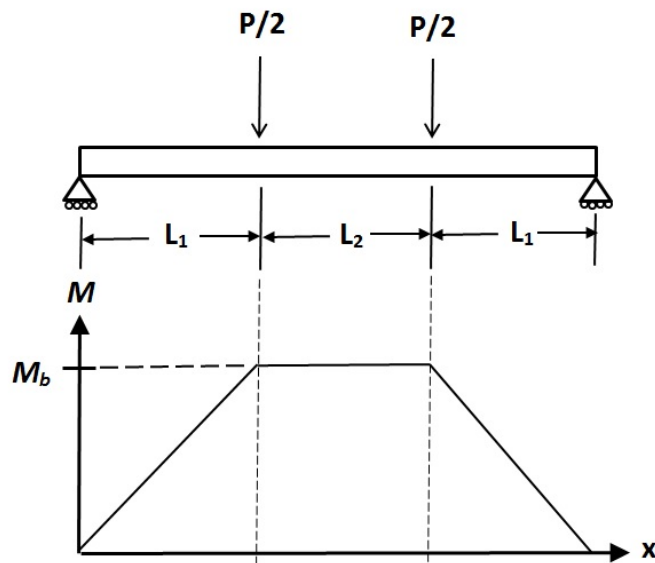


Figure 5-12, Bending moment diagram for four-point bend setup

The resulting bending moment is uniform between the span of the two loading points, which can be given by Eq. 5–6,

$$M_b = \frac{PL_2}{2} \quad 5-6$$

The resulting bending strain can then be related to the applied loading and longitudinal length of the pipe by substituting Eq. 5–6 into Eq. 5–5a and Eq. 5–5b, represented as Eq. 5–7a and Eq. 5–7b,

$$\varepsilon_M = \left[ \frac{P_M L_M y_M}{2(EI_{s-c})_M} \right] \quad 5-7a$$

$$\varepsilon_P = \left[ \frac{P_P L_P y_P}{2(EI_{s-c})_P} \right] \quad 5-7b$$

Comparison between the model and the prototype was performed through the load-strain response. In order to obtain a similar strain output for the model and the prototype, the applied bending load must be multiply by a scale factor. To determine the magnitude of this scale factor, equation Eq. 5–7a was equated against equation Eq. 5–7b. The terms  $L$  and  $y$  can be eliminated by including the geometrical scale factor,  $S$ , between the model and the prototype. Finally the value of the bending load of the full scale model can be computed using Eq. 5–9.

$$\varepsilon_M = \varepsilon_P \quad 5-8a$$

$$\frac{P_M S L_P S y_P}{2(EI_{s-c})_M} = \frac{P_P L_P y_P}{2(EI_{s-c})_P} \quad 5-8b$$

$$P_M = \frac{1}{S^2} \left[ \frac{(EI_{s-c})_M}{(EI_{s-c})_P} \right] \quad 5-9$$

## **5.6 Experimental Validation**

As discussed in section 5.2, three FE models were setup. The details of the mesh, boundary conditions, loading condition and interaction properties of the model were presented in Chapter 4 . A ramp load with fixed time increment was chosen such that the stress-strain behaviour at different bending load can be observed. Perfect bonding between the composite laminate and the steel riser was defined. This conservative solution assumed that maximum load transfer from the steel riser to the composite laminate takes place.

### **5.6.1 Bare Riser without Corrosion**

Figure 5-13 depicts the simulated axial strain plotted against experimental data of mild steel bare pipe without corrosion under a bending load. As demonstrated, the model with the same dimensions and materials were able to capture accurately, the load-strain behaviour of the steel pipe subjected to an incremental bending load. By using the scaling law for a bending moment, a similar load-strain curve can be obtained. It can be demonstrated that the use of reduced integration 4 node shell elements, S4R can accurately capture the bending behaviour of the mild steel pipe. In addition, the mesh density is also proven to be adequate.

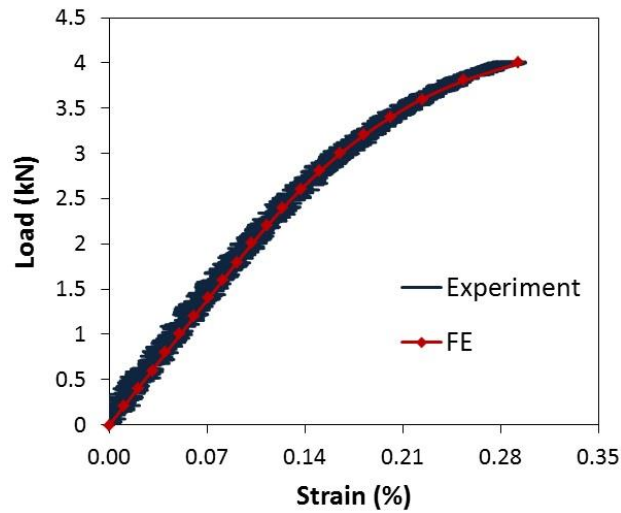


Figure 5-13, Experiment and FE results of mild steel pipe

### 5.6.2 Bare Riser with Corrosion

The mild steel pipe was machined with a 93mm × 8mm (length × width) cut-out, equivalent to 50% loss in wall thickness to simulate a corrosion defect at the centre of the pipe. In the FE model, the section thickness for a predetermined set of elements was defined accordingly while all other portions remains as the original thickness of the pipe, as shown in a contour plot in Figure 5-14.

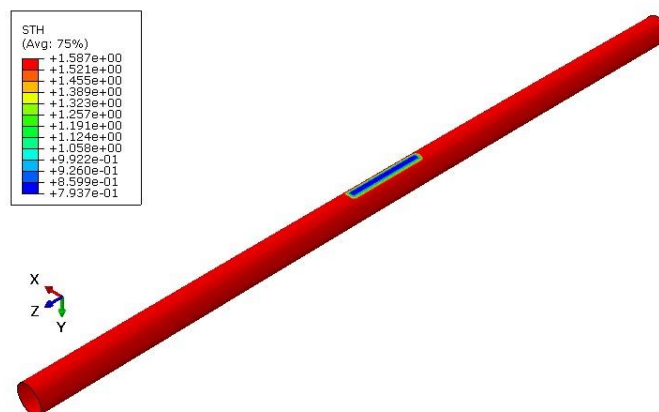


Figure 5-14, Section thickness of pipe in FE model

A comparison of the results between the experimental and the FE model is shown in Figure 5-15. A minor discrepancy exist where the simulated model predicted

a greater capability to sustain higher bending load at the same strain.. One of the potential reasons for this discrepancy could be attributed to the edges of the machined corrosion defect where stress concentration can occur. Due to the relatively large surface of the gauge element on the scaled-down corrosion defect, higher strain values adjacent to the edges of the defect can be recorded.

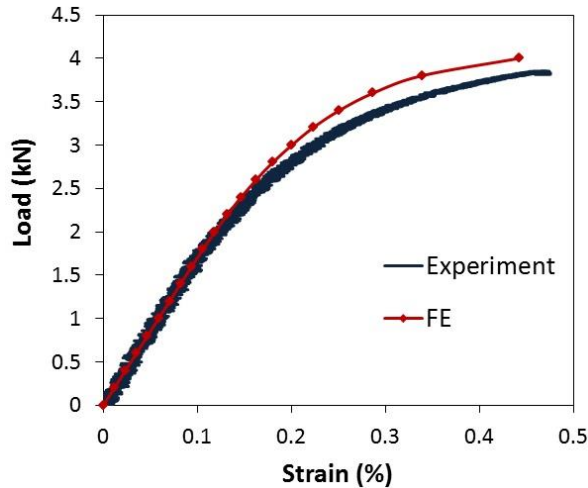


Figure 5-15, Experiment and FE results of corroded mild steel pipe

A third order polynomial curve fit was performed on the experimental data pair to filter out the recorded noise in the test and to produce strain output at specific load increments where comparison between the simulation and experimental data set can be carried out. Figure 5-16 shows the curve of the raw experimental data plotted using approximately 9600 data points and the polynomial curve fitted using 20 data points. Both curves show good agreement with coefficient of determination,  $R^2$  of the fitted polynomial curve being higher than 0.995. Using the data points of the polynomial curve, the percentage difference and root mean square (RMS) error between the experimental and simulation results were calculated. The same computation was done for the rest of the specimens, i.e. bare pipe without corrosion and corroded pipe repaired with varying fibre

orientation of the prepreg wrap. The third order polynomial curve fits of all the respective experimental data for different specimens gave  $R^2$  values of  $\geq 0.995$ . The results of the percentage difference and RMS error are tabulated in Table 5-4.

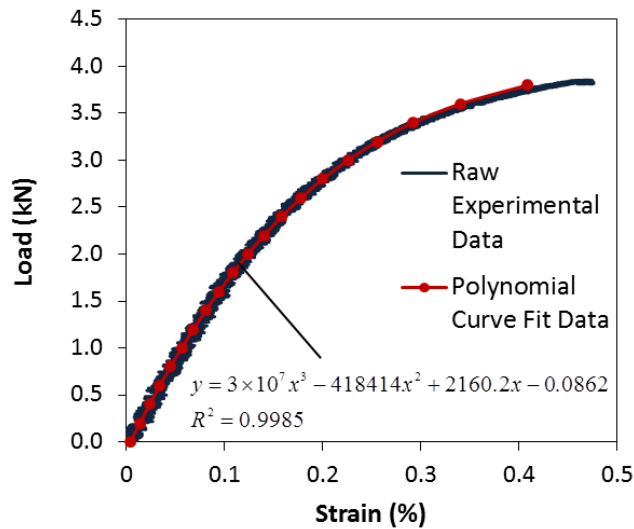


Figure 5-16, Raw experimental data & polynomial curve fit data

Table 5-4, Percentage difference & RMS error between experimental and simulation results

Polynomial Fit vs. Direct FE	Percentage Difference (%)	R.M.S
Bare Pipe	4.44	0.003499
Corroded Pipe	15.95	0.024811
0° Prepreg	25.47	0.023255
30° Prepreg	10.83	0.012443
60° Prepreg	5.61	0.001769
90° Prepreg	7.58	0.009125

The percentage difference and RMS error for the corroded mild steel pipe are computed as 15.95% and 0.024811 respectively. The high values might be attributed to the systematic error in the machining of pipe wall loss. The magnitude of the wall thickness is only in the scale of millimetres (i.e. 1.5875mm)



as the prototype is scaled to a considerably smaller size. A 50% loss in wall thickness amounts to a minimal reduction of 0.79375mm. Fluctuation of less than 0.16mm in the machining of the material loss is equivalent to 10% of systematic error. To study the effect of this systematic error, the wall thickness of the corroded region in the FE model was varied from 20% to 60% of its initial wall thickness. The percentage difference and RMS error between the experimental and simulation results with different wall thickness in the corroded region was recorded, as depicted in Figure 5-17.

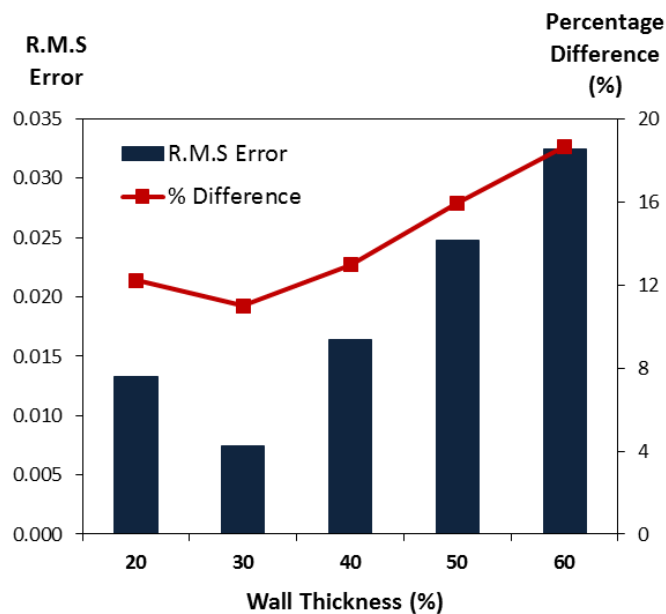


Figure 5-17, Percentage difference & RMS error between experimental and simulation results at varying wall thickness in the corroded region

It can be observed from Figure 5-17 that as the wall thickness in the corroded region changes from 50% to 30%, the percentage difference between the experimental and simulation results drops from 15.95% to 10.99%. This indicates that the systematic error in the machining of the wall loss resulted in a corroded region of approximately 0.48mm. Additional sources of error can be traced to the size of gauge element, where the strain is measured over a larger

surface area in the prototype as compared to the model where strain is extracted from a single element.

### 5.6.3 Repaired Riser

The corroded mild steel pipe were repaired with unidirectional carbon fibre prepreg with the fibres align in angles of  $0^\circ$ ,  $30^\circ$ ,  $60^\circ$  and  $90^\circ$ . Figure 5-18 shows the load-strain curve of the experimental and simulation results.

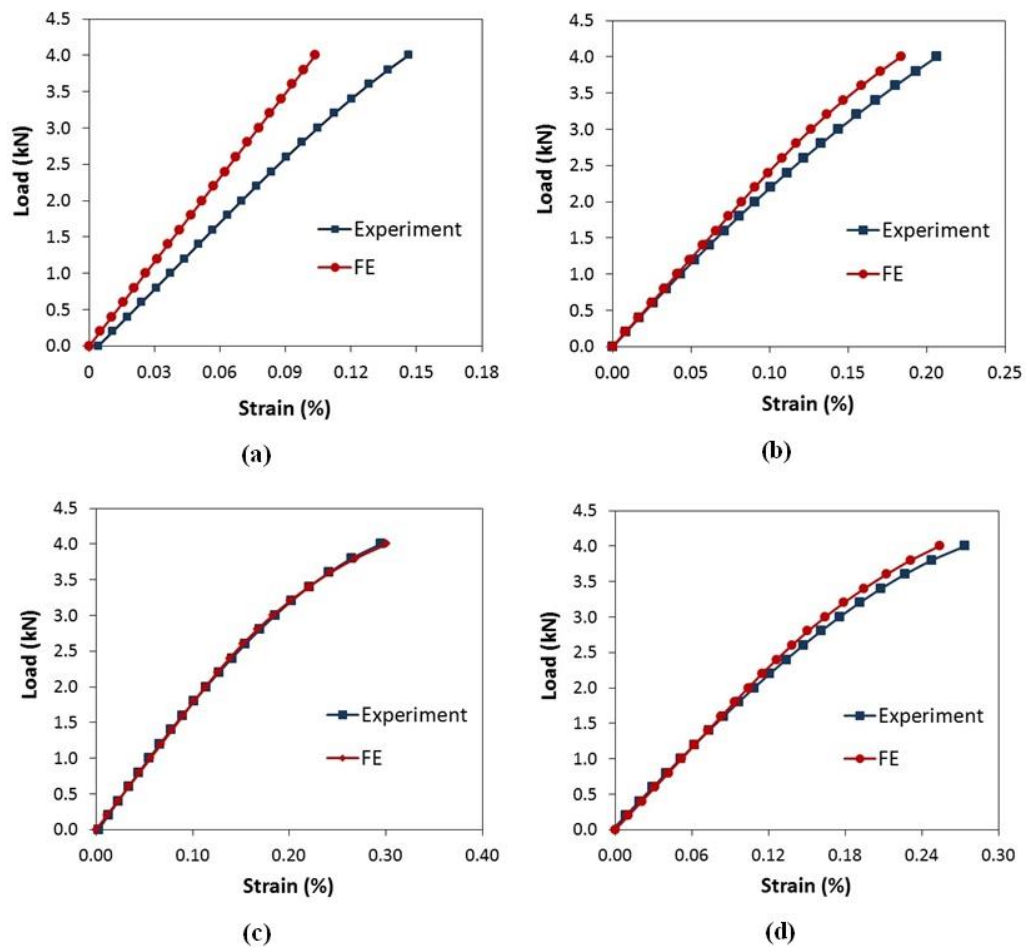


Figure 5-18, Experiment and FE results of corroded mild steel pipe repaired with MTM57 carbon/epoxy prepreg – (a)  $0^\circ$  prepreg, (b)  $30^\circ$  prepreg (c)  $60^\circ$  prepreg (d)  $90^\circ$  prepreg

All prototypes show good agreement with the FE model except for the case of 0° repair with a percentage difference of 25.47%. The percentage difference and RMS error for each case are shown in Figure 5-19.

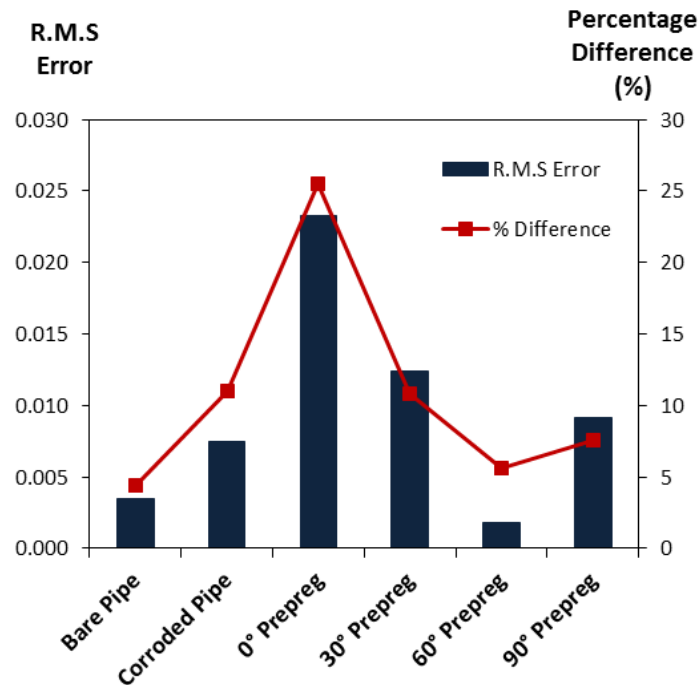


Figure 5-19, Percentage difference & RMS error between experimental and simulation results of different specimens

It is clear from Figure 5-18 that as the fibres aligned closer to the direction of loading, the higher the RMS error between the experimental and simulation results. The FE model overestimated the strengthening effects of the carbon fibre prepreg. This discrepancy could be due to the assumption of perfect bonding between the carbon fibre prepreg and steel pipe, where stress transfer from the steel pipe to carbon fibre prepreg is at its maximum effectiveness. The second possible reason for the overestimated FE results is the scaling of the prototypes. In a real-life pipe repair scenario, the defect area is relatively large compared to the fibre reinforced composite used to wrap around the pipe. This ensures sufficient surface contact between the two while curing takes place. However,

with the pipe scale to a smaller size, the contact area between the carbon fibre prepreg and the defect area is limited during the course of curing. In addition, the ratio of fibre density to volume of repair laminate is lower in a small scale setup. In the micro level, the “number of fibres” in a given thickness of the FRPC laminate cannot be scaled.

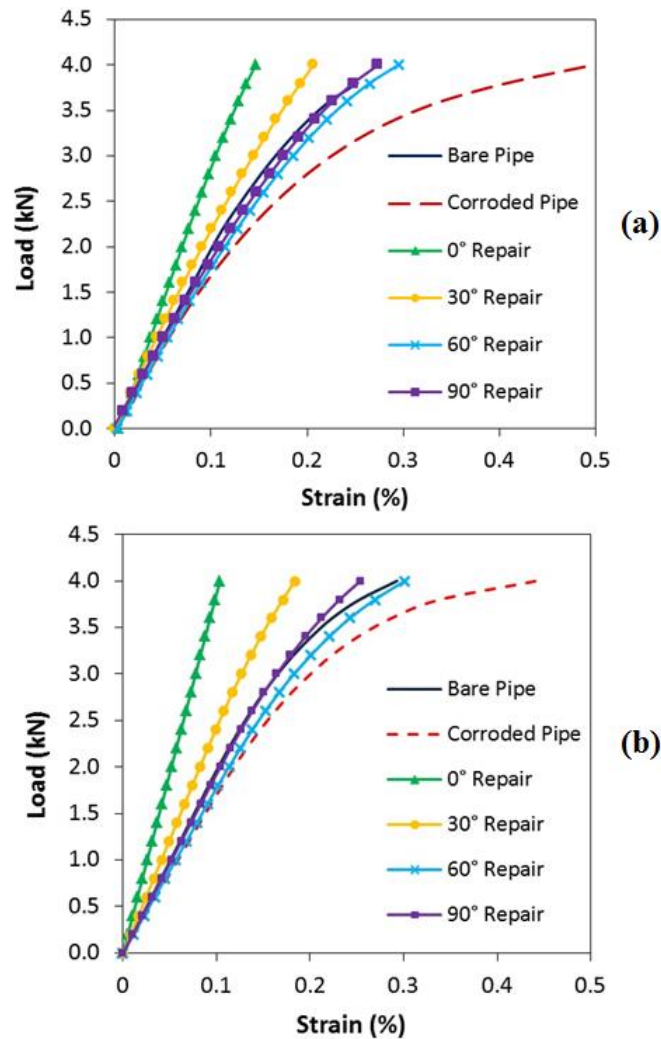


Figure 5-20, Load-strain curve of bare pipe, corroded pipe and corroded pipes (Mild Steel pipe) repair with varying fibre angle orientation (Panex35/MTM57 Carbon/Epoxy prepreg) – (a) Experimental results (b) FE simulation results

Comparison of the load-strain behaviour between the pipes with and without repair is shown in in Figure 5-20(a) and Figure 5-20(b), respectively. The results

demonstrated a similar trend in the pipe specimens with and without repair. The corroded pipe repaired with 0° prepreg shows the best strengthening performance, followed by the 30° repair. The strength properties of FRCP are anisotropic and maximum strengthening could be achieved when the fibres are aligned in the direction of the load, which in this case is the axial stress cause by bending. As the fibres rotated further away from the axial direction of the pipe, the strengthening effect reduces and thicker composite repair will be required to achieve the same amount of strengthening. However, the load-strain curve for the 60° repair shows poorer strengthening compared to the 90° repair even though the fibres are closer aligned to the direction of the load. This can be explained by the higher transverse modulus of the 90° laminate compared to the 60° laminate, as calculated using Eq. 5–10. The higher transverse modulus resists the transverse strain caused by the Poisson’s ratio effect, which in turn reduces the positive axial strain cause by the bending force.

$$\frac{1}{E_{yy}} = \frac{\sin^4 \theta}{E_{11}} + \frac{\cos^4 \theta}{E_{22}} + \frac{1}{4} \left( \frac{1}{G_{12}} - \frac{2\nu_{12}}{E_{11}} \right) \sin^2 2\theta \quad 5-10$$

#### **5.6.4 Comparison between Full Scale Model and Scaled Down Prototype**

The experimental test using mild steel and MTM57 carbon fibre/epoxy prepreg scaled to a smaller size was used to verify the results of an actual size simulation model comprises of materials commonly used in the oil and gas industry. In the earlier section, a full scale model that utilises mild steel and MTM57 carbon fibre/epoxy prepreg was compared to a scaled down model using the same material to validate the accuracy of the scaling law based solely on the change in dimension. Figure 5-21 shows that a scaled model of identical materials is

capable of producing a response that can represent a full scale model by using the appropriate scaling laws.

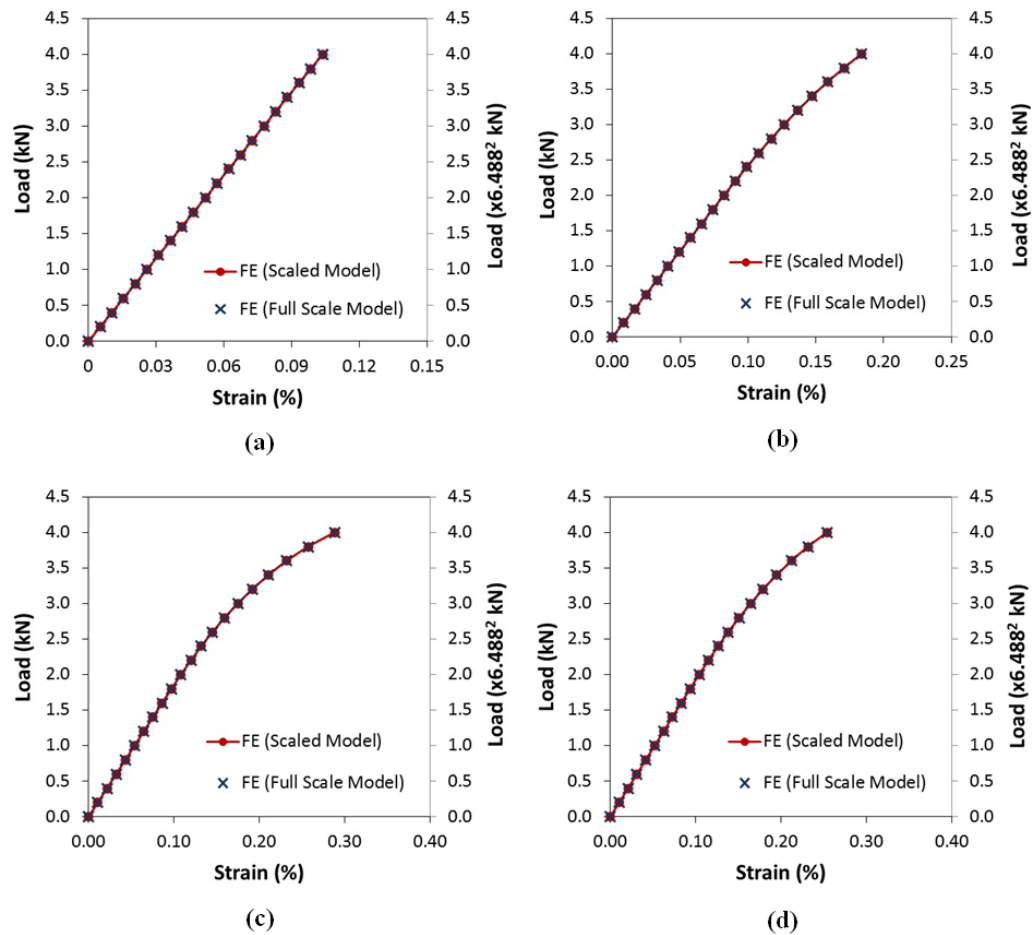


Figure 5-21, FE results of full scale and scaled models for corroded mild steel pipe repaired with MTM57 carbon/epoxy prepreg – (a) 0° prepreg, (b) 30° prepreg (c) 60° prepreg (d) 90° prepreg

A full scale model of API 5L X60 steel pipe repaired with AS4/3501-6 carbon/epoxy prepreg is then studied. As discussed in Chapter 4, Section 4.5, the scale ratio between the prototype and the model can be calculated based on the size ratio, stiffness ratio of the pipe material and stiffness ratio of the FRPC repair material. The results are shown in Figure 5-22.

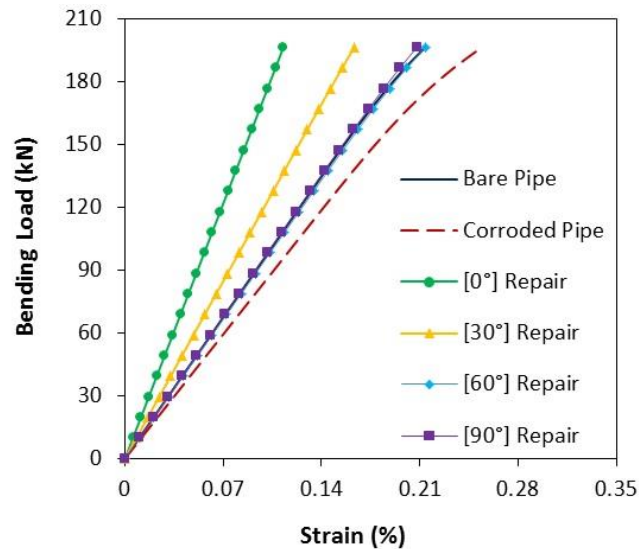


Figure 5-22, Load-strain curve of bare pipe, corroded pipe and corroded pipes (API 5L X60 pipe) repaired with varying fibre angle orientation (AS4/3501-6 Carbon/Epoxy prepreg) – FE simulation results

The load-strain curves showed that all cases have similar trend to those obtained from the scaled experimental tests shown in Figure 5-20(a). However, the load-strain curves for the API 5L X60 steel pipe model repaired with AS4/3501-6 carbon/epoxy show that the structure remains within the elastic region. The scaling between model and prototype of different materials was done on the basis of the elastic stiffness of the materials, hence not accounting for the plastic response. It is apparent that the API 5L X60 steel pipe capable of sustaining much higher bending load as it has a yield stress of 483MPa compared to the mild steel pipe which is only 248MPa.

## 5.7 Concluding Remarks

In this chapter, the setup of scaled experimental tests was discussed in detail. Full size tests were not chosen due to the limitation in various resources. The results of the scaled flexural tests of corroded pipes repaired with varying angle

orientations of FRPC showed a similar trend to those simulated in the FEA model. Using the similitude relations developed, the FEA models show good agreement with the small scale experimental tests, particularly within the elastic region of the stress-strain response, with percentage differences of approximately 2% to 13% for corroded risers repaired with  $[30^\circ]$ ,  $[60^\circ]$  and  $[90^\circ]$  FRPC prepreg. The study of the CRS for corroded risers is conducted via the combination of limit state analysis and FEA model, where the stress-strain values at design condition (elastic response) are considered. With these experimental test results, the accuracy of the FEA model at design conditions is further strengthened, and the parametric study of the CRS in repairing corroded risers can be conducted using the FEA model.



# **Chapter 6 Parametric Study of Composite Repair System for Offshore Riser**

## **6.1 Introduction**

The previous chapters demonstrated that FEA modelling could serve as an effective method for the optimisation oil and gas pipelines CRS and the simulated static and dynamic behaviours of the CRS are broadly within reasonable accuracy. Within the FEA model, the optimized element type, mesh refinement, boundary conditions, interaction properties and loads were established. In the current chapter, the developed model was used to conduct a multi-variables study on the effects of process parameters and material compositions on the performance of the CRS. The parameters being studied include the type of reinforcement fibre, types of laminate orientation, wrapping angle of the FRPC, thickness and length of the repair laminate, and the geometry of the corrosion. For application in the pipeline industries, the study taken into consideration where the parameters must be transferrable to the construction of an automated CRS repair machine. A series of externally applied loads were employed in the current study, the different load profiles are summarised in Figure 6.1 below.

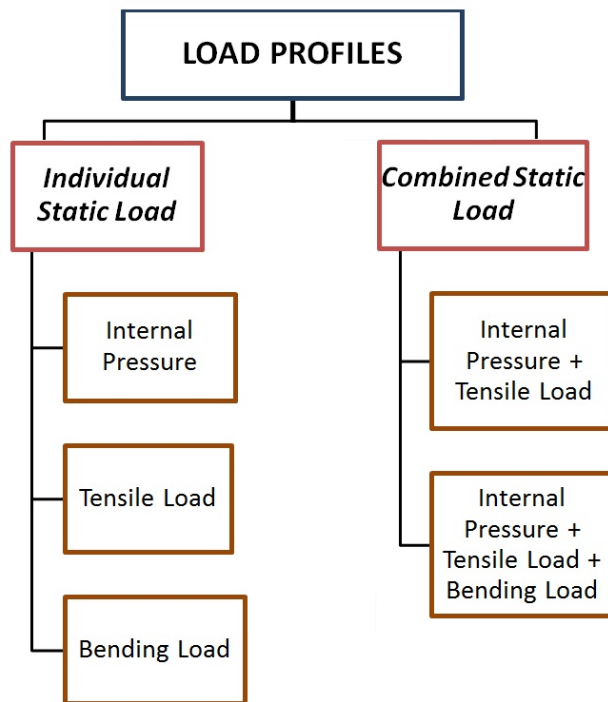


Figure 6-1, Load profiles on composite repair system

## 6.2 Types of Reinforcing Fibres

The reinforcing fibres within a composite material are the primary component that carries the load and the resulting strength of composite is highly directional dependent, with longitudinal along the fibres being much stronger. A wide range of fibres such as carbon, glass, aramid, polyethylene, boron, polyester, nylon and natural fibres are commonly used in composites to suit varying performance requirements of the final products. Among all these, carbon, glass and aramid fibres are those that are widely used commercially as composite repair for onshore pipelines. The choices of selected fibres are dependent on the economic and performance requirement of the rehabilitation. In general, glass fibres are low cost, easily available and more compatible with resin systems while carbon fibres poses concerns in terms of cost, availability and compatibility with certain resin systems. Nevertheless, when compared to glass fibres, carbon fibres exhibit higher strength and stiffness, lower density and superior fatigue performance

(Ochola, et al., 2004) (Wonderly, et al., 2006) (Giancaspro, et al., 2010). Aramid fibres are not suitable for the application of offshore riser repair because they tend to absorb water and degrade in moisture rich conditions (Tanaka, et al., 2002) (Sala, 2000). Both glass and carbon fibres absorb water and exhibit lower strength when immersed in water. However, this effect is more dominant in glass fibre at elevated temperatures (Lassila, et al., 2006) (Ray, 2006). A comparison study of seawater durability of carbon- and glass-polymer composites was conducted by Kootsookos et al. (Kootsookos, et al., 2011). The results of this study showed that the percentage weight gain due to moisture absorption in glass fibre polymer composites is more prominent than carbon fibre polymer composites (Figure 6-2).

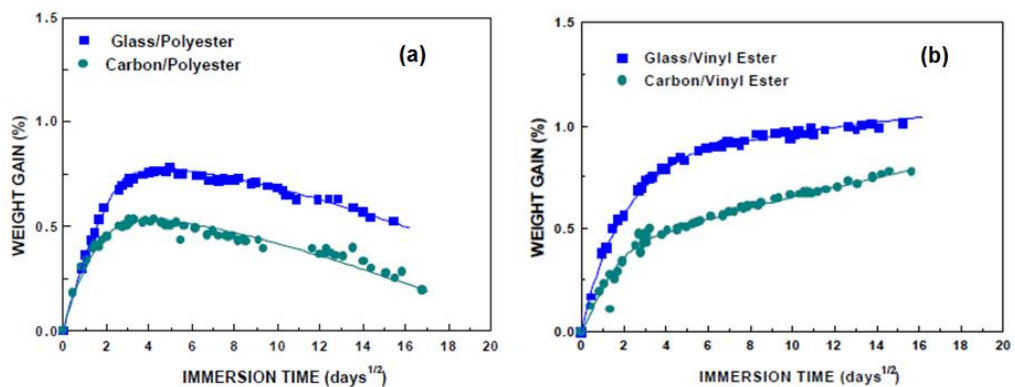


Figure 6-2, Weight gain percentage in glass- and carbon- (a) polyester, (b) Vinyl ester composites (Kootsookos, et al., 2011)

The use of carbon fibre as reinforcement in steel risers can give rise to galvanic corrosion problems. Carbon is a good cathode that can cause electrochemical coupling with steel at the interface of the repair (Tavakkolizadeh & Saadatmanesh, 2001). Since galvanic corrosion can only initiate when there is direct contact between the carbon fibre and the steel in the presence of an electrolyte, measures can be taken to eliminate one of the parameters. For

example, a layer of glass fibre can be applied before the laying of the carbon fibre reinforced composite. Alexander (Alexander, 2007) developed a hybrid composite repair system that utilises the combination of an inner and outer layer circumferential E-glass reinforcement and axial carbon fibre pre-cured halve shells. In addition, application of corrosion-resistance infill on the surface of the steel riser can also inhibit galvanic corrosion.

Considering the suitability and requirement of the application, aramid fibre has been omitted due to its high moisture absorption property and the two types of reinforcing fibres being considered in this study are carbon and glass fibres. The resulting FRPC of the CRS are given below.

- 1) AS4 carbon fibres coupled 3501-6 epoxy matrix;
- 2) E-glass 21×k43 Gevetex fibres coupled LY556/HT917/DY063 epoxy matrix.

The material properties of these composite systems were abstracted from the first world-wide failure exercise (WWFE) as discussed in section 5.4.3b of Chapter 5. Using these two FRPC materials, the composite repair system subjected to different individual and combined loadings are simulated. Serving as a reference for comparison purposes, two additional types of on-axis repair laminates were also considered in the current section, these include:

- 1) Repair where fibres are aligned in the longitudinal axis of the riser ( $0^\circ$ )
- 2) Repair where fibres are aligned in the hoop direction of the riser ( $90^\circ$ )

## 6.2.1 Individual Static Load

### 6.2.1a Internal Pressure, $P_{int}$

As described in Section 3.2.1 of Chapter 3, internal pressure is one of the main loadings sustained by a riser. Figure 6-3 shows the plot of internal pressure against hoop strain for CRS with  $[0^\circ]$  and  $[90^\circ]$  laminates.

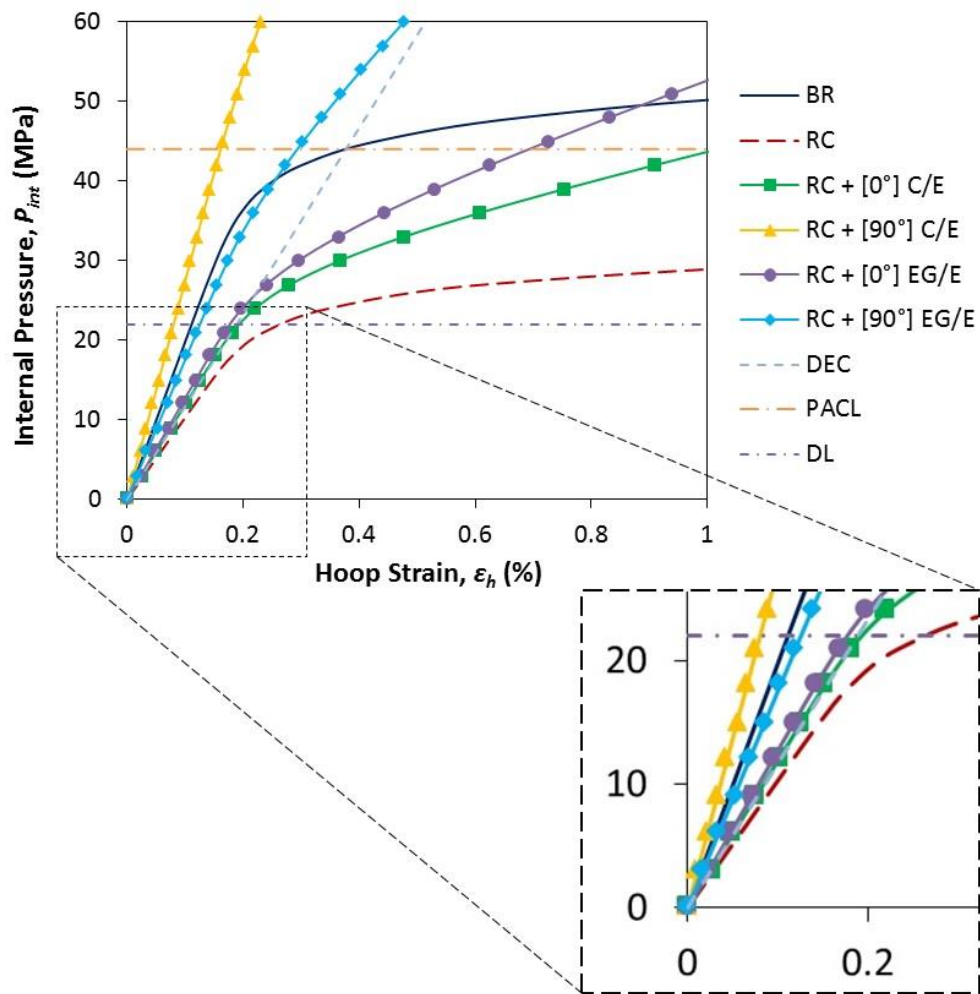


Figure 6-3, Internal pressure vs. hoop strain of corroded riser repaired with  $[0^\circ]$  and  $[90^\circ]$  laminates

The enlarged section shows that for the case of corroded risers repaired with  $[0^\circ]$  carbon/epoxy laminate and E-glass/epoxy laminate, both system experienced hoop strain closed to the maximum permissible hoop strain,  $\epsilon_{h-max}$  at design load

of 22MPa. The maximum hoop strain values at 22MPa for the corroded riser repaired with  $[0^\circ]$  carbon/epoxy and  $[0^\circ]$  E-glass/epoxy are 0.192% and 0.178% respectively. This indicated that reinforcing capability of the FRPC with  $[0^\circ]$  laminates does not fulfil the design requirement regardless of the type of reinforcing fibres used. With  $[90^\circ]$  orientated laminates, the hoop strain in the corroded region at 22MPa for the corroded riser repaired with carbon/epoxy and E-glass/epoxy is 0.08% and 0.125% respectively. Figure 6-4 and Figure 6-5 show the hoop strain contour plot for cases of corroded riser repair with  $[0^\circ]$  and  $[90^\circ]$  carbon fibre and glass fibre laminates. A distinctive different can be observed on the case of CRS using carbon/epoxy, where the maximum hoop strain occurs outside of the repair region, as shown in Figure 6-5(a). The simulated output suggested that the performance of corroded riser repaired with  $[90^\circ]$  carbon/epoxy orientated laminates clearly outweighs the E-glass/epoxy although both have similar fibre volume fraction (60% and 62%).

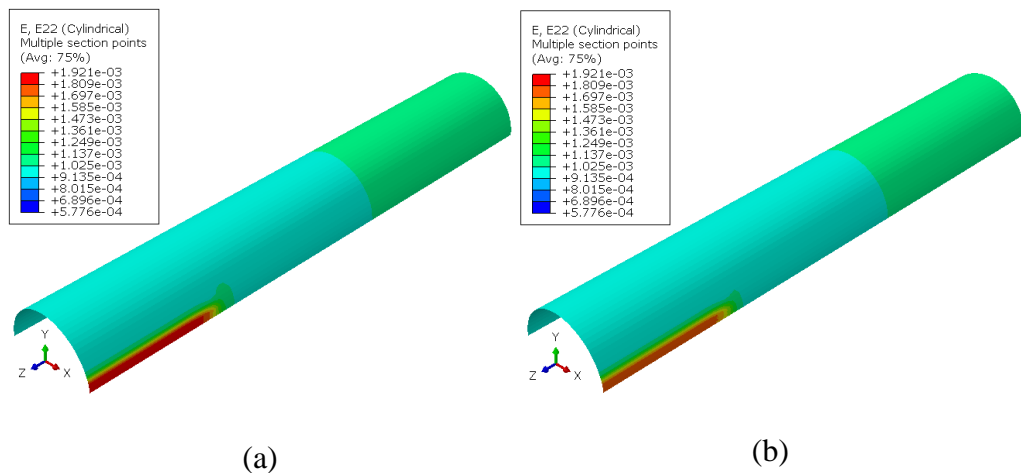


Figure 6-4, Hoop strain contour plot of corroded riser repaired with: (a)  $[0^\circ]$  carbon/epoxy, (b)  $[0^\circ]$  E-glass epoxy at design load of 22MPa

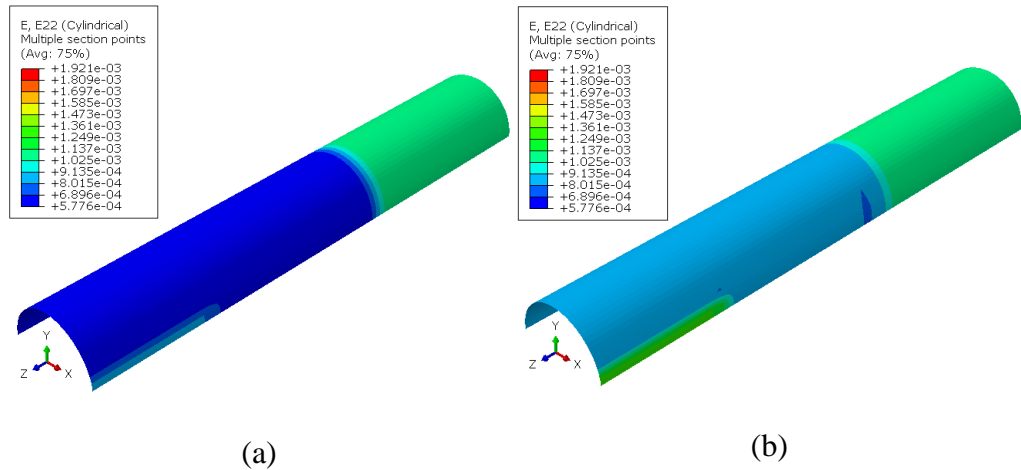


Figure 6-5, Hoop strain contour plot of corroded riser repaired with: (a) [90°] carbon/epoxy, (b) [90°] E-glass epoxy at design load of 22MPa

A summary of the hoop strain values of the bare riser, corroded riser and repaired risers is shown in Table 6-1. The ratio of the simulated CRS hoop strain to the maximum permissible hoop strain is also displayed. Different colours are used to represent the context of the repair quality. Red signifies that the  $\epsilon_{h,max}$  is exceeded and hence not fit for the rehabilitation operation, yellow suggests that the hoop strain has reached 80% of the  $\epsilon_{h,max}$  and improvement on the repair is required while green denotes that the repair is within the safety limit.

Table 6-1, Hoop strain of various riser at 22MPa

	Bare Riser	Corroded Riser	Corroded Riser Repair with FRPC			
			[0°] Repair		[90°] Repair	
			Carbon/Epoxy	E-Glass/Epoxy	Carbon/Epoxy	E-Glass/Epoxy
Hoop Strain, $\epsilon_h$ (%)	0.111	0.279	0.192	0.178	0.08	0.125
$\epsilon_h/\epsilon_{h,max}$ Ratio	<b>0.592</b>	<b>1.488</b>	<b>1.024</b>	<b>0.949</b>	<b>0.427</b>	<b>0.667</b>

### 6.2.1b Tensile Load, $F_t$

As discussed in section 3.2.1 of Chapter 3, tension is another type of load frequently applied on the riser to avoid buckling and excessive bending. This type of loading causes tensile stress in the riser. Hence, axial strain can be used as an indicative output parameter evaluation of the performance of the CRS. Figure 6-6 shows the plot of tensile loading against axial strain for corroded risers repaired with  $[0^\circ]$  and  $[90^\circ]$  carbon/epoxy and E-glass/epoxy laminates.

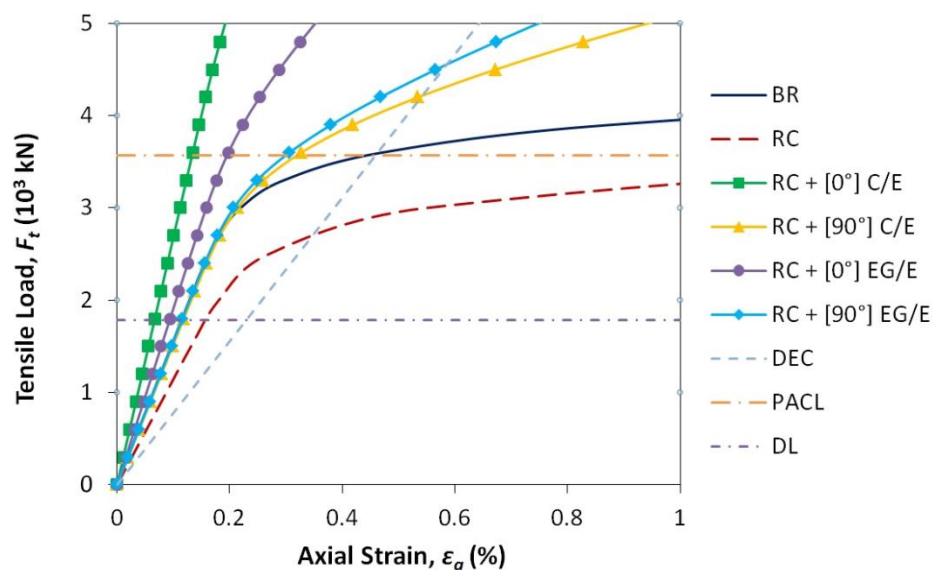


Figure 6-6, Tensile load vs. axial strain of corroded riser repaired with  $[0^\circ]$  and  $[90^\circ]$  laminate

The curves for the bare riser without corrosion and corroded riser were included for comparison purpose. As discussed in section 5.6.2 of Chapter 5, the effect of individual tensile load on the riser is not as significant as internal pressure. Thus, both types of fibre reinforcement were able to restore the corroded riser to or beyond its original non-corroded strength performance as displayed in Figure 6-6. However, the repair with  $[0^\circ]$  laminate seems to be the ideal configuration as the stiffness from the fibres can resist the tensile force, with carbon fibres



showing superiority over glass fibres. The results of the tensile strain values are summarised in Table 6-2.

Table 6-2, Axial strain of various riser at 1785kN tensile load

	Bare Riser	Corroded Riser	Corroded Riser Repair with FRPC			
			[0°] Repair		[90°] Repair	
			Carbon/Epoxy	E-Glass/Epoxy	Carbon/Epoxy	E-Glass/Epoxy
Axial Strain, $\epsilon_b$ (%)	0.115	0.165	0.067	0.094	0.119	0.116
$\epsilon_b/\epsilon_{a,max}$ Ratio	<b>0.511</b>	<b>0.733</b>	<b>0.298</b>	<b>0.418</b>	<b>0.529</b>	<b>0.516</b>

### 6.2.1c Bending Load, $F_b$

Bending load as discussed in section 3.2.2 of chapter 3 is endured by the riser due to wave and current forces in the vicinity of subsea environment. The axial strain in the tensile region of the bent riser is used to evaluate the performance of the CRS when different reinforcing fibres are used. Similar to the case subjected to tensile loading, the [0°] repair capable of providing more strengthening to the corroded riser as shown in Figure 6-7. The [0°] repair reinforcement using carbon fibres showed a slight advantage over E-glass fibres. At the design load of 120kNm, the corroded riser repaired with [90°] carbon and E-glass fibres composites have similar level of axial strains. Table 6-3 summarises the axial strains on the corroded region at design load. As in the case of tensile load, it can be observed that both the [0°] and [90°] composite laminates provide sufficient strengthening to the corroded riser when it is subjected to bending load alone.

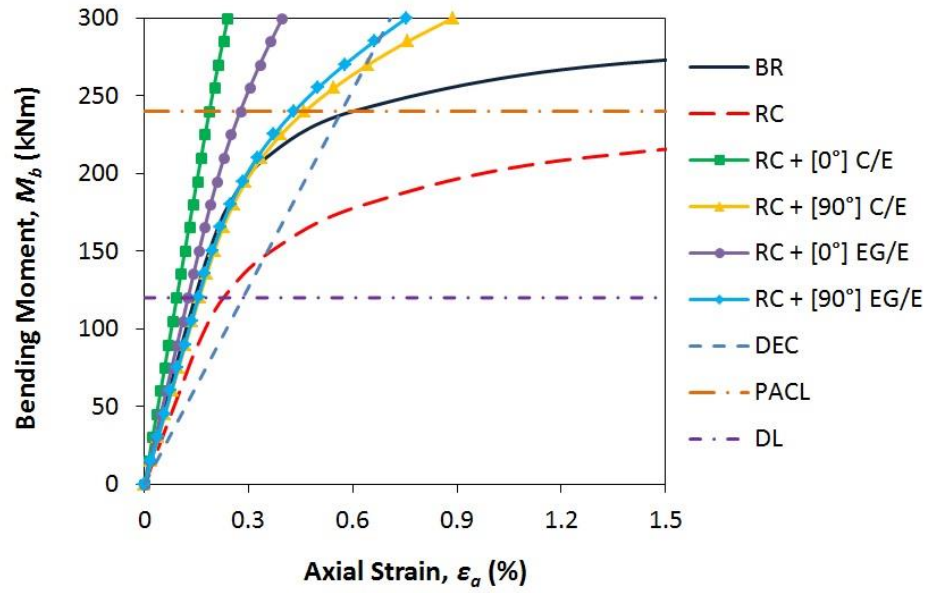


Figure 6-7, Bending Moment vs. axial strain of corroded riser repaired with [0°] and [90°] laminate

Table 6-3, Comparison of axial strain values of riser at 120kNm

	Bare Riser	Corroded Riser	Corroded Riser Repair with FRPC			
			[0°] Repair		[90°] Repair	
			Carbon/Epoxy	E-Glass/Epoxy	Carbon/Epoxy	E-Glass/Epoxy
Axial Strain, $\epsilon_a$ (%)	0.145	0.227	0.093	0.125	0.158	0.155
$\epsilon_a/\epsilon_{a,max}$ Ratio	<b>0.569</b>	<b>0.890</b>	<b>0.365</b>	<b>0.490</b>	<b>0.620</b>	<b>0.608</b>

## 6.2.2 Combined Static Load

### 6.2.2a Internal Pressure, $P_{int}$ & Tensile Load, $F_t$

Combined internal pressure and tensile load were assigned on the corroded riser repaired with FRPC. Both type of loadings were ramped with a fixed time increment such that their stress-strain behaviour at different magnitude can be determined. The output variables used to evaluate the performance of the

composite repair are the hoop strain and axial strain. Figure 6-8 shows the results of the FEA output of the axial strain.

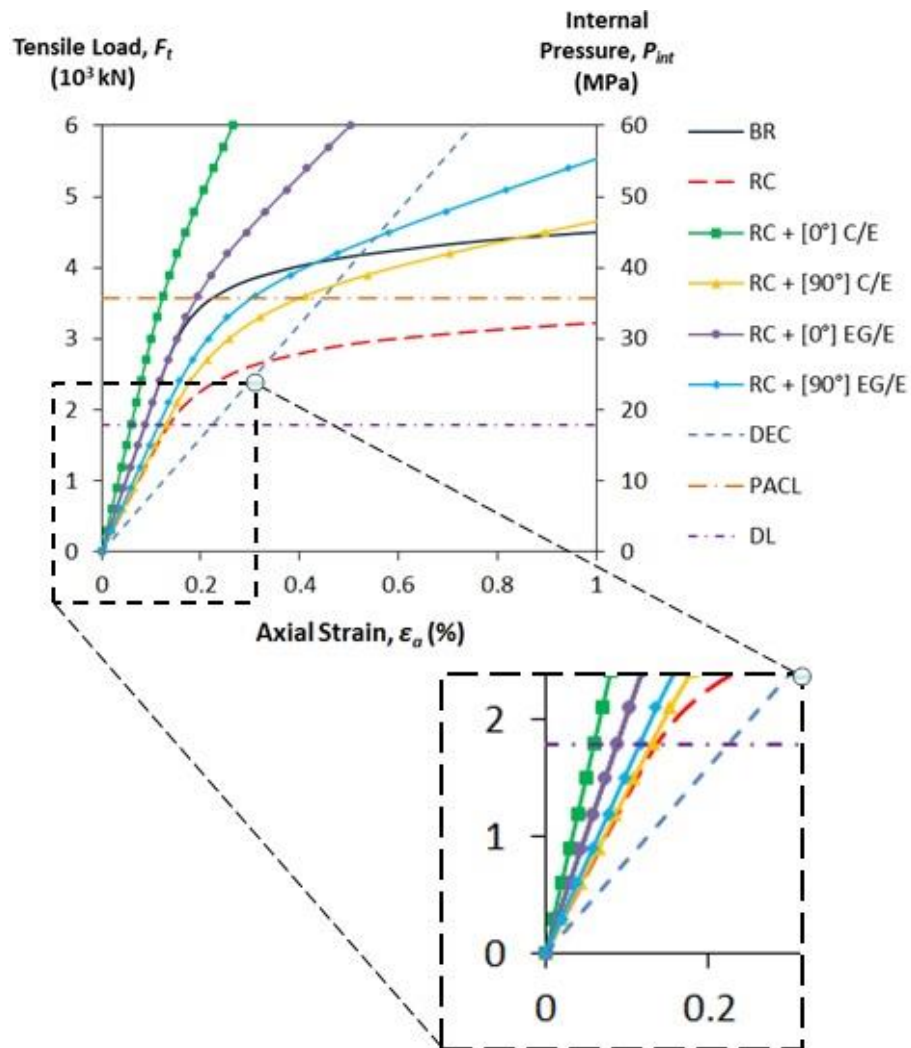


Figure 6-8, Load vs. axial strain plot of corroded riser repaired with unidirectional axially orientated  $[0^\circ]$  and hoop orientated  $[90^\circ]$  laminates

At the DL for tensile force of 1785kN, the simulated output revealed that both  $[0^\circ]$  and  $[90^\circ]$  orientated laminates are sufficient to restore the axial strength of the corroded riser. However, the axial strain at PACL was significantly higher for risers repaired with  $[90^\circ]$  composite laminate, signifying a much weaker performance along the longitudinal axis. In terms of providing reinforcement in the hoop strength of the corroded riser, the use of  $[0^\circ]$  composite laminate was

insufficient as the resulting hoop strain occurred close to the maximum permissible hoop strain (Figure 6-9). The use of carbon fibres shows superiority over E-glass fibres. Table 6-4 shows the computed hoop strain for the different cases of CRS.

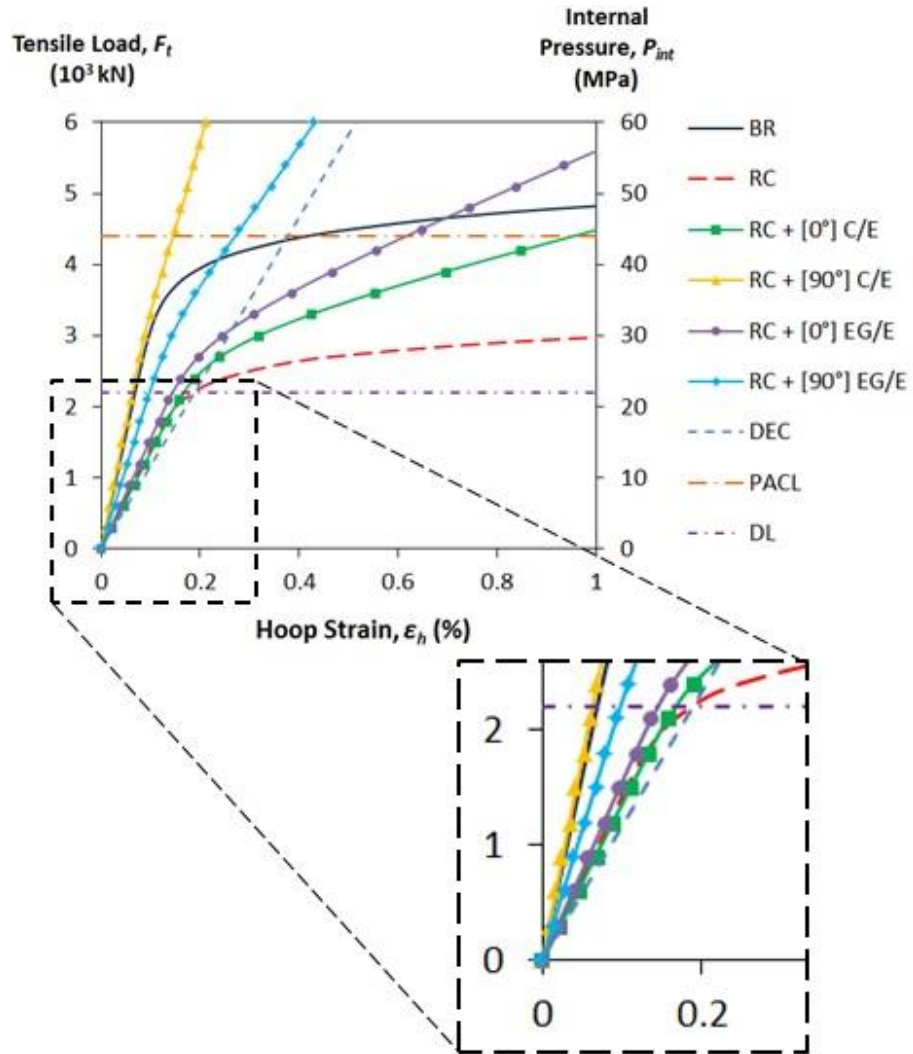


Figure 6-9, Load vs. hoop strain plot of corroded riser repaired with unidirectional axially orientated and hoop orientated laminates

Table 6-4, Axial and hoop strains of riser subjected to combined 22MPa internal pressure and 1785kN tensile load

	Bare Riser	Corroded Riser	Corroded Riser Repair with FRPC			
			[0°] Repair		[90°] Repair	
			Carbon/Epoxy	E-Glass/Epoxy	Carbon/Epoxy	E-Glass/Epoxy
Axial Strain, $\epsilon_a$ (%)	0.081	0.136	0.056	0.081	0.123	0.110
$\epsilon_a/\epsilon_{a,max}$ Ratio	<b>0.360</b>	<b>0.604</b>	<b>0.249</b>	<b>0.360</b>	<b>0.547</b>	<b>0.489</b>
Hoop Strain, $\epsilon_h$ (%)	0.078	0.213	0.171	0.150	0.066	0.103
$\epsilon_h/\epsilon_{h,max}$ Ratio	<b>0.416</b>	<b>1.136</b>	<b>0.912</b>	<b>0.800</b>	<b>0.352</b>	<b>0.549</b>

### 6.2.2b Internal Pressure, $P_{int}$ , Tensile Load, $F_t$ & Bending Moment,

$$M_b$$

In this particular study, combined internal pressure of 22MPa and tensile load of 1785kN were applied onto the riser. At the same time, the riser is also subjected to range of bending moment. Figure 6-10 shows the axial strain of the riser repaired with unidirectional axially orientated [0°] and hoop orientated [90°] laminates. The data for the bare riser and corroded riser were included for comparison purposes. Regardless of the types of reinforcing fibres (i.e. carbon fibre or E-glass fibre) used, the [90°] composite repair was found unable to provide sufficient rehabilitation to the corroded riser as the maximum permissible axial strain has been reached. On contrary, the [0°] composite repair contributes to the flexural strength of the repaired riser, with the stiffer carbon fibres showing higher resistance to the axial stress. However, with the use of the [0°] carbon/epoxy, the resulting hoop strain was relatively high due to its lower

transverse modulus of elasticity. As a result, there is a need to design an improved fibre orientation to provide sufficient overall strengthening in the axial and hoop directions. The values of hoop and axial strains are under combined  $P_{int}$ ,  $F_t$  and  $M_b$  load are summarised in Table 6-5.

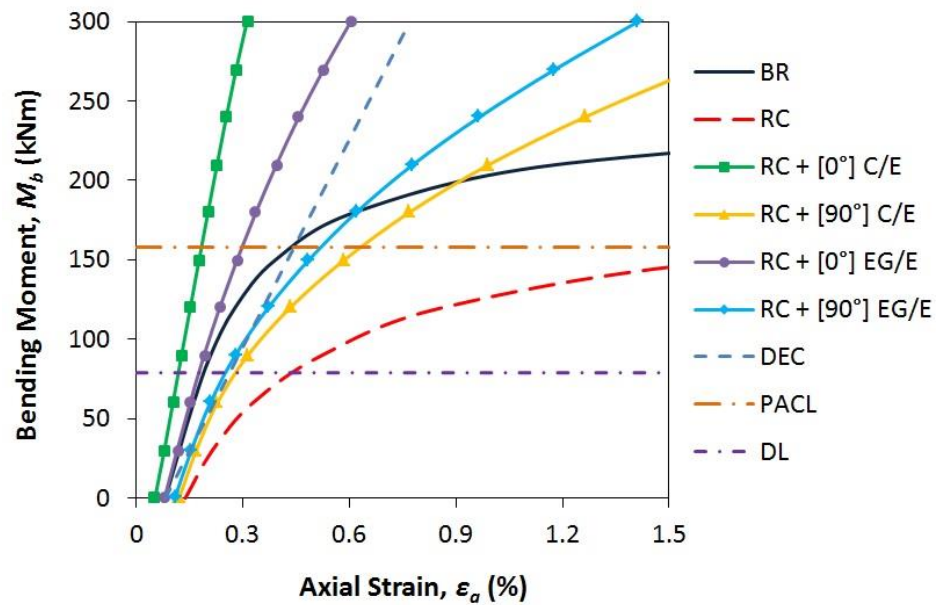


Figure 6-10, Load vs. axial strain plot of corroded riser repaired with unidirectional axially orientated  $[0^\circ]$  and hoop orientated  $[90^\circ]$  laminates

Table 6-5, Comparison of strain values of riser at 22MPa, 1785kN and 78kNm

	Bare Riser	Corroded Riser	Corroded Riser Repair with FRPC			
			$[0^\circ]$ Repair		$[90^\circ]$ Repair	
			Carbon/Epoxy	E-Glass/Epoxy	Carbon/Epoxy	E-Glass/Epoxy
Axial Strain, $\epsilon_a$ (%)	0.188	0.431	0.117	0.174	0.276	0.248
$\epsilon_a/\epsilon_{a,max}$ Ratio	<b>0.737</b>	<b>1.690</b>	<b>0.459</b>	<b>0.682</b>	<b>1.082</b>	<b>0.973</b>
Hoop Strain, $\epsilon_h$ (%)	0.108	0.317	0.158	0.135	0.055	0.088
$\epsilon_h/\epsilon_{h,max}$ Ratio	<b>0.576</b>	<b>1.691</b>	<b>0.843</b>	<b>0.72</b>	<b>0.293</b>	<b>0.469</b>

### 6.3 Laminate/Fibre Orientation

Composite repairs for onshore pipelines have largely evolved based on unidirectional laminate produced in the form of pre-cured half shells or woven fabric. Most of these repairs are carried out by wrapping the composite laminate around the corroded region of the pipe, with the fibres wound in such a way that they align to the hoop direction of the pipe. In the application for offshore riser, mixed loading profiles causes multi-directional stresses in the riser. Hence, it is essential to design a suitable laminate orientation that can provide optimum reinforcement to the corroded riser under the mixed loading profiles. In the past, the use of different laminate orientation that has fibres aligned at different angles with respect to the riser axis has proven to be beneficial in providing the necessary strengthening to a defective riser. In the current project, five types of laminate orientations typically used in the composite industry were selected to study their performance on reinforcing corroded riser.

- 1) 90° unidirectional laminate (in hoop direction) – This type of laminate was selected as strengthening in the hoop direction of the riser is most common in order to sustain the internal pressure caused by the contents being transported.
- 2) 0° unidirectional laminate (in axial direction) – Axial reinforcement is an important element as the riser must sustain various axial stresses caused by the combination of tension and bending loads.
- 3) Quasi-isotropic  $[0^\circ/\pm 45^\circ/90^\circ]_s$  laminate – This type of laminate is common in aerospace industry and is expected to exhibit similar orthogonal response when the composite is loaded in the 0° and 90° directions.

- 4) Balanced and symmetric  $[90^\circ/\pm 30^\circ]_s$  laminate – This laminate consist of a mixture of off-axis and on-axis plies and is different from the quasi-isotropic laminate. The addition of the off-axis plies provides a varying reinforcing behaviour to the composite.
- 5) Angle ply  $[\pm 55^\circ]_s$  laminate – This type of laminate can help in understanding the capability of off-axis plies in sustaining multiple-directional loads. The  $[\pm 55^\circ]_s$  laminate is commonly used in industrial pipework where the composite pipes are manufactured via filament winding.

Figure 6-11 through to Figure 6-15 show the schematic of the five types of laminate orientations investigated in the current study.

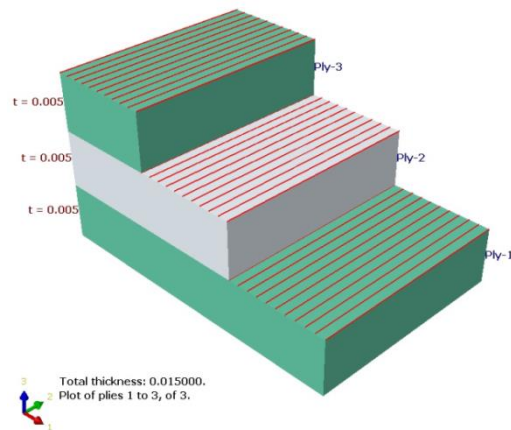


Figure 6-11, Ply stack plot for  $90^\circ$  unidirectional laminate in hoop direction



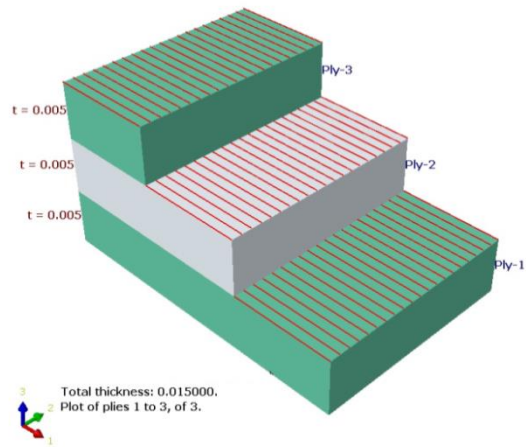


Figure 6-12, Ply stack plot for  $0^\circ$  unidirectional laminate in axial direction

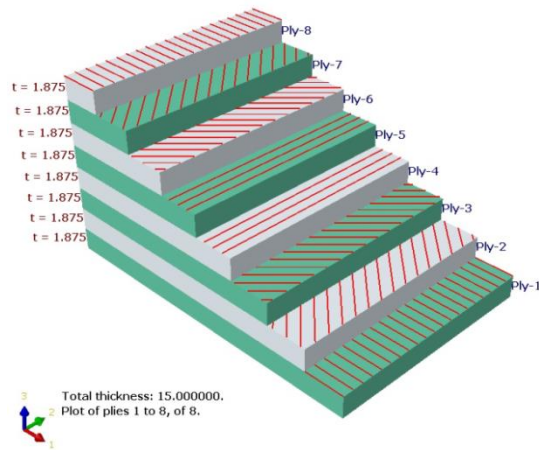


Figure 6-13, Ply stack plot for quasi-isotropic  $[90^\circ/\pm 45^\circ/0^\circ]_s$  laminate

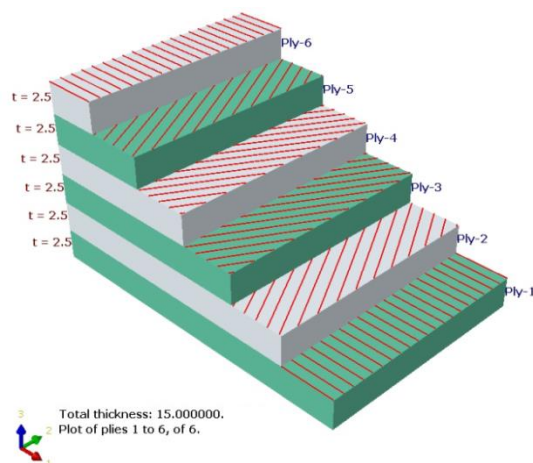


Figure 6-14, Ply stack plot for balanced and symmetric  $[90^\circ/\pm 30^\circ]_s$  laminate

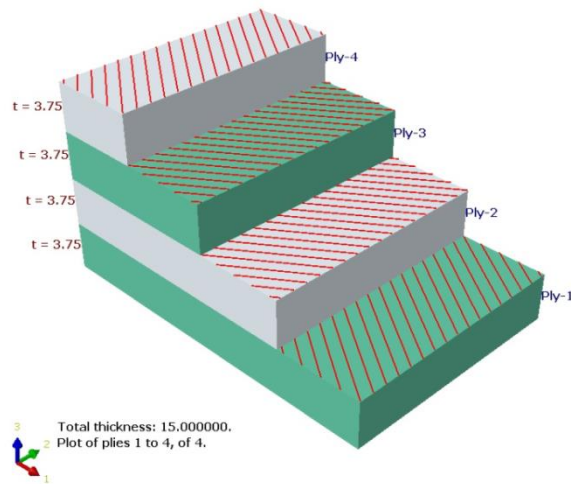


Figure 6-15, Ply stack plot for angle ply  $[\pm 55^\circ]$ s laminate

For this section, individual static loading is not included as it has been determined that on-axis unidirectional laminates provides the best reinforcement under such conditions. The AS4 carbon fibres coupled 3501-6 epoxy matrix was chosen as the CRS for its superior performance over the glass fibres epoxy composite.

### 6.3.1 Combined Internal Pressure, $P_{int}$ & Tensile Load, $F_t$

The results of the corroded risers repaired with different laminate orientations are shown in Figure 6-16 and Figure 6-17. It can be seen that the  $[90^\circ]$  hoop orientated reinforcement capable of providing the greatest strengthening to the corroded riser in resisting hoop strain. However, when the axial strain is taken into consideration, it is evident from Figure 6-17 that the  $[90^\circ]$  hoop orientated laminate cannot restore the performance of the corroded riser as the axial strain beneath the repair is similar to that of a corroded riser. On the other hand, the simulated output revealed that  $[0^\circ]$  axially orientated unidirectional laminates capable of sustaining the highest amount of axial load, where the repaired riser experienced strength improvement beyond that of an uncorroded bare riser in the

longitudinal axis. The combined use of on-axis and off-axis plies increases the stiffness of the laminate in both directions. Both balanced and symmetric  $[90^\circ/\pm 30^\circ]_s$  laminate, and quasi-isotropic  $[90^\circ/\pm 45^\circ/0^\circ]_s$  laminate demonstrated comparable rehabilitation performance where the strength of the repaired riser was found higher than the uncorroded bare riser in both axial and hoop directions. As shown in Figure 6-18, the  $\pm 30^\circ$  plies carries higher fraction of axial stress while the  $90^\circ$  carries higher hoop stress. The angle ply  $[\pm 55^\circ]_s$  repair laminate however showed a comparatively lower strengthening performance (Figure 6-17) but the maximum permissible axial strain was not exceeded at the design load of 1785kN. The axial strain and hoop strain on the riser beneath the repair at design load of 22MPa and 1785kN are recorded in Table 6-6.

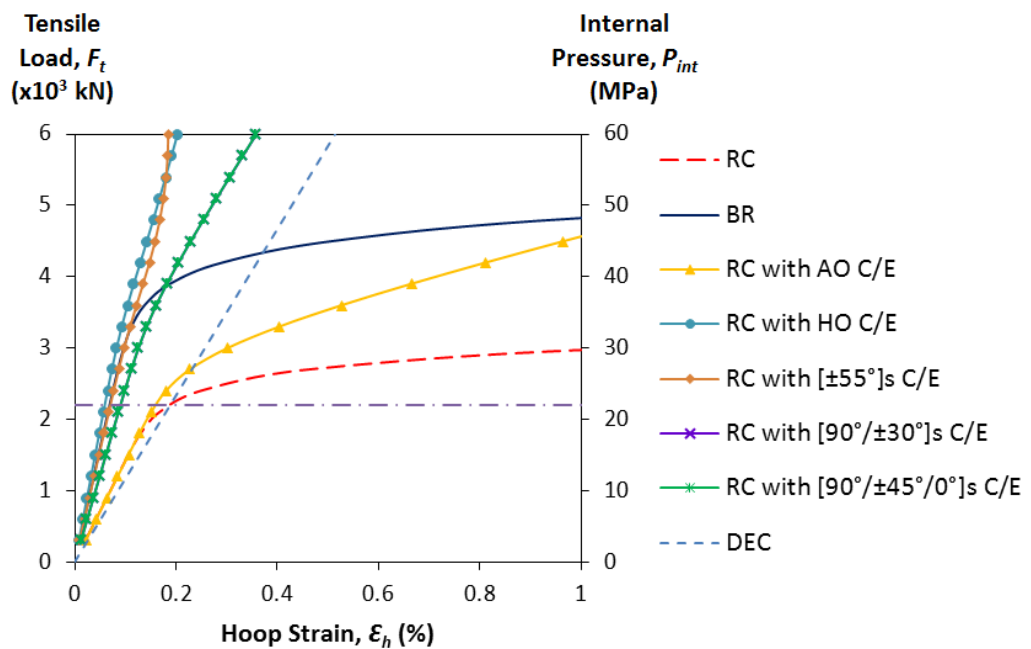


Figure 6-16, Load vs. hoop strain plot of corroded riser repaired with different orientation of carbon/epoxy laminates

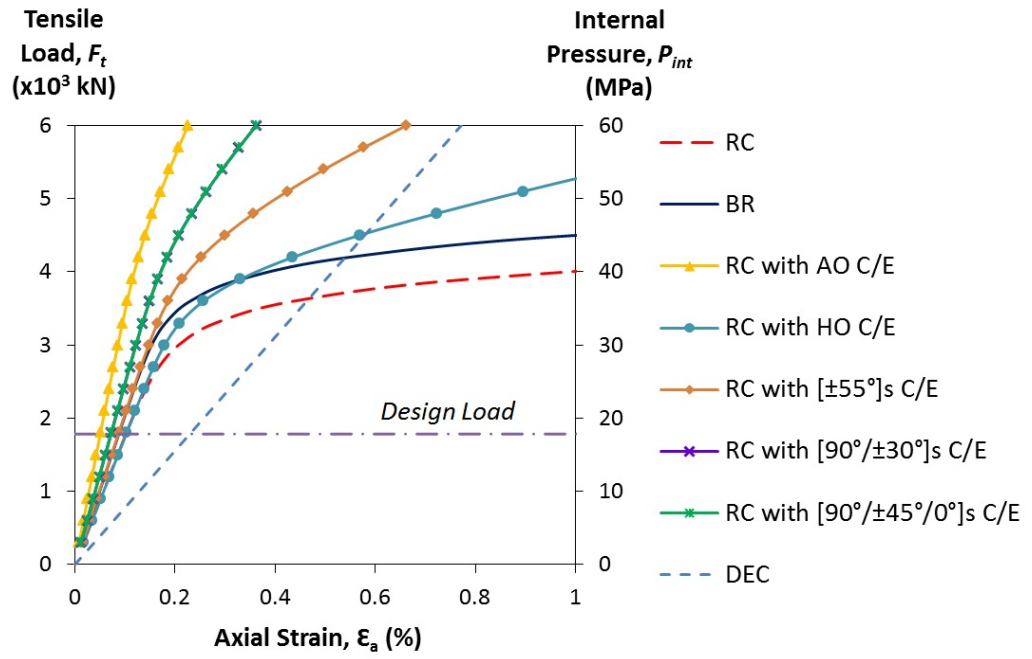


Figure 6-17, Load vs. axial strain plot of corroded riser repaired with different orientation of carbon/epoxy laminates

Table 6-6, Axial and hoop strains of riser repaired with different types of laminate orientation subjected to 22MPa ( $P_{in}$ ) and 1785kN ( $F_t$ )

	Bare Riser	Corroded Riser	Corroded Riser Repair with FRPC				
			[0°]	[90°]	[90°/±30°] <sub>s</sub>	[90°/±45°/0°] <sub>s</sub>	[±55°] <sub>s</sub>
Axial Strain, $\epsilon_a$ (%)	0.081	0.136	0.056	0.123	0.080	0.080	0.097
$\epsilon_a/\epsilon_{a,max}$ Ratio	<b>0.360</b>	<b>0.604</b>	<b>0.249</b>	<b>0.547</b>	<b>0.356</b>	<b>0.356</b>	<b>0.431</b>
Hoop Strain, $\epsilon_h$ (%)	0.078	0.213	0.171	0.066	0.100	0.100	0.086
$\epsilon_h/\epsilon_{h,max}$ Ratio	<b>0.416</b>	<b>1.136</b>	<b>0.912</b>	<b>0.352</b>	<b>0.533</b>	<b>0.533</b>	<b>0.459</b>

Table 6-7, Axial and hoop strains of riser repaired with different types of laminate orientation at 22MPa ( $P_{in}$ ), 1785kN ( $F_t$ ) and 78kNm ( $M_b$ )

	Bare Riser	Corroded Riser	Corroded Riser Repair with FRPC				
			[0°]	[90°]	[90°/±30°] <sub>s</sub>	[90°/±45°/0°] <sub>s</sub>	[±55°] <sub>s</sub>
Axial Strain, $\epsilon_a$ (%)	0.188	0.431	0.117	0.276	0.172	0.172	0.225
$\epsilon_a/\epsilon_{a,max}$ Ratio	<b>0.737</b>	<b>1.690</b>	<b>0.459</b>	<b>1.082</b>	<b>0.675</b>	<b>0.675</b>	<b>0.882</b>
Hoop Strain, $\epsilon_h$ (%)	0.108	0.317	0.158	0.055	0.077	0.077	0.051
$\epsilon_h/\epsilon_{h,max}$ Ratio	<b>0.576</b>	<b>1.691</b>	<b>0.843</b>	<b>0.293</b>	<b>0.411</b>	<b>0.411</b>	<b>0.272</b>

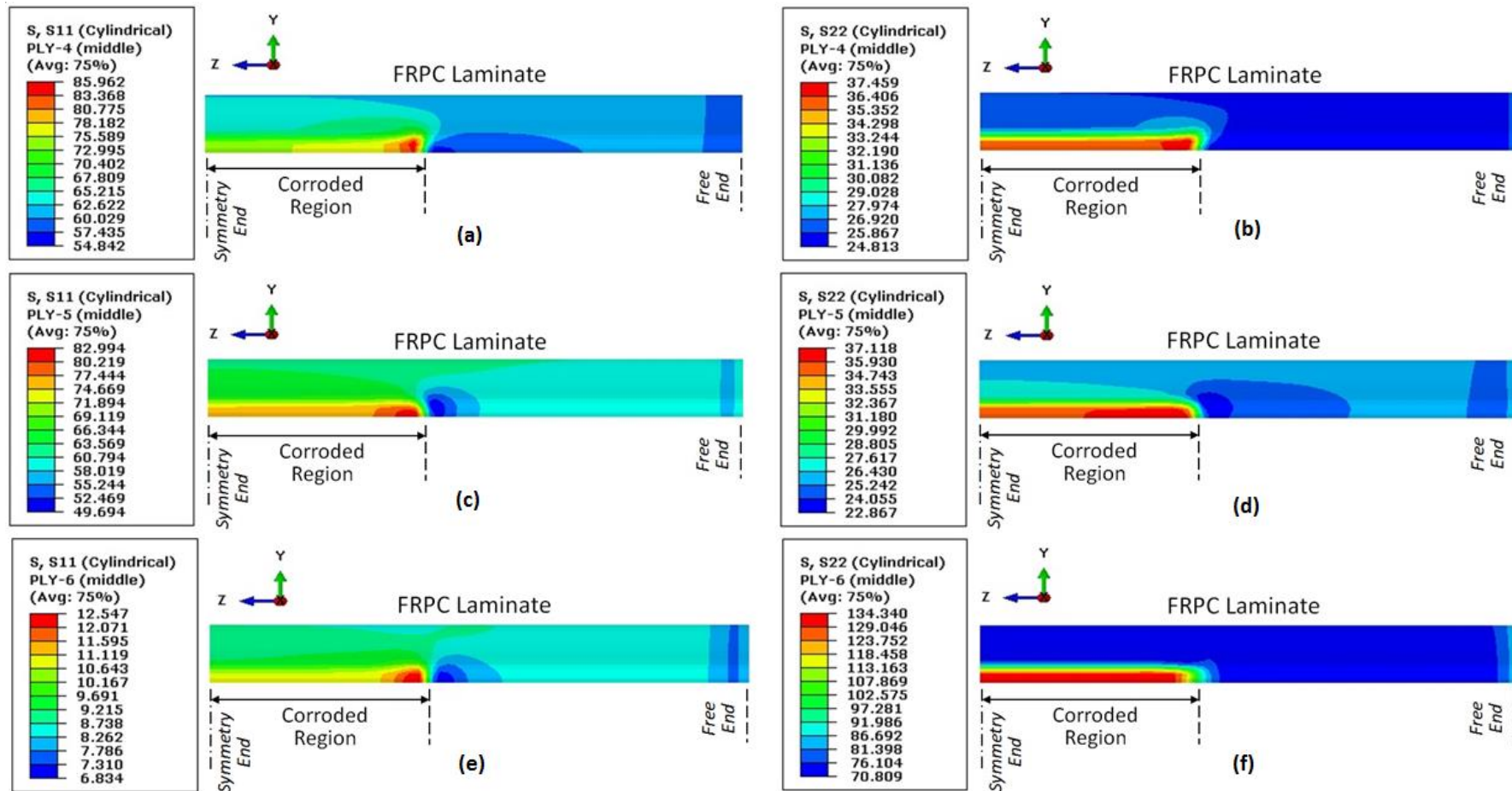


Figure 6-18, Stress at different plies of the  $[90^\circ/\pm 30^\circ]_s$  laminate subjected to combined  $P_{in}$  and  $F_r$ : (a) (b)  $-30^\circ$  ply, (c) (d)  $+30^\circ$  ply, (e) (f)  $90^\circ$  ply

### 6.3.2 Combined Internal Pressure, $P_{int}$ , Tensile Load, $F_t$ & Bending

#### Moment, $M_b$

Bending moment is added to simulate a riser subjected to combined loading under subsea environment. As shown in Figure 6-19, the  $[0^\circ]$  axially orientated laminate is capable of providing the greatest reinforcement in resisting the tensile strain caused by bending. For hoop orientated laminate, maximum permissible axial strain has been reached at design load (78kNm) and hence can be considered as not fit for the repair application.

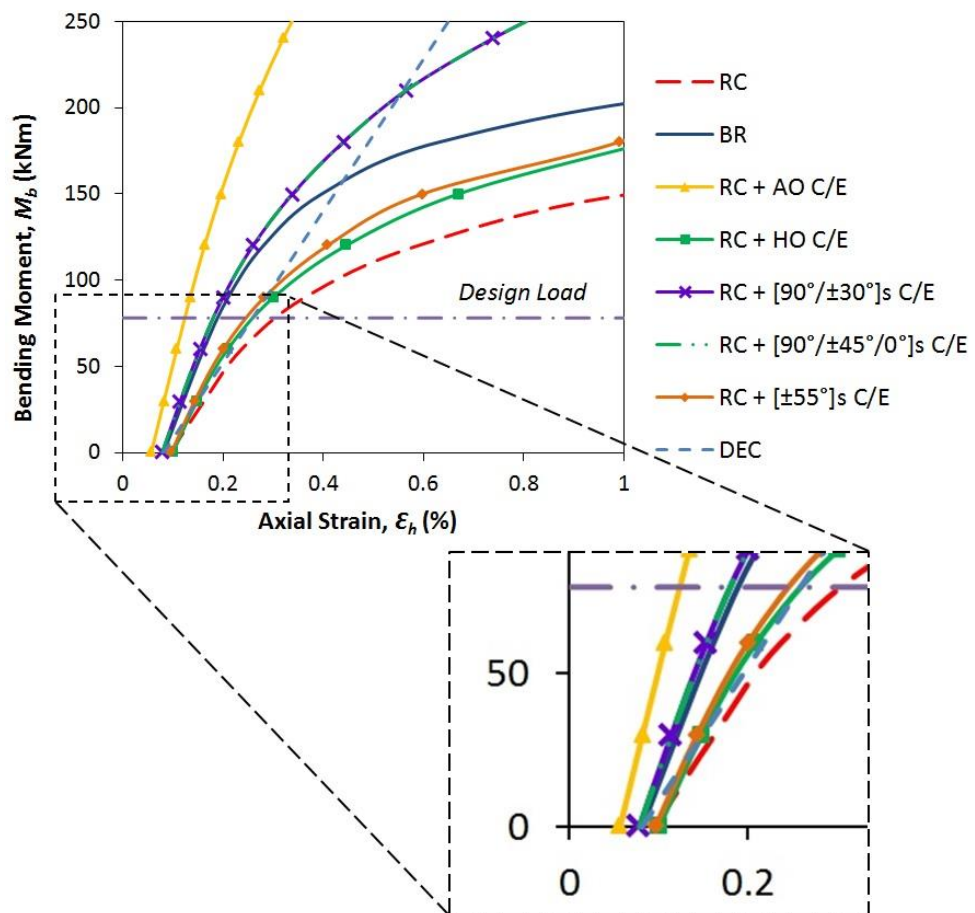


Figure 6-19, Load vs. axial strain plot of corroded riser repaired with different orientation of carbon/epoxy laminates subjected to combined internal pressure, tensile and bending load

For the off-axis laminates, e.g. the balanced and symmetric  $[90^\circ/\pm 30^\circ]_s$  laminate and the quasi-isotropic  $[90^\circ/\pm 45^\circ/0^\circ]_s$  laminate, similar responses were observed, where the strength of the repaired riser being higher than the uncorroded bare riser. Figure 6-20 shows the breakdown of plies within the  $[90^\circ/\pm 30^\circ]_s$  laminate where the hoop and axial stresses within each of the ply were demonstrated. It can be observed that the  $\pm 30^\circ$  plies capable of sustaining higher axial stress as the fibres are aligned closer to the longitudinal axis of the riser. This means that higher fraction of axial stress was transferred from the corroded riser to these  $\pm 30^\circ$  composite plies. In contrast, the  $90^\circ$  ply sustained much lower axial stress but higher hoop stress as the fibres are aligned in the hoop direction. Similarly, Figure 6-21 shows the breakdown for the  $[90^\circ/\pm 45^\circ/0^\circ]_s$  where  $0^\circ$  ply carries the highest axial stress followed by the  $\pm 45^\circ$  and  $90^\circ$  plies.

The angle ply  $[\pm 55^\circ]_s$  repair laminate however was found not suitable as a candidate CRS for repairing the corroded riser because its axial strain has approached the maximum permissible axial strain at the design load of 78kNm, as depicted in Figure 6-19. Table 6-6 summarises the hoop strain and axial strain on the corroded riser beneath the repair. It is evident that the orientation of the multiple-angle laminates significantly affects the final properties of the repaired riser. Both the  $[90^\circ/\pm 30^\circ]_s$  and  $[90^\circ/\pm 45^\circ/0^\circ]_s$  laminates provided sufficient strength rehabilitation to the corroded risers in both hoop and axial directions when the riser is subjected to complex loadings as revealed in the current study. The design of an optimised composite ply orientations provides an effective repair at lower material cost. However, the laying pattern and sequence of ply orientations on a corroded riser is not always practically feasible. The wrapping sequence around a cylindrical riser limits the laminate orientation to a range of



winding angle. The  $0^\circ$  laminate with fibres aligned perfectly along the longitudinal axis of the riser is not feasible unless pre-cured half shells are used.

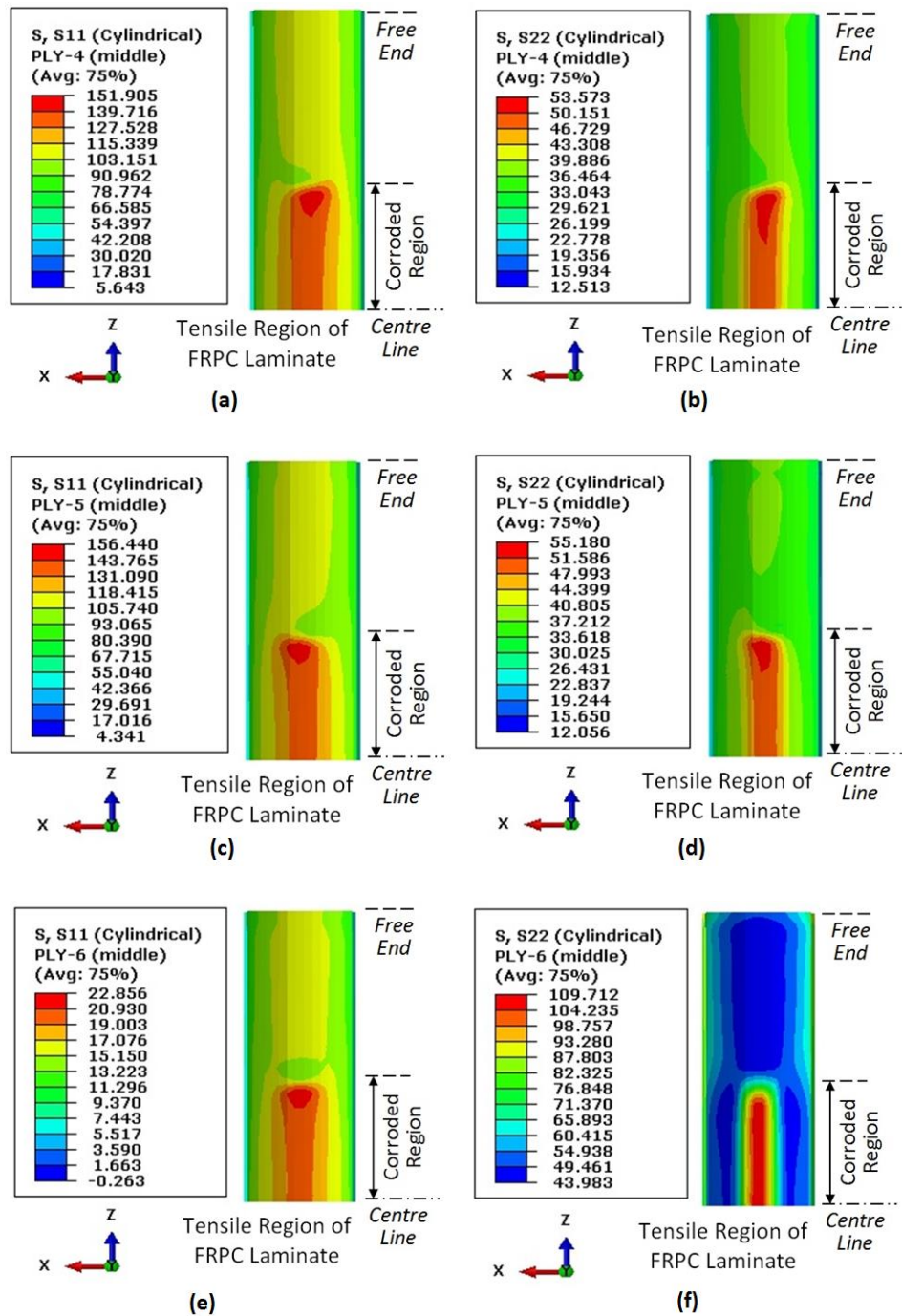


Figure 6-20, Axial and hoop stresses at different plies of the  $[90^\circ/\pm 30^\circ]_s$  laminate subjected to combined  $P_{in}$ ,  $F_t$  and  $M_b$ : (a) (b)  $-30^\circ$  ply, (c) (d)  $+30^\circ$  ply, (e) (f)  $90^\circ$  ply

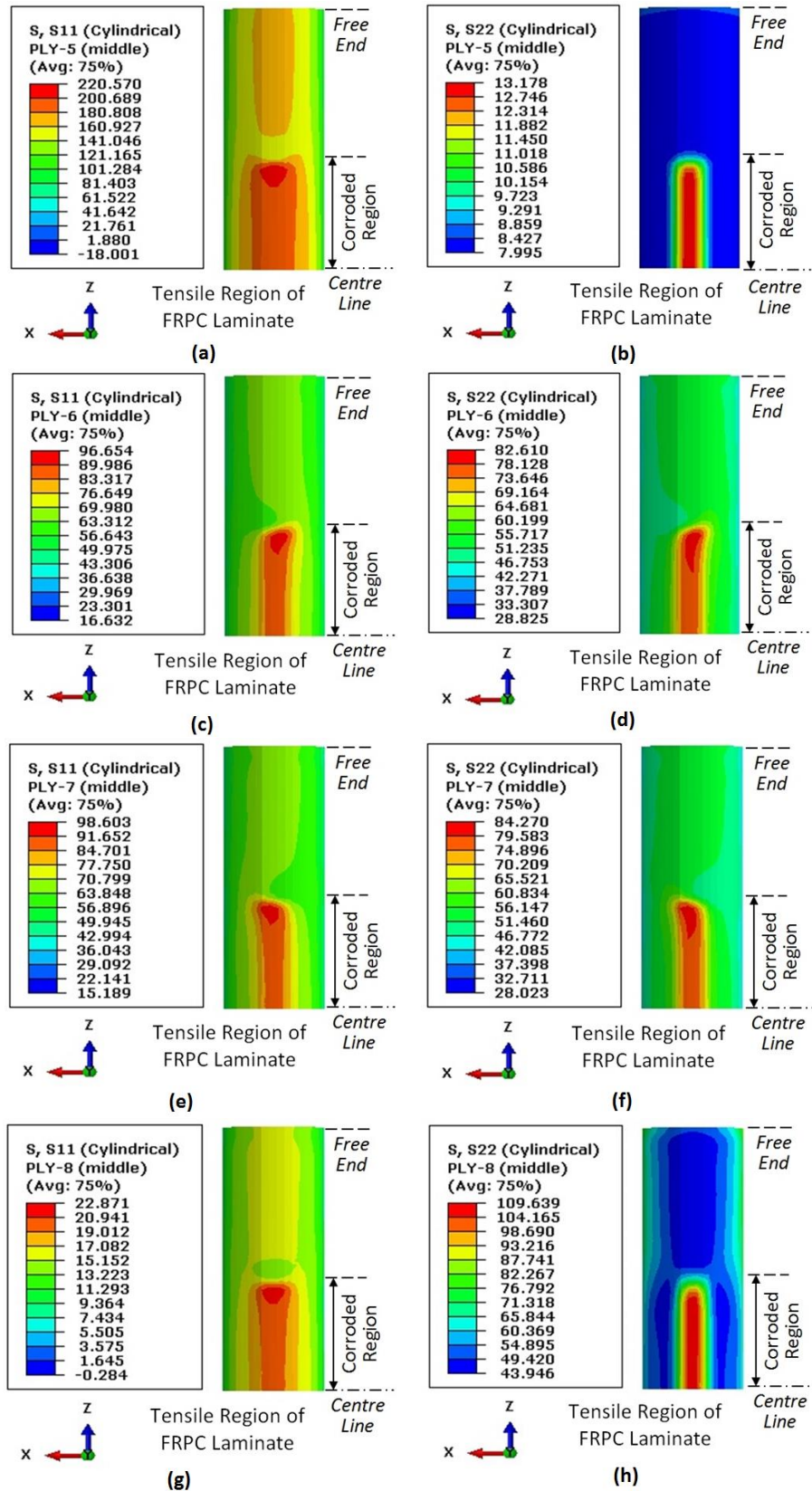


Figure 6-21, Axial and hoop stresses at different plies of the  $[90^\circ/\pm 45^\circ/0^\circ]_s$  laminate subjected to combined  $P_{in}$ ,  $F_t$  and  $M_b$ : (a) (b)  $0^\circ$  ply, (c) (d)  $-45^\circ$  ply, (e) (f)  $+45^\circ$  (g) (h)  $90^\circ$  ply

## 6.4 Wrapping Angle

The previous section demonstrated the need for a customised design of laminate orientation within the composite for effective rehabilitation of weakened/defective offshore riser. When an offshore riser is subjected to combine loadings, it is bound to experience different levels of principal, i.e. axial, hoop and radial stresses. However, the out-of-plane radial stress is negligible in the current case due to the usage of the thin shell formulation. An optimised design of laminate orientation for the FRPC is prudent in providing an effective reinforcement to resist potential failure in these principal directions. However, design and manufacturing of such composite laminates to be applicable for wrapping a corroded riser is not straightforward, as discussed in Section 0. Taking into account the future implementation of automated composite repair for subsea risers, wrapping of unidirectional prepreg is chosen as the best means for application.

The wrapping of prepreg laminate is assumed to traverse along the length of the repair section in a helical manner such that an angle,  $\theta$ , relative to the longitudinal axis of the riser exists. As the repair consists of several layers of laminates, the wrapping process will have to go back and forth along the length of the repair section. In real life, there are bound to be ‘end effects’ in the helical winding of composite tape where accurate angle orientation is not fully achievable. However, as the repair extends sufficiently far beyond the corroded region of the riser, the end effects are assumed to be negligible and are not included in the current FE model. Varying the laminate wrapping angle from  $30^\circ$  to  $90^\circ$  (hoop direction) in step increment of  $15^\circ$ , producing  $[\pm\theta]_n$  of laminate allows the effect of orientation to be observed.

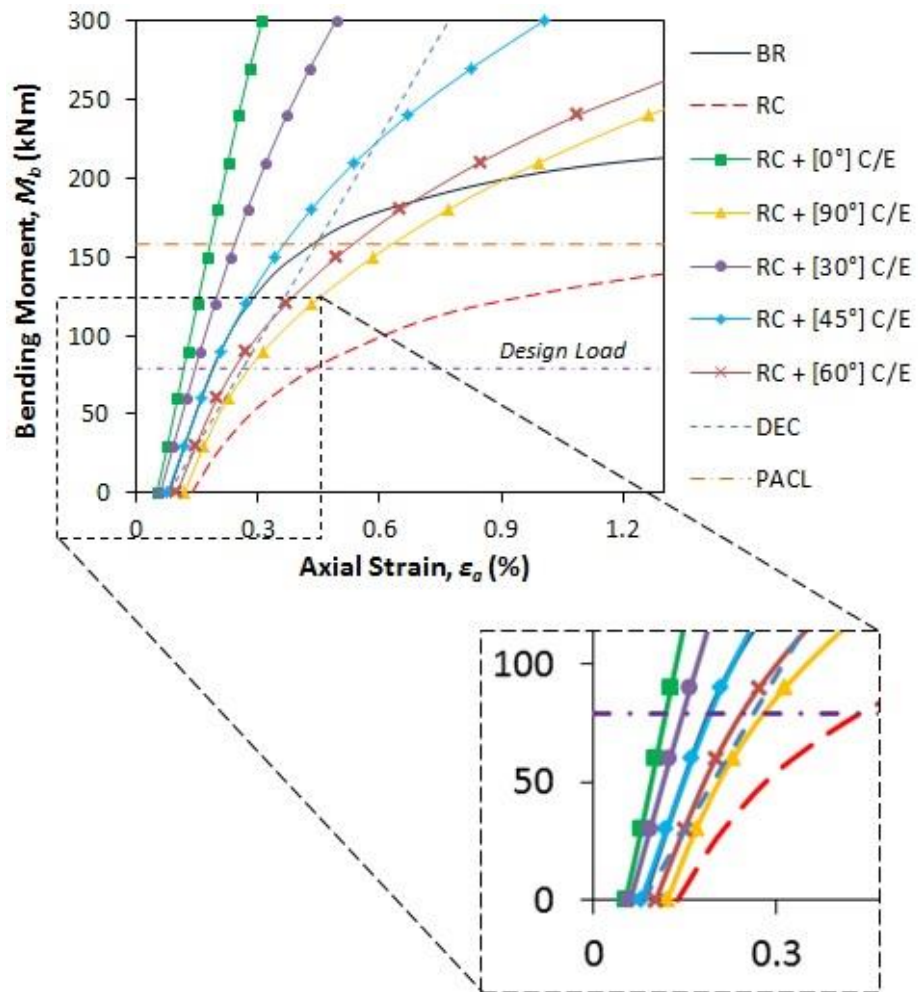


Figure 6-22, Load vs. axial strain plot of corroded riser repaired with varying wrapping angle of carbon/epoxy laminates subjected to combined internal pressure, tensile and bending load

From Figure 6-22, it is apparent that the 90° laminate is ideal for reinforcing the hoop strength of a corroded riser when it is purely subjected to internal pressure. Vice versa, the  $[\pm 30^\circ]_s$  laminate which has fibres aligned closest to the axis of the riser provides highest strengthening when the riser is subjected to pure tensile load and bending moment respectively. When subjected to combined internal pressure, tensile load and bending moment, the performance of the repaired riser in the axial direction deteriorates (i.e. increasing strain) as the wrapping angle of the FRPC laminate relative to the longitudinal axis increases, as depicted in

Figure 6-22. The  $[90^\circ]$  repair which emulates the common composite repair in the industry of onshore pipelines show poor performance in strengthening a riser subjected to combined loading. Similar to the  $[90^\circ]$  laminate repair, the pure  $[\pm 60^\circ]_s$  laminate repair is also no suitable for offshore pipeline rehabilitation application due to the high strain sustained by the composite at the design load. The  $[\pm 30^\circ]_s$  and  $[\pm 45^\circ]_s$  repairs are both capable of reinforcing the corroded riser, with the  $[\pm 30^\circ]_s$  showed better strengthening capability. However, application of such composite repairs via helical wrapping depends on the tack of the prepreg composite used and friction coefficient of the riser surface. Both must be sufficient in order to prevent slipping of the prepreg tape during the wrapping process.

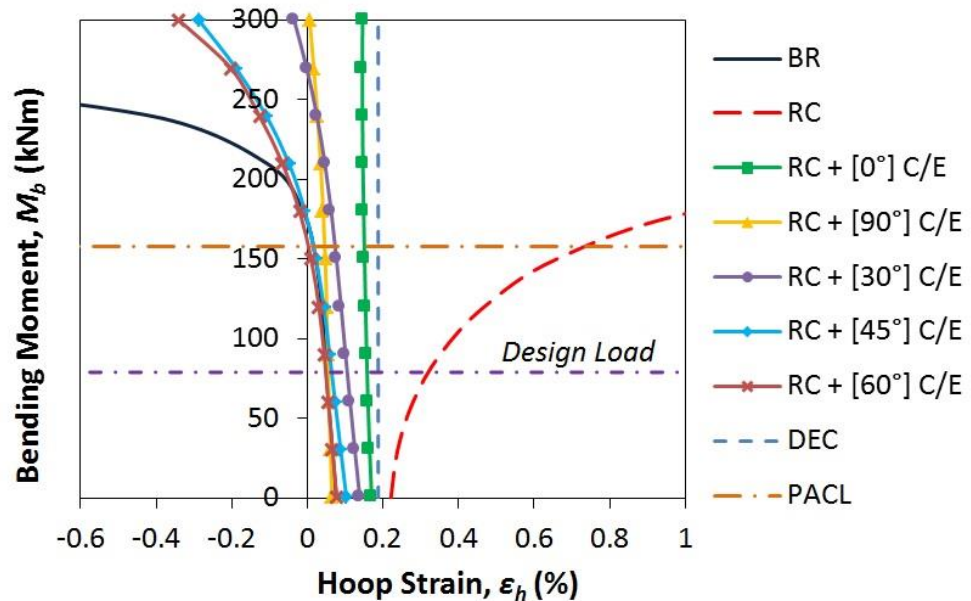


Figure 6-23, Load vs. hoop strain plot of corroded riser repaired with varying wrapping angle of carbon/epoxy laminates subjected to combined internal pressure, tensile and bending load

Figure 6-23 shows the plot of bending moment against hoop strain. The current study suggested that all repair laminates with varying wrapping angles were able to minimize the hoop strain significantly as discussed in Section 5.6.2 of Chapter 5. Under design load condition,

## **6.5 Varying Corrosion Defects**

An external defect or corrosion on a riser can take various shapes and sizes due to the diverse nature of the corrosion mechanism. The effects of defect geometry on the load transfer mechanism need to be identified to understand the system behaviour. However, it is difficult to develop a single universal solution that determines the strength of the corroded riser and the degree of repair required. Most of the available equations obtainable from industrial standards, such as the ASME B31G (ASME, 1991), compute the residual strength of a corroded pipe based on the length and depth of the corrosion. In this study, simulation of various sizes of corrosion defects on the external surface of the riser was conducted. The corrosion which is manifested as a metal loss was modelled in the centre of the riser. CRS with varying thickness and fibre orientation was modelled on the corroded risers. An optimized repair can then be determined by plotting the stress and strain of the corroded section beneath the repair. The resulting stress-strain plot can be used as a guide in the selection process of an optimum CRS.

### **6.5.1 Varying Corrosion Length**

Risers are more susceptible to localised corrossions and therefore need to be analysed based on orientation and severity from a case by case basis. Herein, the

width of the corrosion was set to a constant arc length of 50mm around the circumference of the riser. The length of the corrosion along the longitudinal direction of the riser was varied at an increment of 200mm, from an initial 200mm to 1200mm total corroded length along the riser, as shown in Figure 6-24.

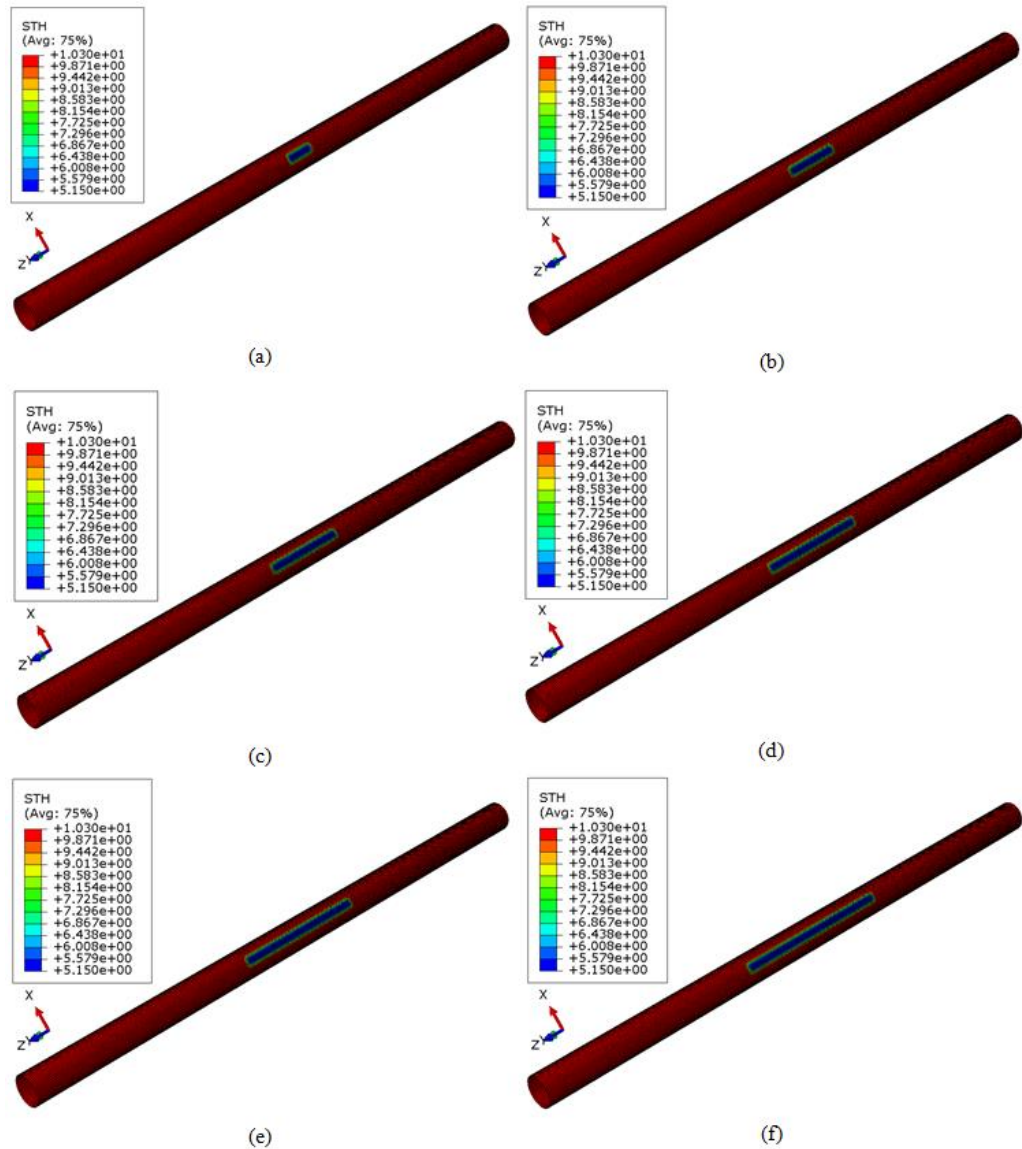


Figure 6-24, Varying corrosion length with constant width of 50mm (a) 200mm (b) 400mm (c) 600mm (d) 800mm (e) 1000mm (f) 1200mm

Figure 6-25 showed that the tensile strain on the corroded steel riser beneath the repair is not significantly affected by the length of the corrosion defect along the

axis of the riser. As the length of the corrosion increases while the width (corroded arc length) remains constant, the cross-sectional area of the corroded region does not change. The tensile force per unit area and the second moment of area remains unchanged. Therefore, dimensional change in the corrosion length does not affect the overall axial stress of the riser in this loading setup where tension and bending loads were applied.

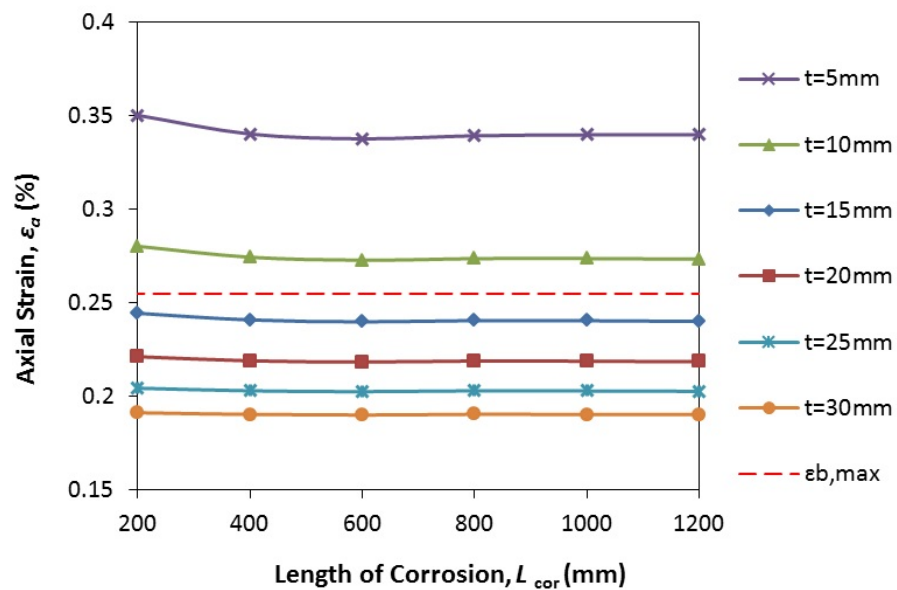


Figure 6-25, Axial strain vs. length of corrosion with varying thickness of the composite repair

### 6.5.1a Comparison with ASME PCC-2

Figure 6-26 shows the axial strain plotted against the thickness of the composite repair. The maximum permissible bending strain determined via the limit analysis of an uncorroded bare riser subjected to combined loading is also shown in the graph. With the simulated curves, the minimum repair thickness of the composite laminate can be determined. The values are compared to those obtained using the equations provided in the ASME-PCC-2 standard. The comparison between the two sets of data are tabulated in Table 6-8 and plotted



in Figure 6-27. As observed, the required thickness of repair for a corrosion of 200mm in length calculated using the ASME PCC-2 is significantly lower due to the smaller length-to-diameter ratio. At greater corrosion lengths, the required thickness increases as the residual strength for the corroded riser is based solely on the hoop stress sustained by the riser. The FE simulation shows the effects of combined loading where axial stress is the main concern. The addition of tensile load and bending moment on the structure reduced the effect of the hoop stress cause by the internal pressure. The longer corrosion defect along the axis of the riser causes the axial stress to be distributed more evenly along the span of the corrosion, reducing the maximum axial strain sustained by the riser and the CRS.

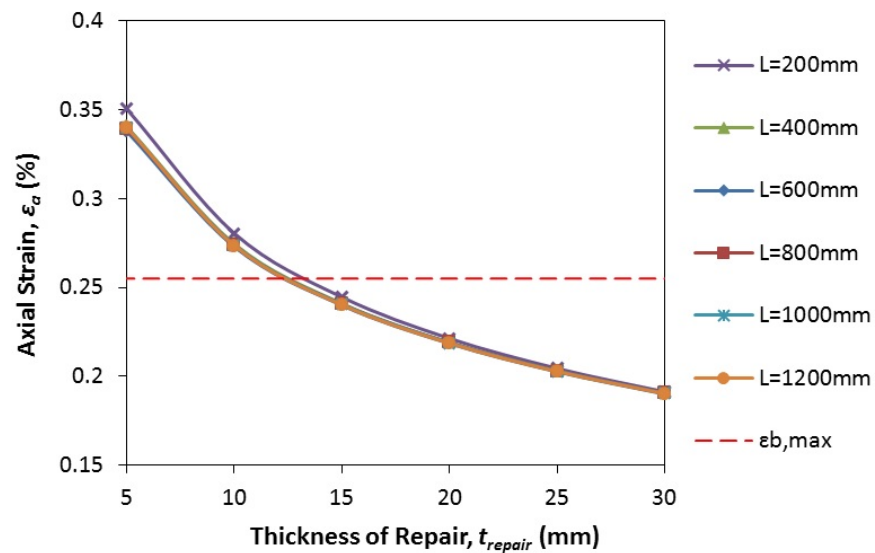


Figure 6-26, Axial strain vs. thickness of repair at varying length of corrosion

Table 6-8, Appropriate thickness of repair at varying length of corrosion

Length of Corrosion, $L_{cor}$ (mm)		200	400	600	800	1000	1200
Thickness of Repair, $t_{repair}$ (mm)	ASME PCC-2	17.40	39.36	41.39	42.64	43.40	43.88
	FE Simulation	13.25	12.50	12.44	12.38	12.31	12.25

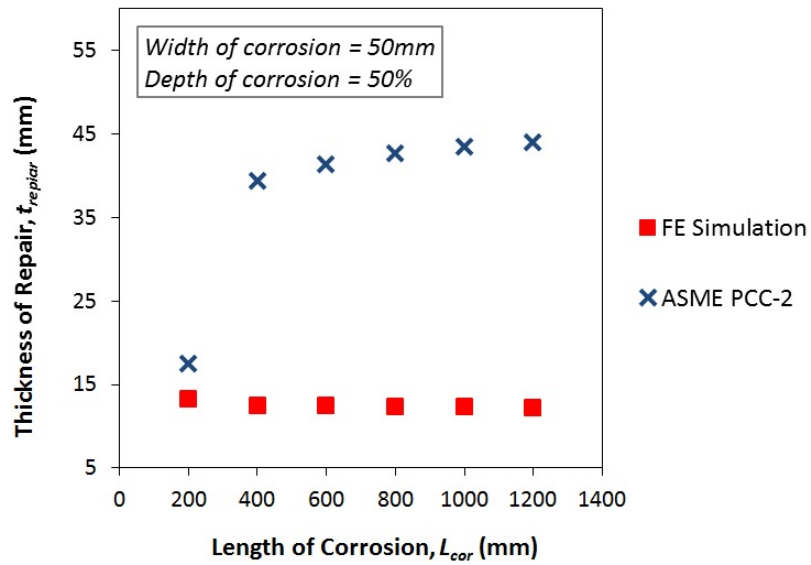


Figure 6-27, Comparison between ASME PCC-2 and FE simulation results at varying length of corrosion

### 6.5.2 Varying Corrosion Width

The length of the corrosion is set to a constant value such that the effects of varying corrosion width, from  $60^\circ$  to  $120^\circ$  around the circumference of the riser can be studied. The width of the corrosion is measured as the angle of the arc length along the circumference of the riser as depicted in Figure 6-28.

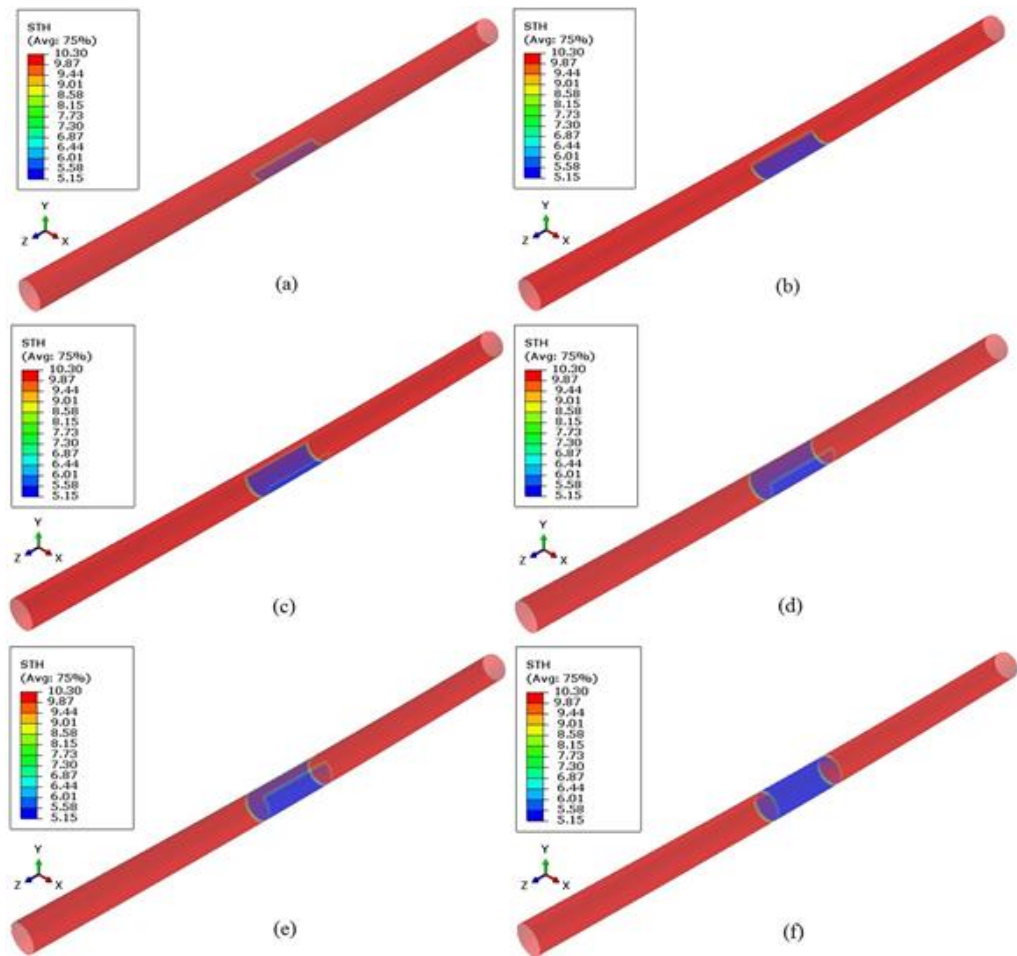


Figure 6-28, Varying corrosion width with constant defect length of 600mm (a) 60° (b) 120° (c) 180° (d) 240° (e) 300° (f) 360°

Figure 6-29 shows that increasing corrosion width from 60° to 180° causes the axial strain on the corroded region beneath the repair to increase significantly. As the width passes the 180° mark, the axial strain remains approximately constant with any further increase in the width of the corrosion. The highest stress region within the riser falls within the ‘tensile’ region of the bent riser, where the corrosion is located. Larger corrosion width causes a decrease in the overall flexural rigidity of the repaired riser. The maximum axial strain was reached when the corrosion covers the entire bottom half circumference of the riser. After that, any increase in the width of the corrosion extends to the top half

the riser which falls under the compressive region of the bent riser, where stress effects are minimal.

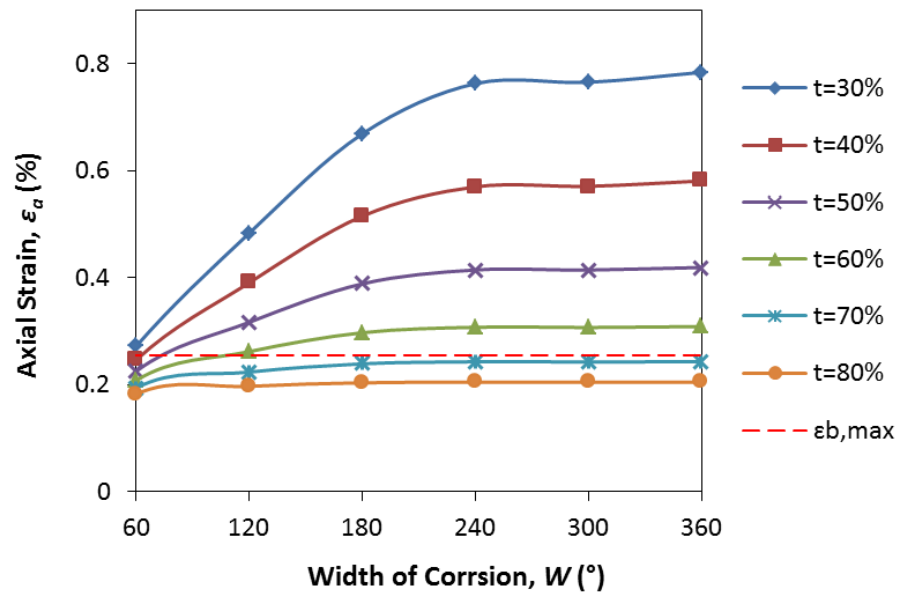


Figure 6-29, Axial strain vs. width of corrosion at varying percentage wall thickness on the corroded region

A plot of axial strain against the depth of the corrosion is shown in Figure 6-30. As the wall thickness of the riser within the corroded region decreases, the axial strain increases exponentially. The thinner cross section of the riser increases the force per unit area acting on the riser. Evaluation of the remaining strength within a corroded riser prior to the determination of the suitable CRS is crucial. The average wall thickness at the corroded region must be measured accurately in order to compute the required thickness of the CRS. The curves for  $W=240^\circ$ ,  $W=300^\circ$  and  $W=360^\circ$  were observed to be overlapped, signifying that further increase in the width of the corrosion does not affect the performance of the CRS significantly, as discussed earlier.

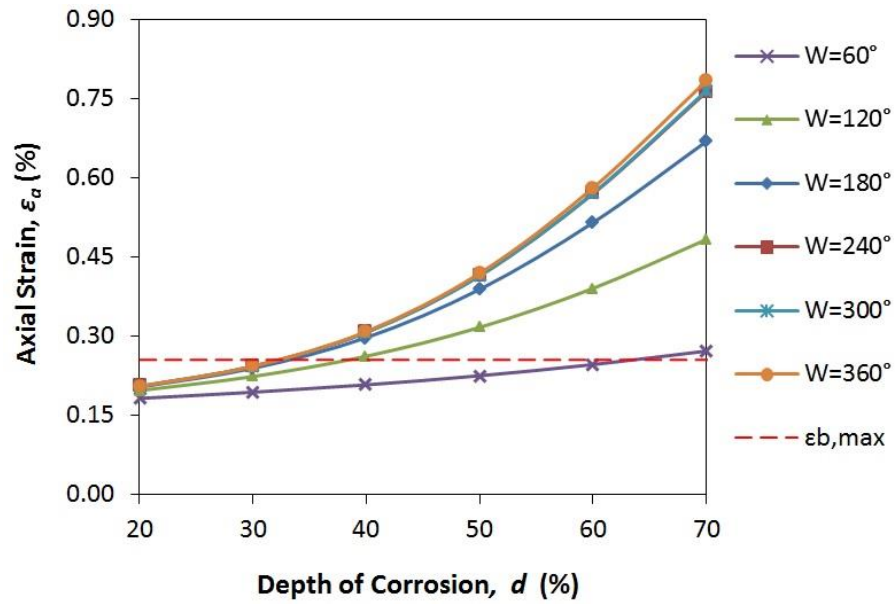


Figure 6-30, Axial strain vs. wall thickness of corroded region at varying width of corrosion

### 6.5.2a Comparison with ASME PCC-2

The results as obtained from the current FEA were compared to those calculated using the ASME PCC-2. The required thickness of the composite repair was computed using the curves shown in Figure 6-31 and tabulated in Table 6-9. The maximum permissible axial strain was chosen as the reference where the required thickness of repair is determined.

Figure 6-32 shows a clear comparison between the computed thickness values using the ASME PCC-2 and FEA model. At lower corrosion depths, both ASME PCC-2 and FEA yield similar thickness values. As the depth of the corrosion increases, the ASME PCC-2 shows overly conservative results compared to the FE simulations results. The equations in the ASME PCC-2 standard is based on the elastic constants of the composite material and yield strength of the riser material. It fails to account for the nonlinearity in the structures when yielding

occurs. In contrast, the FEA is able to capture the nonlinear behaviour of the structure, where stress is transferred from the riser to the composite material.

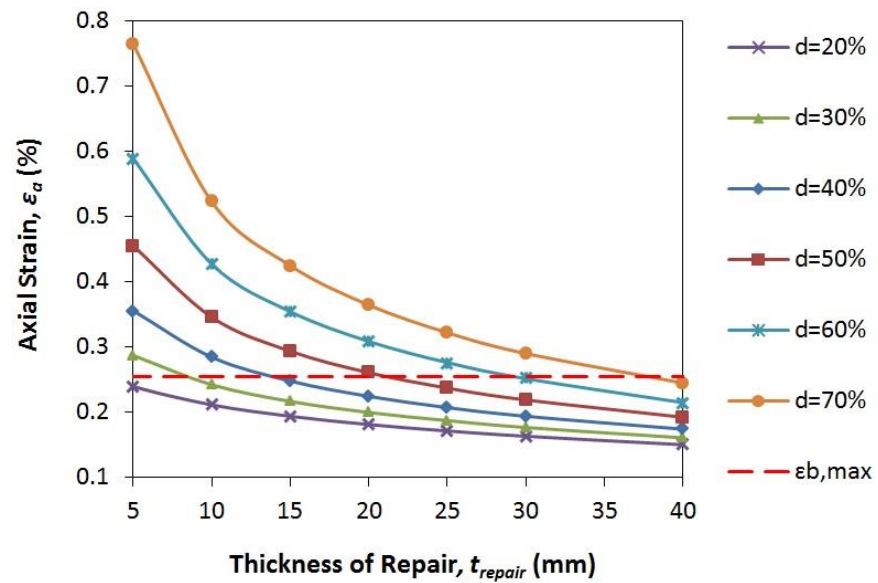


Figure 6-31, Axial strain vs. thickness of repair at varying depth of corrosion

Table 6-9, Thickness of repair at varying depth of corrosion

Depth of Corrosion, $d$ (%)		20	30	40	50	60	70
Thickness of Repair, $t_{repair}$ (mm)	ASME PCC-2	8.67	19.29	30.19	41.39	52.89	64.71
	FE Simulation	3.38	8.5	13.88	21.13	29.25	37.75

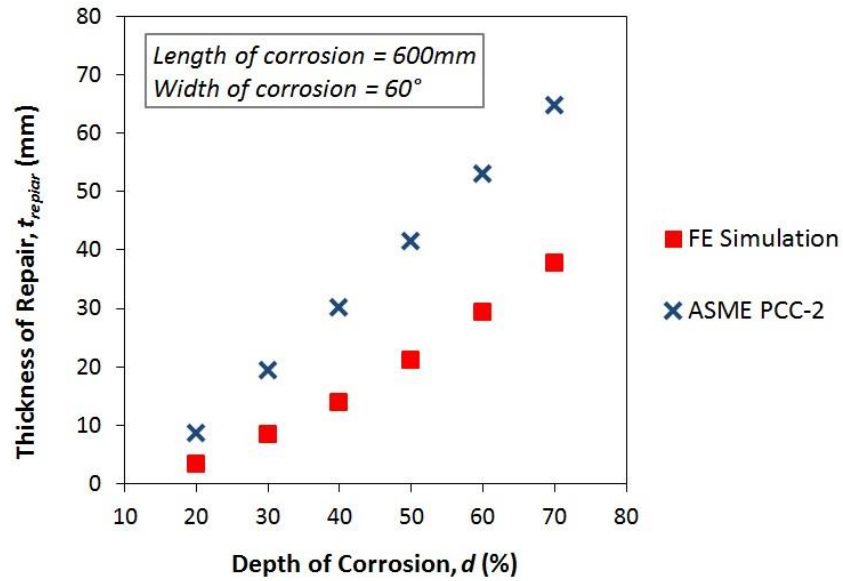


Figure 6-32, Comparison between ASME PCC-2 and FE simulation results at varying depth of corrosion

### 6.5.2b Development of a Simple Relation

Based on the results of the simulation, a simple relation can be formulated to relate the required thickness of repair to the width and depth of the corrosion defect. As determined in section 6.5.1, the length of the corrosion defect does not affect the axial strain of the repaired riser significantly under the combined loading conditions. The relation must exist between the parameters such that given a particular diameter and thickness of the riser; one must be able to find the optimum thickness of the required composite repair. The thickness of repair are related to the depth and width of corrosion defect via the expression shown below,

$$\frac{t_r}{t_p} = A \left( \frac{d_c}{t_p} \right)^m \left( \frac{W_c}{C_p} \right)^n, \quad \frac{W_c}{C_p} \leq 0.5 \quad 6-1$$

Where  $d_c$  = the depth of the corrosion,  $t_p$  = wall thickness of the pipe/riser,  $W_c$  = width of the corrosion,  $C_p$  = circumference of the pipe/riser and  $t_r$  = required

thickness of the composite repair.  $A$  represents a constant while  $m$  and  $n$  are the power values. As seen in the equation, the depth and width of the corrosion are both expressed in normalised terms such that it is applicable to pipes/risers of different dimensions. The condition for the relation is for the ratio of  $W_c$  to  $C_p$  to be equal or less than 0.5 as further increase in the width of corrosion does not significantly affect the axial strain as shown in Figure 6-29. Using a nonlinear regression analysis, the values for  $A$ ,  $m$  and  $n$  can be computed.

$$\frac{t_r}{t_p} = 14.83 \left( \frac{d_c}{t_p} \right)^{1.685} \left( \frac{W_c}{C_p} \right)^{0.468}, \quad \frac{W_c}{C_p} \leq 0.5 \quad 6-2$$

Figure 6-33 shows a comparison between the predicted data using Eq. 6-2 and the input data from the FE simulation. The correlation between the predicted and input data is considerably high with a coefficient of multiple determination,  $R^2 = 0.995$ .

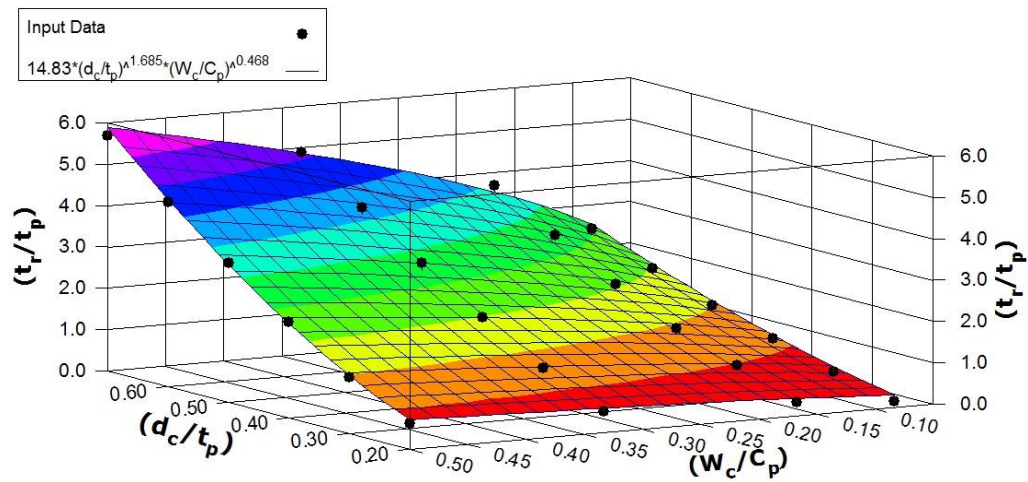


Figure 6-33, 3D plot of input data (FE simulation) and predicted data (regression analysis)

In Chapter 3, it has been discussed that the design of the CRS is based on limit analysis where the design conditions are determined based on the load-strain curve of an uncorroded bare pipe. Hence, by assuming that pipe/riser of different



materials and sizes will still operate under similar constraints, Eq. 6–2 can be used to determine the required thickness of the CRS. However, the accuracy of Eq. 6–2 outside the simulated range needs to be further investigated. A simple example of a riser with different material and dimension was conducted to determine the accuracy and robustness of the relation. An API 5L X52 steel pipe with a diameter of 323.85mm and wall thickness of 15.875mm was studied. Using the double elastic curve method (DEC) as discussed in Chapter 3, the design conditions were calculated and shown in Table 6-10.

Table 6-10, Design load and maximum permissible strain for API 5L X52 steel riser

<b>Loading Case</b>	<b>Design Load</b>	<b>Maximum Permissible Strain,</b>
Internal Pressure, $P_{in}$	19.5MPa	$\epsilon_{h,max}$ 0.17%
Tensile Load, $F_t$	2750kN	$\epsilon_{a,max}$ 0.17%
Combined Load ( $P_{in} = 19.5\text{MPa}$ , $F_t = 2750\text{kN}$ )	160.5kNm	$\epsilon_{a,max}$ 0.18%

FE models of the corroded API 5L X52 steel riser repaired with AS4/3501-6 carbon/epoxy subjected to combined load were simulated to determine the required thickness of the CRS. The length of the corrosion defects were kept at a constant value of 600mm while the width and depth of the corrosion were varied, ranging from 30° to 120° and 30% to 70%, respectively. The  $t_r$  values as computed from the FE models were compared to those calculated using Eq. 6–2. The results are shown in Figure 6-34.

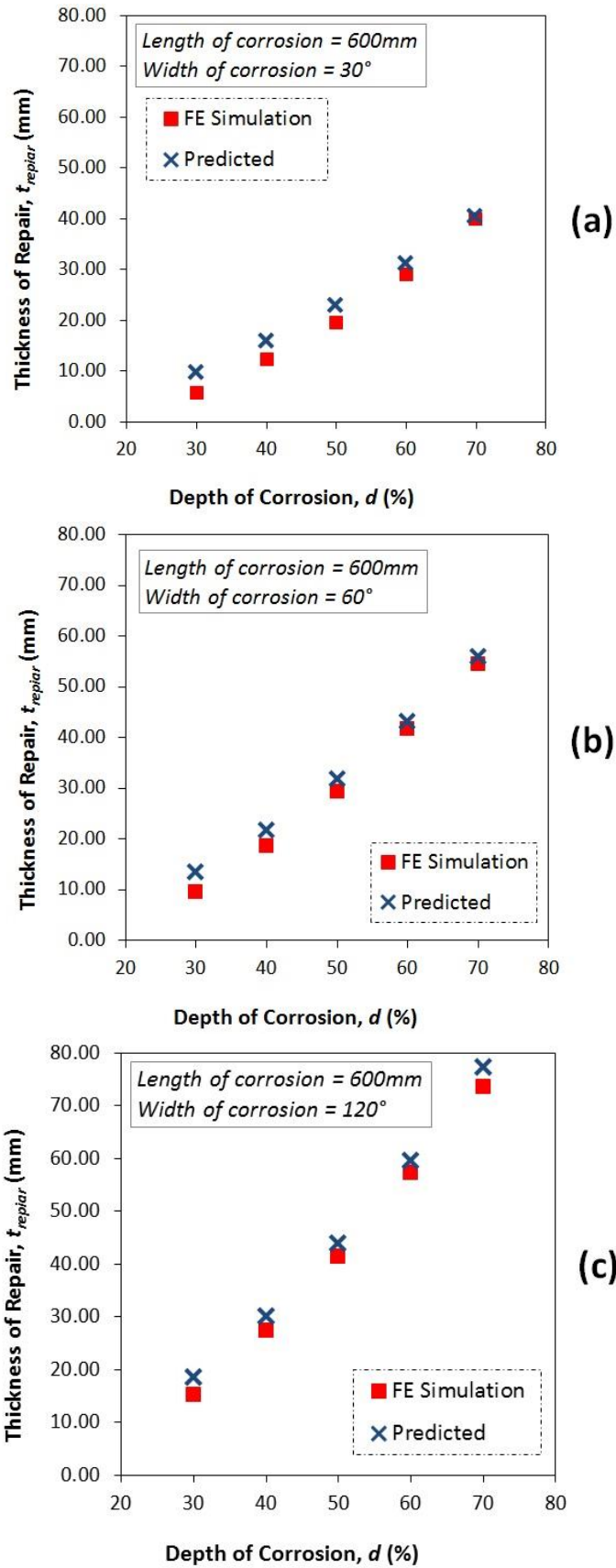


Figure 6-34, Comparison of FE simulation and predicted results for  $t_{repair}$  of repaired API 5L X52 steel riser: (a)  $W_c = 30^\circ$ , (b)  $W_c = 60^\circ$  and (c)  $W_c = 120^\circ$

As observed, the relation formulated using the nonlinear regression analysis was found capable to produce accurate prediction on the required thickness of CRS, with tolerance of  $\pm 4\text{mm}$ . The percentage error tends to increase in scenario where the corrosion defects are less detrimental (i.e. smaller width and lower depth). Such defects require relatively thin repair and hence fluctuation in magnitude of  $\pm 4\text{mm}$  will result in a higher percentage difference.

## **6.6 Concluding Remarks**

The simulation using FEA has demonstrated that carbon reinforcing fibres provide much better strengthening to a corroded riser. However, the main strengthening occurs in the direction parallel to the fibres. Hence, mixed laminate orientations can be beneficial to a CRS as they can provide a much balanced reinforcement to a corroded riser, in both hoop and axial directions where stresses are most significant. Section 6.3 demonstrated the need for reinforcement to sustain the hoop stress caused by internal pressure as well as axial stress caused by the combined tensile force and bending load. However, fabrication of laminates with mixed lamina orientations is not always feasible, in particular in the case where fibre orientation is aligned along the longitudinal axis of the riser, such laminates are usually fabricated as full-cured parts prior to rehabilitation installation.

The automation of subsea composite repair on corroded riser can be made feasible by employing a simple application mechanism, which is the winding of prepreg tapes. The winding/wrapping angle determines the strength of the CRS. Under combined loading of internal pressure, tension and bending moment, winding angle that aligns the fibres closest to the longitudinal axis of the riser

provides highest resistance to the axial stress. The current study revealed that  $[\pm 30^\circ]$  and  $[\pm 45^\circ]$  laminates capable to provide sufficient axial strengthening. However,  $[\pm 45^\circ]$  laminates provides an additional advantage to strengthen the corroded riser in the hoop direction. This is essential as the bending force usually fluctuates depending on the wave and current forces. When bending force is at its minimal, the effects of hoop stress from the internal pressure become more significant.

A simple relation has been developed for computation of the required thickness of the CRS under combined loadings. This relation determines the optimum thickness of the repair based on the width and depth of the corrosion defect and is different from those available in ASME PCC-2 as the computation in ASME PCC-2 fails to account for the increase in width of corrosion as well as the effects of axial stress on the corrosion defect. The prediction via this relation produces great accuracy assuming that risers are designed based on limit analysis.

## Chapter 7 Conclusions

### 7.1 Primary Achievements and Contributions to New Knowledge

The current section concludes primary achievements, main findings and contributions of this research work.

- CRS using pre-impregnated FRPC in the form of a tape is effective in reinforcing a corroded riser subjected to combined loading, where the use of carbon/epoxy show superior strengthening performance (reduces axial strain in corroded region by up to 58%) compared to glass/epoxy (reduces axial strain in corroded region by up to 36%).
- The effects of individual static loading (i.e. internal pressure, tension and bending) on a corroded riser repair with CRS. With individual loading, the CRS used should consist of unidirectional laminates where fibres are aligned with the direction of the load. However, CRS with pure axially orientated fibres (parallel with axis of riser) are not practically achievable via helical wrapping.
- The effects of combined static loading on a corroded riser repair with CRS. With combined internal pressure, tension and bending, the dominant stress which is most likely to cause failure of the repaired riser in the axial stress. CRS for this combined loading case is very much different compared to individual loading cases. Fibres more closely aligned in the axial direction of the riser will provide better strengthening to a corroded riser.
- The use of strain energy release rate to characterise the bond integrity between the FRPC laminate and the steel riser under static and cyclic bending. Current standard on composite repair for oil and gas pipelines such

as ASME PCC-2 (ASME, 2008) and ISO/TS 24817 (ISO, 2006) addresses the bond integrity through the measurement of lap shear strength where an average of 4MPa must be demonstrated. With the complex loading conditions sustained by a riser, strain energy release rates used in mixed mode failure criteria will give more in-sight into the failure mechanism of the CRS and hence improved qualification data.

- In practice, full-scaled experiments are used to validate the accuracy of a numerical model in predicting the stress-strain behaviour of a CRS. This research has proven that validation via small-scaled tests are equally achievable with percentage difference of less than 13%. The small-scaled tests developed through similitude relations can reduce the cost and resources needed for the experiment.
- The effects of length, width and depth of the corrosion defect on the required thickness of the CRS. When subjected to combined loading of internal pressure, tension and bending at design conditions, the increase in length width and depth cause an increase in the required thickness of repair. However, increase in length does not affect the thickness of repair significantly. This suggested that the bi-axial loading condition is very much different from conventional onshore pipeline repair where major loading is only in the hoop direction.
- Development of an accurate FEA model capable of predicting the performance of a CRS in strengthening a corroded riser, which can be used to conduct a comprehensive parametric study on the CRS. Careful selection of different parameters such as element type, mesh refinement, interaction properties and boundary conditions was performed to ensure that minimum

simulation time and resources without compromising the accuracy of the results. This FEA model which was validated through scaled-down flexural tests can be used to optimize the different parameters of the CRS. The detailed framework in optimizing the CRS through the FEA model can be summarized as

- 1) As a reference point, the equation in ASME PCC-2 was used to obtain the probable thickness of the repair that should be modelled.
  - 2) Reduced integration shell elements, S4R which are capable of capturing large strain (i.e. inelastic deformation) under different loading conditions were used to model both the corroded riser and CRS. Stress-strain behaviour of both the CRS and corroded riser was studied.
  - 3) Fracture mechanics using strain energy release rate was applied to study the bond integrity at the interlaminar interface and steel-composite interface.
  - 4) Multi-Continuum Theory (MCT) failure criteria was incorporated to study the tendency of the FRPC to fail under the assigned loading conditions.
  - 5) Fibre angle, thickness of repair, length of defect and width of defect were easily changed via the input file of the FEA model in the process of optimizing the CRS.
- A design tool for CRS on offshore risers which combines the use of accurate FEA model, limit analysis and a simple relation equation. The minimum thickness of the CRS can be determined using the simple relation, followed by a performance analysis using the developed FEA model and limit analysis.

## **7.2 Recommendations for Future Work**

The preliminary design of the composite repair machine currently proposed in the Appendix A can be further developed into a fully functional prototype. Initial stages can involve the development of the prototype for wrapping module alone where the desired thickness, length and angle of the composite wrap can be achieved. This prototype can be a scaled-down version where the demonstration of the wrapping sequence can be demonstrated on a smaller pipe spool in a laboratory environment. Once wrapping has been proven to be feasible, testing of the wrapping spool can be done by loading the specimen onto a test rig.

The procedures and results of the small-scaled experiment on the flexural properties of the CRS were discussed. Future work can include the development of a small-scale cyclic bending rig which can be used to validate the behaviour of the CRS subjected to cyclic bending. This can be highly valuable as offshore risers are continuously subjected to cyclic bending forces due to wave and sea current.

The study on response of the FRPC laminate under static loading conditions using MCT failure criterion has proven that the repair laminate will not fail under static design conditions. The FEA model can be further improved by incorporating a user-subroutine that characterizes the FRPC material via fatigue failure criterion. Hence, the behaviour of both the steel-composite interface bond and FRPC laminate of the CRS subjected to cyclic loading can be studied simultaneously to observe the failure mechanism of the CRS.



## References

- ABS, 2008. Guide for Building and Classing Subsea Riser Systems. *American Bureau of Shipping, Houston, TX, USA.*
- Alexander, C., 2005. *Evaluation of the AquaWrap® System in Repairing Mechanically-Damaged Pipes*, Azusa, California: Air Logistics, Inc..
- Alexander, C., 2006. *Assessing the Use of Composite Materials in Repairing and Reinforcing Offshore Riser Pipes*. s.l., s.n.
- Alexander, C., 2006. *State of the Art Assessment of Composite Systems Used to Repair Transmission Pipelines*. Calgary, Alberta, Canada, s.n.
- Alexander, C., 2007. Development of a Composite Repair System for Reinforcing Offshore Risers. *PhD Thesis, Texas A&M University.*
- Alexander, C., 2012. *Design of An Optimized Composite Repair System for Offshore Risers Using Integrated Analysis and Testing Techniques*. 30 April - 3 May, Houston, Texas, USA, s.n., p. OTC 23164.
- Alexander, C. & Bedoya, J., 2011. *Using Composite Materials to Reinforce Onshore Pipelines: New Insights and Lessons Learned*. October 31 - November 3, Houston, Texas, USA, s.n.
- Alexander, C. & Ochoa, O., 2010. Extending Onshore Pipeline Repair to Offshore Steel Risers with Carbon-Fibre Reinforced Composites. *Composite Structures*, pp. 92: 499-507.
- Alexander, C. & Wilson, F., 2000. *Recent Test Results and Field Experience with Armor Plate Pipe Wrap in Repairing Corroded and Mechanically-Damaged Pipes*, Houston, Texas, USA: Stress Engineering, Inc..
- Andre, A., Haghani, R. & Biel, A., 2012. Application of Fracture Mechanics to Predict the Failure Load of Adhesive Joints used to Bond CFRP Laminates to Steel Members. *Construction and Building Materials*, pp. 27: 331-340.
- Andre, A. & Linghoff, D., 2009. *Damage Modelling of Adhesive Joint in Composite Reinforced Metallic Beams*. September, Malmo, Sweden, s.n.
- Anyfantis, K. N. & Tsouvalis, N. G., 2013. Loading and Fracture Response of CFRP-to-Steel Adhesively Bonded Joints with Thick Adherents - Part I: Experiments. *Composite Structures*, Volume 96, pp. 850-857.
- API, 1998. API Recommended Practice 2RD: Design of Risers for Floating Production Systems (FPSs) and Tension-Leg Platforms (TLPs). *American Petroleum Institute, Washington, DC, USA .*

API, 1999. API Recommended Practice 1111: Design, Construction, Operation and Maintenance of Offshore Hydrocarbon Pipelines (Limit State Design). *American Petroleum Institute, Washington DC, USA.*

ASME, 1991. ASME B31G: Manual for Determining the Remaining Strength of Corroded Pipelines. *The American Society of Mechanical Engineers, New York, USA.*

ASME, 2003. ASME B31.8: Gas Transmission and Distribution Piping System. *The American Society of Mechanical Engineers, New York, USA.*

ASME, 2006. ASME B31.4: Pipeline Transportation Systems for Liquid Hydrocarbons and Other Liquids. *The American Society of Mechanical Engineers, New York, USA.*

ASME, 2007. ASME Boiler & Pressure Vessel Code. Rules for Construction of Pressure Vessels. Section VIII, Division 2, Alternative Rules. *The American Society of Mechanical Engineers, New York, USA.*

ASME, 2008. ASME PCC-2: Repair of Pressure Equipment and Piping. *The American Society of Mechanical Engineers, New York, USA.*

ASTM, 2000. *Standard Test Method for Tensile Properties of Polymer Matrix Composite Materials*, West Conshohocken, United States: ASTM International.

ASTM, 2008. *ASTM D3165: Standard Test Method for Strength Properties of Adhesives in Shear by Tension Loading of Single-Lap-Joint Laminated Assemblies*, West Conshohocken, PA, USA: The American Society of Testing and Materials.

ASTM, 2012. *E8/E8M-11: Standard Test Method for Tension Testing of Metallic Materials*, West Conshohocken, United States: ASTM International.

ASTM, 2012. *Standard Test Method for Shear Properties of Composite Materials by the V-Notched Beam Method*, West Conshohocken, United States: ASTM International.

Balaji, G., Biradar, P., CN, S. & Venkata Ramaiah, K., 2008. *An SMA-actuated, Compliant Mechanism-based Pipe-crawler*. July 24-26 Bangalore, India, s.n.

Banea, M. & da Silva, L., 2009. Adhesively Bonded Joints in Composite Materials: An Overview. *Proceedings of the IMechE, Part L: Journal of Materials and Applications*.

Bedoya, J., Alexander, C. & Precht, T., 2010. *Repair of High Pressure Pipe Fittings Using Composite Materials*. Sep 27 - Oct 1, Calgary, Alberta, Canada, 8th International Pipeline Conference.

Biel, R. & Alexander, C., 2005. *Applications of Limit Load Analyses to Assess the Structural Integrity of Pressure Vessels*. 17-21 July, Denver, ASME.

Bocciarelli, M., Colombi, P., Fava, G. & Poggi, C., 2008. *Cohesive Delamination in Steel Elements Strengthened with CFRP Plates*. 22-24 July, Zurich, Switzerland, s.n.

Bogy, D., 1968. Edge Bonded Dissimilar Orthogonal Elastic Wedges Under Normal and Shear Loading. *Journal of Applied Mechanics*, pp. 35: 460-466.

Boulet d'Auria, S. et al., 2013. *Subsea Pipeline Repair by Composite System: One Step Deeper*. 6-9 May, Houston, Texas, USA, s.n.

C, A., 2007. Development of a Composite Repair System for Reinforcing Offshore Risers. *PhD Thesis, Texas A&M University*.

Carey, A. & Johnson, M., 2013. *Cleaning Mechanism for Oil Riser Repair System*, Report submitted for Individual Project: The University of Nottingham.

CaviDyne, 2014. *CaviBlaster™ Underwater Cleaning System*. [Online] Available at: [http://www.cavidyne.com/Downloads/CaviBlaster\\_Web\\_Brochure\\_020808.pdf](http://www.cavidyne.com/Downloads/CaviBlaster_Web_Brochure_020808.pdf) [Accessed September 2014].

CEN, 1997. ES EN ISO 377, Steel and Steel Products - Location and Preparation of Samples and Test Pieces for Mechanical Testing. *European Committee for Standardization, Brussels, Belgium*.

CEN, 2001. ES EN 10002-1, Metallic Materials - Tensile Testing - Part 1: Method of Test at Ambient Temperature. *European Committee for Standardization, Brussels, Belgium*.

Chakrabarti, S. & Frampton, R., 1982. Review of Riser Analysis. *Applied Ocean Research*, pp. 4(2): 73-90.

Chatzakos, P., Papadimitriou, V. & Psarros, D., 2010. *On the Development of an Unmanned Underwater Robotic Crawler for Operation on Subsea Flexible Risers*. s.l., s.n.

Citadel Technologies, 2011. *Diamondwrap®: Structural Carbon/Epoxy Rehab System for the Prevention and Repair of Corroded Pipe System*. [Online] Available at: <http://cittech.com/documents/diamondwrapinfo.pdf> [Accessed 6 November 2011].

Clock Spring, 2012. *Clock Spring® Pipe Reinforcement and Repair System*. [Online] Available at: [www.clockspring.com/wp-content/uploads/2011/12/Clock-](http://www.clockspring.com/wp-content/uploads/2011/12/Clock-)

[Spring-2012web.pdf](#)

[Accessed November 2011].

Considine, J., 2010. *Inherent Defect Size: Calculation and Use for Composite Materials*. Pennsylvania, USA, s.n., pp. June 27 - July 2.

Coutts-Smith, L., Heslehurst, R. & Smith, W., 2013. *Tailoring Laminate Bend-Twist Coupling Through Ply Position*. Melbourne, Australia, CRC-ACS, Composites Australia.

DEKOTECT GmbH, 2014. *Product Information on DEKOMAT KGR- Junior*. [Online]

Available at:

[http://www.speccoats.co.za/DataSheets/Dekomat\\_KGR\\_Junior.pdf](http://www.speccoats.co.za/DataSheets/Dekomat_KGR_Junior.pdf)

[Accessed April 2014].

Derisi, B., Hoa, S. & Hojjati, M., 2012. Similitude Study on Bending Stiffness and Behavior of Composite Tubes. *Journal of Composite Materials*, pp. 0(0): 1-16.

DNV, 2010. Offshore Service Specification DNV-OSS-302: Offshore Riser Systems. *Det Norske Veritas, Norway*.

DNV, 2010. Offshore Standard DNV-OS-F201: Dynamic Risers. *Det Norske Veritas, Norway*.

DNV, 2010. Recommended Practice DNV-RP-F101: Corroded Pipelines. *Det Norske Veritas, Norway*.

Duell, J., Wilson, J. & Kessler, M., 2008. Analysis of a Carbon Composite Overwrap Pipeline Repair System. *International Journal of Pressure Vessels and Piping*, pp. 85: 782-788.

Esmael, R., Khan, M. & Taheri, F., 2012. Assessment of the Environmental Effects on The Performance of FRP Repaired Steel Pipes Subjected to Internal Pressure. *Journal of Pressure Vessel Technology*, pp. 134(041702): 1-7.

Farwest Corrosion Control, 2014. *Tapecoat Hand Wrapster #3 Tape Wrapping Tool*. [Online]

Available at: <http://www.farwestcorrosion.com/tapecoat-hand-wrapster-3-tape-wrapping-tool.html>

[Accessed April 2014].

Francini, R. & Kiefner, J., 2006. *Evaluation of the AquaWrap® Composite Repair System*, Azusa California: Air Logistics, Inc..

Giancaspro, J., Papakonstantinou, C. & Balaguru, P., 2010. Flexural Response of Inorganic Hybrid Composites with E-glass and Carbon Fibres. *Journal of Engineering Materials and Technology*, pp. 132: 1-8.

Grewal, H. S. & Hojjati, M., 2015. *Inter-ply Friction Measurement of Out-of-Autoclave Thermosetting Prepreg Composites*. Montreal, Quebec, Canada, 62nd CASI Aeronautics Conference and AGM 3rd GARDN Conference.

Haghani, R., 2010. Analysis of Adhesive Joints Used to Bond FRP Laminates to Steel Members - A Numerical and Experimental Study. *Construction and Building Materials*, pp. 24: 2243-2251.

Hashin, Z., 1980. Failure Criteria for Unidirectional Fiber Composites. *Journal of Applied Mechanics*, pp. 47: 329-334.

Hinton, M., Kaddour, A. & Soden, P., 2004. The World-Wide Failure Exercise: Its Origin, Concept and Content. In: *Failure Criterion in Fibre Reinforced Polymer Composites: The World-Wide Failure Exercise*. Oxford: Elsevier, pp. 2-26.

Howells, H., 1995. *Advances in Steel Catenary Riser Design*. Aberdeen, s.n.

Innospection Ltd, 2013. [Online]

Available at: <http://www.innospection.com/pdfs/Data%20Sheet%20MEC-Combi%20Crawler%20v01-2013.pdf>

[Accessed 1 July 2014].

ISO, 2006. ISO/TS 24817: Petroleum, Petrochemical and Natural Gas Industries – Composite Repairs for Pipework – Qualification and Design, Installation, Testing and Inspection. *International Organization for Standardization, Geneva, Switzerland*.

Khan, R., Kaur, A., Singh, S. & Ahmad, S., 2011. Nonlinear Dynamic Analysis of Marine Risers under Random Loads for Deepwater Fields in Indian Offshore. *Procedia Engineering*, 14, pp. 1334-1342.

Kootsookos, A., Mouritz, A. & St John, N., 2011. *Comparison of Seawater Durability of Carbon- and Glass-Polymer Composites*. Beijing, China, Proceedings of ICCM-13.

Krueger, R., 2011. *Development and Application of Benchmark Examples for Mode II Static Delamination Propagation and Fatigue Growth Prediction*, Hampton, Virginia, USA: Report prepared for NASA, NASA/CR-2011-217305.

Lam, C., Cheng, J. & Yam, C., 2011. Finite Element Study of Cracked Steel Circular Tube Repaired by FRP Patching. *Procedia Engineering*, Volume 14, pp. 1106-1113.

- Land, P. et al., 2012. *Creepy Crawler*, Report submitted for Group Design Project: University of Nottingham.
- Lassila, L., Nohrstrom, T. & Vallittu, P., 2006. The Influence of Short-term Water Storage on The Flexural Properties of Unidirectional Glass Fibre-Reinforced Composites. *Biomaterials*, pp. 298: 111-117.
- Liao, W. & Sun, C., 1996. The Determination of Mode III Fracture Toughness in Thick Composite Laminates. *Composite Science and Technology*, pp. 56: 489-499.
- Li, S. & Reid, S., 1992. On the Symmetry Conditions for Laminated Fibre-Reinforced Composite Structures. *International Journal of Solids and Structures*, pp. 29(23): 2867-2880.
- Lukacs, J. et al., 2010. Experimental and Numerical Investigations of External Reinforced Damaged Pipelines. *Procedia Engineering*, Issue 2, pp. 1191-1200.
- Machado Filho, R. et al., 2001. *The Monitoring System for A Steel Catenary Riser Suspended from A Floating Platform in Deepwater*. s.l., s.n.
- Madelpech, P., Juaneda, S. & Pradels, M., 2009. *Bonded Composite Patch to Repair Metallic Structures: Fatigue Behaviour of a Disbond*. Edinburgh, United Kingdom, s.n., p. July.
- Mallick, P., 2007. *Fibre-Reinforced Composites: Materials, Manufacturing and Design, 3rd ed.*. New York, USA: CRC Press, Taylor & Francis Group.
- Margerison, B. & Johnson, M., 2012. *Drive Mechanism for an Oil Riser Repair System*, Report submitted for Individual Project: University of Nottingham.
- Martine, R., 2007. *A Technology Gap Review of Composites in the UK Oil and Gas Industry*, Hertfordshire, UK: Materials Engineering Research Laboratory Ltd.
- Meniconi, L., Freire, J., Vieira, R. & Diniz, J., 2002. *Stresss Analysis of Pipelines with Composite Repairs*. 29 September - 3 October, Calgary, Alberta, Canada, s.n., pp. IPC02-2372.
- MT/9, A. S. C., 1997. Metal Finishing - Preparation and Pretreatment of Surfaces, Method Selection Guide. AS 1627, Part: 0.. *Homebush, NSW: Standards Association of Australia*.
- Murad, M., 2011. *An Intergrated Structural Health Monitoring Approach to Composite-Based Pipeline Repair*. Thesis submitted for PhD, s.l.: Cranfield University.

Murad, M., Frost, S. & Brennan, F., 2013. Bonding Integrity Study between Steel Pipeline and Composite Wraps Using Structural Health Monitoring Technique. *Journal of Pipeline Systems Engineering and Practice* 4, pp. 68-73.

Nace International, 2011. *MP Buyers Guide: Wil Cor, Inc.*. [Online]  
Available at: <http://mpbuyersguide.com>  
[Accessed 4 November 2011].

NACE/SSPC, 2006. *Joint Surface Preparation Standard NACE No.2/SSPC-SP 10, Near-White Metal Blast Cleaning*. Houston, Texas, USA, s.n.

Narmashiri, K., Jumaat, M. & Ramli Sulong, N., 2010. Shear Strength of Steel I-Beam by Using CFRP Strips. *Scientific Research and Essays*, pp. 5(16): 2155-2168.

O'Brien, T., Johnston, W. & Toland, G., 2010. *Mode II Interlaminar Fracture Toughness and Fatigue Characterization of Graphite Epoxy Composite Material*, Hampton, Virginia, USA: Report prepared for NASA, NASA/TM-2010-216838.

Ochoa, O. & Salama, M., 2005. Offshore Composites: Transition Barriers to an Enabling Technology. *Composite Science and Technology*, pp. 65: 2588--2696.

Ochola, R., Marcus, K., Nurick, G. & Franz, T., 2004. Mechanical Behaviour of Glass and Carbon Fibre Reinforced Composites at Varying Strain Rates. *Composite Structures*, pp. 63: 455-467.

Palmer, A. & King, R., 2008. *Subsea Pipeline Engineering 2nd ed.*. s.l.:Penwell.

Patrick, A., 2004. Composite - Case Studies of Pipeline Repair Applications. *Pigging and Services Association*.

Patrick, A., 2010. The Use and Application of Composite Repairs. *PetroMin Pipeliner*.

Pipe Wrap, 2011. *Pipe Repair Product: A+ Wrap*. [Online]  
Available at: <http://www.piperepair.net/pwplus.html#proc>  
[Accessed 8 November 2011].

Proserv, 2014. *Proserv Marine Growth Removal (MGR) Tool. Product Specification Sheet*. [Online]  
Available at:  
[http://www.proserv.com/uploads/filemanager/media/Literature/MARINE/Marine\\_Growth\\_Removal/Spec\\_Sheets/Proserv\\_Marine\\_Growth\\_Removal\\_%28MGR%29\\_Tool.pdf](http://www.proserv.com/uploads/filemanager/media/Literature/MARINE/Marine_Growth_Removal/Spec_Sheets/Proserv_Marine_Growth_Removal_%28MGR%29_Tool.pdf)  
[Accessed September 2014].

Psarros, D. et al., 2010. A Service Robot for Subsea Flexible Riser - Analysis and Systematic Design. *IEEE Robotic & Automation Magazine*, pp. 55 - 63.

- Ramu, M., Prabhu Raja, V. & Thyla, P., 2012. Establishment of Structural Similitude for Elastic Models and Validation of Scaling Laws. *KSCE Journal of Civil Engineering*, pp. 17(1): 139-144.
- Ray, B., 2006. Temperature Effect During Humid Ageing on Interfaces of Glass and Carbon Fibres Reinforced Epoxy Composites. *Journal of Colloid Interface Science*, pp. 298: 111-117.
- Rehberg, T., Schad, M. & Green, M., 2010. Non-Metallic Composite Repair Systems for Pipes and Pipelines. *Pipe Technology 3R International Special Edition*.
- RSPA, 2000. 2000. *Department of Transportation, 98-4733, Pipeline Safety: Gas and Hazardous Liquid Repair*.
- Ruggieri, C. & Fernando, D., 2011. Numerical Modelling of Ductile Crack Extension in High Pressure Pipelines with Longitudinal Flaws. *Engineering Structures*, pp. 33: 1423-1438.
- Sala, G., 2000. Composite Degradation due to Fluid Absorption. *Composite Engineering B*, pp. 31: 357-373.
- Seica, M. & Packer, J., 2007. FRP Materials for the Rehabilitation of Tubular Steel Structures for Underwater Applications. *Composite Structures*, pp. 80: 440-450.
- Serta, O. et al., 1996. *Steel Catenary Riser for Marlim Field FPS P-XVIII*. Houston, 6-9 May.
- Shamsuddoha, M. et al., 2013. Effectiveness of Using Fibre-Reinforced Polymer Composites for Underwater Steel Pipeline Repairs. *Composite Structures*, pp. 100: 40-54.
- Shouman, A. & Taheri, F., 2011. Compressive Strain Limits of Composite Repaired Pipelines under Combined Loading States. *Composite Structures*, pp. 93: 1538-1548.
- SMC, 2011. *Accuwrap™ II - Hand Held Pipe Wrapping Machine*. [Online] Available at: <http://sawyermfg.com/wp-content/uploads/2011/07/Accuwrap-II.pdf> [Accessed April 2014].
- Soden PD, H. M. K. A., 1998. Lamina Properties, Lay-Up Configurations and Loading Conditions for a Range of Fibre-Reinforced Composite Laminates. *Composite Science and Technology*, pp. 58: 1011-1022.
- Soden, P., Hinton, M. & Kaddour, A., 1998. Biaxial Test Results for Strength and Deformation of a Range of E-Glass and Carbon Fibre Reinforced Composite



- Laminates: Failure Exercise Benchmark Data. *Composite Science and Technology*, p. 58(7): 1225.
- Soden, P., Kaddour, A. & Hinton, M., 1998. Lamina Properties, Lay-Up Configurations and Loading Conditions for a Range of Fibre-Reinforced Composite Laminates. *Composite Science and Technology*, pp. 58: 1011-1022.
- Stanton, P., 2006. Overview of Deepwater Drilling and Production Risers. *Technip*.
- Tanaka, K., Minoshima, K., Grela, W. & Komai, K., 2002. Characterization of The Aramid/Epoxy Interfacial Properties by Means of Pull-out Test and Influence of Water Absorption. *Composite Science and Technology*, pp. 62: 2169-2177.
- Tavakkolizadeh, M. & Saadatmanesh, H., 2001. Galvanic Corrosion of Carbon and Steel in Aggressive Environments. *Journal of Composites for Construction*, pp. 5: 200-210.
- Tiratsoo, J., 2003. *Pipeline Pigging and Integrity Technology 3rd ed.*. s.l.:Clarion Technical Publishers.
- UES, 2014. *UES Marine Cleaning Tool Model: MC211 Data Sheet*. [Online] Available at: <http://www.uesltd.net/pdf/MC211%20Data%20Sheet.pdf> [Accessed September 2014].
- UMECO, 2012. *MTM57 Series MSDS Sheet*, s.l.: Umeco Structural Materials Ltd.
- Walker, A. & Williams, K., 1995. *Strain Based Design of Pipelines*. Copenhagen, Denmark, s.n., pp. 5: 345-350.
- Webb, G., 1980. Inspection and Repair of Oil and Gas Production in Deep Water. *Ocean Management*, pp. 7: 31-326.
- Wonderly, C., Grenestedt, J., Fernlund, G. & Cepus, E., 2006. Comparison of Mechanical Properties of Glass Fibre/Vinyl Ester and Carbon Fibre/Vinyl Ester Composites. *Composites: Part B*, pp. 36: 417-426.
- Worth, F., 2005. *Analysis of AquaWrap® for Use in Repairing Damaged Pipelines: Environmental Exposure Conditions, Property Testing Procedures, and Field Testing Evaluations*, Azusa, California: Air Logistics.
- Yang, J., Smith, S. & Feng, P., 2013. Effect of FRP-to-Steel Bonded Joint Configuration on Interfacial Stresses: Finite Element Investigation. *Thin-Walled Structures*, pp. 62: 215-228.

Yukawa, T., Suzuki, M., Satoh, Y. & Okano, H., 2006. *Design of Magnetic Wheels in Pipe Inspection Robot*. October 8-11, Tapei, Taiwan, s.n., pp. 235-240.

Zhao, X., Fernando, D. & Al-Mahadi, R., 2006. CFRP Strengthened RHS Subjected to Transverse End Bearing Force. *Engineering Structures*, pp. 28: 1555-1565.

# **Appendix A Industrial Needs for Composite Repair Machine and Its Preliminary Design**

## **A.1 Background**

Exploration for new oil reserves has been mounting over the years and oil companies have been probing ever deeper into the seabed. With greater sea depths, rehabilitation of corroded risers are becoming increasingly challenging and inaccessible to human divers. Hence, the need for developing an automated pipeline repair machine is apparent. Until recently, there has been numerous attempt to develop an efficient and functional automated subsea pipeline repair machine amongst oils companies. Most of these works are based on isolated efforts and the relevant technologies are kept within the company. In the current chapter, the recent development and design characteristics of the automated pipeline repair machine are reviewed and summarised. With sufficient literature knowledge and understanding on the design requirements of an automated pipeline repair machine, the specific functional design was categorised into multiple modules which jointly make up the complete automated pipeline repair system. Each of these modules was tested based on the input parameters obtained through the developed FE models. With these analyses, the necessary modifications required to cater for deep subsea pipeline repair operation are appended.

The design characteristics of the main modules within the automated pipeline repair machine is discussed and documented in the current chapter. The main focus of the automated composite repair machine is on the wrapping module.

The feasibility of the machine to perform the designated repair operation is demonstrated, with FE analysis to validate the quality of the repair.

The work carried out herein successfully identified the conceptual design of crucial functional modules for an automated risers repair machine, which in turn provide inputs for further development of the actual prototype. The detailed selections and calculations of actuation and control components are parts of the future work and hence not explicitly investigated.

## A.2 Statement of Requirements

The design of the repair machine is based on the optimised inputs/requirements determined from the FEA of CRS. These requirements, shown in Figure A-1, are derived based on the stress-strain behaviours of the CRS subjected to various types of external loadings.

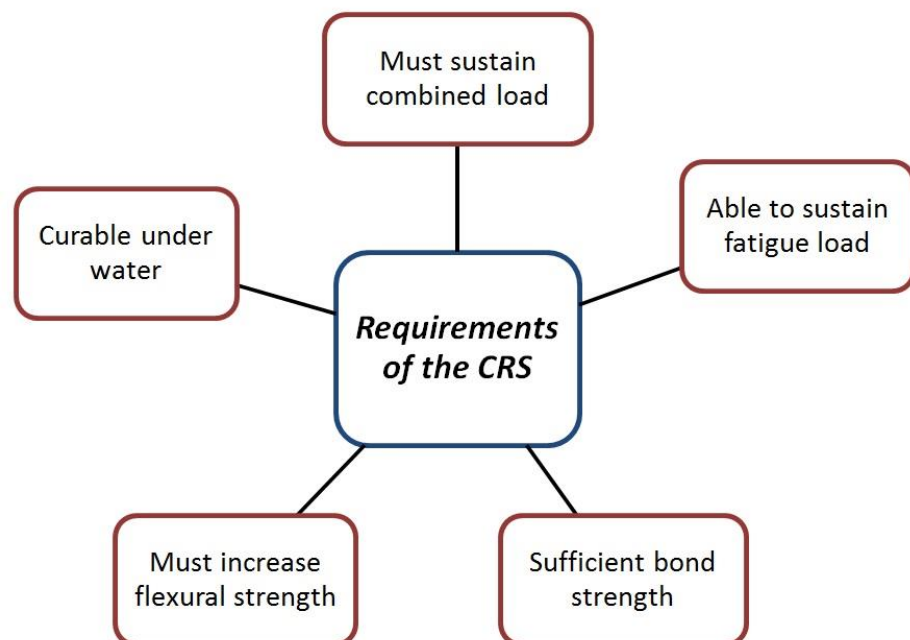


Figure A-1, Requirements of the CRS

For the composite to be curable under water, selection of the suitable FRPC has to be done. At present, there are various composite repair products that are made to be curable through contact with moisture and UV light. Thermal curing is often not recommended in offshore environment due to the highly flammable nature of the hydrocarbon fluids. It is hence assumed that products for repair of subsea risers are readily available and the actual design (i.e. dimensions) of the repair can be optimised based on the mechanical properties of the FRPC.

The ability of the CRS to sustain combined load and to increase the flexural strength of the corroded riser depends very much on the design of the repair, which is dependent of the size of the corrosion defect. This includes the thickness, length, and types of material of the repair which has been discussed in the previous chapters. In addition, the wrapping must be made so that the combined orientation of the laminate (alignment of fibres with respect to longitudinal axis of the riser) is optimum. Hence, an inspection device must be included in the automated repair machine to measure and determine the severity of the corrosion defect. Furthermore, the repair machine must be able to carry sufficient material, able to deposit the material along a designated length of the riser, and able to control the angle of wrap.

As highlighted in Chapter 4 , one of the main failure mechanism of the CRS is dictated by the disbonding between the FRPC and steel riser surface interfaces, whereas failure via delamination within the FRPC plies is not the dominant factor. It is therefore essential for the CRS to establish sufficient bond strength for adequate load transfer as well as to endure the cyclic loading in an offshore environment. In conventional pipeline repair, the quality of this bond strength is highly dependent on the method of surface preparation employed, as well as the

skill and experience of the applicator. In essence, the repair machine with a surface preparation module can ensure the consistency and quality of the surface preparation on the repair region of the pipeline prior to the application of the FRPC prepreg. The desired surface profile and surface preparation techniques are discussed in Section 4.3.2c .

In addition, tension device must be an integral component of the machine such that the FRPC prepreg can be tightly wrapped around the riser to provide the proper consolidation. Using these requirements of the CRS, a few key elements needed on the repair machine can be mapped out. These key elements can be categorised as shown in Figure A-2.

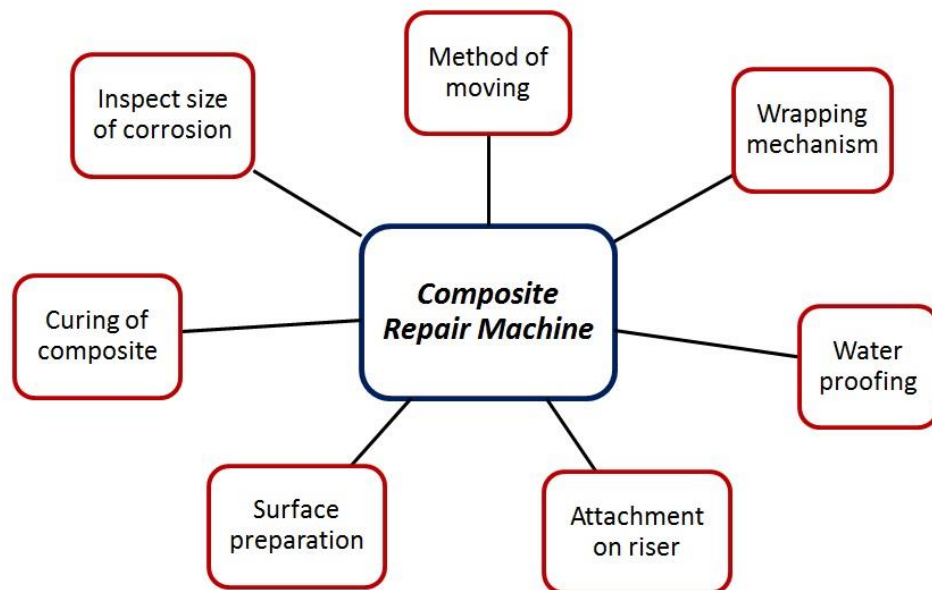


Figure A-2, Key elements of composite pipeline repair machine

These key elements can basically be established via four main modules, (1) riser traversing module, (2) inspection module (3) surface preparation module and (4) wrapping module. The current focus is directed at the wrapping module as it is an integral part of the machine that produces the optimum thickness, fibre angle

and length of the CRS. Other modules will be discussed on a conceptual level where previous designs are reviewed.

### **A.3 Riser Traversing Module**

The design of the riser traversing module is based on two of the key elements of the composite repair machine – (i) method of moving/traversing of FRPC prepreg and (ii) method of attaching the FRPC onto the defective riser surface. The in-depth literature review carried out in Chapter 2 highlighted that various work has been conducted to develop pipe crawling machine that can travel up and down along a vertical pipe. In order to draw out a conceptual design for the riser traversing module, it is important to determine the specific type of riser which the machine is supposed to operate on. The CRS studied in this research project has been focusing on rehabilitation for single-walled steel riser experienced a certain level of corrosion defects. In this respect, the path of travel over the flange of the steel riser has to be taken into consideration. In general, the common traversing mechanisms along a cylindrical pipe can be divided into two major categories, as showed in Figure A-3. The continuous motion uses wheeled motion, while the discrete motion includes legged motion and inchworm motion, shown in Figure A-4

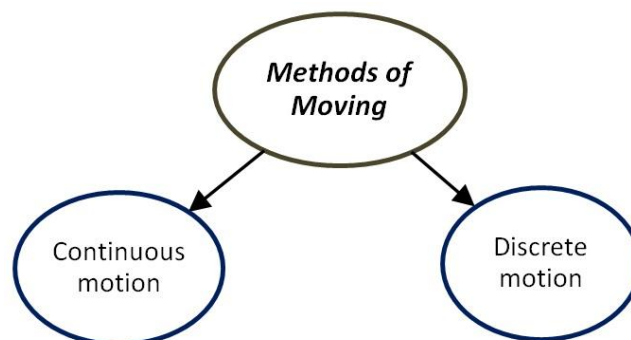


Figure A-3, Two main methods of moving along pipe

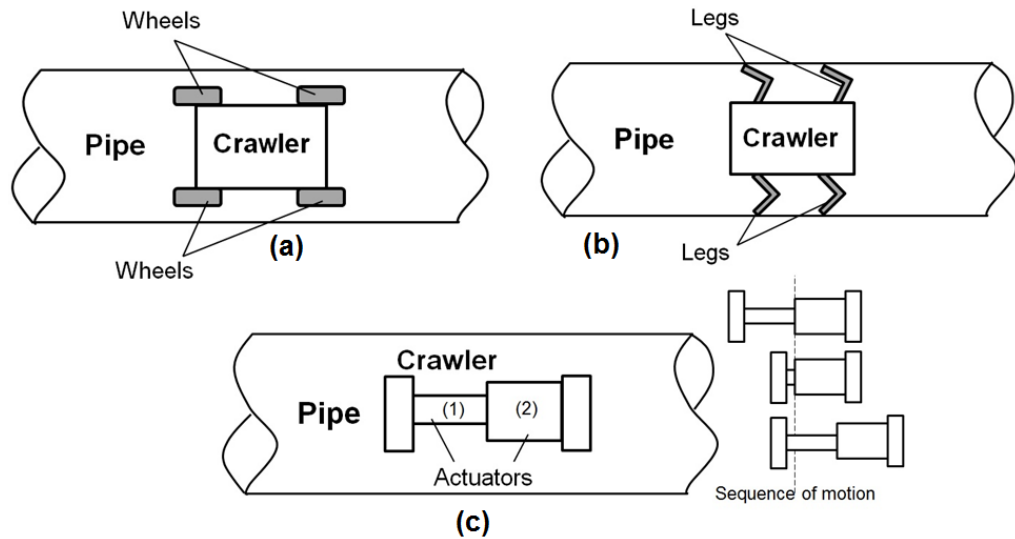


Figure A-4, Method of moving along pipe: (a) Wheeled motion, (b) Legged motion, (c) Inchworm motion

The wheeled motion is rejected as the transmission of motion depends on friction between the wheels and the surface of the riser. In an underwater environment, the existence of water can distort the frictional force, causing the application to be risky and highly complicated from a mechanical design point of view. The continuous motion also signifies that the wheels will have to be in contact with the riser at all times. This makes travelling over the flange of the steel riser unachievable. The discrete motion on the other hand is more suitable for navigating over the flange of the riser. The inchworm motion can be implemented with clamping mechanism such that the traversing module is made out of at least two articulated bodies. As one body is clamped on the riser, the other body can move away from the first body. As soon as the second body completes its motion, the roles of clamping and moving are interchanged between the first and second body. This discrete motion enables the machine to move pass the flange of the riser as the clamp opens.



A prototype pipe crawler developed by Bill Margeison is shown in Figure A-5. This riser traversing machine combines the use of continuous motion and inchworm motion to travel along the riser and to manoeuvre over the flanges. The machine attaches to the riser via a drive wheel and a set of rollers sliding along a linear rail that forms a clamp. The arrangement of the rollers is such that the machine is fully constrained on the riser through an optimal three point contact in the X, Y and Z planes (Margerison & Johnson, 2012).

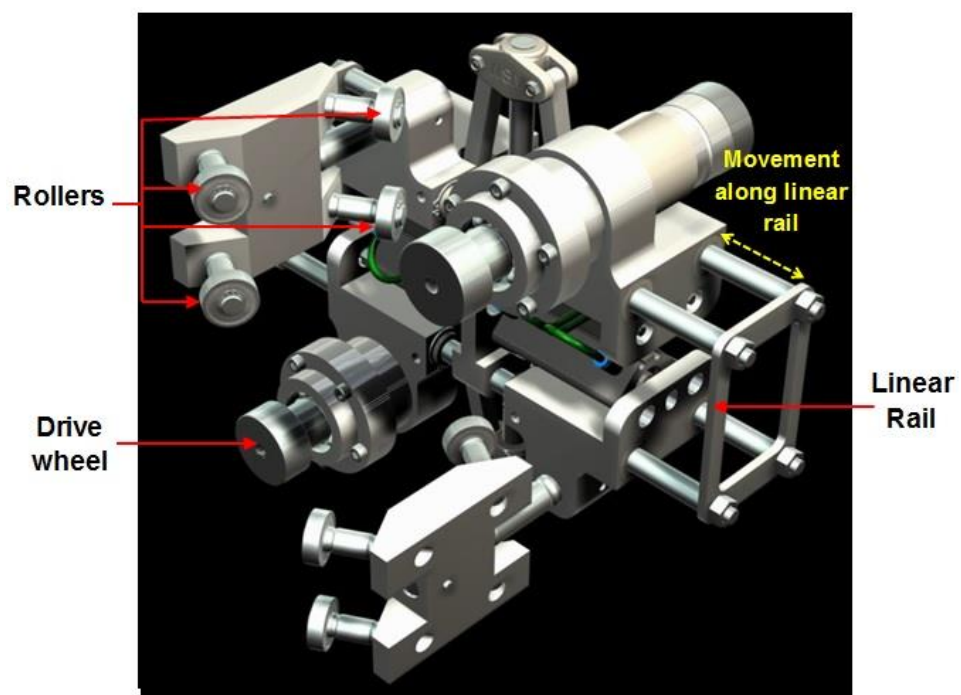


Figure A-5, 3D model of pipe crawler prototype developed by Bill Margeison  
(Margerison & Johnson, 2012)

The sequence of navigation over the flange is shown in Figure A-6. Tests carried out on this prototype proved that the clamping force applied to the rollers and the drive wheel was insufficient to support the weight of the machine, which is the weight of the traversing module itself without adding the weight from other modules. Despite the failure to provide sufficient clamping force to support its own weight, the design possesses a notable advantage on its ability to manoeuvre

over the pipe flanges. The particular traversing mechanism of this pipe crawler was taken into the current design while other aspects were critically reviewed.

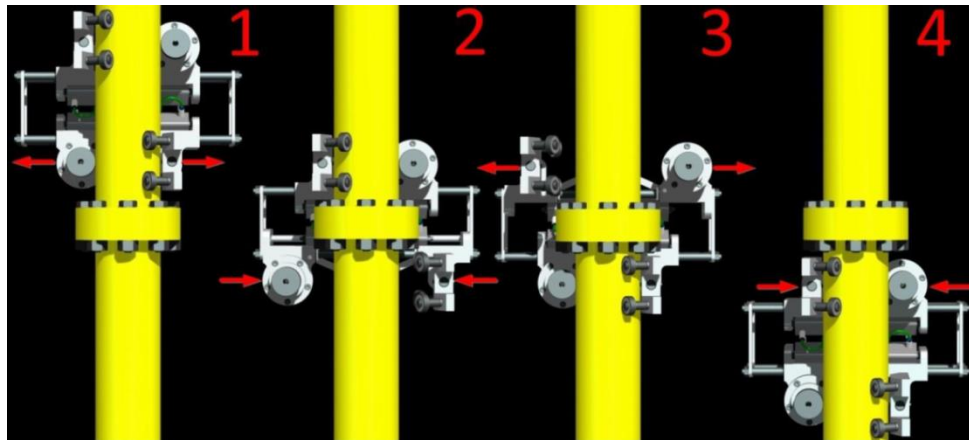


Figure A-6, Sequence of the pipe crawler navigating over a flange (Margerison & Johnson, 2012)

### **A.3.1 Improvements on Design**

The advantage of the design discussed above is its capability to move along the riser and manoeuvre over the flanges through the combination of continuous and discrete motion. However, the clamping force provided by the pneumatically actuated cylinders is insufficient. This shortcoming can be rectified by introducing the use of magnetic rollers in addition to the pneumatic clamping. The total clamping force must be capable of carrying the entire weight of the composite repair machine, which includes the inspection module, surface preparation module and wrapping module.

### **A.4 Inspection Module**

The inspection module is essential within the composite repair machine as it determines the severity of the corrosive damage on the riser. Non-destructive

testing (NDT) techniques are required to ensure that the measurement mechanism does not impose any damage on the riser during the whole inspection process. An ideal inspection technique is one that does not require the temporary shutting down of the riser such that the operation will not be halted. In order to compute the required specifications (i.e. laminate orientation, thickness, length of repair) of a CRS for rehabilitation of a corroded riser, accurate quantitative data on the depth of corrosion must be recorded.

Magnetic flux leakage (MFL) inspection is used widely to inspect low-alloy carbon steel components. Its advantage over ultrasonic inspection is that no acoustic coupling is needed between the sensor system and the object. This makes testing of risers or pipelines feasible without inserting any component into the risers/pipelines. However, this method is only limited to thickness of no more than 15mm. Besides that, the MFL method provides qualitative data rather than quantitative, making ultrasonic inspection the preferable choice when quantitative data such as the exact material loss in wall thickness is required.

Improvement on the MFL method can be done by using eddy current sensors to detect the flux leakage. This “new” MFL technology is also known as the SLOFEC<sup>TM</sup>, which stands for saturation low frequency eddy current. It is capable of detecting the defect severity in wall loss, distinguishing internal and external corrosion defects, and analyse the volume of the corrosion defect. Innospection Ltd. is the main provider of the SLOFEC<sup>TM</sup> inspection services. They developed several inspection machine such as the M-PS200, M-PS200+, MEC-Hug and MEC-Combi Crawler which are designed to inspect risers, subsea structures and subsea pipelines. These remotely operated vehicle (ROV) deployable subsea inspection tools are designed to be able to self-crawl along

pipeline using continuous motion provided by wheels and are attached onto the riser/pipelines via magnetic force. Figure A-7 shows the MEC-combi crawler along with its operation in subsea condition.



(a)



(b)

Figure A-7, MEC-Combi Crawler developed by Innospection Ltd (a) crawler machine (b) subsea inspection (Innospection Ltd, 2013)

The features of this inspection method can be implemented into the automated composite repair machine. With SLOFEC™ system, location and depth of the corrosion defect can be obtained. This data can be translated into the input data for programmable code used to calculate the required dimensions of the CRS.

### **A.5 Surface Preparation Module**

As discussed in Section 4.3.2c of Chapter 4, the effectiveness of the CRS is highly dependent on the bond strength between the FRPC and steel riser surface interfaces. The ideal condition is a perfect bond where no slip and delamination take place between the two. The surface preparation can be done in according to

the Australian standard series AS1626 entitled “Metal Finishing-Preparation and Pretreatment of Surfaces” (MT/9, 1997).

There are products readily available in the market that specializes in surface cleaning of subsea pipes. These products work on different principles such as water blasting and brush based cleaning. Figure A-8 shows the CaviDyne CaviBlaster™ which utilises a high-pressure water blasting system that removes any foreign contaminants such as marine growth through the use of hydrodynamic cavitation (explosive bubbles) (CaviDyne, 2014). The disadvantage of this system is that it is diver-operated and hence is only applicable at a limited depth.



Figure A-8, Diver operating the Cavidyne CaviBlaster™ (CaviDyne, 2014)

Brush based cleaning tools can be used to provide the required surface preparation prior to the application of the composite repair. These tools can be diver-operated or attached to an ROV for operation. The MC211 developed by Underwater Engineering Services Ltd, shown in Figure A-9, is a diver operated

hydraulically powered twin brushes that can be catered for both tubular and flat surfaces (UES, 2014).



Figure A-9, MC211 hydraulically powered twin brushes device (UES, 2014)

As highlighted in Section 5.4.2c, water jet is probably the most suitable method for surface preparation of offshore risers due to the sensitivity and highly flammable environment. Proserv developed a circular frame surface cleaning tool that contains a series of high-pressure water jets mounted on a track. This tool can accomplish a full 360° by 450mm-wide path surface cleaning around a pipe. The main advantage of this tool is that no diver is needed for its operation (Proserv, 2014).



Figure A-10, Proserv marine growth removal (MGR) tool (Proserv, 2014)

By utilising sea water as the source of the jet stream, the operation can be carried out without depositing contamination to the environment. The 360° array of water jets ensure that the entire circumference of the riser can be cleaned. Figure A-11 shows the embodiment of a design developed by Adele Carey in the University of Nottingham (Carey & Johnson, 2013). This design utilises similar concept to that of the Proserve MGR tool. A series of fan jet nozzles are strategically positioned to allow the water jets to overlap each other. The nozzles are positioned at a 45° inclination angle such that the water jet acts as a spraying blade to remove foreign particles growth on the surface of the riser. The feed rate of the water jet and the speed at which the machine traverses along the riser can be controlled to vary the condition of the completed surface.

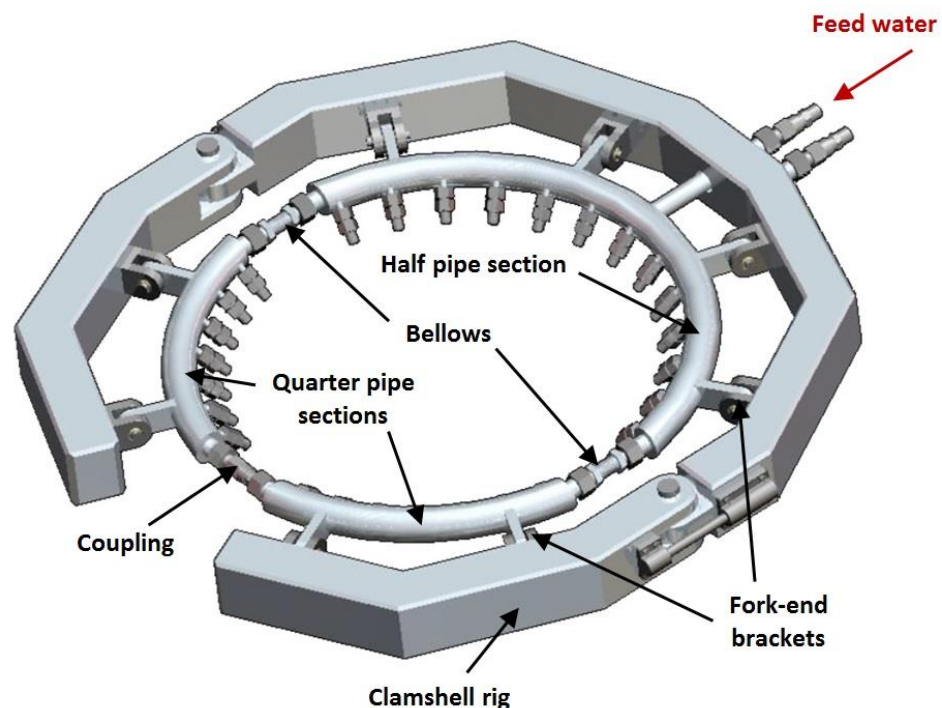


Figure A-11, Cleaning module prototype (Carey & Johnson, 2013)

The assembly is built up from a combination of one half pipe section and two quarter sections as indicated in Figure A-11. Bellows are used to connect the two

quarter sections to the half pipe section, thus providing an expandable and flexible joint between these sections. A coupling is used to join the quarter sections together such that the water can flow around the full circumference of the assembly. The pump that supplies the high pressure water feed is located on the top surface and connected to the cleaning module via umbilical.

The attachment brackets on the pipe sections of the cleaning module are fastened on fork-end brackets of a subsea clamshell rig. The rig is a standard clamshell specifically designed for underwater applications. It is hinged and controlled by hydraulic jacks whereby it can be opened and closed for installation purposes. This design is superior over the Proserv design as it can be easily mounted onto a riser due to the detachable coupling.

#### **A.6 Wrapping Module**

The wrapping module is the part which is given the most emphasis in the current research project. The mechanism of wrapping the composite prepreg tape around the corroded riser determines the effectiveness of the CRS. Factors such as wrapping angle, material overlap, end effects and curing can significantly affect the performance of the repair. In the previous chapters, the stress-strain behaviour of the CRS with respect to various wrapping angle was studied. It was determined that an optimum wrapping angle is needed to be determined such that the reinforcement fibres can provide sufficient strengthening in both hoop and axial direction to sustain the complex load profiles. Withal, the wrapping module must be designed in a manner where the prepreg tape can be wound around the riser at the desired angle. In order to make this possible, the dimension of the prepreg tape must be predefined to determine a suitable



wrapping in both the simultaneous rotational and traversing motions. The whole process resembles filament winding used in producing non-geodesic cylindrical tubes, with the only difference that the wrapping must be carried out on a stationary mandrel in the current CRS.

#### **A.6.1 Assumptions**

In most repair cases of corroded steel pipes/risers with fibre reinforced composite laminate, several layers of the wrap are required to form the total thickness of the repair. By considering this fact, it is assumed that the effects of material overlap is negligible as the consolidation from consecutive layers of wrap and the curing process will essentially form a consolidated “sleeve” as a whole.

In the design of the CRS for offshore riser, the main strengthening is focused on the corroded, weaken region. Higher stresses and strains may exist at regions of the riser adjacent to the corrosion. In regions of the riser that extend well beyond the corroded region, the stress-strain behaviour is expected to be almost identical to that of an uncorroded riser. Therefore end effects of the composite repair are negligible on un-corroded regions.

The wrapping profile of the FRPC prepreg tape imitates those in filament winding of a constant diameter cylindrical tube. However, instead of a rotating mandrel, a ring fixture that rotates around the riser will be needed to complete the wrap operation. A composite tape that is being wound around the riser at an off-axis angle will have to be aligned to the hoop direction of the riser before reversing the winding direction. Ultimately, the completed composite repair is assumed to have majority of the wrap being completed at a designated off-axis

angle with both ends having wrapped in orientation close to the circumferential hoop direction, i.e.  $90^\circ$  as shown in Figure A-12.

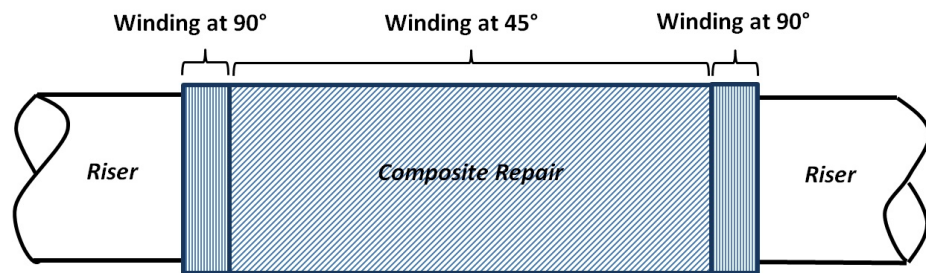


Figure A-12, Typical completed CRS wrap showing the end effect geometry at both ends of the repair

A finite element model was built to study the effects of having hoop orientated wrap at both end of the repair. This is accomplished by assigning two separate composite layups with different orientation angle. Figure A-13 showed the comparison of axial strain on the composite sleeve with (a) uniform  $45^\circ$  helical wrap and (b)  $45^\circ$  helical wrap with  $90^\circ$  on both ends. The end effects did not alter the performance of the rehabilitation in the corroded region as the maximum strain on the corroded region of the riser beneath the repair remains the same for both cases

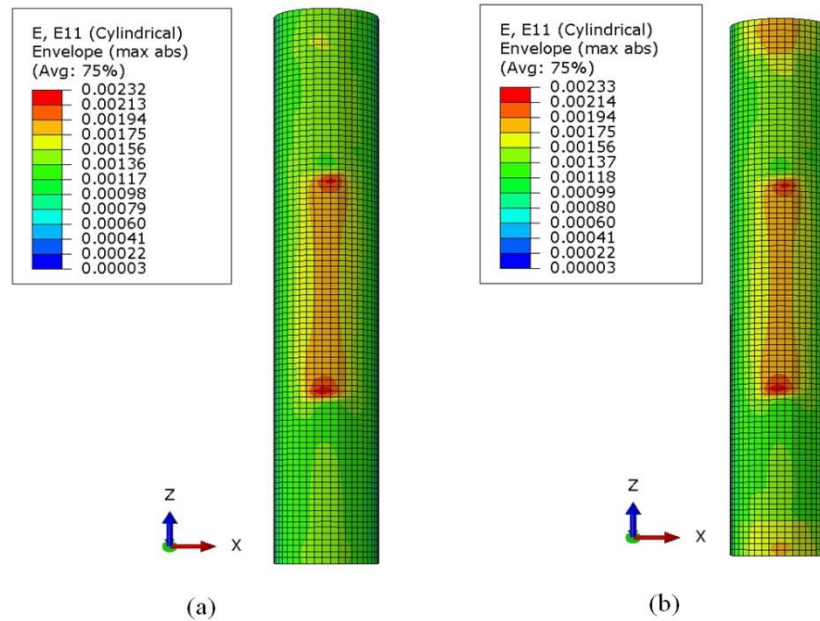


Figure A-13, Contour plot of axial strain on the composite repair sleeve with (a) uniform 45° helical wrap, (b) 45° helical wrap with 90° on both ends

Figure A-14 shows the response of the FRPC sleeves with and without the end effects of wrapping geometry. The SDV2 is a variable that indicates the fraction of the matrix failure criterion that has been satisfied. SDV2 = 0 implies that the matrix stress state is zero, while SDV2 = 1 implies that the matrix stress state has reached failure level. A noteworthy observation is that the FRPC sleeve with 90° orientation on both ends resulted in higher matrix stress levels. However, no failure was observed on the FRPC. The SDV2 state variable indicates that the stress state of the matrix is still well below the failure level. Therefore, the design of the wrapping geometry which includes 90° orientated wraps at both ends to accommodate the back and forth motion of helical wrap is expected to be feasible to function well within the design load limits.

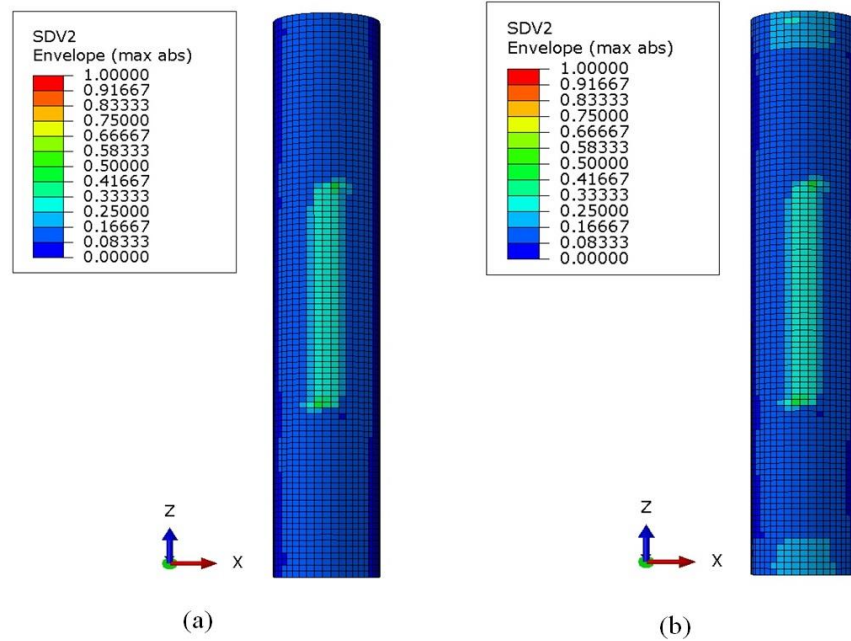


Figure A-14, Contour plot of *SDV2* on the composite repair sleeve with (a) uniform 45° helical wrap, (b) 45° helical wrap with 90° wrap at both ends

### A.6.2 Calculations of Wrapping Geometry

As discussed in previous sections, it is best to have the composite prepreg tape wound around the corroded riser at a combination of off-axis angle ( $\pm\theta$ ) built up from multiple overlapping lamina. This implies that the composite tape within a particular laminate essentially follows a helical path with constant angle while it is being laid around the circumference of the corroded region of the riser. Taking this into consideration, the wrapping/winding process of the prepreg tape around the cylindrical riser can be evaluated based on a helix equation. A circular helix of radius  $R_o$  and pitch  $2\pi b$  in the  $x, y, z$  Cartesian coordinates can be described using Eq. A-1, A-2 and A-3,

$$x(t) = R_o \cos(t) \quad \text{A-1}$$

$$y(t) = R_o \sin(t) \quad \text{A-2}$$

$$z(t) = bt \quad \text{A-3}$$

Where  $t$  represents the rotation angle in radians and  $b$  is related to the wrapping angle,  $\theta$  by Eq. A-4,

$$b = \frac{D \tan(1 - \theta)}{2} \quad \text{A-4}$$

The final state of the repair requires the fully wound structure to take up a cylindrical shape. The necessity for the composite tape to reverse winding direction when it reaches the end repair region along the corroded riser requires a wrapping path with non-constant winding angle. A predefined width of the prepreg tape must be obtained to calculate the exact helical path of the composite repair.

The wrapping profile imitates those used in filament winding. However, a specific module capable of rotating around the riser must be incorporated to provide the circular wrapping motion instead of a rotating mandrel. A carriage that houses the prepreg roll and the rotation mechanism are regulated to generate the desired winding angle. The methodology for the calculation of the winding profile can be shown in Appendix A. MATLAB code (shown in Appendix B) that defines the wrapping profile was developed to demonstrate the wrapping of FRPC in accordance to a specific orientation angle. The developed MATLAB code serves as a base function which can be modified to accommodate different wrapping geometries. The main input parameters employed in the MATLAB

code along with the values used in the examples of the CRS wrapping profile showed in Figure A-15 are tabulated in Table A-1.

Table A-1, Input parameters for wrapping profile

Parameters	Values
Diameter of the riser/pipe, $D$ (mm)	239.6
Wall thickness of the riser/pipe, $t_p$ (mm)	10.3
Depth of the corrosion defect, $d_c$ (mm)	5.15
Circumferential width of the corrosion defect, $W_c$ (mm)	125.45
Length of the corrosion defect, $L_c$ (mm)	600
Bandwidth of the prepreg tape, $B$ (mm)	20
Thickness of the prepreg tape, $t_{prepreg}$ (mm)	1
Wrapping angle of repair, $\alpha$ (°)	30; 45; 60; 90

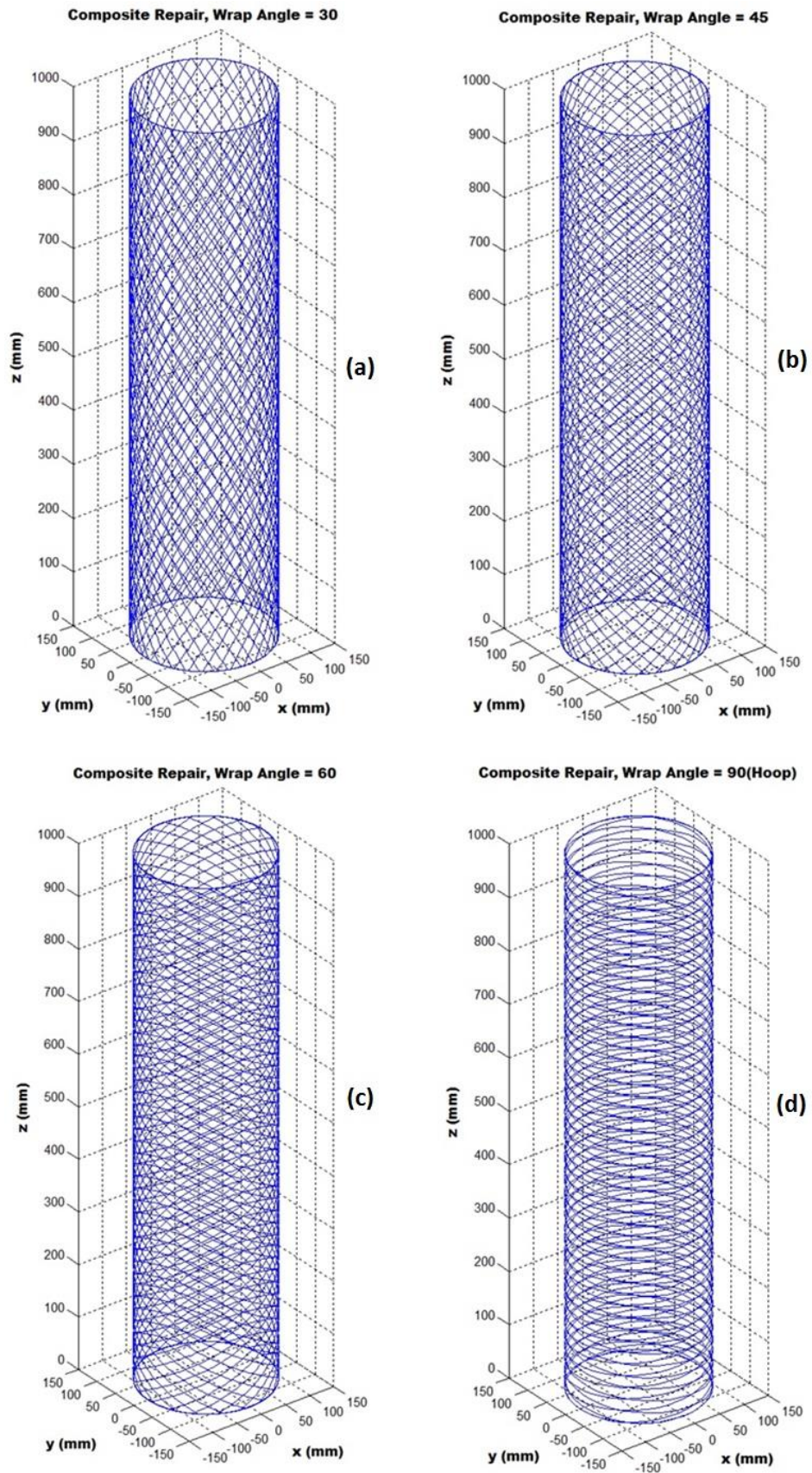


Figure A-15, Wrap profile for the CRS at varying angles - (a) 30°, (b) 45°, (c) 60° and (d) 90° (hoop)

During the winding of the prepreg tape around a riser, tape slippage might occur if the winding angle exceeds a certain threshold. To prevent this from happening, adequate tension must be applied on the tape during the winding process. Figure A-16 shows the direction of the tension force,  $F_{tension}$  during a helical winding process. The tension applied on the prepreg tape can be resolved into two components – the axial component,  $F_x$  and the transverse component,  $F_y$ . The transverse component of the tension force exerts a force on the riser, which is equivalent to the normal force,  $F_N$  on the prepreg tape. The friction between the prepreg tape and the surface of the steel riser,  $F_{friction}$  can be determined by multiplying the coefficient of friction to the normal force. The resulting friction must be equivalent or larger than the axial force generated by the tension to prevent any slippage.

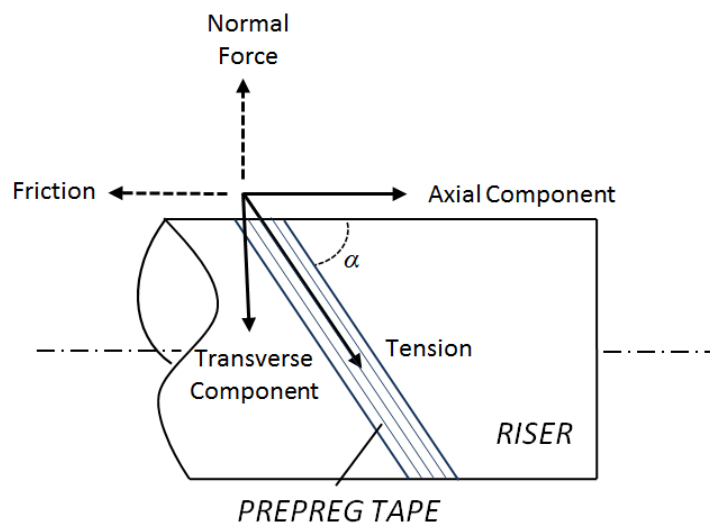


Figure A-16, Force components acting on the prepreg tape and riser

For example, in order to produce a CRS with winding angle of  $45^\circ$ , the axial force component of the tension can be calculated using Eq. A-5

$$F_x = F_{tension} \cos \alpha \quad \text{A-5a}$$

$$F_x = F_{tension} \cos 45^\circ \quad \text{A-5b}$$



$$F_x = 0.7071F_{tension} \quad \text{A-5c}$$

The transverse component of the tension can be calculated using Eq. A-6,

$$F_y = F_{tension} \sin \alpha \quad \text{A-6a}$$

$$F_y = F_{tension} \sin 45^\circ \quad \text{A-6b}$$

$$F_y = 0.7071F_{tension} \quad \text{A-6c}$$

The frictional force is equivalent to the coefficient of friction of the prepreg tape multiply by the normal force acting on the prepreg tape (Eq. A-7a), where the normal force is equivalent to transverse force component (Eq. A-7b).

$$F_{friction} = \mu F_N \quad \text{A-7a}$$

$$F_{friction} = \mu \cdot F_y = \mu \cdot 0.7071F_{tension} \quad \text{A-7b}$$

In order to prevent slippage of the prepreg tape during winding at an angle of 45°, the minimum value of the coefficient of friction can be calculated by equating Eq. A-5c to Eq. A-7b,

$$\mu \cdot 0.7071F_{tension} \geq 0.7071F_{tension} \quad \text{A-8}$$

$$\mu \geq 1$$

Hence, the coefficient of friction between the prepreg tape and the steel surface must be at least 1 to produce a CRS via winding at 45°. The coefficient of friction is affected by the temperature of the prepreg during the winding operation. The coefficient of friction decrease with the increase in temperature as the viscosity of the resin in the prepreg system decreases exponentially. In addition, the coefficient of friction increases with the velocity at which the prepreg is being pulled (Grewal & Hojjati, 2015). Hence, the wrapping speed and the temperature

must be regulated effectively in order to produce a CRS at a desired winding angle.

### A.6.3 Mechanical System Design

A prototype wrapping machine developed within the University of Nottingham was used as the basis for designing the wrapping module of the composite repair machine (Land, et al., 2012). The final rendered image of this original wrapping machine is shown in Figure A-17.

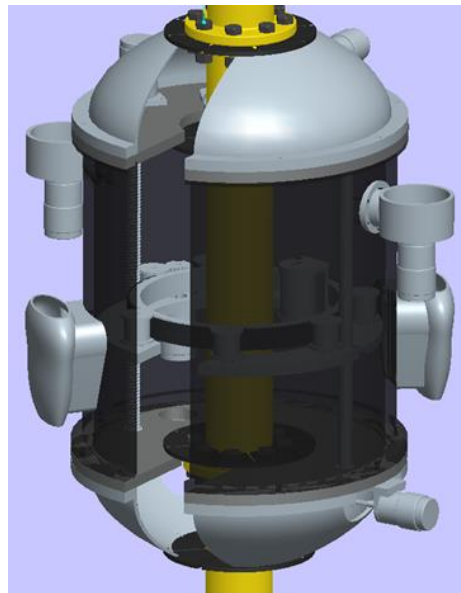


Figure A-17, Rendered image of the pipe wrapper prototype (Land, et al., 2012).

The functionality of the wrapping module can be categorised into two parts: traversing unit and rotary unit. The traversing unit consists of a lead screw, a rotary ring and a motor as shown in Figure A-18. The rotation of the lead screw is accomplished via a variable speed motor. This lead screw translates the rotary motion into the traversing motion of the rotary ring along the length of the repair. The traversing speed of the ring is controlled by the speed of the motor and the pitch of the lead screw.

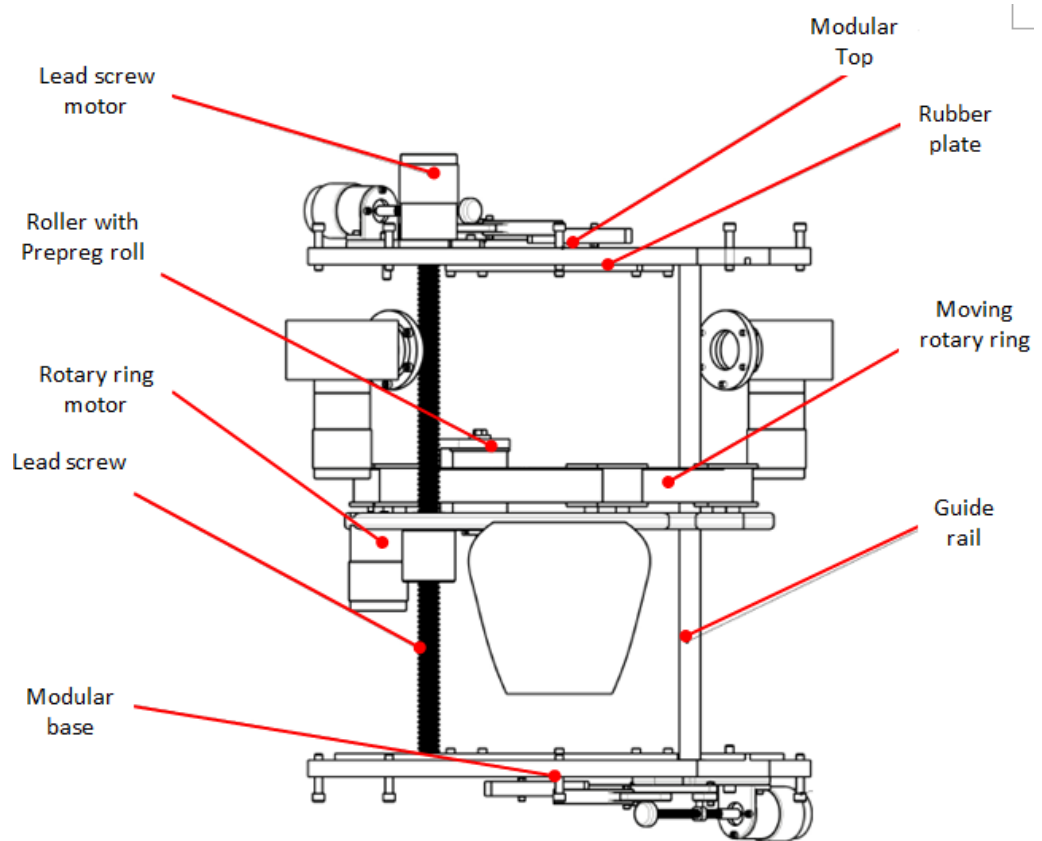


Figure A-18, Diagram of pipe wrapper prototype (Land, et al., 2012)

The rotary unit consists of a ring gear, prepreg holder (roller), tensional device and rollers guide. The ring gear is rotated by spur gear which is driven by an additional motor that is connected to the ring of the traversing unit. The prepreg holder, tensional device and roller guides are mounted on the ring gear. A 360° rotation of the ring gear around the riser enables the prepreg tape to be wound as the traversing unit moves along the length of the riser. The clearance between the prepreg holder and the riser must be sufficient such that the required amount of material can be carried on board the machine. The length of the prepreg required to complete one circuit can be calculated via Eq. A-9,

$$L_{comp} = \pi D \cdot \left( \frac{2\theta_{dwell}}{360^\circ} + n \right) \quad \text{A-9}$$

where  $n$  is the number of revolutions required to complete one circuit. The total length of prepreg tape required to complete a specific repair can be calculated by simply multiplying  $L_{comp}$  with the number of circuits,  $N_c$ , needed to achieve the desired thickness of CRS.

$$L_{comp,Total} = L_{comp} N_c \quad \text{A-10}$$

Based on this computed length, the outer diameter of the prepreg roll shown in Figure A-19 can be determined via Eq. A-11,

$$t_{prepreg} = \frac{\pi \left( \frac{D_{roll,o}^2}{4} - \frac{D_{roll,i}^2}{4} \right)}{L_{comp,Total}} \quad \text{A-11}$$

where  $D_{roll,o}$  and  $D_{roll,i}$  are respectively the outer and inner diameter of the prepreg roll.  $t_{prepreg}$  is the thickness of the prepreg tape which is usually obtainable from the manufacturer specifications.

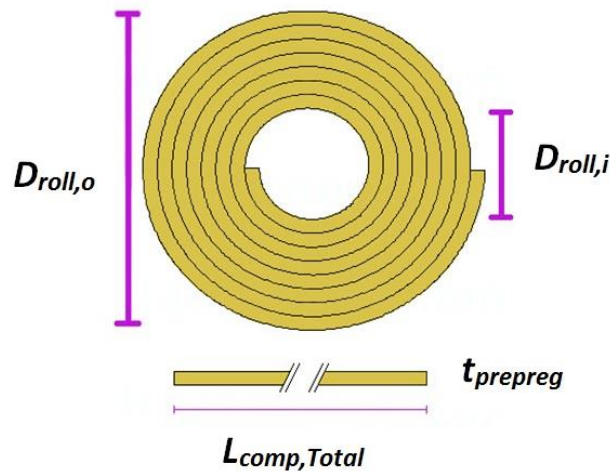


Figure A-19, Dimensions of the roll

For example, if the total length of prepreg tape required to conduct a wrap on a corroded riser is 10m while the thickness of the prepreg tape and diameter of the roller are 1mm and 20mm respectively, the outer diameter of the prepreg roll can be calculated as,

$$0.001 = \frac{\pi \left( \frac{D_{roll,o}^2}{4} - \frac{0.2^2}{4} \right)}{10}$$

$$D_{roll,o}^2 = 0.05273m^2$$

$$D_{roll,o} = 22.96mm$$

The tensional device is designed to generate a constant tension force in the prepreg tape throughout the winding process. As discussed, this tension force is needed to prevent the slipping of the prepreg tape during the winding process. In addition, adequate tension force can ensure proper consolidation of the prepreg on the riser during the curing process.

#### **A.6.4 Improvements on Design**

This existing repair machine, shown in Figure A-17, contains two propellers which serve to help the device traverse along the length of the riser. This feature can be discarded as the movement of the composite repair machine will be facilitated by continuous motion of the magnetic rollers (wheeled motion along the riser) and discrete motion of the linear rail clamps (inchworm motion of the clamp over the flanges) to accommodate the traversing motion over a flange (discussed in section A.3). A preliminary model of the wrapping module was developed to aid in the visualization of the wrapping mechanism. The major parts in the module are labelled as shown in Figure A-20. The length of the lead



module while other modules are omitted. It is assumed that the riser traversing module is attached to the inspection module, surface preparation module, wrapping module and curing module to form the complete machine of the CRS. Hence, no clamping mechanism is required for the wrapping module as depicted in the Figure A-21.

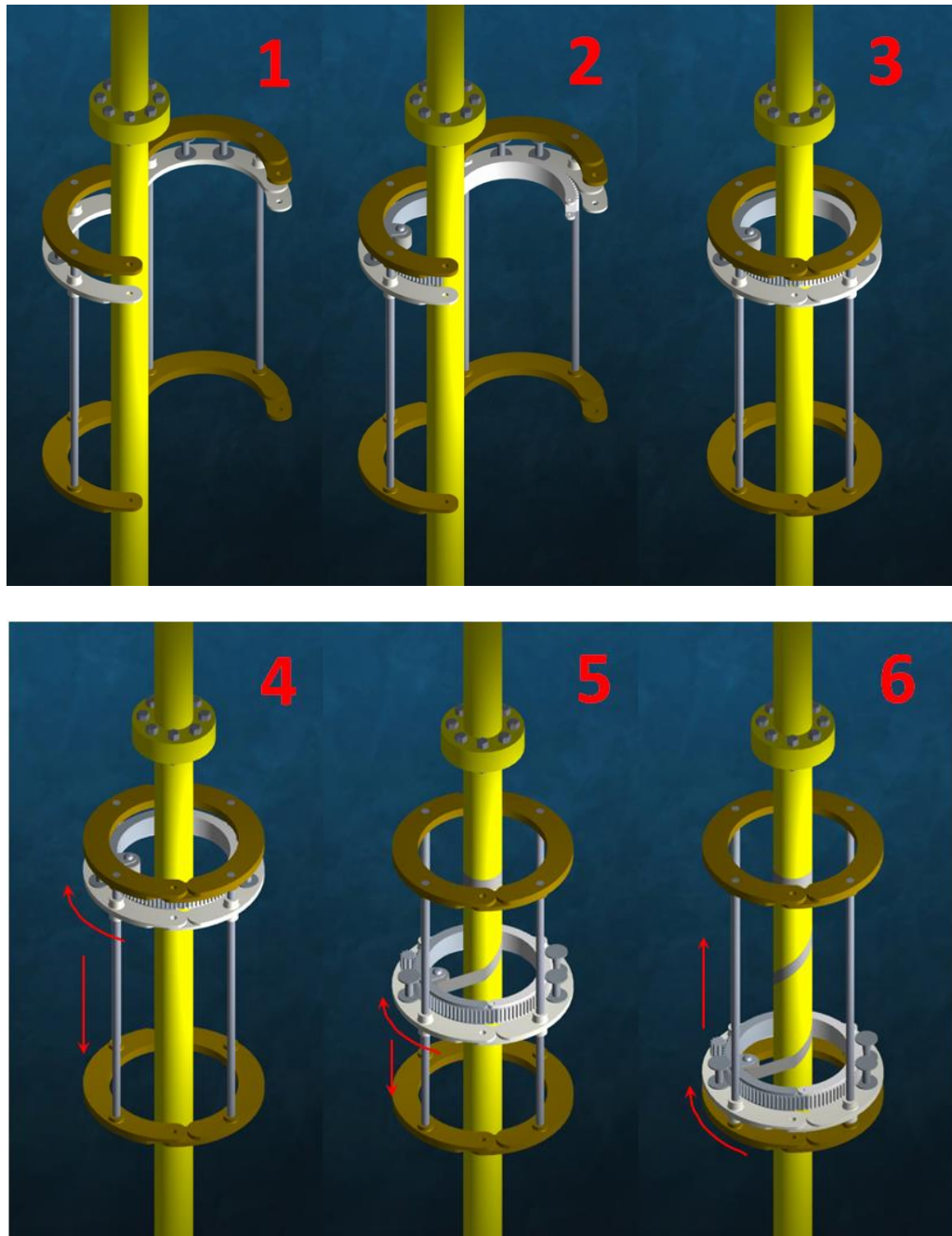


Figure A-21, Wrapping sequence of the wrapping module

During the deployment of the composite repair machine on a live riser, the supporting rings and traversing ring are expanded (1). The ring gear is fitted on to the traversing ring, ensuring that the teeth of the ring gear and spur gear matches each other (2). The supporting rings and traversing ring are closed and locked in place via bolted joints while the ring gear is close via an interlocking mechanism (3). The spur gear which is rotated by a motor drives the rotation of the ring gear. Simultaneously, a variable speed motor rotates the lead screw, enabling the traversing unit to traverse downwards (4). The prepreg tape is wound around the riser due to the combination of these movements (5). Once the traversing unit reach the designated length of repair, the rotation of the lead screw is reversed so that the traversing unit moves upwards along the riser (6).

#### **A.6.5 Controlling**

To produce the composite repair according the desired path as calculated above, the speed of the rotating ring and carriage unit must be controlled. The speed of the rotating ring is set to a constant value while the carriage unit traverse along the length of the riser at varying velocities. Higher velocity results in a smaller helical angle (i.e. fibres aligned closer to the longitudinal axis of the riser) whereas lower velocity produces wrap closer to the hoop winding. The relationship between the speed of the rotating ring and carriage unit can be defined through Eq. A-12,

$$N_s = \frac{r2\pi N_m}{L \tan \theta} \quad \text{A-12}$$

Where  $N_s$  is the rotational speed of the lead screw in RPM,  $N_m$  is the rotational speed of the ring gear in RPM,  $L$  is the pitch of the lead screw and  $\theta$  is the winding angle of the composite repair. In order for the prepreg wrap to travel



back and forth along the riser at the designated length of repair, instructions have to be given to the traversing unit such that it will stop and reverse its direction. This can be achieved by calculating the cycle time for the traversing unit to travel from one end to the other end of the repair. A timer along with a position sensor can be used to provide feedback to the current position of the traversing unit and the ring gear. A flow chart for the control of the wrapping sequence is shown in Figure A-22. Input values for the position and timing sensors are based on the calculated values from the wrapping geometry code.

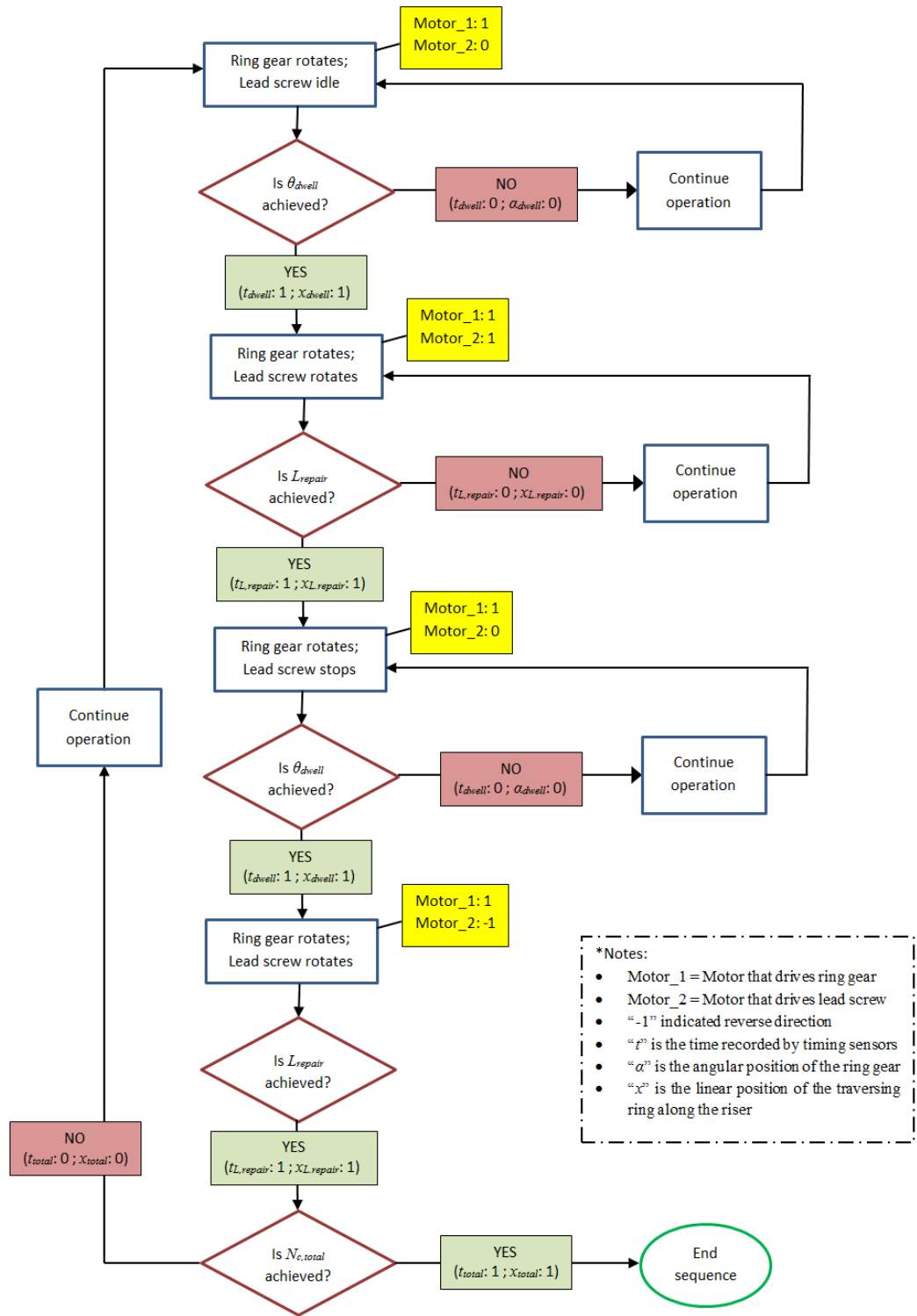


Figure A-22, Flow chart for the wrapping sequence

## **A.7 Summary**

To the knowledge of the project team, an automated composite repair machine that can operate in subsea conditions is not currently available in the commercial market. Preliminary design for the major modules crucial for the accomplishment of the automated riser repair operation was proposed in the present work. These conceptual designs were achieved by implementing various improvements on the existing modules available in the literature. For the traversing module, surface preparation module and inspection module, it is determined that various systems exist in the market where modifications can be implemented to suit the function of the automated repair machine.

Based on the developed MATLAB code for the wrapping geometry of the composite repair and the preliminary 3D CAD model, a probable form of the wrapping module was designed, whereby the model can be further developed to build up the complete automated repair machine for CRS. The developed concept which is based on the principles of filament winding is a simple two-degrees-of-freedom machine. Initial aim would be to produce the prototype that is capable of producing the desired wrapping geometry without considering the use of proper prepreg material and its curing. Extensions can then be made to incorporate the actual wrapping and curing on a scaled pipe to study the stress-strain behaviour of the CRS produced in a dry environment prior to its implementation under a water enclosure.

## Appendix B Calculations of wrapping geometry

The winding sequence of the CRS imitates those used in filament winding. When the prepreg tape is wound and completes one full cycle through the entire length of the repair, one circuit is formed. Due to an offset reach of a different point it might take more than one cycle of the entire length for the tape to reach the start point. Hence, when the winding reaches its starting point after a certain number of circuits, it is referred to as a pattern. In order to achieve the desired pattern, a dwell angle,  $\theta_{dwell}$ , is introduced at both ends of the repair wound. In addition, the dwell angle can ensure that there is sufficient traction between the prepreg tape and the riser before the carriage reverses its direction of travel.

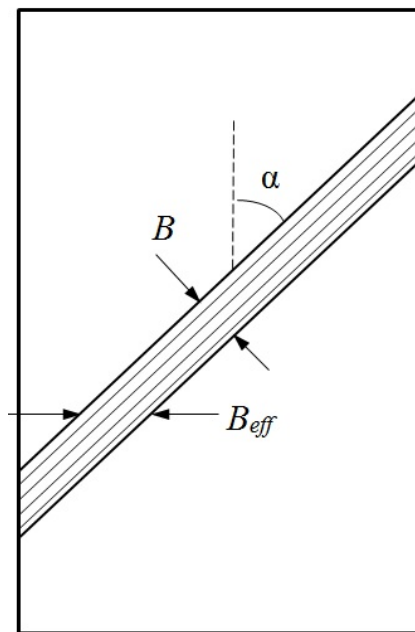


Figure 0-1, Developed envelope of prepreg path

Figure B-1 shows a schematic diagram of a developed envelope with the prepreg path.  $B_{eff}$  represents the effective bandwidth of the prepreg tape along the circumference of the riser and is calculated by,

$$B_{eff} = \frac{B}{\cos \alpha} \quad \text{B-1}$$

In order for the wrapping sequence to complete one circuit, the prepreg band has to travel twice the length of the repair. The corresponding number of revolutions of the prepreg band around the riser for one complete circuit can be computed using Eq. A-2

$$n = \frac{2L_r \tan \alpha}{\pi D} \quad \text{B-2}$$

Where  $n$  = number of revolutions required to complete one circuit,  $L_r$  = the length of the composite repair system. The value of  $n$  can be expressed in terms of degrees ( $^\circ$ ). Two times the dwell angle can be added to determine total number of degrees required to make a full circuit,

$$\theta = \theta_n + 2\theta_{dwell} \quad \text{B-3}$$

The value  $\theta$  is then subtracted by a whole multiple of  $360^\circ$  to obtain the angular advance,  $\theta_{adv}$  of the prepreg band once a circuit is completed. This angular advance exists as the prepreg band will often not be able to return to its original starting point due to the complexity of the motion. In order to make a pattern, there needs to be a multiple of advance angles such that this multiple will be equal to a multiple of  $360^\circ$ . This can be expressed as,

$$(m) \cdot \theta_{adv} = (k) \cdot 360^\circ \quad \text{B-4}$$

Where  $m$  and  $k$  are integers and should be as small as possible. However, the value of  $\theta_{adv}$  might not be a whole number that is a factor of  $360^\circ$ , causing  $m$  and  $k$  to be very large before Eq. B-4 can be satisfied. This can be resolved by adjusting the dwell angle. For example if  $\theta_{adv} = 81^\circ$ , it can be adjusted to a whole number  $90^\circ$  which is a factor of  $360^\circ$ . The dwell angle can then be adjusted to

be  $\theta_{dwell} + (90^\circ - 81^\circ)/2$ . The ratio of  $(m/k)$  gives the number of circuit (number of advance angles) required to complete a pattern.

In the computation of a complete pattern as described above, the prepreg band will go back exactly to the same position where it originally started. This is undesirable because if the process continues, the prepreg tape will follow the same path over and over again without covering the whole surface of the riser. It is hence desirable to advance the position of the prepreg band, one bandwidth distance along the circumference of the riser after the completion of one circuit. This distance can be expressed in angular value and is calculated via Eq. B-5

$$\Delta\theta = \frac{B_{eff}}{\pi D} \times 360^\circ \quad \text{B-5}$$

This advanced angular value,  $\Delta\theta$  can be accumulated over the total number of circuits needed to form a pattern. In each circuit, the divided value of  $\Delta\theta$  is shared by two dwell angles as the prepreg band travel back and forth in one circuit. In other words, the new dwell can hence be obtained by adding the values below,

$$\Delta\theta \left( \frac{k}{m} \right) \times \frac{1}{2} \quad \text{B-6}$$

A pattern may consist of intersections of prepreg band (i.e. band crossovers) at certain sections. Crossovers can occur at more than one section depending on the dimension of the riser and the winding angle. A layer is defined as a set of patterns that provides complete surface coverage along the entire length of the repair. As discussed earlier,  $B_{eff}$  represents the effective bandwidth of the prepreg

tape along the circumference of the riser. Hence, for full surface coverage, the number of circuits required can be calculated as,

$$N_c = \frac{\pi D}{B_{eff}} \quad \text{B-7}$$

where  $N_c$  is the total number of circuits needed to form a layer. In order to form a composite repair that has the required thickness, several layers have to be wound. The total number of circuits needed to form the complete CRS can be computed with the knowledge of the thickness value of the prepreg tape.

$$N_{c,total} = \frac{t_{repair} N_c}{t_{prepreg}} \quad \text{B-8}$$

## Appendix C MATLAB Code for Wrap Geometry

```
%Key in required input data
D = 239.6;
tp = 10.3;
dc = 5.15;
Wc = 125.45;
Lc = 600;
Cp = pi*D;
B = 20;
tpreg = 1;
theta = 45*pi/180;

%D = Outer diameter of the pipe
%tp = Thickness of the pipe
%dc = Depth of the corrosion defect
%Wc = Width of the corrosion defect
%Lc = Length of the corrosion defect
%Cp = Circimference of the pipe
%B = Bandwidth of the prepreg tape
%tpreg = Thickness of cured prepreg
%theta = Winding angle of the composite repair relative to the
axis of the pipe

%The required length and thickness of the composite repair
tr = (14.83*((dc/tp)^1.685)*((Wc/Cp)^0.468))*tp;
Lo = 2.5*((D*tp/2)^0.5);
Lr = round(2*Lo + Lc + 224.3626);

%tr = Thickness of the repair
%Lo = Length of the repair extending over one side of the
corrosion defect
%Lr = Total length of the composite repair

%%CALCULATION OF THE COMPOSITE REPAIR SYSTEM'S WRAPPING SEQUENCE%%
%The the effective bandwith of the composite prepreg wrap around
the
%circumference of the pipe
Be = B/cos(theta);

%The number of revolutions required for the prepreg tape to travel
the
%required length of the repair
Nr = Lr*tan(theta)/(pi*D);

%The number of revolutions required for the prepreg tape wrap to
complete
%one circuit (i.e. back and forth the length of repair, Lr)
Nc = 2*Nr;

%The value of Nc expressed in terms of radians,
Ncr = 2*pi*Nc;

%The dwell angle has to be added to both ends of the winding in
order to
%obtain the total number of degrees required to make a circuit
Ncrd = Ncr + 2*pi;
```



```

%Determine the angular advance
Ne = Ncrd - 2*pi;
    if Ne >= 2*pi;
        Ne = Ncrd - 2*(2*pi);
        if Ne >= 2*pi;
            Ne = Ncrd - 3*(2*pi);
            if Ne >= 2*pi;
                Ne = Ncrd - 4*(2*pi);
            end
        end
    end
end

%Calculate the number of circuits required to complete one pattern
if rem(Ne,(pi/6)) == 0;
    Cn = (2*pi)/Ne;
else i = 1;
    e = (pi/6)*i - Ne;
    while e < 0
        i = i+1;
        e = (pi/6)*i - Ne;
    end
    Cn = (2*pi)/(Ne+e);
end

%The angular shift of the prepreg tape so that the tape does not
return to
%its starting point after the completion of one pattern
Shift = Be/(pi*D)*(2*pi);
dwa = pi + e/2 + Shift/(2*Cn);

%The number of circuits for surface coverage
Cnc = round ( Cp/Be );
%The number of circuits for the wrap to achieve the required
%thickness of composite repair system
Cnt = round((tr/tpreg)*Cnc);

%%PLOT OF THE WRAPPING SEQUENCE FOR THE DESIGNED COMPOSITE REPAIR
SYSTEM%%
%number of revolutions per circuit
rev = (Ncr + 2*dwa)/(2*pi);

%Generates an angle vector with Cnc*1200 values
a = [0: Cnc*rev*2*pi/(Cnc*1200-1) : Cnc*rev*2*pi];

% transforms angle vector into displacement vector
%d = a/n;

% calculates x, y, and z
x = (D/2)*cos(a);
y = (D/2)*sin(a);
% z = ((1)*(cos(d)+1)/2);

%Generating the vector for z based on the calculated parameters
cla_dwell = [zeros(1,(round(dwa/(2*pi))*1200/rev))-1];
cla_wrap = [0:(Lr/round(((Ncr/2)/(2*pi))*(1200/rev))):Lr];
clb_dwell = [Lr*ones(1,(round(dwa/(2*pi))*1200/rev))-1];
clb_wrap = [Lr:- (Lr/round(((Ncr/2)/(2*pi))*(1200/rev))):0];

z = [cla_dwell, cla_wrap, clb_dwell, clb_wrap];
zt = repmat(z,1,Cnc);

```

```
%3D plot of the composite repair system winding pattern
plot3(x,y,zt, 'linewidth',1)
grid on
axis equal
title('A helix - 3D view')
xlabel('x = cos(a)')
ylabel('y = sin(a)')
zlabel('z = d')
```